Università degli Studi di Pavia

**DOTTORATO DI RICERCA**

Medicina Sperimentale
Chirurgia Sperimentale e Microchirurgia

CICLO XXIX

# Development of novel platforms for diagnosis and therapy in experimental medicine


Presentata da: **Elena Piera Porcu**

Coordinatore Dottorato: **Prof. Paolo Dionigi**

Tutor esterno: **Prof. Paolo Giunchedi**


Esame finale anno accademico 2015 – 2016

*To my Family…*

**List of publications**

*I.* **Development of thermosensitive chitosan/glicerophospate injectable in situ gelling solutions for potential application in intraoperative fluorescence imaging and local therapy of hepatocellular carcinoma: a preliminary study.** Salis, A., Rassu, G., Budai-Szűcs, M., Benzoni, I., Csányi, E., Berkó, S., Maestri M., Dionigi P., Porcu E.P., Gavini E.,Giunchedi, P. *Expert Opinion on Drug Delivery*, **2015**, 12(10), 1583-1596.

*II.* **Engineered microparticles based on drug-polymer coprecipitates for ocular controlled delivery of Ciprofloxacin: influence of technological parameters.** Gavini, E., Bonferoni, M. C., Rassu, G., Sandri, G., Rossi, S., Salis, A., Porcu E.P., Giunchedi P. *Drug Development and Industrial Pharmacy*, **2016**, 42(4), 554-562.

*III.* **Composite chitosan/alginate hydrogel for controlled release of deferoxamine: a system to potentially treat iron dysregulation diseases.** Rassu, G., Salis, A., Porcu, E. P., Giunchedi, P., Roldo, M., Gavini, E. *Carbohydrate Polymers*, **2016**, 136, 1338-1347.

*IV.* **Indocyanine green delivery systems for tumour detection and treatments** Porcu, E. P., Salis, A., Gavini, E., Rassu, G., Maestri, M., Giunchedi, P. *Biotechnology Advances*, **2016**, 34(5), 768-789.

*V.* **In situ forming biodegradable poly(ε-caprolactone) microsphere systems: a challenge for transarterial embolization therapy. In vitro and preliminary ex vivo studies** Salis A., Porcu E. P., Gavini E., Fois G. R., Cornaglia A.I., Rassu G., Diana M., Maestri M., Giunchedi P., Nikolakakis I. *Expert Opinion on Drug Delivery*, accepted manuscript.

**SUMMARY INDEX**

**ABSTRACT**

Transcatheter intra-arterial therapies are widely used for the palliative treatment of intermediate and relatively advanced stages of hepatocellular carcinoma (HCC), which are not suitable for surgical resection. The most common loco-regional therapies used to treat unresectable HCCs are transarterial chemoembolization (TACE) and transarterial embolization (TAE). In contrast to the normal liver, which has dual blood supply, HCC is supplied almost exclusively by hepatic artery. For this reason, these procedures involve the localized delivery of embolic agents alone (TAE) or combined with cytotoxic drugs (TACE) to the tumour through its feeding hepatic artery, leading to local cancer destruction and preserving the normal hepatic parenchyma.

TAE is a minimally invasive procedure that induces tumour regression blocking the blood flow by injection of embolic microparticulate agents. Commercial embolic products are constituted by calibrated microspheres with different range size in order to achieve an accurate targeting.

The main aim of the present thesis was the development of alternative platforms for the application in TAE. In some cases, it has been decided to combine the embolic agents with the indocyanine green (ICG) fluorescence. Indeed, the microspheres currently used in clinical application cannot be visualized *in vivo* but the intraoperative detection of embolic agents could be exploited by surgeon during resection of the tumour.

As an alternative to preformed embolic microspheres, thermosensitive chitosan/glycerophosphate (C/GP) solutions loaded with ICG were prepared for the imaging and loco-regional treatment of HCC. These systems consisted of injectable hydrogel platforms, which exhibited sol-gel transition around body temperature. The technological properties of these formulations (such as gelling time, injectability, compactness and resistance of gel structure, gelling temperature, biodegradability and in vitro dye release behavior) were investigated. Preliminary e*x vivo* studies were performed using an isolated bovine liver. It was observed an increase of gel strengths and gelation rates increased for the systems having highest cross-link density between C and GP. This aspect is more evident for C/GP solutions that showed a gel-like precipitation at 4°C. Furthermore, the best injectability has been displayed by formulations with the lowest cross-linking density between the polymer and the cross-linker. The loading of ICG did not influence the gelation rate. In addition, it was observed no significant release of ICG

from the hydrogels due to the strong interaction between C and ICG. *Ex vivo* studies revealed the fast gelation of thermosensitive solutions in correspondence of the injection site. Therefore, the developed ICG-loaded hydrogels have the potential for transarterial therapy of HCC as embolic agents and following intraoperative fluorescence imaging for the resection of tumour nodules.

Calibrated microspheres with fluorescent properties were developed. Biocompatible ICG-loaded microspheres were prepared through multi-step method. Chitosan-ICG complexes were nebulized by using spray-dryer and then inclused into polymeric microspheres, based on cellulose acetate butyrate (CAB) and fabricated by emulsion/solvent extraction method. Technological parameters such as yield, size, encapsulation efficiency and morphology were investigated. Final microparticles showed spherical shape and smooth surface, as well as good injectability, confirming their suitability for transarterial administration. In addition, ICG release from these systems was very low, due to the significant interaction between chitosan and the dye. This property was also confirmed by *in vitro* fluorescence imaging studies, conducted using Photodynamic Eye (PDE) for the detection of microspheres incubated in human plasma. These systems were able to maintain the fluorescence selectivity for 4 weeks, releasing low ICG amount.

The intra-arterial injection of preformed microspheres can cause the catheter clogging. To overcome this limit, the formulation of novel *in situ* forming microspheres could be advantageous. These systems could be suggested as a novel tool for the TAE treatment of HCC. Indeed, they consist of injectable emulsions in which an internal organic polymer phase is emulsified in an oil phase resulting in a stable dispersion of polymer–organic solvent solution microglobules (premicrospheres) dispersed in a continuous oil phase.

Upon *in vivo* injection, the system is exposed to the water from body fluids and the microglobules hardens to solid microspheres due to the diffusion of solvent out of the microglobules In this research work, *in situ* forming microsphere system based on biodegradable poly(ε-caprolatone) and loaded with Ibuprofen sodium were prepared and characterized. The influence of technological parameters on formulation properties, such as the size, encapsulation efficiency and drug release was studied through a mixture experimental design. In addition, an *ex vivo* experiment was carried out on isolated rat

livers in order to confirm the *in situ* hardening of microspheres. All formulation parameters affected the investigated properties and *ex vivo* studies revealed that emulsions were able to form microspheres inside the vessels.
During PhD program, other research lines involving different therapeutic applications (ocular infections and iron dysregulation) were developed.

Fluoroquinolones show a remarkable activity against Gram-positive and Gram-negative ocular pathogens. Among them, ciprofloxacin can be currently considered the anti-bacterial agent of choice for the eye. Nevertheless, this drug is characterized by low compliance because it requires frequent administrations. The formulation of topical controlled release systems of ophthalmic drugs could improve their low ocular bioavailability compared to the traditional eye drops. To this end, the ionic interactions between ciprofloxacin and the polyelectrolytes lambda carrageenan or chondroitin sulfate were exploited for the preparation of coprecipitates that can act as microparticulate carriers for the controlled release of ciprofloxacin. The influence of several technological parameters such as drug and polymer concentration, use of surfactant and stirring of solutions was investigated in order to obtain coprecipitates with a size suitable for the ocular administration.
The results obtained from this study showed that chondroitin sulfate coprecipitates were the best formulations for ophthalmic administration. A further improvement of the particle size characteristics has been obtained with the addition of surfactants during the preparation process.

Iron is a redox active metal, indispensable for life. Nevertheless, its excess causes the release of reactive oxygen species (ROS), which produce oxidative damage to various cell components, resulting in toxic effects. Indeed, iron dysregulation plays a key role in the etiology of aging and several pathologies, such as neurological disorders, cancer and stroke. Recently, the potential application of deferoxamine (DFO) in several iron dysregulation diseases has been studied. DFO is an iron chelator which presents important limitations in clinical use due to its poor absorption in the intestine and short plasma half-life. In order to overcome these drawbacks, chitosan/alginate hydrogels as prolonged delivery systems of DFO were developed. Hydrogel alone and composite hydrogel with poly(d,l-lactide-co-glycolide) microspheres were formulated and characterized *in vitro*. The influence of the preparation methods on the performance of composite hydrogels on

controlled DFO release was investigated. Although spray-dried microspheres were able to load DFO, only the composite hydrogels were able to provide controlled drug release. The inclusion of microspheres into pre-formed chitosan/alginate hydrogel provided a slow DFO release by diffusion, leading to an efficient delivery system.

# CHAPTER 1

## Drug delivery systems

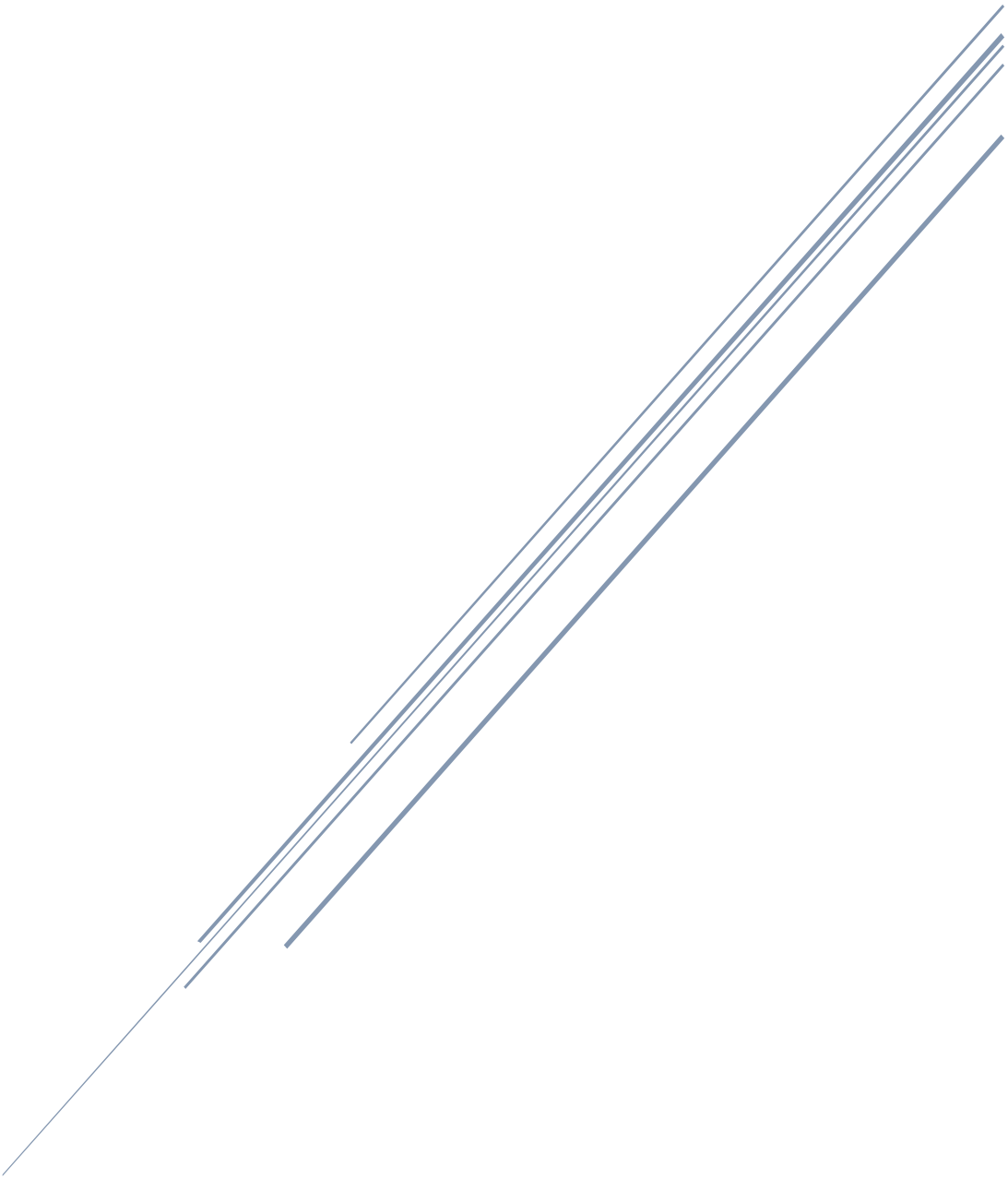

## 1.1 GENERAL BACKGROUND

### *1.1.1 Drug delivery systems*

Conventional pharmacotherapy involves the use of drugs for the treatment of health related dysregulations. Nevertheless, their therapeutic action is limited by various factors, including their solubility and degradation, their interaction with other cells, and their incapacity to target specific tissue because of their physical and chemical properties [1,2]. In general, the conventional dosage forms provide immediate drug release. In addition, the nature of conventional therapeutics leads to indiscriminate drug distribution with resulting systemic side effects [3]. This behaviour entails the need to administrate higher and frequent doses of the drug in order to obtain a satisfactory pharmacological response. For these reasons, in the past decades, great attention has been focused on the development of varied drug delivery systems (DDSs). Various types of formulations, approaches, technologies and systems have been proposed to transport drugs [4,5].

During the last years, researchers have contributed to the advancement of controlled drug delivery technology. Due to this approach, it is possible to elicit grater therapeutic effect. In general, DDS is a system in which the active compound is integrated with an inert agent (carrier) which allows a predetermined drug release.

In addition to controlling the rate and duration of the drug release, the DDSs should be able to manipulate the site of action, targeting the molecule to specific cells, organs and tissues. In this way, these systems can offer numerous advantages compared to conventional dosage forms, such as improved efficacy, reduced harmful side effects and increased compliance and satisfaction in patients [6,7]. Moreover, new DDSs overcome solubility problems of drugs and protect them from the external environment such as pH changes and photodegradation [8].

Various classes of drugs take advantage from controlled delivery [2,9], such as anti-inflammatory agents [10], antibiotics [11,12,13], vaccines [14], chemotherapeutic drugs [15,16,17], anesthetics [18,19] and hormones [20,21,22].

The use of controlled release technology may reduce variability of performance of drug products. The strategies used to achieve controlled release are various and complex, because different mechanisms may operate simultaneously or at different steps of a

delivery process [23]. DDSs are categorized on the basis of the drug release profile, which can be classified as sustained, extended, pulsatile, delayed and site-specific [2].

In extended-release formulations, the concentration of the active agent is within the therapeutic range for a long time because the system continues releasing drug after the initial therapeutic effect. Depending on the type of material used as carrier, different drug release kinetics is obtained. Formulations in the form of hydrogels, nano- and micro-carriers are able to release the loaded drug over time, not necessarily in constant manner. When the therapeutic molecule is incorporated in sustained-release systems, it is steadily released with a kinetic profile of zero-order and pharmacological effect is maintained over a long period. Osmotic pump represents a typical formulation with this property.

Pulsatile-release systems are able to deliver the drug at the right time, at the right site of action and in the right amount [23]. Pulsatile drug delivery formulations can be classified into three categories depending on factor stimulating release of therapeutic agent: time-controlled pulsatile release systems, stimuli-induced pulsatile release systems (by biological factor, like temperature or any other chemical stimuli) and externally regulated pulsatile release systems (by ultrasound or magnetic field). These responsive DDSs show numerous advantages, because they can adapt to circadian rhythms of body functions or diseases. Moreover, they are also used for extended day time or night time activity. Nevertheless, it is not possible to achieve the complete release of drug.

As regards delayed-release systems, the release of the active ingredient does not coincide with the time of administration and its therapeutic action is not prolonged. This approach is recommended for drugs, which are unstable in certain environments such as in plasma or in acidic conditions. Therefore, it is necessary to protect them by using appropriate carrier.

Ideally, a drug-loaded carrier should contain structural moieties that specifically interact with the designated target [24]. In this way, it is possible to control drug distribution in the body. Indeed, the treatment of many diseases requires the distribution of the drug at a specific site. For this reason, several efforts have been made by researchers in order to develop valuable targeted drug carriers. Two basic types of targeting can be exploited by DDSs: passive and active [25]. As concerns passive targeting, the size of carrier is the critical parameter. For example, it was demonstrated that systems small than 200 nm can be accumulated in cancerous tissue through EPR (enhanced permeability and retention)

effect. The active targeting can be realized by surface functionalization of DDSs exploiting specific interactions, such as ligand-receptor and antigen-antibody binding, to target specific site.

Imaging can be used to support and improve various aspects of drug delivery and drug therapy [26]. According to this consideration, DDSs can be also used to visualize and quantify the biodistribution and target site accumulation of drugs and DDSs. In addition, by exploiting specific molecular probes or contrast agents, this technique allows the detection and characterization of disease, providing a rapid method for evaluating the treatment [27]. Furthermore, drug targeting and imaging can be combined in the same carrier to obtain multifunctional systems. In particular, nanoparticle technology is significantly affecting the development of both therapeutic and diagnostic carriers [28,29,30].

Ideally, the drug carrier must be non-toxic, non-immunogenic, biocompatible and biodegradable. Biocompatibility is the main pre-requisite for pharmaceutical use of DDSs. Selection of carrier is very important for controlled drug release. Its choice depends on the physico-chemical nature of loaded drug as well as on disease conditions.

Although different systems have been developed over the years (such as lipid carriers) (Fig.1.1), the majority of DDSs for controlled drug delivery are based on polymeric materials. Several types of polymers have been tested as potential DDSs, including drug conjugates, nano- and micro-carriers, and hydrogels [2,31,32,33].

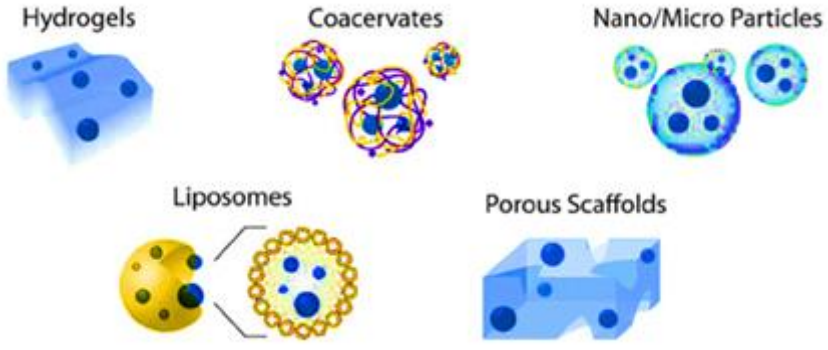


,

**Figure 1.1** Commonly used drug delivery systems (DDSs).

Hydrogels are widely used because of their three-dimensional structure and physical properties that make them similar to living tissue, especially regarding their high water

content and also soft consistency and elasticity [34,35]. They can provide spatial and temporal control of release drug. In addition, hydrogel are suitable for the incorporation of smaller DDSs, such as nano- and microcarriers.

The application of nanoparticles and microparticles as DDSs has received increasing attention [36,37,38]. The size is the distinction property between the two categories of carriers. In both cases, the drug can be entrapped or embedded within the polymer.

Nanoscale carriers with optimized physicochemical and biological properties are taken up by cells more easily than larger molecules, providing a useful tool for diagnostic and therapeutic goals [39]. Liposomes, solid lipids nanoparticles, dendrimers, polymeric micelles, silicon or carbon materials are some examples of nanocarriers that have been developed as DDSs. Due to their small dimensions, nanocarriers are able to operate on cellular sites. Although nanoparticles show several advantages, only a handful of nanometric carrier for clinical application are available on the pharmaceutical market (. Indeed, safety issues with nanoparticles are not very well known but their potential for danger is possible. Other limitations include low drug loading capacity, low loading efficiency, and difficult to control the size distribution of carriers [39].

Microparticles are a generic term to indicate microcapsules and microspheres, which can be made of polymers or lipids, with sizes ranging from 1 to 1000 μm [40]. Microparticles can be prepared by well-established manufacturing processes. An incorporated drug can be distributed homogenously within the polymer matrix (microparticles), or it can be encapsulated into a polymeric shell forming a drug reservoir (microcapsules). These systems play an important role as DDSs aiming at improved bioavailability of conventional drugs and reducing side effects. Microscale carriers offer a method to deliver different molecules by a variety of routes [. Here too, polymers remain the most versatile class of biomaterials for micro DDSs production.

**Aim of the work**

On the basis of the multiple advantages and versatility of the delivery systems for the loading and release of diagnostic and therapeutic compounds, the main aim of the present work was to prepare and to characterize embolizing formulations (thermosensitive hydrogel, preformed microspheres, *in situ forming* microspheres) for transarterial

embolization. In some cases, indocyanine green, a fluorescent agent, was loaded into embolic systems in order to obtain multifunctional platforms.

In addition, other systems for different applications have been developed, with the aim of controlling drug release performance.

## References


[1] Tiwari, G., Tiwari, R., Sriwastawa, B., Bhati, L., Pandey, S., Pandey, P., Bannerjee, S. K. (2012). Drug delivery systems: an updated review. *International journal of pharmaceutical investigation*, 2(1), 2-11.

[2] Vilar, G., Tulla-Puche, J., Albericio, F. (2012). Polymers and drug delivery systems. *Current Drug Delivery*, *9*(4), 367-394.

[3] Ummadi, S., Shravani, B., Rao, N. R., Reddy, M. S., Sanjeev, B. (2013). Overview on controlled release dosage form. *International Journal of Pharma Sciences*, *3(4)*, 258-269.

[4] Khadka, P., Ro, J., Kim, H., Kim, I., Kim, J. T., Kim, H., Cho, J. M., Yun, G., Lee, J. (2014). Pharmaceutical particle technologies: an approach to improve drug solubility, dissolution and bioavailability. *Asian Journal of Pharmaceutical Sciences*, *9(6*), 304-316.

[5] Gupta, S., Kesarla, R., Omri, A. (2013). Formulation strategies to improve the bioavailability of poorly absorbed drugs with special emphasis on self-emulsifying systems. *ISRN Pharmaceutics*, 2013.

[6] Lattin, J. R., Belnap, D. M., Pitt, W. G. (2012). Formation of eLiposomes as a drug delivery vehicle. *Colloids and Surfaces B: Biointerfaces*, *89*, 93-100.

[7] Brannon-Peppas, L., Blanchette, J. O. (2012). Nanoparticle and targeted systems for cancer therapy. *Advanced drug delivery reviews*, *64*, 206-212.

[8] Martinho, N., Damgé, C., Reis, C. P. (2011). Recent advances in drug delivery systems. *Journal of biomaterials and nanobiotechnology*, *2*(05), 510.

[9] Uhrich, K. E., Cannizzaro, S. M., Langer, R. S., Shakesheff, K. M. (1999). Polymeric systems for controlled drug release. *Chemical reviews*, *99*(11), 3181-3198.

[10] Chung, M. F., Chia, W. T., Wan, W. L., Lin, Y. J., Sung, H. W. (2015). Controlled release of an anti-inflammatory drug using an ultrasensitive ROS-responsive gas-generating carrier for localized inflammation inhibition. *Journal of the American Chemical Society*, *137(39),* 12462-12465.

[11] Anal, A. K., Stevens, W. F., Remunan-Lopez, C. (2006). Ionotropic cross-linked chitosan microspheres for controlled release of ampicillin. *International Journal of Pharmaceutics*, *312(1)*, 166-173.

[12] Adi, H., Young, P. M., Chan, H. K., Salama, R., Traini, D. (2010). Controlled release antibiotics for dry powder lung delivery. *Drug development and industrial pharmacy*, *36(1)*, 119-126.

[13] Hickok, N. J., Shapiro, I. M. (2012). Immobilized antibiotics to prevent orthopaedic implant infections. *Advanced drug delivery reviews*, 64(12), 1165-1176.

[14] Saroja, C. H., Lakshmi, P. K., Bhaskaran, S. (2011). Recent trends in vaccine delivery systems: a review. *International journal of pharmaceutical investigation*, *1(2)*, 64.

[15] Farokhzad, O. C., Cheng, J., Teply, B. A., Sherifi, I., Jon, S., Kantoff, P. W., Langer, R. (2006). Targeted nanoparticle-aptamer bioconjugates for cancer chemotherapy in vivo. *Proceedings of the National Academy of Sciences*, *103(16)*, 6315-6320.

[16] Ong, B. Y., Ranganath, S. H., Lee, L. Y., Lu, F., Lee, H. S., Sahinidis, N. V., Wang, C. H. (2009). Paclitaxel delivery from PLGA foams for controlled release in post-surgical chemotherapy against glioblastoma multiforme. *Biomaterials*, *30(18)*, 3189-3196.

[17] Rapoport, N. Y., Kennedy, A. M., Shea, J. E., Scaife, C. L., & Nam, K. H. (2009). Controlled and targeted tumor chemotherapy by ultrasound-activated nanoemulsions/microbubbles. *Journal of Controlled Release*, *138(3)*, 268-276.

[18] Araújo, D. R. D., Pinto, L. D. M. A., Braga, A. D. F. D. A., & Paula, E. D. (2003). Drug-delivery systems for local anesthetics: therapeutic applications. *Revista brasileira de anestesiologia*, *53(5)*, *663-671*.

[19] de Paula, E., Cereda, C., Tofoli, G. R., Franz-Montan, M., Fraceto, L. F., de Araújo, D. R. (2010). Drug delivery systems for local anesthetics. *Recent patents on drug delivery & formulation*, 4(1), 23-34.

[20] Lipp, R. (2001). Novel drug delivery systems for steroidal hormones. *Expert Opinion on Therapeutic Patents*, *11(8)*, 1291-1299.

[21] Ameller, T., Legrand, P., Marsaud, V., & Renoir, J. M. (2004). Drug delivery systems for oestrogenic hormones and antagonists: the need for selective targeting in estradiol-dependent cancers. *The Journal of steroid biochemistry and molecular biology*, *92(1)*, 1-18.

[22] Yoo, J. W., Lee, C. H. (2006). Drug delivery systems for hormone therapy. *Journal of controlled release*, *112(1)*, 1-14.

[23] Siegel, R. A., Rathbone, M. J. (2012). Overview of controlled release mechanisms. In *Fundamentals and Applications of Controlled Release Drug Delivery*, 19-43. Springer US.

[24] Petrak, K. (2005). Essential properties of drug-targeting delivery systems. *Drug discovery today*, *10*(23), 1667-1673.

[25] Torchilin, V. P. (2010). Passive and active drug targeting: drug delivery to tumors as an example. *Drug delivery*, *197*, 3-53. Springer Berlin Heidelberg.

[26] Sahoo, S. K., Labhasetwar, V. (2003). Nanotech approaches to drug delivery and imaging. *Drug discovery today*, *8*(24), 1112-1120.

[27] Janib, S. M., Moses, A. S., MacKay, J. A. (2010). Imaging and drug delivery using theranostic nanoparticles. *Advanced drug delivery reviews*, *62*(11), 1052-1063.

[28] Cho, K., Wang, X. U., Nie, S., Shin, D. M. (2008). Therapeutic nanoparticles for drug delivery in cancer. *Clinical cancer research*, *14(5)*, 1310-1316.

[29] Parveen, S., Misra, R., Sahoo, S. K. (2012). Nanoparticles: a boon to drug delivery, therapeutics, diagnostics and imaging. *Nanomedicine: Nanotechnology, Biology and Medicine*, *8(2)*, 147-166.

[30] Liu, Y., Miyoshi, H., Nakamura, M. (2007). Nanomedicine for drug delivery and imaging: a promising avenue for cancer therapy and diagnosis using targeted functional nanoparticles. *International Journal of Cancer*, *120(12)*, 2527-2537.

[31] Liechty, W. B., Kryscio, D. R., Slaughter, B. V., Peppas, N. A. (2010). Polymers for drug delivery systems. *Annual review of chemical and biomolecular engineering*, *1*, 149-173.

[32] Srivastava, A., Yadav, T., Sharma, S., Nayak, A., Kumari, A. A., Mishra, N. (2016). Polymers in Drug Delivery. *Journal of Biosciences and Medicines*, *4(01)*, 69.

[33] Schmaljohann, D. (2006). Thermo-and pH-responsive polymers in drug delivery. *Advanced drug delivery reviews*, *58(15)*, 1655-1670.

[34] Caló, E., Khutoryanskiy, V. V. (2015). Biomedical applications of hydrogels: A review of patents and commercial products. *European Polymer Journal*, *65*, 252-267.

[35] Vashist, A., Vashist, A., Gupta, Y. K., Ahmad, S. (2014). Recent advances in hydrogel based drug delivery systems for the human body. *Journal of Materials Chemistry B*, *2*(2), 147-166.

[36] Kumar, M. N. V. R. (2000). Nano and microparticles as controlled drug delivery devices. *Journal of Pharmacy & Pharmaceutical Sciences, 3*(2), 234-258.

[37] Lu, Y., & Chen, S. C. (2004). Micro and nano-fabrication of biodegradable polymers for drug delivery. *Advanced drug delivery reviews*, *56(11)*, 1621-1633.

[38] Kohane, D. S. (2007). Microparticles and nanoparticles for drug delivery. *Biotechnology and bioengineering*, 96(2), 203-209.

[39] Wilczewska, A. Z., Niemirowicz, K., Markiewicz, K. H., Car, H. (2012). Nanoparticles as drug delivery systems. *Pharmacological reports*, *64*(5), 1020-1037.

[40] Singh, M. N., Hemant, K. S. Y., Ram, M., Shivakumar, H. G. (2011). Microencapsulation: A promising technique for controlled drug delivery. *Research in pharmaceutical sciences*, *5(2)*, 65-77.

[41] Kumari, S., Nagpal, M., Aggarwal, G, Jain, U. K., Sharma, P. (2016). Microparticles drug delivery system: a review. *World Journal of Pharmacy and Pharmaceutical Sciences, 5(03),* 543-566.

# CHAPTER 2

## Diagnosis and treatment of hepatocellular carcinoma

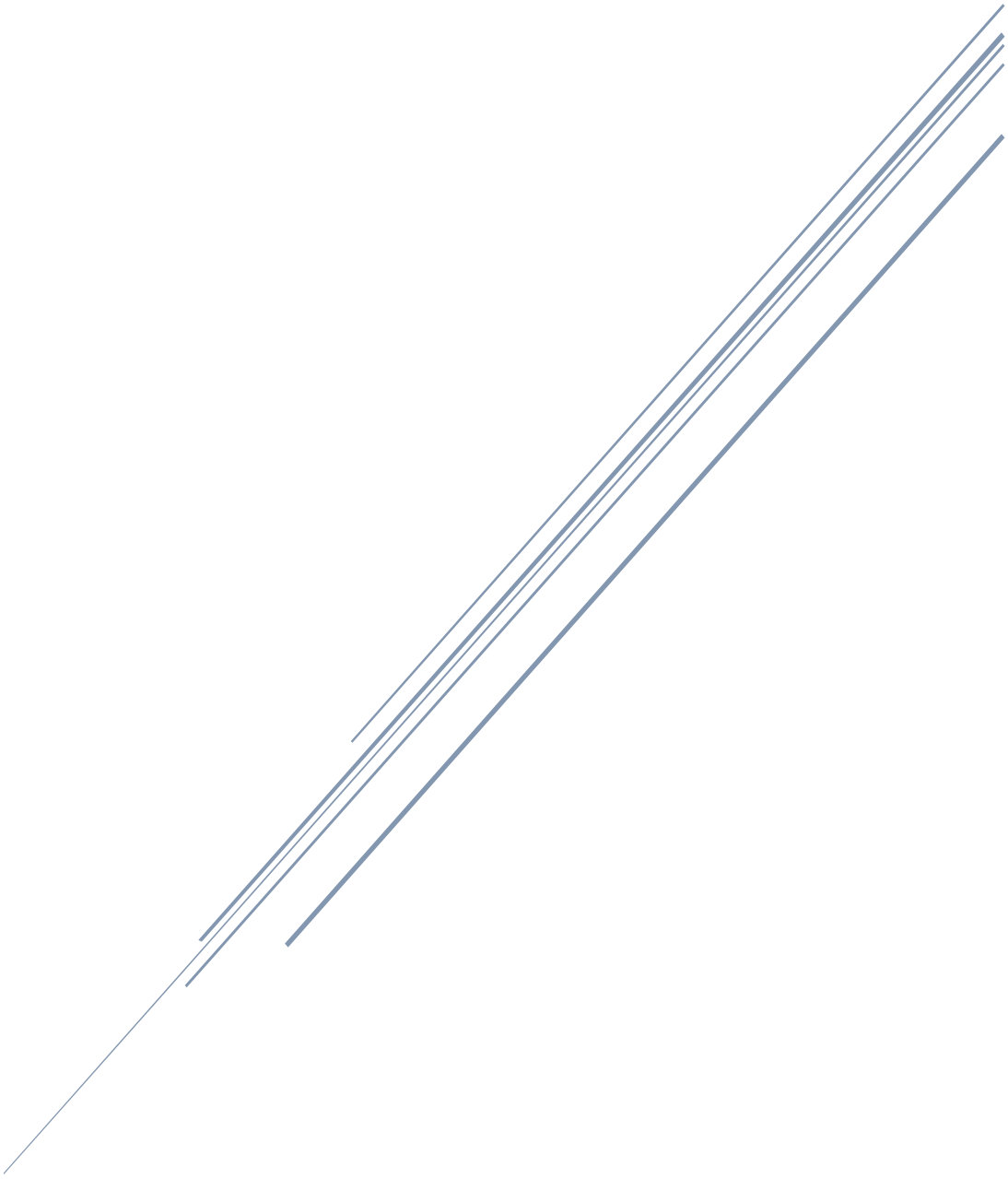

## 2.1 INTRODUCTION

### *2.1.1 Hepatocellular carcinoma: Epidemiology*

Hepatocellular carcinoma (HCC) is one of the most prevalent cancers in the world. It represents the second most frequent cause of cancer death [1]. HCC is the predominant primary malignant cancer affecting the liver. Indeed, other types of liver tumours, including intrahepatic cholangiocarcinoma, are relatively infrequent compared to HCC [2,3].

HCC incidence varies widely with respect to gender, race and geographical region. HCC occurs more often among men than women. In addition, the global distribution of HCC is disproportionate, being most common in areas where risk factors, such as chronic hepatitis B virus infection (HBV), are highly prevalent (Fig. 2.1). For this reason, the majority of HCC cases occur in less developed areas, particularly in Eastern and South-Eastern Asia and sub-Saharan Africa [1].

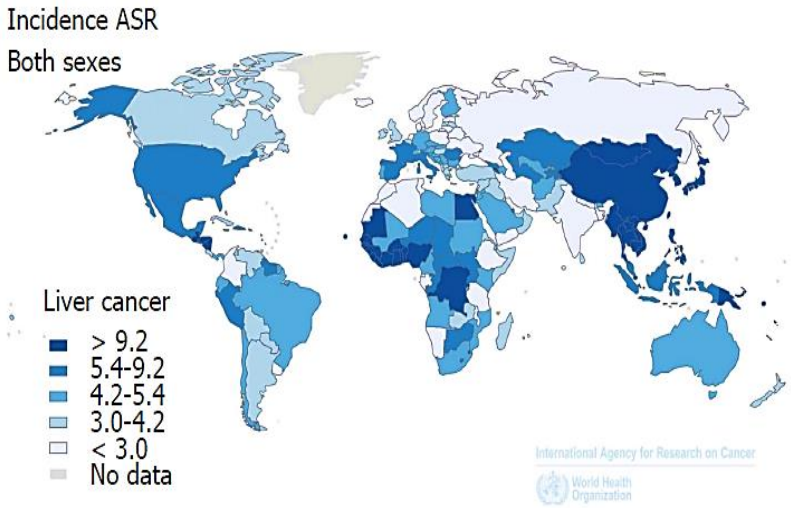


**Figure 2.1** Global incidence of hepatocellular carcinoma (HCC). Sourced from GLOBOCAN 2012 [4].

HCC is a complex disease with several possible etiologies, which may interact synergistically to increase the risk of HCC development. The primary risk factor for developing HCC is cirrhosis (80 to 90% cases) [5] which can be connected to chronic infection including (HBV), hepatitis C virus (HCV), alcoholic liver disease, and nonalcoholic steatohepatitis [6].

### *2.1.2 Surveillance, diagnosis and staging of HCC*

Management of HCC involves diagnosis, staging and treatment of patients. An important aspect of management is surveillance for HCC, which aims to reduce disease-related mortality [7]. Indeed, the capability to treat early stage HCC is highly effective in comparison with alternative treatments for late stage HCC. Screening should be encouraged in regions in which it is possible to offer curative treatment for HCC. The surveillance process proposes a standard to identify the risk level of HCC, the screening tests to apply and their administration rate [5]. Therefore, it is established a guideline in order to diagnose and treat the disease based on the results of the screening tests. Surveillance is the widely practiced approach to manage HCC especially in patients with hepatitis B, hepatitis C or cirrhosis [8]. The tests used to identify suspected HCCs include radiography (computed tomography and contrast magnetic resonance imaging), biopsy, and alpha-fetoprotein (AFP) serology. Nevertheless, the ultrasonography is the favoured imaging method for surveillance due to its properties such as good sensitivity, specificity and wide availability [9]. The size of tumour detected during surveillance process determines the following approach sequence (Fig. 2.2).

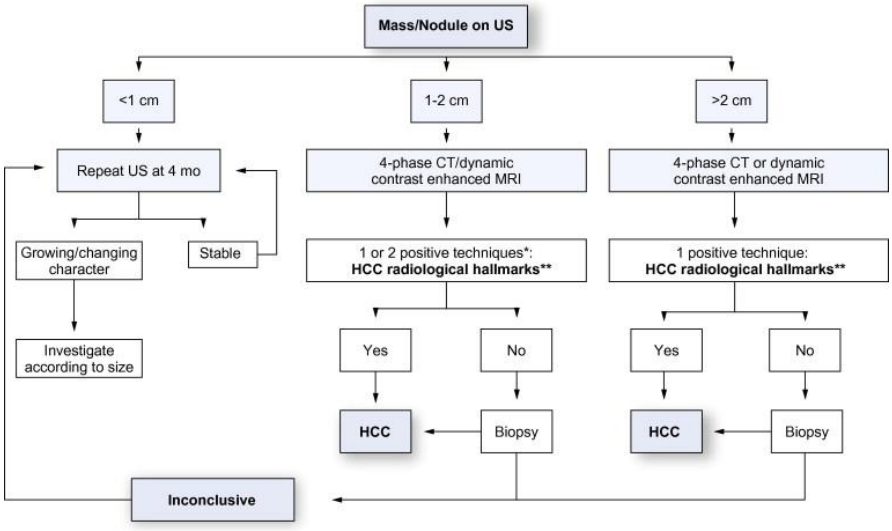


**Figure 2.2** Diagnostic algorithm and recall policy (EASL-EORTC clinical practice guidelines, 2012) [10].

The decision about the selection of treatment for HCC depends on the stage of disease (tumour size and location) and the degree of liver function impairment [5,11]. For this reason, many prognostic systems have been developed to classify the patients. The most

commonly used systems include Child-Pugh, Okuda, Barcelona Clinic Liver Cancer, Japan Integrated Scoring, and Tumor-Node- Metastasis [12-14]. (Fig. 2.3).

| System | Tumor factors | | | | | Liver factors | | | | | PS |
|---|---|---|---|---|---|---|---|---|---|---|---|
| | Size | Nodes | Met | PVT | AFP | CTP | Alb | Bili | ALP | Ascites | |
| TNM | ✓ | ✓ | ✓ | | | | | | | | |
| Okuda | ✓ | | | | | | ✓ | ✓ | | ✓ | |
| BCLC | ✓ | | ✓ | ✓ | | ✓ | | ✓ | | | ✓ |
| CLIP | ✓ | | | ✓ | ✓ | ✓ | | | | | |
| JIS | ✓ | ✓ | ✓ | | | ✓ | | | | | |
| CUPI | ✓ | ✓ | ✓ | | ✓ | | | ✓ | ✓ | ✓ | |
| French | | | | ✓ | ✓ | | | ✓ | ✓ | | ✓ |

Met, metastases; PVT, portal vein thrombosis; CTP, Child-Turcotte-Pugh; Alb, albumin; Bili, bilirubin; ALP, alkaline phosphatase; PS, performance status.

**Figure 2.3.** Comparison of HCC staging systems [14].

Different staging classifications for HCC have been proposed in order to fully encompass all the features that affect the categorization of this liver cancer. Among them, the system Barcelona Clinic Liver Cancer (BCLC) [15] is widely used by the hepatologists as it has shown to provide the most accurate prognostic stratification and appears to be the most useful approach to stage HCC patients [16-17]. Indeed, this classification links patient outcome with treatment indication [5] in a single unified proposal, including the Okuda stage and Child-Pugh score. BCLC takes into account size and extent of the primary tumour, liver function and physiological factors, linking tumour stages with a treatment algorithm [18] (Fig. 2.4).

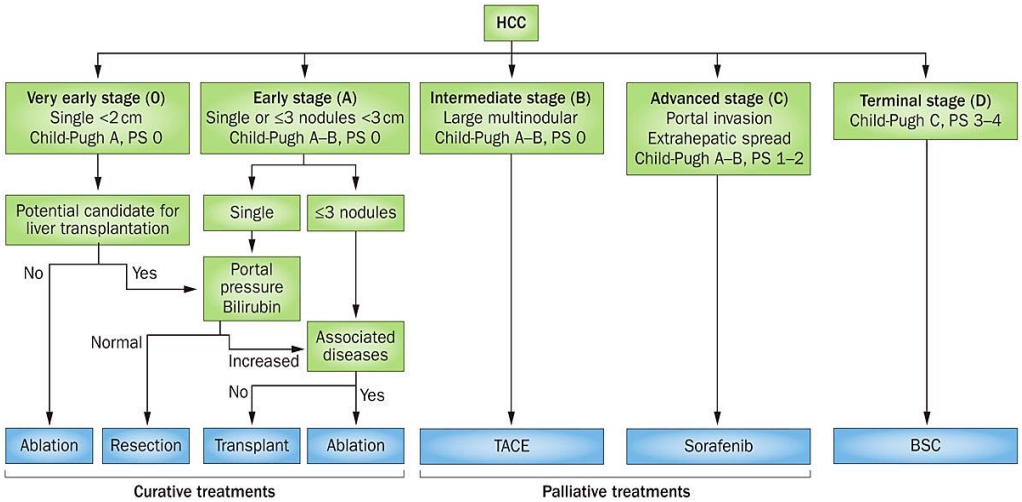


**Figure 2.4.** Barcelona-Clinic Liver Cancer (BCLC) staging classification and treatment schedule [19].

The BCLC establishes five major categories: very early, early, intermediate, advanced and terminal stage.

Very early stage HCCs (*BCLC-0*) are usually asymptomatic and the affected patients show a well-preserved hepatic function [20]. Therefore, it is possible to diagnose the tumour during surveillance process. These patients are ideal candidates for curative treatments including surgical approaches (resection or transplantation) and percutaneous ablation [11,21,22]. Furthermore, radiofrequency ablation (RFA) appears to be a first-line therapy in patients with operable HCC.

In the cases of early-stage HCC (*BCLC-A*), liver transplantation or RFA are proposed. Clearly, an accurate assessment of hepatic function is required prior to surgery because resection may enhance the progression of the disease [17]. Liver resection should be considered in patients that present solitary tumour and no portal hypertension.

HCC patients with a large or multifocal tumour mass without cancer-related symptoms, macrovascular invasion, or extrahepatic spread are classified with intermediate-stage HCC (*BCLC-B*). This stage is not suitable for radical approach but other treatments are available. For example, transarterial therapies, especially TACE, are recommended for this stage of HCC by the EASL-AASLD guidelines [17,20].

Patients with mild cancer-related symptoms and/or vascular invasion or extrahepatic spread are considered as advanced stage (*BCLC-C*) [23]. The therapeutic recommendation for this stage is sorafenib treatment by oral route. Although this therapy represents the main option in these cases, embolic therapies may increase survival in well-selected patients.

Terminal-stage HCC includes severe physical impairment and symptoms related to liver failure. At this stage, in order to prevent unnecessary pain, symptomatic treatments are available [11].

### *2.1.3 Treatment modalities for HCC*

Taking into account the stage of HCC, several treatments can be used. The options that are most commonly used include surgical approaches (resection and liver transplantation), ablative techniques such as percutaneous ethanol injection (PEI) and RFA, and transarterial therapies (Fig. 2.5) [23,24].

| Treatment | Survival | Special issues |
|---|---|---|
| Surgical resection | 1 y: 97%<br>3 y: 84%<br>5 y: 26%–57% | Choice of therapy for patients without cirrhosis (low morbidity)<br>5%–15% of HCC patients eligible<br>Right hepatectomy has higher risk than left hepatectomy<br>Pre/postresection adjunct therapy not recommended |
| Transplantation (LT) | 1 y: 91%<br>2 y: 75%<br>5 y (MILAN): >70%<br>5 y (extended): ~50% | Curative treatment for chronic disease and HCC<br>MELD exception points for HCC<br>Effective corresponding to UNOS criteria (1 tumor ≤5 cm; up to 3 tumors <3 cm<br>Liver donor LT considered for HCC progression outside MILAN criteria<br>UCSF criteria not implemented in current MELD exception allocation policy |
| Radiofrequency ablation (RFA) | 1 y: 90%<br>3 y: 74%<br>5 y: 40%–50% | Effect is more predictable in all tumor sizes than following PEI<br>Superior to PEI in larger tumors; equivalent in small tumors<br>Requires fewer treatment sessions |
| Percutaneous ethanol injection (PEI) | 1 y: 85%<br>3 y: 50%<br>5 y: 40%–50% | Early HCC patients not suitable to resection or OLT or RFA not available or contraindicated<br>Highly effective for small HCC (<2 cm)<br>Low rate of AEs |
| Transarterial chemoembolization (TACE) | 1 y: 82%<br>2 y: 63% | Nonsurgical patients with large/multifocal HCC w/o vascular invasion or extrahepatic spread |

**Figure 2.5.** Therapeutic modalities for HCC and their outcomes [23].

*Surgical resection*

Surgical resection is the treatment of choice for HCC in non-cirrhotic patients because in this case hepatic functionality is preserved [25]. This radical treatment represents the primary approach for candidates with very early- and early-stage HCC. Before surgery, it is indispensable to evaluate the liver functional reserve because cirrhosis affects the majority of patients with HCC. Unlike local ablative therapy, liver resection enables complete pathological analysis of malignant sample [20]. In order to decrease the risk of recurrence, complete resection is necessary. Nevertheless, adequately sized residual liver tissue is required to avoid postoperative hepatic failure [26]. Although surgery is the most efficient option for individuals with HCC, most patients are not suitable for surgical intervention [27].

*Liver transplantation*

Liver transplantation is the ideal treatment for HCC patients that cannot be submitted to surgical resection; it simultaneously eliminates the tumour and cures the coexisting hepatic disease.

The best candidates for transplantation are patients who meet the Milan Criteria. They are patients with a single tumour 5 cm or less in diameter or up to three nodules ≤3 cm and without vascular invasion or extrahepatic metastases [28,29]. Unfortunately, transplant

involves some drawbacks, principally the shortage of donors as well as the increasing number of candidates for this procedure [30]. This situation lead to long waiting times. For this reason, pre-liver transplantation co-adjuvant treatments are proposed when waiting time exceeds 6 months in order to prevent tumour progression (ablation, transarterial chemoembolization) even though real effectiveness is controversial [31,32]. However, the combination of techniques, such as embolization and alcoholization, has shown a satisfactory antitumoural effect before hepatic transplantation [33]. The increase of the donor pool by using living donors, domino/split liver transplantation, and high-risk donors would reduce the wait time for patients needing liver transplantation [17]. In addition, transplantation entails high costs, the possibility of tumour recurrence and the frequent postoperative infections [33].

*Ablation therapies*

Loco-regional therapies, including direct tumour ablation techniques and transcatheter procedures, play a key role in the clinical management of HCC. Percutaneous treatments are minimally invasive alternatives to surgical resection. They represent the first option for early-stage HCC patients not suitable for radical approaches. Ablation induces tumour necrosis by direct administration of chemicals (acetic, acid ethanol) or by temperature modification (radio frequency, microwave, or laser, or cryoablation) in order to achieve cancer eradication [5,34,35]. The seminal ablative techniques used for the treatment of HCC are percutaneous ethanol injection (PEI) and radiofrequency ablation (RFA) [17].

PEI involves direct injection of absolute ethanol in the lesion using ultrasonography. Absolute alcohol causes extensive coagulative cell necrosis so large volumes are not recommend because of the risk of the occurrence of a wide area of hepatic necrosis [33]. PEI is safe, well-tolerated by patients and inexpensive. Moreover, repeated sessions of this procedure can be applied. PEI may have a therapeutic efficacy similar to resection. It was observed that PEI, in combination with ultrasounds, achieves complete tumour necrosis in 70%–80% of single HCC <3 cm and in almost 100% in tumours less than 2 cm [23]. Therefore, PEI is an effective option, but is usually indicated if surgery is impracticable.

RFA produces thermal damage that is dependent on both the tissue temperature achieved and the duration of heating. With RFA, the tissue injury is achieved through

electromagnetic energy in the radiofrequency range (460 – 500 kHz) [17]. Radiofrequency has been used successfully for patients with HCC. It can be performed percutaneously using imaging guidance techniques, laparoscopically or during laparotomy. Unlike PEI, RFA requires few sessions to obtain necrosis with tumours >3 cm. Nevertheless, superficial lesions are not eligible for RFA treatment because of the risk of cancer dissemination through the needle.

RFA is an expensive procedure; it requires the hospitalization and produces several adverse side effects.

*Systemic therapy*

HCC is usually refractory to conventional chemotherapy and cytotoxic drugs are usually poorly tolerated by patients with hepatic dysfunction [24,36]. Several drugs have been tested both as single agents and in combination in patients with advanced HCC, but none of them had been shown to improve survival. Nevertheless, during the last years, many mechanisms involving molecular signaling pathways have been identified in HCC as potential targets for innovative therapies [37].*Transcatheter intraarterial therapies*

Transarterial therapies are suggested for the treatment of multinodular and unresectable HCC in asymptomatic patients. Arterial embolization is used to prolong survival and to prevent tumour progression in patients on the waiting list [8,38].

### *2.1.3.1 Embolization of HCC*

Transcatheter intraarterial therapies are based on the fact that majority of hepatic tumours supply derives from an arterial source (mainly hepatic artery), while the noncancerous liver is supplied mainly from the portal vein [39]. This anatomical structure allows for selective therapy delivery to hepatic cancer tissue and preserve noncancerous parenchyma [40].

The main transarterial methods of treatment of HCC include radioembolization (TARE), bland embolization (TAE) and chemoembolization (TACE). Transcatheter approaches imply the intravascular delivery of different agents through catheter, placed accurately using imaging guidance [41] (Fig. 2.6). The terminal arterial blockade resulting from embolization causes ischemia and following tumour necrosis.

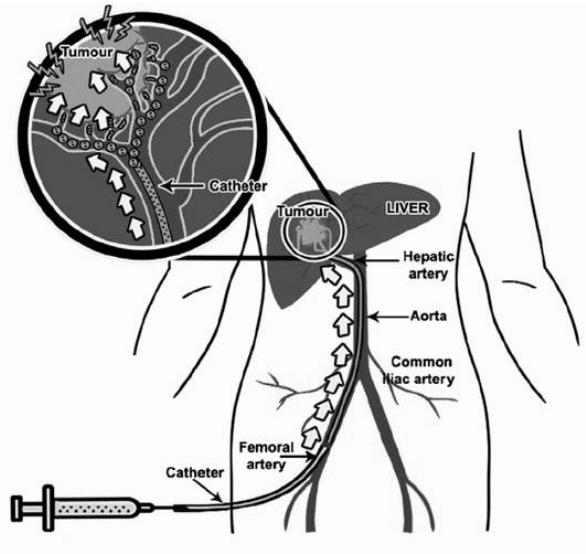


**Figure 2.6.** Principle of conventional transarterial embolization [42].

Trans-arterial radioembolization consists of intra-arterial delivery of microspheres (25-35 μm) loaded with radioactive agents, such as Yttrium$^{90}$ or Lipiodol labelled with Iodine$^{131}$ or Rhenium$^{188}$ - through a percutaneous access [17,41,43]. In this way, high radiation dose is addressed to cancer cells sparing the liver tissue. Furthermore, the small size of particles injected and their low embolic effect reduce the incidence of post-embolization syndrome.

Transarterial bland embolization (TAE) is performed injecting embolic agents in the arterial vessel in order to block blood flow to the tumour without administration of chemotherapeutic agents [44]. Treatment of liver cancers by embolization was introduced in the 1960s [45] and it is still used in the treatment of unresectable HCC [46,47].

When catheter is placed as close as possible to the HCC, the release of embolizing agents occurs. In the case of TACE, this procedure is combined with the injection of chemotherapeutic agents (eg doxorubicin, cisplatin) with the aim of performing synergistic antitumoural action [48]. In conventional TACE (cTACE) cytotoxic drug is usually emulsified in Lipiodol, an oily contrast agent used as a carrier for local chemotherapy and retained within the tumour. Although cTACE has been the most popular procedure for a long time, the introduction of embolic, drug-eluting microspheres has provided an efficient alternative.

In all cases described in literature, embolic procedure should be selective to limit damage to the surrounding nontumoral liver [49]. Although transarterial therapies are minimally

invasive, they are not innocuous. Postembolization syndrome, consisting of fever, nausea and abdominal pain, represents the commonest side effect of embolization procedure. Some important complications related to the procedure as ischemic cholecystitis, hepatic abscess, arterial dissection and biliary strictures may occur [50]. Complications for TAE are similar to those for TACE. Obviously, chemotherapy-related side effects affect TACE only [40].

The role of chemotherapeutic agents in embolic techniques remains unclear. Some researchers believe that bland embolization may be as equally effective as TACE for palliative treatment of primary liver tumour. Indeed, several trials have demonstrated the non-superiority of TACE with respect to TAE [50-54]. In some cases, TAE appears even safer when compared to cTACE [55].

#### *2.1.3.1.1 Embolic agents*

Transcatheter vascular occlusion can be achieved by using various embolic agents such as gelatin sponge and polyvinyl alcohol (PVA) particles, widely used as conventional particulate agents [44,56]. These systems are usually heterogeneous in size and show irregular shape. For this reason, they produce unpredictable occlusion. Indeed these particles tend to aggregate avoiding more distal occlusion [57].

Non-spherical PVA particles have a diameter between 50 and 1200 μm in the dry state and they are injected in suspension with diluted contrast media. PVA causes permanent or semi-permanent vessel occlusion [58], as well as probable catheter clogging. PVA polymer is not biodegradable. For this reason, repeated intrarterial injections are performed with biodegradable agents such as gelatin sponge and starch microspheres.

Gelatine sponge or Gelfoam® has been one of the most commonly used embolization agents [59]. It is a haemostatic agent available in two forms: powder and sheet, from which is possible to obtain cubes or pledgets. Since 2006, gelatine particles (1 and 2 mm) for TACE have been introduced on market [60]. Gelatine sponge, which is an absorbable embolic agent, causes a temporary vessel occlusion, allowing repeated intra-arterial treatments. Gelfoam® is inexpensive and versatile, but it can induces infection because of trapped air bubbles [61]. In addition, it tends to occlude larger artery due to its particle size. Nevertheless, the use of gelatine as powder is not recommended because the small particles can potentially cause nontargeted embolization [59].

With the aim of overcome the drawbacks concerning conventional embolic agents, during the last decades new spherical and calibrated particles have been developed. Several PVA-based microspheres specifically for TACE (eg Contour SE® particles, Bead Block®, DC/LC Bead®) have been commercialized recently [56].

Gelatine has been employed in combination with cross-linked acrylic polymer for the fabrication of permanent Embosphere®. They are available in six size ranges and can penetrate deeper and embolize smaller vessels than PVA particles.

Among several spherical embolic agents, Embozene® were approved for clinical use in 2007. The microspheres are composed of a hydrogel core of polymethylmethacrylate and a coating of polyphosphazene, which has anti-inflammatory and bacterial-resistant properties [62].

The severity of post-embolization syndrome can be reduced using temporary embolic agents, as reported by Tam et al. [59]. To this end, degradable starch microsphere (Spherex®, EmboCept®) have been developed. These systems are enable to provide transient occlusion of small arteries. Indeed, the blood flow is fully restored within 60 minutes because the starch is degraded by serum α-amilases.

Recently, new drug-eluting microspheres or beads (DEB) have been introduced in TACE procedure. These spheres are capable of loading and releasing chemotherapeutic agents in a controlled manner. DC Bead/LC Bead and HepaSphere/QuadraSphere have been approved to treat hepatic tumour.

DC Bead is a PVA based microspherical embolization agent, having anionic sulfonate group which can interact with the positively charged protonated of different drugs, such as doxorubicin, epirubicin or irinotecan, by an ion-exchange process [63].

Hepaspheres are nonresorbable and expandable particles composed of sodium acrylate and vinyl alcohol copolymer. After swelling, which happen within several minutes, the particles appear soft and deformable, allowing a facilitated delivery through microcatheter. They are not only able to adsorb a specific drug through an ionic exchange mechanism, but also to absorb drugs in solution by reservoir effect [63].

In order to maximize the effects of vascular occlusion, it is necessary to use embolizing agents having suitable size compared with the size of the capillary in the targeted tissue. Embolic effect can be achieved by using particles of sizes larger than 10 μm. Indeed, the

average diameter of small capillary is approximately 5–8 μm [64]. It was observed that a mean particle diameter of at least 40 μm is required for embolization.

This aspect is very important because the distribution of particles smaller than 40 μm can affect other organs, such as spleen and lung [65].

Nevertheless, small particles are usually favourite over larger particles because these particles penetrate deeply into the cancer vascular bed. Larger particles induce inadequate hypoxia due to the proximal vessel occlusion. This outcome may be dangerous because some studies have reported that inadequate hypoxia can lead to increased cell survival through the expression of hypoxia-inducible factor [40].

On the other hand, particle size much greater than 1000 μm can induce catheter clogging during the intra-arterial administration. For all the reasons described above, microspheres with diameters ranging from 40 to 1200 μm would be desirable.

Besides sizes, elasticity and shape of the particles also play a role in injectability and repartition in vascular network. For example, microspheres with a high degree of elasticity are more likely to reach deep areas within target tissue [66].

As reported previously, cytotoxic drugs can be loaded into embolic microspheres. Moreover, it is possible to load different therapeutic agents such as antiangiogenic factors and anti-inflammatory drugs [63].

However, these systems show an important drawback: microsphere cannot be directly visualized. The incorporation of imaging agents into the platforms may lead to more accurate spatial localization of embolic agents.

### *2.1.4 Indocyanine green (ICG)*

Liver resection has played an important role in the treatment of HCC. Nevertheless, the intraoperative diagnosis of small tumours (< 2cm) is insufficient. For this reason, the researchers are focusing their attention on real-time identification of cancer by using fluorescence probes, in order to improve the tumour detection and the accuracy of resection. In 2009, a new fluorescent imaging technique for detection of liver cancers using indocyanine green (ICG) has been developed. During cholangiography fluorescence, it was observed ICG accumulation in cancerous tissue of HCC and in parenchyma around carcinoma foci [67]. Experimental results showed the highly sensitive identification of HCC by intraoperative ICG imaging [67,68].

The mechanism of ICG accumulation was unclear but recently it has been elucidated by Ishizawa et al. [69]. Immunohistochemical staining and gene analysis have been performed. The results clarified the different ICG distribution in well- or moderately differentiated HCC and poorly-differentiated HCC. In the first case, even if expression levels of ICG uptake transporters are preserved, morphological and functional biliary excretion are compromised. As a result, ICG retention occurs in cancer cells after preoperative injection. On the other hand, poorly-differentiated HCCs show a downregulation of ICG uptake transporters and biliary excretion disorders. For this reason, they exhibit rim-type fluorescence [70]. Therefore, intraoperative fluorescence imaging is an efficient tool for the detection of liver cancers in open and laparoscopic/robotic hepatic surgery. In particular, this imaging technique is significant during laparoscopic hepatectomy, as visual inspection and palpation are limited [70].
ICG is a safe dye, already approved for several application by Food and Drug Administration [71]. The reported incidence of adverse reactions after the intravenous injection of ICG is quite low [67]. It is a water-soluble compound dye (Fig. 2.7) that absorbs and emits in the near infrared window, where the autofluorescence of tissue and blood is relatively low [72].

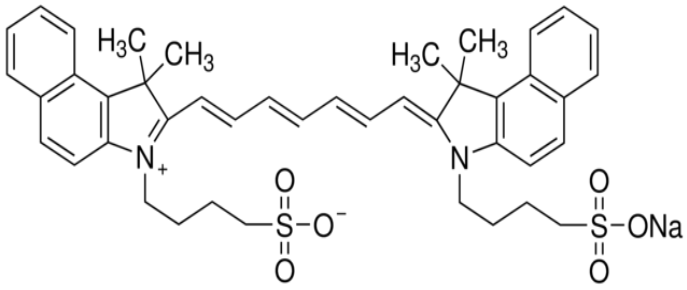


**Figure 2.7.** Chemical structure of indocyanine green (ICG).

The ICG fluorescence in the NIR wavelength can penetrate living tissue and it is useful for obtaining visual information [68]. In addition to false positive results seen in the cirrhotic liver, inability to visualize deeply-located tumours is the major drawback of ICG fluorescence imaging. Indeed, structures in which ICG is present can be visualized through 5–10 mm of tissue by using an appropriate camera, which simultaneously induces and collects the fluorescence, combined with an appropriate filter [73]. After preoperative injection and intrasurgical illumination of the surface of liver, it is possible to perform

cancer resection due to the contrast between fluorescent (tumour) and non-fluorescent (non-tumoural parenchyma) areas [69].

Despite its several benefits, the uses of ICG in all clinical applications is still limited. The main disadvantage of using ICG is its non-specific bonding to plasma proteins. For this reason, ICG exhibits short half-life (2–4 min) and a remarkable instability *in vivo*. Moreover, it is unstable in water solutions and it is prone to aggregation because of its physicochemical properties. Due to these limitations, ICG itself is not always suitable for cancer detection [74]. With the aim of addressing the several issues, the loading of the ICG into numerous carriers has been proposed. Several studies showed that this approach improves ICG stability, prolongs its circulation in the blood and targets the dye to a specific site. Therefore, ICG loading into delivery systems makes its application in cancer diagnosis and therapy, as well as in cancer theranostics, more valuable.

## References


[1] Mittal, S., El-Serag, H. B. (2013). Epidemiology of HCC: consider the population. *Journal of clinical gastroenterology*, *47*, S2.

[2] Altekruse, S. F., McGlynn, K. A., Reichman, M. E. (2009). Hepatocellular carcinoma incidence, mortality, and survival trends in the United States from 1975 to 2005. *Journal of clinical oncology*, 27(9), 1485-1491.

[3] Zhu, R. X., Seto, W. K., Lai, C. L., Yuen, M. F. (2016). Epidemiology of Hepatocellular Carcinoma in the Asia-Pacific Region. *Gut and liver*, 10(3), 332-339.

[4] Ferlay J, Soerjomataram I, Ervik M, Dikshit R, Eser S, Mathers C, Rebelo M, Parkin DM, Forman D, Bray, F. GLOBOCAN 2012 v1.0, Cancer Incidence and Mortality Worldwide: IARC CancerBase No. 11 [Internet]. Lyon, France: International Agency for Research on Cancer; 2013. Available from: http://globocan.iarc.fr.

[5] Forner A., Llovet J. M., Bruix J. (2012). Hepatocellular carcinoma. *Lancet,* 379(9822),1245-55.

[6] El–Serag, H. B., Rudolph, K. L. (2007). Hepatocellular carcinoma: epidemiology and molecular carcinogenesis. *Gastroenterology*, 132(7), 2557-2576.

[7] Bruix, J., Sherman, M. (2011). Management of hepatocellular carcinoma: an update. *Hepatology*, 53(3), 1020-1022.

[8] Llovet, J. M. (2004). Treatment of hepatocellular carcinoma. *Current treatment options in gastroenterology*, 7(6), 431-441.

[9] Singal, A., Volk, M. L., Waljee, A., Salgia, R., Higgins, P., Rogers, M. A. M., Marrero, J. A. (2009). Meta-analysis: surveillance with ultrasound for early-stage hepatocellular carcinoma in patients with cirrhosis. *Alimentary pharmacology & therapeutics*, 30(1), 37-47.

[10] European Association For The Study Of The Liver. (2012). EASL–EORTC clinical practice guidelines: management of hepatocellular carcinoma. *Journal of Hepatology*, 56(4), 908-943.

[11] Bruix, J., Sherman, M. (2005). Management of hepatocellular carcinoma. *Hepatology*, 42(5), 1208-1236.

[12] Pons, F., Varela, M., Llovet, J. M. (2005). Staging systems in hepatocellular carcinoma. *Hpb*, 7(1), 35-41.

[13] Maida, M., Orlando, E., Cammà, C., Cabibbo, G. (2014). Staging systems of hepatocellular carcinoma: a review of literature. *World Journal of Gastroenterology: WJG*, 20(15), 4141-4150.

[14] Subramaniam, S., Kelley, R. K., Venook, A. P. (2013). A review of hepatocellular carcinoma (HCC) staging systems. *Chinese clinical oncology*, 2(4), 33.

[15] Forner, A., Reig, M. E., de Lope, C. R., Bruix, J. (2010). Current strategy for staging and treatment: the BCLC update and future prospects. *Seminars in liver disease*, 30(1), 61-74.

[16] Hassoun, Z., Gores, G. J. (2003). Treatment of hepatocellular carcinoma. *Clinical Gastroenterology and Hepatology*, 1(1), 10-18.

[17] Forner, A., Hessheimer, A. J., Real, M. I., Bruix, J. (2006). Treatment of hepatocellular carcinoma. *Critical reviews in oncology/hematology*, 60(2), 89-98.

[18] Llovet, J. M., Brú, C., Bruix, J. (1999). Prognosis of hepatocellular carcinoma: the BCLC staging classification. *Seminars in liver disease*, 19(3), 329-338.

[19] Forner, A., Gilabert, M., Bruix, J., Raoul, J. L. (2014). Treatment of intermediate-stage hepatocellular carcinoma. *Nature Reviews Clinical Oncology*, 11(9), 525-535.

[20] Lin, S., Hoffmann, K., Schemmer, P. (2012). Treatment of hepatocellular carcinoma: a systematic review. *Liver cancer*, *1*(3-4), 144-158.

[21] Roayaie, S., Obeidat, K., Sposito, C., Mariani, L., Bhoori, S., Pellegrinelli, A., Labow, D., Llovet, J. M., Schwartz, M., Mazzaferro, V. (2013). Resection of hepatocellular cancer≤ 2 cm: results from two Western centers. *Hepatology*, *57*(4), 1426-1435.

[22] Kuang, M., Xie, X. Y., Huang, C., Wang, Y., Lin, M. X., Xu, Z. F., Liu, G. J., Lu, M. D. (2011). Long-term outcome of percutaneous ablation in very early-stage hepatocellular carcinoma. *Journal of Gastrointestinal Surgery*, *15*(12), 2165-2171.

[23] El-Serag, H. B., Marrero, J. A., Rudolph, L., Reddy, K. R. (2008). Diagnosis and treatment of hepatocellular carcinoma. *Gastroenterology*, *134*(6), 1752-1763.

[24] Llovet, J.M., Burroughs, A., Bruix J. (2003) Hepatocellular carcinoma. *Lancet*, 362(9399), 1907-1917.

[25] Song, T. J., Ip, E. W. K., Fong, Y. (2004). Hepatocellular carcinoma: current surgical management. *Gastroenterology*, 127(5), S248-S260.

[26] Jarnagin, W. R. (2010). Management of small hepatocellular carcinoma: a review of transplantation, resection, and ablation. *Annals of surgical oncology*, 17(5), 1226-1233.

[27] Delis, S. G., Dervenis, C. (2008). Selection criteria for liver resection in patients with hepatocellular carcinoma and chronic liver disease. *World Journal of Gastroenterology: WJG*, 14(22), 3452–3460.

[28] Duffy, J. P., Vardanian, A., Benjamin, E., Watson, M., Farmer, D. G., Ghobrial, R. M., Lipshutz, G., Yersiz, H., Lu, D. S. K., Lassman, C., Tong, M. J., Hiatt, J. R., Busuttil, R.W. (2007). Liver transplantation criteria for hepatocellular carcinoma should be expanded: a 22-year experience with 467 patients at UCLA. *Annals of surgery*, 246(3), 502-511.

[29] Mazzaferro, V., Regalia, E., Doci, R., Andreola, S., Pulvirenti, A., Bozzetti, F., Montalto, F., Ammatuna, M., Morabito, A., Gennari, L. (1996). Liver transplantation for the treatment of small hepatocellular carcinomas in patients with cirrhosis. *New England Journal of Medicine*, 334(11), 693-700.

[30] Freeman, R. B., Edwards, E. B., Harper, A. M. (2006). Waiting list removal rates among patients with chronic and malignant liver diseases. *American journal of transplantation*, 6(6), 1416-1421.

[31] Lopez, P. M., Villanueva, A., Roayaie, S., Llovet, J. M. (2006). Neoadjuvant therapies for hepatocellular carcinoma before liver transplantation: a critical appraisal. *Liver transplantation*, *12*(12), 1747-1754.

[32] Llovet, J. M., Mas, X., Aponte, J. J., Fuster, J., Navasa, M., Christensen, E., Rodés, J., Bruix, J. (2002). Cost effectiveness of adjuvant therapy for hepatocellular carcinoma during the waiting list for liver transplantation. *Gut*, 50(1), 123-128

[33] França, A. V. C., Elias Júnior, J., Lima, B. L. G. D., Martinelli, A. L., Carrilho, F. J. (2004). Diagnosis, staging and treatment of hepatocellular carcinoma. *Brazilian journal of medical and biological research*, *37*(11), 1689-1705.

[34] Brown, D. B., Gould, J. E., Gervais, D. A., Goldberg, S. N., Murthy, R., Millward, S. F. (2009). Society of Interventional Radiology Technology Assessment Committee and the International Working Group on Image-Guided Tumor Ablation. Image-guided tumor ablation: standardization of terminology and reporting criteria. *Journal of Vascular and Interventional Radiology*, 20(7), S425-S434.

[35] Li, D., Kang, J., Golas, B. J., Yeung, V. W., Madoff, D. C. (2014). Minimally invasive local therapies for liver cancer. *Cancer biology & medicine*, *11*(4), 217-236.

[36] Tsai, Y. S. L., Yang, C. C., Hsueh, C. W., Kuo, W. H. (2015). Current systemic treatment of hepatocellular carcinoma: A review of the literature. *World*, *7*(10), 1412-1420.

[37] Germano, D., Daniele, B. (2014). Systemic therapy of hepatocellular carcinoma: current status and future perspectives. *World Journal of Gastroenterology*, *20*(12), 3087-3099.

[38]Graziadei, I. W., Sandmueller, H., Waldenberger, P., Koenigsrainer, A., Nachbaur, K., Jaschke, W., Mrgreiter, R., Vogel, W. (2003). Chemoembolization followed by liver transplantation for hepatocellular carcinoma impedes tumor progression while on the waiting list and leads to excellent outcome. *Liver Transplantation*, *9*(6), 557-563.

[39] Lewandowski, R. J., Geschwind, J. F., Liapi, E., Salem, R. (2011). Transcatheter intraarterial therapies: rationale and overview. *Radiology*, 259(3), 641-657.

[40] Kumar, Y., Sharma, P., Bhatt, N., & Hooda, K. (2016). Transarterial Therapies for Hepatocellular Carcinoma: a Comprehensive Review with Current Updates and Future Directions. *Asian Pacific Journal of Cancer Prevention*, *17*(2), 473-478.

[41] Lencioni, R. (2010). Loco-regional treatment of hepatocellular carcinoma. *Hepatology*, 52(2), 762-773

[42] Idée, J. M., Guiu, B. (2013). Use of Lipiodol as a drug-delivery system for transcatheter arterial chemoembolization of hepatocellular carcinoma: a review. *Critical reviews in oncology/hematology*, *88*(3), 530-549.

[43] Sacco, R., Mismas, V., Marceglia, S., Romano, A., Giacomelli, L., Bertini, M., Federici, G., Metrangolo, S., Parisi, G., Tumino, E., Bresci, G., Corti, A., Tredici, M., Piccinno, M., Giorgi, L., Bartolozzi, C., Bargellini, I. (2015). Transarterial radioembolization for hepatocellular carcinoma: An update and perspectives. *World Journal of Gastroenterology*, *21*(21), 6518-6525.

[44] Wáng, Y. X. J., De Baere, T., Idée, J. M., Ballet, S. (2015). Transcatheter embolization therapy in liver cancer: an update of clinical evidences. *Chinese Journal of Cancer Research*, *27*(2), 96-121.

[45] Mori, W., Masuda, M., Miyanaga, T. (1966). Hepatic artery ligation and tumor necrosis in the liver. *Surgery*, 59(3), 359-363.

[46] Tsochatzis, E. A., Fatourou, E., O'Beirne, J., Meyer, T., & Burroughs, A. K. (2014). Transarterial chemoembolization and bland embolization for hepatocellular carcinoma. *World Journal of Gastroenterology*, *20*(12), 3069-77.

[47] Boulin, M., Guiu, B. (2016). Chemoembolization or bland embolization for hepatocellular carcinoma: The question is still unanswered. *Journal of Clinical Oncology*, *35*(2), 256-257.

[48] Shin, S. W. (2009). The current practice of transarterial chemoembolization for the treatment of hepatocellular carcinoma. *Korean journal of radiology*, *10*(5), 425-434.

[49] Sacco, R., Bertini, M., Petruzzi, P., Bertoni, M., Bargellini, I., Bresci, G., Romano, A. Capria, A. (2009). Clinical impact of selective transarterial chemoembolization on hepatocellular carcinoma: a cohort study. *World Journal of Gastroenterology: WJG*, *15*(15), 1843-1848.

[50] Marelli, L., Stigliano, R., Triantos, C., Senzolo, M., Cholongitas, E., Davies, N., Tibballs, J., Meyer, T., Patch, D. W., Burroughs, A. K. (2007). Transarterial therapy for hepatocellular carcinoma: which technique is more effective? A systematic review of cohort and randomized studies. *Cardiovascular and interventional radiology*, 30(1), 6-25.

[51] Camma, C., Schepis, F., Orlando, A., Albanese, M., Shahied, L., Trevisani, F., Andreone, P., Craxì, A., Cottone, M. (2002). Transarterial chemoembolization for unresectable hepatocellular carcinoma: meta-analysis of randomized controlled trials 1. *Radiology*, *224*(1), 47-54.

[52] Llovet, J. M., Real, M. I., Montaña, X., Planas, R., Coll, S., Aponte, J., Rodés, J., Bruix, J. (2002). Arterial embolisation or chemoembolisation versus symptomatic treatment in patients with unresectable hepatocellular carcinoma: a randomised controlled trial. *The Lancet*, 359(9319), 1734-1739.

[53] Kluger, M. D., Halazun, K. J., Barroso, R. T., Fox, A. N., Olsen, S. K., Madoff, D. C., Siegel, A. B., Weintraub, J. L., Sussman, J., Brown, R. S., Cherqui, D., Emond, J. C. (2014). Bland embolization versus chemoembolization of hepatocellular carcinoma before transplantation. *Liver Transplantation*, *20*(5), 536-543.

[54] Brown, K. T., Do, R. K., Gonen, M., Covey, A. M., Getrajdman, G. I., Sofocleous, C. T., Jarnagin, W. R., Brody, L. A., Abou-Alfa, G. K. (2016). Randomized trial of hepatic artery embolization for hepatocellular carcinoma using doxorubicin-eluting microspheres compared with embolization with microspheres alone. *Journal of Clinical Oncology*, 34 (17), 2046-2053.

[55] Tsochatzis, E. A., Fatourou, E. M., Triantos, C. K., Burroughs, A. K. (2013). Transarterial therapies for hepatocellular carcinoma. *Multidisciplinary Treatment of Hepatocellular Carcinoma*, 195-206, Springer Berlin Heidelberg.

[56] Osuga, K., Maeda, N., Higashihara, H., Hori, S., Nakazawa, T., Tanaka, K., Nakamura, M., Kishimoto, K., Ono, Y., Tomiyama, N. (2012). Current status of embolic agents for liver tumor embolization. *International journal of clinical oncology*, 17(4), 306-315.

[57] Khankan, A. A., Osuga, K., Hori, S., Morii, E., Murakami, T., Nakamura, H. (2003). Embolic effects of superabsorbent polymer microspheres in rabbit renal model: comparison with tris-acryl gelatin microspheres and polyvinyl alcohol. *Radiation medicine*, 22(6), 384-390.

[58] Davidson, G. S., Terbrugge, K. G. (1995). Histologic long-term follow-up after embolization with polyvinyl alcohol particles. *American journal of neuroradiology*, 16(4), 843-846.

[59] Tam, K. Y., Leung, K. C. F., Wang, Y. X. J. (2011). Chemoembolization agents for cancer treatment. *European Journal of Pharmaceutical Sciences*, *44*(1), 1-10.

[60] Sone, M., Osuga, K., Shimazu, K., Higashihara, H., Nakazawa, T., Kato, K., Aozasa, K. (2010). Porous gelatin particles for uterine artery embolization: an experimental study of intra-arterial distribution, uterine necrosis, and inflammation in a porcine model. *Cardiovascular and interventional radiology*, 33(5), 1001-1008.

[61] Vaidya, S., Tozer, K. R., Chen, J. (2008). An overview of embolic agents. *Seminars in interventional radiology*, 25 (3), 204-215. Thieme Medical Publishers.

[62] Bonomo, G., Pedicini, V., Monfardini, L., Della Vigna, P., Poretti, D., Orgera, G., Orsi, F. (2010). Bland embolization in patients with unresectable hepatocellular carcinoma using precise, tightly size-calibrated, anti-inflammatory microparticles: first clinical experience and one-year follow-up. *Cardiovascular and interventional radiology*, 33(3), 552-559.

[63] Giunchedi, P., Maestri, M., Gavini, E., Dionigi, P., Rassu, G. (2013). Transarterial chemoembolization of hepatocellular carcinoma–agents and drugs: an overview. Part 2. *Expert opinion on drug delivery*, *10*(6), 799-810.

[64] Illum, L., Davis, S. S. (1982). The targeting of drugs parenterally by use of microspheres. *PDA Journal of Pharmaceutical Science and Technology*, *36*(6), 242-248.

[65] Bastian, P., Bartkowski, R., Köhler, H., Kissel, T. (1998). Chemo-embolization of experimental liver metastases. Part I: distribution of biodegradable microspheres of different sizes in an animal model for the locoregional therapy. *European journal of pharmaceutics and biopharmaceutics*, *46*(3), 243-254.

[66] Siskin, G. P., Dowling, K., Virmani, R., Jones, R., & Todd, D. (2003). Pathologic evaluation of a spherical polyvinyl alcohol embolic agent in a porcine renal model. *Journal of vascular and interventional radiology*, 14(1), 89-98.

[67] Ishizawa, T., Fukushima, N., Shibahara, J., Masuda, K., Tamura, S., Aoki, T., Hasegawa, K., Beck, Y., Fukayama, M., Kokudo, N. (2009). Real-time identification of liver cancers by using indocyanine green fluorescent imaging. *Cancer*, 115(11), 2491-2504.

[68] Gotoh, K., Yamada, T., Ishikawa, O., Takahashi, H., Eguchi, H., Yano, M., Ohigashi, H., Tomita, Y., Miyamoto, Y., Imaoka, S. (2009). A novel image-guided surgery of hepatocellular carcinoma by indocyanine green fluorescence imaging navigation. *Journal of surgical oncology*, 100(1), 75-79.

[69] Ishizawa, T., Masuda, K., Urano, Y., Kawaguchi, Y., Satou, S., Kaneko, J., Hasegawa, K., Shibahare, J., Fukayama, M., Tsuji, S., Midorikawa, Y., Aburatani, H., Kokudo, N. (2014). Mechanistic background and clinical applications of indocyanine green fluorescence imaging of hepatocellular carcinoma. *Annals of surgical oncology*, 21(2), 440-448.

[70] Ishizawa, T., Saiura, A., Kokudo, N. (2016). Clinical application of indocyanine green-fluorescence imaging during hepatectomy. *Hepatobiliary Surgery and Nutrition*, 5(4), 322.

[71] Alander, J. T., Kaartinen, I., Laakso, A., Pätilä, T., Spillmann, T., Tuchin, V. V., Venermo, M., Välisuo, P. (2012). A review of indocyanine green fluorescent imaging in surgery. *Journal of Biomedical Imaging*, 2012, 7.

[72] Frangioni, J. V. (2003). In vivo near-infrared fluorescence imaging. *Current opinion in chemical biology*, 7(5), 626-634.

[73] Yamamichi, T., Oue, T., Yonekura, T., Owari, M., Nakahata, K., Umeda, S., Nara, K., Ueno, T., Uehara, S., Usui, N. (2015). Clinical application of indocyanine green (ICG) fluorescent imaging of hepatoblastoma. *Journal of pediatric surgery*, 50(5), 833-836.

[74] Shemesh, C. S., Hardy, C. W., David, S. Y., Fernandez, B., Zhang, H. (2014). Indocyanine green loaded liposome nanocarriers for photodynamic therapy using human triple negative breast cancer cells. *Photodiagnosis and photodynamic therapy*, 11(2), 193-203.

# 2.2 Indocyanine green delivery systems for tumour detection and treatments

*Adapted from:*

**Indocyanine green delivery systems for tumour detection and treatments**

Elena P. Porcu, Andrea Salis, Elisabetta Gavini, Giovanna Rassu, Marcello Maestri, Paolo Giunchedi

*Biotechnology Advances*, September-October 2016, Volume 34, Issue 5, pages 768-789.

License Number: **3966390979594**

## 1. INTRODUCTION

Indocyanine green (ICG) is an amphiphilic, inert (nonionizing) and non-toxic compound having a molecular weight of 751.4 Da (Alander et al., 2012) and a hydrodynamic diameter of 1.2 nm (Polom et al., 2011). The tricarbocyanine dye is composed of two hydrophobic polycyclic parts connected to a carbon chain. Each polycyclic part is attached to a sulphate group, which results in hydrophilic properties (Desmettre et al., 2000). Kodak (Rochester, NY) developed ICG in 1955 using near infrared (NIR) technology (Dip et al., 2015) and the Food and Drug Administration (FDA) immediately commended this fluorescent agent for clinical use (Engel et al., 2008; Fox et al., 1956). ICG, as well as other NIR fluorescent dyes, has achieved notable attention in many fields of biomedicine due to several advantages, such as decreased light scattering, as well as optimal level of tissue penetration and minimal levels of interference concerning auto-fluorescence frombiological samples (Escobedo et al., 2010).

In spite of the numerous benefits showed by different dyes within the NIR spectrum, the only fluorescent dye introduced in clinical application is ICG (Pauli et al., 2010). Its wide acceptance is due to its low toxicity (after intravenous administration LD50 of 50–80 mg/kg for animal subjects) (Costa et al., 2001), the fast binding with plasma proteins and quick excretion by the liver into bile juice. This dye fixes rapidly and intensely to serum proteins in vivo after intravenous injection, producing a fluorescence signal (Shimada et al., 2015) without alteration of protein structures (Kochubey et al., 2005). In addition,

ICG exhibits absorption maximum at a hemoglobin isosbestic point, hence the spectrophotometric evaluation of the dye is not dependent on oxygen saturation and serumbilirubin level (Vos et al., 2014). In tissue and cells, the ICG emission peak is slightly moved to longer wavelengths compared with the ICG peak in aqueous solution (Desmettre et al., 2000).

Fluorescent luminescence is emitted at 840 nm as an ICG–protein complex is exposed to an excitation source with a wavelength between 750 and 810 nm (Kokudo and Ishizawa, 2012). Because hemoglobin and water absorb intensely at this wavelength, structures in which ICG is present can be visualized through 5–10 mmof tissue by using an appropriate camera that is sensitive to infrared light, combined with an appropriate filter (Yamamichi et al., 2015). As reported in literature, halogen lamps (Meier et al., 2008) and LEDs (Tsujino et al., 2009) are used as light sources in imaging instruments for ICG detection. In this case, an appropriate filter is required to avoid the mixing of excitation and emission rays (Alander et al., 2012). On the contrary, no filter is usually needed when using a laser source (Raabe et al., 2003). The emitted fluorescence can be detected using specific cameras and identified on the monitor connected to the camera. With this mechanism, a fluorescence imaging device allows the detection of anatomical structures where ICG is present such as blood vessels, lymph nodes and biliary ducts (Boni et al., 2015). Currently, ICG iswidely employed for diagnostic and therapeutic applications by virtue of its fluorescent properties. During the twenty-first century, ICG applications have been remarkably increased, confirming the multifunctional role of ICG. For many years, this dye has been employed in medicine in several clinical settings such as ophthalmic angiography (Destro and Puliafito, 1989; Flower and Hochheimer, 1976; Stanga et al., 2003), cardiac output measurements (Desai et al., 2006; Lund-Johansen, 1990; Reuthebuch et al., 2004) and hepatic function studies (Caesar et al., 1961; Dorshow et al., 1998; Halle et al., 2014; Meijer et al., 1983), but recently many studies proving the potential of ICG in other fields have been published.

The use of ICG has been extended to open and laparoscopic/robotic surgery, especially in angiography allowing the direct intraoperative visualization of the blood vessels in several surgical procedures. The use of ICG video angiography in vascular surgery was discussed for the first time by Raabe et al. (2003), proving that the new procedure is very promising. Over the years, ICG became very popular in neurosurgery and it was found to

be clinically useful for various diseases such as complex aneurysms, atero-venous fistulas and atero-venous malformations (Scerrati et al., 2014). Afterwards cardiovascular surgery represents another application field for ICG fluorescence imaging, as the dye can be used in simple angiography, in cardioplegia delivery, and other several procedures. By exploiting the ICG excretion by the bile, it seems obvious that one of its applications is the visualization of the biliary tree (Boni et al., 2015).

In addition to ICG application in open cholecystectomy (Ishizawa et al., 2009), Ishizawa et al. (2010) developed a newICG fluorescent cholangiography technique to delineate the bile duct anatomy during laparoscopic cholecystectomy. The authors confirmed the potential of the ingenious procedure as a possible alternative for conventional radiographic cholangiography, preventing bile duct injury in laparoscopic surgery. Another study was conducted by Y. Kono et al. (2015) to evaluate the effect of clinical and technical conditions on the ability

of the technique after preoperative intravenous injection of ICG. *Ex vivo* studies performed with five laparoscopic fluorescence systems and one conventional system for open surgery confirmed that it is necessary to optimize the fluorescence systemto allowthe use of ICG cholangiography as an essential tool for bile duct navigation. Other experimental works support the applicability of ICG for additional purposes, including rheumatoid arthritis (Fischer et al., 2010; Werner et al., 2013), burns and other trauma (Fourman et al., 2014; Kamolz et al., 2006) and muscle perfusion (Habazettl et al., 2010; Vogiatzis et al., 2015), but nowadays ICG plays themain role in the diagnosis and treatments of tumours. On the one hand, ICG imaging permits confirming the targeting of the tumour region. On the other hand, ICG induces the production of a hyperthermia effect and/or reactive oxygen species (ROS) irradiating the specific region with a laser light having a suitable wavelength.

At present, ICG is extensively employed in NIR fluorescence (NIRF) cancer surgery because it has multiple roles within this context. In fact, ICG applications in this field concern sentinel lymph node (SLN) detection and identification of cancers during surgical procedure, as well as intraoperative angiography (Schaafsma et al., 2012). SLN biopsy using ICG fluorescence reduces time of surgery, and improves lymph node detection allowing a surgeon to make a minimal incision and prolonging high identification rate for hours (Schaafsma et al., 2012).

To date, ICG-guided SLN mapping has been extensively considered for several cancers: breast cancer (Murawa et al., 2009; Samorani et al., 2015; Tagaya et al., 2008; Troyan et al., 2009; Verbeek et al., 2014), gastric cancer (Miyashiro et al., 2008; Kusano et al., 2008; Tajima et al., 2009; Takeuchi and Kitagawa, 2015), vulvar cancer (Crane et al., 2011; Hutteman et al., 2012), endometrial cancer (Holloway et al., 2012, Plante et al., 2015), cervical cancer (Crane et al., 2011; Schaafsma et al., 2012; Jewell et al., 2014), lung cancer (Moroga et al., 2012; Yamashita et al., 2011), head and neck cancer (Betz et al., 2009; Kogashiwa et al., 2015; Nakamura et al., 2015), skin cancer (Gilmore et al., 2013; van der Vorst et al., 2013b), colorectal cancer (Cahill et al., 2012; Hirche et al., 2012; Hutteman et al., 2011; Liberale et al., 2015), atero-venous fistulas and others (Handgraaf et al., 2015; Hirche et al., 2011). In addition, some combinations of NIRF and radioactivity for SLN mapping have been reported (Brouwer et al., 2012; Stoffels et al., 2015; Tsuchimochi et al., 2013; Van den Berg et al., 2012; Van der Poel et al., 2011). Although ICG use in SLN mapping has introduced NIRF imaging in cancer surgery, its key application is in intraoperative tumour detection. Indeed, optical imaging represents a valuable non-invasive and high resolution approach during surgical procedures.

Among various cancers, the identification of hepatic tumours has received a lot of attention as a model of cancer-specific fluorescence imaging during open and laparoscopic surgery (Kudo et al., 2014). Particularly, selective uptake and retention of ICG by hepatocellular carcinoma (HCC) tumours has been revealed. As reported by Limet al. (2014), the contrast between fluorescent cancer and non-fluorescent tissue depends on the time between ICG injection and the fluorescence measurement. In 2009, Ishizawa et al. first introduced the application of ICG imaging in hepatic surgery for the visualization of colorectal liver metastases and hepatocellular carcinomas (HCCs). Although further studies are needed to clarify the accumulation mechanism of ICG, the authors confirmed the ICG detection in non-cancerous hepatic parenchyma around metastases in the majority of poorly differentiated HCCs. On the contrary, biliary excretion disorders associated with cancer progression led to accumulation of the dye in the tumour tissue, corroborating the feasibility of fluorescence imaging as an identification technique for cancers (Ishizawa et al., 2014; van der Vorst et al., 2013a). In literature, many other studies report ICG use as a “real-time” tool for intraoperative identification of several solid tumours and metastases (Hagen et al., 2009; Holt et al.,

2014; Hwang et al., 2010; Morita et al., 2013; Peloso et al., 2013; Poellinger et al., 2011; Satou et al., 2013; Yokoyama et al., 2012) (Fig. 1). As reported by Boni et al. (2015), ICG fluorescence can assist the vascular dissection in different situations such as nephrectomies, metastatic melanoma and splenectomy. Indeed, the application of ICG permits achieving "real time" visualization of blood vessels that could facilitate the dissection procedure. Moreover, ICG fluorescence technique is also useful for postoperative pathological identification of lesions in tissue samples as ICG fluorescence is stable in paraffin-embedded tissue samples and formalin-fixed sections (Shimada et al., 2015). To date, some works of NIRF angiography using ICG in reconstructive surgery are reported in literature (Lee et al., 2010; Newman and Samson, 2009; Pacheco et al., 2013), confirming that this procedure allows excellent imaging of blood flow and tissue perfusion during surgical operation (Schaafsma et al., 2011).

The role of ICG regarding tumour treatment involves different techniques. In the past years, the interest in the use of ICG in photodynamic therapy (PDT) and photothermal therapy (PTT) has widely increased owing to its strong absorption band that allows deeper tissue penetration causing significant heating (Skřivanová et al., 2006). In PDT, the agent, which is absorbed by cells and selectively retained by malignant tissue (Dougherty et al., 1998), is promoted to an excited state as it is exposed to light. Light absorption causes the generation of singlet oxygen ROS, and a necrotic and apoptotic result on tumour tissues is achieved (Abels, 2004). Furthermore, the generated ROS provoke indirect cytotoxicity such as hypoxia and starvation (Robertson et al., 2009), cross-links, strand breaks and DNA base oxidative damage (El- Daly et al., 2013). In the case of ICG, it appears that its decomposition products are linked immediately to the singlet oxygen (Engel et al., 2008). In another way, PTT employs photoresponsive agents, which generate local heating after cellular uptake. Thus, the malignant tissue can be destroyed (Miao et al., 2015). By virtue of its good properties in these contexts, several research groups (Bäumler et al., 1999; Gamal-Eldeen et al., 2013; Jian et al., 2015; Kuo et al., 2012; Ma et al., 2013; Shemesh et al., 2014; Urbanska et al., 2001; Yanina et al., 2012; Zheng et al., 2014) have proposed the use of ICG for PDT and PTT. Because ICG displays a moderate fluorescence quantum yield, it has also been suggested as a contrast agent in photoacoustic (PA) imaging (Miyata et al., 2014). The PA effect is generated from the acoustic wave, following the absorption of optical energy. Briefly, PA imaging consists in the irradiation, with a laser

light, of a determined tissue. Then, the energy of this laser is absorbed by exogenous contrast agents and transformed to heat. An ultrasound (US) transducer is able to reveal the pressure wave generated by thermoelastic expansion of the tissue after heating. The results of this process are notable functional, cellular, and molecular images (Luke et al., 2012).

The clinical approved safety and the intrinsicmultiple capabilities of ICG make it a better candidate for imaging and treatment of cancer, compared with other photothermal agents. A few reviews summarize photophysical and photochemical properties of NIR organic dyes used for potential bioimaging applications (Escobedo et al., 2010; Yuan et al., 2013). In this context, several fluorophores have been proposed but further studies are required before their introduction in human application. Indeed, these compounds should have specific properties such as good photostability and high quantum yield, as well as functional groups that can permit easy chemical modifications (Guo et al., 2014).

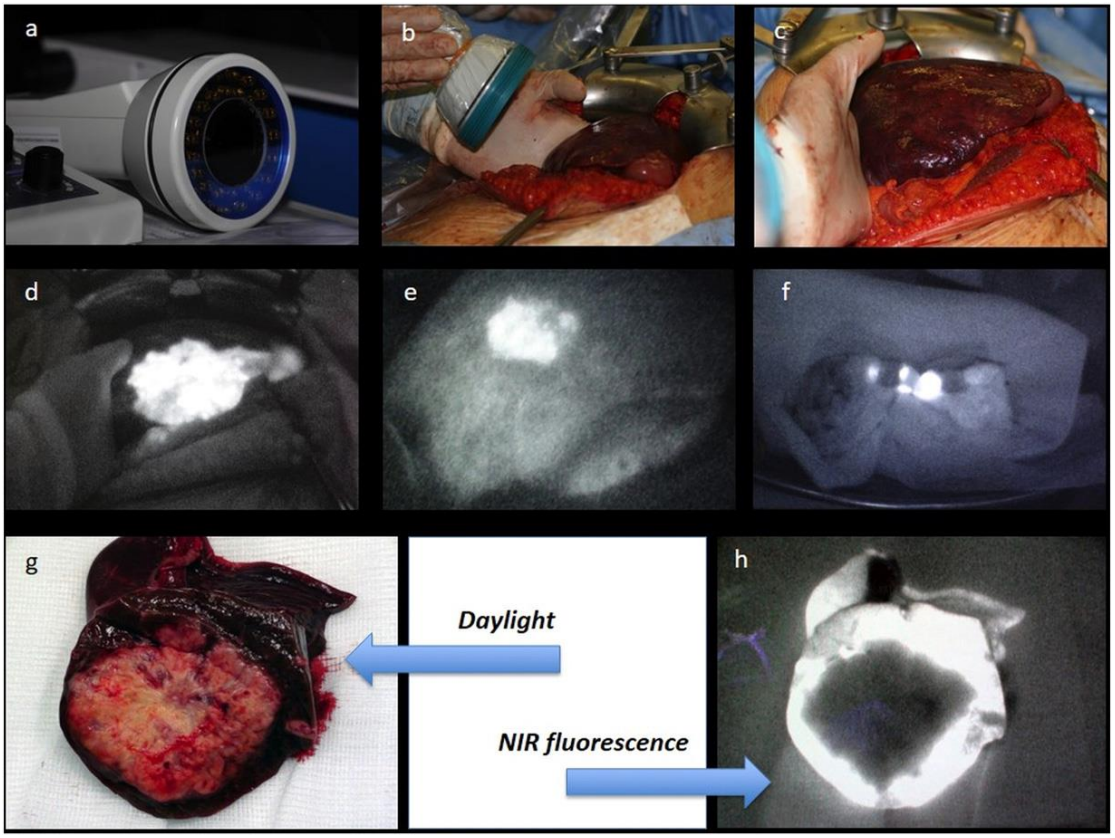


**Fig. 1.** ICG use as a "real-time" tool for intraoperative identification of solid tumours and metastases. **a**: The photodynamic eye (PDE) is basically a charge-coupled device (CCD) camera with an outer ring of diodes. These emit a near infrared light, which stimulates the fluorescence of ICG, previously administered by systemic i.v. infusion; **b**: intraoperative use of PDE; **c**: daylight view of a liver. The patient has a metastatic colon cancer; **d**: the same liver upon NIR light. The bright area is a metastasis, which concentrates the ICG while the normal parenchyma has already washed off; **e**: a further lesion; **f**: postoperative specimen. Peripheral lesions (diameter ranging from 1 to 5 mm) are frequently found around the primary lesion. These are below the resolution of routinary preoperative examinations (computed tomography (CT) scan, ultrasound, magnetic resonance imaging (MRI)) and can escape the resection, thus frustrating the attempt to eradicate the cancer burden from the liver; **g**: postoperative specimen. A small lesion surrounded by normal parenchyma; **h**: postoperative specimen at NIR light. The outer layer is brightly fluorescent, as the parenchyma does not eliminate the dye for a defective secretion.

Despite its several advantages, the employment of ICG in all clinical uses is still limited. The main drawback of using ICG is non-specific bonding to plasma proteins without difficulty. Consequently, ICG exhibits a fast body clearance (plasmatic half-life of 2–4 min) and a marked instability in vivo, with a lack of target specificity. In addition, this contrast agent is unstable in water solutions and it is prone to aggregation because of its physicochemical properties, inducing self quenching and low quantum yield (Sheng et al., 2013). As reported by Saxena et al. (2003) in vitro degradation of ICG in water solutions is strongly accelerated by high temperatures and light exposure. Due to these limitations, ICG itself is not always suitable for cancer detection (Shemesh et al., 2014). For example, easy diffusion of free ICG and the attenuation of fluorescence in SLNmapping involve a rapid incision procedure of SLN within 30min, but this time is not always sufficient for the biopsy of a deep lymph node (Mok et al., 2012). For this reason, developing long-lasting ICG-loaded probes to allow efficient and prolonged imaging is needed. Furthermore, the peripheral distribution of ICG after systemic administration is limited by hepatobiliary elimination, which restricts its tumour accumulation for specific treatment (Ott, 1998). In addition, PDT-induced DNA damage may be minimized in normal tissue, localizing the therapeutic effect to tumour cells by using targeting strategies (Shemesh et al., 2014). In order to address the several issues, the encapsulation of the dye into numerous carriers has been proposed. Experimental studies demonstrated that this approach improves ICG stability, prolong its circulation in the blood and target the dye to a specific site, making ICG an ideal fluorescence marker (Saxena et al., 2006). For these reasons, the ICG loading into delivery systems makes its application in cancer diagnosis and therapy as well as in cancer theranostics more valuable, combining imaging and therapy in a single platform in order to get therapeutic protocols that are more specific to individuals (Xie et al., 2010). The main objective of this review is the classification of nanoparticulate formulations as a promising approach for ICG delivery, because their size and structure can alter tissue distribution of the dye, allowing these carriers to achieve a successful cancer imaging and treatment. In addition to nanosystems, other formulations including hydrogel and microsystems loaded with ICG are illustrated. Examples of ICG delivery systems and their applications are shown in Table 1. In addition, their biological
properties are summarized in Table 2.

## 2. POLYMERIC NANOCARRIERS

### 2.1. Polymeric Nanoparticles

With the aim of avoiding degradation and *in vivo* instability of ICG, several nanometer sized systems encapsulating this agent have been constructed. The employment of fluorescent dye loaded polymeric nanoparticles represents a potential tool for in vivo tumour imaging thanks to the low toxicity, biodegradability and biocompatibility of these systems (Vollrath et al., 2013). Among several materials, biodegradable poly(lactide-co-glycolide) (PLGA) nanocarriers are commonly used to deliver ICG. Saxena et al. (2004b) developed ICG loaded PLGA nanospheres by the emulsion solvent diffusion method, observing that the increase of polymer amount led to high ICG entrapment. It was demonstrated that the aqueous, photo and thermal stability of the encapsulated dye was improved more than free ICG (Saxena et al., 2004a). Regarding biodistribution, the accumulation of the delivered dye in organs and in blood was much higher compared to ICG solution, confirming the enormous potential of PLGA nanoparticles in tumour diagnosis and PDT (Saxena et al., 2006). In order to evaluate the potential application of PLGA nanoparticles in PDT, Gomes et al. (2006) carried out in vitro experiments.

The nanocarriers were fabricated by using the W/O/W double emulsion technique. Studies performed on P388-D1 cells in the presence of ICG containing PLGA nanoparticles, showed nanoparticle-uptake by cells after a few hours of incubation. Moreover, cellular damage was observed after laser irradiation, leading to a series of processes caused essentially by the local production of ROS inside the cells. The characterization and in vitro evaluation of another nanoparticulate system entrapping ICG within the PLGA system were carried out by Patel et al. (2012), resulting in the preservation of ICG optical properties and revealing the efficacy of simple formulations. In addition, Subhash et al. (2012) firstly reported the detection of dye-loaded PLGA nanoparticles using photothermal optical coherence tomography, confirming the potential application of the system for structural and molecular imaging. In the literature, dual loading of drug and dye in PLGA nanoparticles has also been investigated. Manchanda et al. (2010) reported simultaneous doxorubicin (DOX) and ICG loading into a single platform (ICG– DOX NPs), prepared with a method of O/W single emulsion. These ICG–DOX NPs have shown potential for chemotherapy combined with localized hyperthermia as well as for the localization and visualization of the tumour thanks to the imaging

properties of ICG. The same research group conjugated ICG–DOX NPs with antibodies for Human Epithelial Receptor-2 (HER-2) to specifically target SKOV-3 cells that overexpress HER-2. In vitro experiments proved in vivo that the antibody conjugated nanoparticles were a good candidate for targeted chemotherapy and hyperthermia treatment (Srinivasan et al., 2014). ICG was combined with DOX into PLGA nanoparticles by Tang et al. (2010) in order to assess the cytotoxic effect of hyperthermia coupled with chemotherapy in human ovarian cell lines resistant to DOX (SKOV-3 and Dx-5). The exposition of the cells to hyperthermia combined with DOX produced superior cell death compared to a simple treatment with DOX, confirming a synergistic effect of the formulation for cancer treatment. Hao et al. (2015) developedmultifunctional PLGA nanoparticles able to deliver docetaxel (DTX) and ICG to the brain. These particles were functionalized on the surface with the peptide angiopep-2, which is a brain-targeting peptide. The formulation was fabricated via an O/W emulsion solvent evaporation method. These systems allowed combined chemo-phototherapy for glioma. Indeed, nanoparticles induced U87MG cell killing in vitro and extended survival of mice xenografted with U87MG glioma, revealing that these nanoparticles could be useful in clinical applications to treat this type of cancer. Polymeric nanoparticles administrated intravenously are rapidly removed from the bloodstream but the application of hydrophilic coatings made with polymers (i.e. polyethylene glycol (PEG)) onto the surface of these nanoparticles may prolong their residence in blood. Ma et al. (2012) developed PLGA nanoparticles coated with PEG and folic acid (FA). The biodistribution of this formulation was evaluated in the MDA-MB-231 breast cancer cell xenograft mouse model. Thanks to the prolonged circulation and specific uptake, the accumulation of these modified nanoparticles in the cancer was markedly higher than non-modified nanoparticles. Bahmani et al. (2013) also evaluated the influence of PEG on ICG-doped nanosystems. The authors developed ICG-doped nanocapsules made with polyallylamine hydrochloride (PAH) and subsequently coated with PEG (5000 Da) by using reductive amination. After injection of the particles in the tail vein of healthy mice, *in vivo* quantitative fluorescence imaging was carried out. Experimental data corroborated their capability of extending the applications of ICG thanks to its enhanced bioavailability. The same research group (Bahmani et al., 2014) coated these PAH nanosystems with PEG and monoclonal antibodies (mAbs) against HER2 as an ovarian cancer biomarker. The

results obtained from *in vitro* studies proved that these nanoparticles were able to perform imaging, intraoperative detection and photothermal treatment of this type of tumour. Furthermore, they could be considered suitable for a combination of the abovementioned treatments with open surgical procedures. Yu et al. (2010) described the synthesis of about 120-nm nanocapsules, by using a three-step technique, including ICG within PAH particles and using antibodies for the anti-epidermal growth factor receptor (EGFR) as coating agents. The authors investigated the affinity of these systems for three different types of tumour cells (1483 cells, SiHa cells and 435 cells) as well as their photothermal effects on these cell lines. Loaded ICG caused *in vitro* significant thermal toxicity, in comparison with free ICG, confirming capability to generate heat using noncovalent chemistry. In addition to PLGA and PAH, other authors reported the synthesis of ICG-containing nanosystems using different polymers. Liu et al. (2013) constructed ICG-loaded theranostic nanocarriers for tumour imaging and treatment using dextran, awater-soluble polysaccharide. ICG nanoparticles were incubated with breast cancer cells (MCF-7) to assess the NIRF in an intracellular environment. It was demonstrated that these particles can be activated from "OFF" to "ON" by NIRF and they can be employed for NIR imaging and PTT. The recent work by Kim et al. (2015) reported the use of levan for the fabrication of polymeric nanoparticles. Although the application of this biocompatible material is limited by the difficult polymer purification,

ICG loaded levan nanoparticles were prepared for target detection of breast cancers. ICG was easily loaded in levan systems via hydrophobic interactions between these two components, obtaining nanoparticles with a size of 138 nm. In vivo experiments in breast cancer bearing mice showed the usefulness of these nanosystems for imaging this type of tumour. In addition to the above-mentioned polymers, even chitosan is an ideal candidate to engineer ICG-loaded carriers. Also in this case, the surface modification with specific moieties improved nanoparticle delivery. Recently, X. Song et al. (2015) fabricated PEGylated chitosan (CG-PEG) nanoparticles with a small size (about 5 nm) by means of a W/O reverse microemulsion method, using genipin as a cross-linker. Chitosan–genipin nanoparticles after PEG introduction showed good dispersibility, monodispersity and stability at different pH values. ICG was simply added to the CG-PEG aqueous solution by using a self assembly method via electrostatic interaction. The resultant ICG nanocarriers (CG-PEG–ICG) exhibited improved photo- and thermal stability, good

biocompatibility, and low toxicity. Glioma U87 cells were incubated with CG-PEG–ICG nanoparticles. The irradiation of these cells induced very low cell viability (15%), reflecting high *in vitro* photothermal toxicity of the formulation. In vivo mice experiments were performed in order to assess the PTT effect of CG-PEG–ICG nanoparticles on the destruction of U87 xenograft tumours. The CG-PEG– ICG nanoparticles were directly injected into the tumour site. The results showed that the growth of U87 tumours was inhibited by CGPEG– ICG nanoparticles. The therapeutic efficacy and toxicity of the systems were also confirmed by histological tissue analysis. Recently, Jheng et al. (2015) combined a basic amino acid, arginine (Arg) with chitosan in order to obtain a stronger positively charged chitosan–arginine (CSN- Arg) conjugate. ICG-loaded nanoparticles (CS-N-Arg/ICG NPs) based on electrostatic attractions between the positively charged CS-N-Arg conjugate and the negatively charged ICG were fabricated to stabilize ICG for drug delivery inside the cells. The optical properties of the conjugates were investigated, as well as cell imaging and photothermal enhanced chemotherapy of the CS-N-Arg/ICG NPs in breast cancer cells, MCF-7 and MCF-7/ADR cells (DOX resistant). The results showed that ICG entrapment in CS-N-Arg/ICG NPs notably enhanced its stability in phosphate-buffered saline (PBS) preventing ICG from aggregating and precipitating and causing a more rapid increase in temperature and better hyperthermia effect than free ICG under irradiation. Cell viability assay proved that CS-N-Arg/ICG NPs could efficiently suppress the growth of MCF-7/ADR cells under PTT. Additionally, the combination of free DOXwith CS-N-Arg/ICG NPs led to a combined effect inMCF-7/ADR breast cancer cells, due to both chemical therapeutic efficacy and hyperthermia. For these reasons, CS-N-Arg/ICG NPs could be a new tool for hyperthermia treatment to overcome DOX-resistant breast cancer cells. In 2011 Ranjan et al. (2011) developed biodegradable ICG loaded nanoparticles made with a polymer mixture of chitosan, poloxamer (Pluronic F68) and poly(L-lactide-co-epsilon-caprolactone) (PLCL). The preparation procedure was an emulsification solvent diffusion method where chitosan and polyvinyl alcohol were the stabilizing agents. The presence of PLCL extended the ICG release from these systems. As shown by confocal laser scanning microscopy, nanoparticles were internally delivered to prostate and breast cancer cells. Furthermore, nanoparticle biodistribution was evaluated in mice for 24 h after intravenous administration. The resulting higher cell uptake and accumulation confirmed that these systems could be considered a potential

non-invasive deep tissue imaging approach for diagnosis and treatment of tumours. Water soluble chitosan modified with folate has been used for the production of ICG-loaded nanoprobes (Wu et al., 2014). The particles exhibited efficient properties in terms of photostability and cytotoxicity. Moreover, tumour accumulation was observed in a Hela (human cervical cancer) xenograft-bearingmicemodel,making chitosan nanocystals a potential tool for tumour targeting and NIR molecular imaging. ICGincorporated chitosan hybrid nanoparticles were developed by a nonsolvent counterion complexation method and electrostatic interaction and used for combined PTT and PDT (Chen et al., 2013). In order to develop this formulation, gold nanorods (GNRs) have been mixed with chitosan:EDTA (ethylenediaminetetraacetic acid) solution in the presence of ethanol and the final particles cross-linked by glutaraldehyde. *In vivo* experiments performed in hepatic H22 tumour-bearing mice demonstrated synergistic properties of this formulation. Indeed, the particles were able to generate efficiently hyperthermia and ROS in tumour cells. An original polymer–protein hybrid nanocarrier containing ICG has been designed by Yoon et al. (2013). This system made of polyacrylamide nanoparticles (PAA NPs) contained human serum albumin (HSA). The preparation method consisted of a W/O emulsion where HSA was conjugated with a functionalized monomer and the final polymerization was achieved by using biodegradable cross-linkers. Then, ICG was incorporated in PAA NPs conjugated with HSA (HSA– PAA NPs). The stability of ICG (chemical and physical) was higher in HSA–PAA NPs compared to the PAA polymer matrix. The authors demonstrated that the reason for this improvement was the existence of hydrophobic pockets in the hybrid nanocarrier. ICG loading corresponding to 3%was the ideal value to achieve the strongest fluorescence intensity. The nanocarriers were coated with F3–Cys peptide for cancer cell targeting. Specifically, the optical imaging properties of these systems were assessed on the gliosarcoma cell line (9L) from rat. Taking into account the results, these nanoparticles could be used as an efficient cargo ì ì for fluorescent molecules in fluorescence and PA imaging. In order to fabricate ICG delivery systems, the PEBBLE technique has also been employed. PEBBLE is the acronym of “Photonic Explorer for Biomedical use by Biologically Localized Embedding” technology. It allows the production of nanoscale systems, where an inert matrix entraps sensor molecules. In 2007 Kim et al. developed an ICG-loaded nanoparticulate system as a PA imaging device based on PEBBLE. The matrix of this

nanocarrier was an organically modified silicate (ormosil). Compared with ICG alone, the stability in an aqueous solution of ICG-loaded ormosil PEBBLEs was higher. The conjugation of theseparticles with HER-2 antibody revealed an efficient binding of these conjugated particles to prostate cancer cells. El-Daly et al. (2013) modified the synthesis process of ICG-embedded ormosil PEBBLEs described by Kimet al. (2007) and investigated their photodynamic effect on two different cell lines:MCF-7 and HepG2 (hepatocellular carcinoma cells). The results indicated similar phototoxic activity for ICG-ormosil PEBBLEs and ICG alone, inducing DNA damage after irradiation. Nevertheless, final data suggested that loading ICG in these polymeric nanosystems improved the aqueous stability of the dye and retained its photodynamic activity. In 2013 Gamal-Eldeen et al. conjugated ICG-embedded ormosil PEBBLEs with EGFR antibody and evaluated the PDT effect on skin cancer in CD1 mice. In vivo studies proved that PDT using ICG-PEBBLE with or without the conjugated antibody produced a decrease of skin cancer sizes. The authors found that the conjugation of ICG-PEBBLE to EGFR antibody induced more vascular endothelial growth factor (VEGF) inhibition and higher levels of caspase-3. Nevertheless, other PDT effects induced by antibody conjugation were not revealed. Mok et al. (2012) employed hyaluronic acid to synthesize ICG incorporated nanogels for imaging targeting of tumours. Hyaluronic acid is a stimuli responsive component susceptible to hyaluronidase (HAdase), highly expressed in tumour tissue. In vivo studies were performed in mice xenografted withMDA-MB-231 cancer cells. The systemic administration of these nanocarriers revealed a prolonged visualization of tumours. In addition, HAdase and nanogelswere mixed and administered into the forepaw of animals with the aim of mimicking metastatic lymph nodes. ICG-loaded HA nanogels showed lowICG fluorescence intensity in SLN but the presence of HAdase markedly improved ICG fluorescence signal. These results confirmed that these systems are a potential approach for the visualization of HAdase-overexpressing cells, in which ICG could be “switched on”. Recently, in order to detect positive tumour margins and malignant masses during surgical operation, Hill et al. (2015) engineered different hyaluronic acid-derived nanoparticles that entrapped ICG (NanoICG). The matrix of these nanocarriers was composed of aminopropyl-1- pyrenebutanamide (PBA) or octadecylamine (ODA) or aminopropyl- 5β-cholanamide (5βCA). The preparation method was a self-assembly process. Quenched fluorescence of NanoICG was achieved

through a disassembly process in a mixed solvent. Furthermore, NanoICG was nontoxic at physiological concentrations. By using a specific apparatus for imaging, the efficacy of NanoICG was tested on MDA-MB-231 tumour xenograft model mice. A strong fluorescence improvement in tumourswas observed. Further studies are necessary to establish howthe intratumoural biodistribution influences the surgeon's ability to detect cancer margins by imaging during surgical procedure. As mentioned above, ICG represents a good imaging probe for SLN mapping, a procedure applied for the diagnosis of cancer metastasis. Unfortunately, ICG exhibits limitations such as low photostability and fast diffusion through SLN. For these reasons, Noh et al. (2011) decided to develop nanoparticulate systems composed of poly (γ-glutamic acid) (γ-PGA) polymer and ICG as a new NIR agent for SLN mapping. The photostability, the intensity of the signal and retention time of ICG combined with this formulation were drastically enhanced compared to those shown by ICG alone, providing strong evidence that this formulation is a good candidate for better SLN mapping. Taking into account these results, Kong et al. (2015) compared this system with the IRDye900-conjugated pullulan-cholesterol nanoprobe. Dogs and pigs were used and both formulations were injected into their stomachs. Then, the distribution of these dispersions was detected using an NIR imaging system. In vivo data suggested that both NIR-PNG and ICG/γ-PGA could be good candidates for SLN mapping in gastric cancer. In all mentioned papers, the capability to overcome several drawbacks of free ICG by loading it into polymeric nanoparticles was proven. With regard to ICG biodistribution, active targeting with specific molecules on the surface of polymeric nanocarriers can also be used to get a better profile in terms of long circulation and tumour specificity. In addition, the accumulation of these nanocarriers in tumour region is facilitated by the enhanced-permeability-and-retention (EPR) effect which allows the passive delivery of nanoparticles. In spite of their palpable advantages, fluorescent polymeric nanosystems have not yet been employed for clinical application because more studies are required to better understand their in vivo distribution and interactions (Vollrath et al., 2013).

## 2.2. POLYMERIC MICELLES

Polymeric systems provide ICG with good stability and among them micelles are extremely successful. Polymeric micelles are nano-sizedcore–shell constructs formed in

aqueous solution via self-assembly of amphiphilic block copolymers (Riess, 2003). The self-assembly process takes place when the concentration of block copolymer is higher than critical micelle concentration (CMC). At this point, the formation of micellar structures is gained thanks to the association in water of the hydrophobic parts of block copolymers with each other (Xu et al., 2013). These systems have been positively proposed as pharmaceutical vehicles for ICG delivery because their size, varying from 20 to 100 nm (Tan et al., 2013), permits efficient EPR effect-mediated passive accumulation in pathological tissues and the prolongation of circulation time (Jones and Leroux, 1999). Several groups have studied ICGcontaining polymeric micelles. Zheng et al. (2011) described the use of phospholipid (PL)-PEG for the development of ICG-containing nanosystems. Indeed, PL-PEG forms polymeric micelles in an aqueous environment due to its amphiphilic nature. In order to explore ICG for dual applications, optical imaging and PTT, the authors developed new carriers (ICG–PL-PEG) by noncovalent self-assembly between the amphiphilic molecule and the dye. The surface of the nanoprobes was coated with folic acid (FA) and integrin Rvβ3mAb in order to create a selective targeting platform. These nontoxic systems showed a stable structure and good fluorescent properties.With the aimof examining the real effectiveness of the platform in optical imaging and selective phototherapy, ICG–PL-PEG conjugated with mAb were tested in nude mice bearing U87-MG tumour. This work represents the first study where systemic administration has been used to assess photothermal effects of ICG-containing nanocarriers. The results demonstrated that the developed polymeric micelles were useful for cancer diagnosis and treatment, due to passive and active targeting (X. Zheng et al., 2012). The efficacy of ICG–PL-PEGmicelles (Zheng et al., 2011) asgood contrast agents for PA imaging has been proved by the studies conducted by Zhong and Yang (2014). Previously, Zhong et al. (2013) proposed nanoparticles made with ICG, PL-PEG and FA as tumour-targeting nanoprobes. These biocompatible nanocarriers provided several advantages such as improved stability of ICG, extravasation and permeation into tumour tissue due to their size (about 18 nm) and increased circulation time by PEG coating on the nanoparticle surface. *In vitro* and *in vivo* experiments were performed in order to assess the PA effect, which appears when the nanoparticles are exposed to irradiation. Target specificity and in vivo distribution of these probes were examined, obtaining an efficient damage of tumours by PA therapy. The authors revealed that the effects caused

by particles on tumour cells depended on the mechanical effect induced by the shockwave rather than the high temperatures. Recently, ICG has been encapsulated in hybrid polymeric nanomicelles (PNMs) by a simple nanoprecipitation (Jian et al., 2015). The nanomicelles were featured by a hydrophobic PLGA/ICG/PEI poly(ethylenimine) hybrid core surrounded by the highly hydrated PEG shells. To demonstrate the effectiveness of the system, various *in vitro* studies were performed. A great potential for practical applications in tumour imaging and PTT was proven. The PNMs exhibited a good optical and colloidal stability, reduced ICG leakage, enhanced intracellular ICG transport and photothermal cytotoxicity on HeLa cells. PLGA has also been used by Situ et al. (2015) to synthesize dextrang-PLGA (Dex-PLGA) micelles, functionalized with A54 peptide (A54-Dex-PLGA) and loaded with DOX. A54-Dex-PLGA micelles have been proposed for active targeted drug delivery. Indeed, these systems demonstrated efficient *in vitro* internalization capability into hepatoma cells (BEL-7402 and HepG2), with a specific cellular uptake by the BEL-7402 cells. In addition, in vivo biodistribution experiments showed the higher distribution capability of A54- to BEL-7402 tumours, compared to HepG2 ones. The functionalization in A54-Dex-PLGA micelles improved the target of nanocarriers to the tumour tissue. Other ICG-loaded micelles were developed by Rodriguez et al. (2008), who used poly(styrene-alt-maleic anhydride)-block–poly(styrene) (PSMA-b–PSTY) diblock copolymers. The micellization was performed with the solvent evaporation method. In aqueous solution, self assembling diblock copolymers formed stable micelles (about 55 nm),in which ICG was preserved from aqueous and thermal degradation. In this case, only in vitro studies were conducted using breast cancer cell lines. The toxicity in cells of these polymericmicelles was not significant. Studies performed revealed that these platforms have the potential to enhance NIR imaging detection of tumours. Among various nano-sized polymeric systems, Pluronic micelles seem to be a promising carrier for non-invasive tumour imaging. In 2010 Kim et al. reported that the ICG loading within polymeric micelles consisted of the block copolymer Pluronic F-127 (PF-127) composed of poly(ethylene oxide)–poly(propylene oxide)–poly(ethylene oxide) (PEO100–PPO65–PEO100). These micelles showed excellent capability to stabilize ICG at body temperature thanks to the thermosensitive properties of PF-127. In addition, a strong enhancement of tumour localization in a mouse xenograft model with CT-26 murine colon adenocarcinoma cells

was observed, due to longer blood circulation of these systems. Some modifications were carried out in the work published in 2012 (Kim et al., 2012) where micelles were prepared using different ratios of poly(ethylene oxide)–poly[(R)-3-hydroxybutyrate]–poly(ethylene oxide) (PEO–PHB–PEO) and the thermosensitive PF-127 for ICG encapsulation. These changes were required in order to overcome some disadvantages such as the high temperatures required for their preparation and low drug loading efficiency. Mixed micelles composed of 7:3 PEO–PHB–PEO:PF-127, exhibited several advantages including ease of preparation at room temperature, a filamentous structure that enhanced passive cancer accumulation and reduced plasmatic clearance, compared with both puremicelles. Moreover, the mixed micelle system stabilized ICG fluorescence at physiological temperature. With these systems, a notable increase (60%) in tumour fluorescence (colon carcinoma CT-26 tumour-bearing mice) was achieved by comparison with spherical PF-127 micelles. Other materials have been employed to develop ICG-containing polymeric micelles. For example, ICGwas loaded in the core of micelles, consisting of self-assembling amphiphilic PEG-polypeptide hybrid triblock copolymers of PEG-b–poly(L-lysine)-b–poly(L-leucine) (PEG– PLL–PLLeu), where PEG was the hydrophilic shell and PLLeu was the hydrophobic core. The loading of ICG into the developed micelles (PEG–PLL–PLLeu–ICG) occurred through hydrophobic interaction and electrostatic adsorption. In vitro and in vivo experiments confirmed a possible application of PEG–PLL–PLLeu–ICG as a photothermal agent (Wu et al., 2013). Photothermal capability and stable NIR properties of ICG were also shown from poly(2-ethyl-2-oxazoline)-b–poly(ε-caprolactone) (PCL) micelles conjugated with folate, prepared by Yan and Qiu (2015) using the solvent evaporation method. The experiments revealed that these micelles targeted human epidermoid carcinoma (KB) tumours, generated heat from the absorbed NIR laser energy and then caused tumour damage. Yang et al. (2013) developed ICG and Cypate micelles made with monomethoxypoly(ethylene glycol) and alkylamine-grafted poly(L-aspartic acid) (mPEG-b-PAsp). Alkylamines with different chain lengths including octylamine (OA), decylamine (DA), and tetradecylamine (TA) have been screened. The moieties were grafted into the backbones of copolymers for the synthesis of mPEG-b- PAsp(OA), mPEG-b-PAsp(DA), and mPEG-b-PAsp(TA), subsequentlyemployed to assemble ICG into ICG-loaded mPEG-b-PAsp(OA) micelles (ICG-OA-M), mPEG-b-PAsp(DA) micelles (ICG-DA-M), and

mPEG-b- PAsp(TA) micelles (ICG-TA-M), respectively. ICG-DA-M exhibited the slowest release rate, a good internalization into cancer cells and the capacity to improve the fluorescent signal for a long period after their injection into the mice bearing A549 tumour. Wan et al. (2014) evaluated the anticancer efficacy of novel theranostic micelles including ICG in combination with DOX, composed of mPEG and decylamine-grafted poly(L-aspartic acid) (mPEG-b- PAsp(DA)). These platforms exhibitedmultiple functionalities including NIRF, hyperthermia and ROS from ICG, and cytotoxicity induced by DOX, making them suitable for efficient cancer imaging and therapy. Makino et al. (2007) synthesized theranostic photosensitive nanoparticles composed of micelles assembled from poly(sarcosine)– poly(L-lactic acid) (PS–PLLA) block copolymers and loading a dye derivative, ICG-loaded lactosome (ICGm). Tsujimoto et al. (2014) revealed the efficacy of ICGm for diagnosis and treatment of the peritoneal spread of gastric cancer. *In vivo* imaging studies confirmed the usefulness of ICGm as a novel theranostic nanodevice. The authors observed that ICGm selectively accumulated in tumoural areas. In addition, PDT with these systems reduced the disseminated nodules and remarkably improved survival rate. On the basis of these results, Tsujimoto et al. (2015) decided to investigate the theranostic value of ICGm(containing 22% of ICG–PLLA and 78% of PS–PLLA) using amurinemodel of draining lymph node metastasis of gastric cancer. The studies confirmed that ICGmmight be a novel and safe theranostic tool, allowing the visualization of metastatic popliteal lymph nodes and the inhibition of their growth. ICGm with a diameter of 30–40 nm showed an efficient escape capability from the reticuloendothelial system (RES), and accumulated to the tumour region by the EPR effect. Funayama et al. (2012) previously examined the usefulness of ICGm in intraoperative NIRF imaging. ICGm were tested in vivo in different rat models, bearing subcutaneous mammary tumour and spinal metastasis of breast cancer. The results demonstrated that tumour regions showed high fluorescence intensity for at least 24 h in all cases. Moreover, the efficacy of ex vivo NIRF imaging was also evaluated on the dissected lumbar spine of the rats. Further studies are needed but all results confirmed that ICGm are an effective platform for intraoperative imaging of spinal metastasis as well as for PDT. Ma et al. (2013) developed a theranostic nanoplatform for dualmodal imaging, fluorescence/magnetic resonance, and PTT. ICG was loaded into a lipid coating, composed of 1.2-distearoyl-snglycero-3-phosphoethanolamine-N-[methoxy (PEG)]

(DSPE-PEG), which surrounded superparamagnetic iron oxide (SPIO) nanoparticles. The final nanoparticles (SPIO@DSPE-PEG/ICG NPs) were able to simultaneously improve *in vivo* optical and magnetic resonance imaging. After systemic injection, tumour ablation due to a photothermal effect was observed, following tumour-specific accumulation of nanoparticles. Although the stability of polymer micelles depends on their CMC,
these systems are widely accepted as imaging agent delivery systems due to several benefits, such as the easiness of production, high stability, biocompatibility, and chemical functionalization for selective targeting, making them suitable for diagnosis and treatment of various tumours.

**Table 1.** Examples of ICG-containing delivery systems for cancer diagnosis and/or treatment with their respective advantages and limitations.

| Delivery systems | Advantages/Limitations | Composition | Application | Ref. |
|---|---|---|---|---|
| Polymeric nanoparticles | ADVANTAGES<br>-good biocompatibility<br>-low or nontoxicity<br>-biodegradability<br>-versatility of polymer chemistry<br>-ability to form stable particles<br><br>LIMITATIONS<br>-insufficient knowledge of their<br>interactions and distributions *in vivo*<br>-lack of reproducible production | PLGA | PDT/chemoterapy | Srinivasan et al., 2014 |
| | | PAH | NIRF imaging/PTT | Bahami et al., 2014 |
| | | Dextran | NIRF imaging/PTT | Liu et al., 2013 |
| | | Levan | NIRF imaging | Kim et al., 2015 |
| | | Chitosan | PTT | X. Song et al., 2015 |
| | | PLCL:poloxamer-chitosan | NIRF imaging | Ranjan et al., 2011 |
| | | PAA | NIRF imaging/PA imaging | Yoon et al., 2013 |
| | | Ormosil | PDT | Gamal-Eldeen et al., 2013 |
| | | Hyaluronic acid | NIRF imaging | Mok et al., 2012 |
| | | γ-PGA | NIRF imaging | Noh et al., 2011 |
| Polymeric micelles | ADVANTAGES<br>-feasibility to delivery lipophilic and<br>hydrophilic drugs<br>-protection from opsonin adsorption<br>due to the hydrophilic shell<br>-long blood circulation time<br>-small size<br><br>LIMITATIONS<br>-low toxicity<br>-CMC-dependent stability<br>-lack of methods for large-scale<br>fabrication<br>-limited polymers for use | PL-PEG | NIRF imaging/PTT | Zheng et al., 2011 |
| | | PL-PEG | PA imaging | Zhong and Yang., 2014 |
| | | PLGA-PEI-PEG | PTT | Jian et al., 2015 |
| | | Dextran-g-PLGA | NIRF imaging | Situ et al., 2015 |
| | | PSMA-b-PSTY | NIRF imaging | Rodriguez et al., 2008 |
| | | Pluronic F-127 | NIRF imaging | Kim et al., 2011 |
| | | PEG-PLL-PLLeu | NIRF imaging/PTT | Wu et al., 2013 |
| | | mPEG-b-PAsp(DA) | PTT/PDT/chemoterapy | Wan et al., 2014 |
| | | PS–PLLA | NIRF imaging/PDT | Tsujimoto et al., 2014 |
| | | DSPE-PEG-SPIO | NIRF imaging/MR imaging/PTT | Ma et al., 2013 |
| Liposomes | ADVANTAGES<br>-flexible<br>-biocompatible and nonimmunogenic<br>-biodegradable<br>-suitable for the conjugation with<br>ligands or antibodies<br><br>LIMITATIONS<br>-low solubility<br>-short half-life<br>-possibility of oxidation and<br>hydrolysis-like reaction | DPPC, Soy-PC, Chol, DSPE-PEG2000 | NIRF imaging/PDT | Shemesh et al., 2015 |
| | | HSPC/Chol/DSPE-PEG2000 | MSOT/chemoterapy | Lozano et al., 2015 |
| | | DOPC | NIRF imaging/PDT/ PTT | Suganami et al., 2012 |
| | | Phospholipon 50 | NIR imaging | Portnoy et al., 2011 |
| | | HSPC/Chol/DSPE-PEG2000 | MSOT | Beziere et al., 2015 |
| Lipid-polymer nanoparticles | ADVANTAGES<br>-combination of mechanical properties of polymeric nanoparticles<br>and biomimetic benefits of liposomes<br>-potential to deliver multiple drugs<br>-surface functionalization | PLGA-lecithin-PEG | NIRF imaging/PTT | Zhao et al., 2014 |
| | | PLGA-lecithin-PEG | PTT/chemotherapy | Zheng et al., 2013 |
| | | PLGA, lecithin, DSPE-PEG2k-FA | NIRF imaging | C. Zheng et al., 2012 |
| | | PLGA, lecithin, DSPE-PEG2k-FA | PA imaging | Wang et al., 2014 |

| | | | | |
|---|---|---|---|---|
| | LIMITATIONS<br>-stabilization with PEG layer<br>-critical targeting ligand density<br>-possible limitation in the synergistic<br>effects of combined drugs<br>-high production costs | | | |
| Inorganic particles | ADVANTAGES<br>-hydrophilic nature<br>-chemical inertia<br>-ease of surface functionalization<br>-chemically and thermally stable<br><br>LIMITATIONS<br>-not well defined toxicity<br>-simple functional groups on their<br>surface for functionalization | TA-TEOS | NIRF imaging | Lee et al., 2009 |
| | | TEOS | NIRF imaging | Stöber et al., 1968 |
| | | TEOS-GNRs | NIRF imaging /PTT | Liu et al., 2015 |
| | | TEOS-GNRs | NIRF imaging | Luo et al., 2011 |
| | | Calcium phosphate/silicate | NIRF imaging | Altınoğlu et al., 2008 |
| | | Calcium phosphate/silicate | PDT | Barth et al., 2011 |
| | | Calcium phosphate/Gd/ $^{99m}$Tc | NIRF imaging/MR imaging/<br>nuclear imaging | Ashokan et al., 2013 |
| Carbon nanomaterials | ADVANTAGES<br>-high specific surface area<br>-enhanced loading capacity<br>-high cell permeability<br><br>LIMITATIONS<br>-potential toxicity of carbon nanostructures<br>-expensive process | GO | NIRF imaging /PTT/<br>PDT | Chavva et al., 2014 |
| | | rGO/ poly(PDMAEMA) | NIRF imaging /PTT | Sharker et al., 2015 |
| | | rGO/ hyaluronic acid | NIRF imaging /PTT | Miao et al., 2015 |
| | | Carbon (SWNT) | PA imaging | Nguyen et al., 2015 |
| | | Carbon (spheres) | NIRF imaging /PTT | Li et al., 2015 |
| Bioconjugates | ADVANTAGES<br>-good toxicity profile<br>-quenched systems<br>-activation after cell internalization<br>-discrimination between healthy and<br>diseased tissue<br>-stable in blood circulation<br><br>LIMITATIONS<br>-high production costs<br>-in solid tumours, antigen expression could be heterogeneous | Trastuzumab | NIRF imaging | Sano et al., 2012 |
| | | Panitumumab | PA imaging | Sano et al., 2015 |
| | | Panitumumab-PEG | NIRF imaging | Sano et al., 2013 |
| | | Anti-PSMA-PEG | NIRF imaging | Watanabe et al., 2014 |
| | | HSA | NIRF imaging/PDT/<br>PTT | Sheng et al., 2014 |
| Others | - | Glycerophosphate/chitosan (hydrogel) | NIRF imaging | Salis et al., 2015 |
| | | PFC/$^{19}$F (nanoemulsion) | NIRF imaging/MR imaging/PTT | Lee et al., 2015 |
| | | PLGA (microbubbles) | NIRF imaging | Bae et al., 2014 |
| | | DSPE-PEG2000-DOTA/ $^{177}$Lu (cerosomes) | NIRF imaging/PTT/<br>nuclear imaging | Wang et al., 2013 |

| Formulation | Size (nm) | Additional agent | Cancer cell line | *In vitro* and *in vivo* studies | Biological results | Ref. |
|---|---|---|---|---|---|---|
| **POLYMERIC NANOPARTICLES** | | | | | | |
| **AIDNPs** | 210 | DOX | Human ovarian adenocarcinoma cells (SKOV-3), human uterine sarcoma cells (MES-SA and Dx5) | *In vitro* | Anti-HER-2 targeted PLGA nanoparticles significantly enhanced toxicity in SKOV-3 upon laser exposure. Combined tumour therapeutic efficacy *in vitro*. | Srinivasan et al., 2014 |
| **ANG/PLGA/DTX/ICG NPs** | 222 | DTX | Human glioma cells (U87MG) | *In vitro* and *in vivo* in mice | Ability of angiopep-2-conjugated nanoparticles to bind to and enter glioma cells, inducing more cell apoptosis than non-targeting systems. Retention in the brain after i.v. injection. Combined chemo-phototherapy. | Hao et al., 2015 |
| **Levan-ICG NPs** | 139 | - | Human breast cancer cells (MDA-MB-231), lung cancer cells (A549), ovarian cancer cells (SKOV-3), cervical cancer cells (HeLa), nasopharyngeal cancer cells (KB), mouse fibroblast cells (NIH3T3) | *In vitro* and *in vivo* in mice | Higher uptake by MDA-MB-231 than other cell lines, via Glut5. *In vivo* studies confirmed their utility as imaging tool, with selective accumulation of the NPs in the breast tumour. | Kim et al., 2015 |
| **CG-PEG-ICG NPs** | 73 | - | Human glioma cells (U87) | *In vitro* and *in vivo* in mice | High stability of CG-PEG-ICG nanostructures against the light quenching, and high *in vitro* photothermal toxicity. After i.v. administration in mice, higher accumulation of ICG in tumour than free ICG due to EPR effect. Photothermal efficacy following intra tumoural injection of NPs. | Song X. et al., 2015 |
| **PLCL:poloxamer NPs** | 146-260 | - | Human prostate cancer cells (DU-145) and human breast cancer cells (MDA-MB-231) | *In vitro* and *in vivo* in mice | Ability of PLCL to prolong *in vitro* release of ICG. The positive charge of chitosan allows for higher cell/tissue uptake, improving imaging and detection. | Ranjan et al., 2011 |

| | | | | | | |
|---|---|---|---|---|---|---|
| **ICG-PEBBLE** | 200-300 | - | - | *In vivo* in mice | Inhibitor ability for tumour size, apoptosis, angiogenesis and tumour inflammation in skin squamous cell carcinoma, induced in CD1 mice by 12-O-tetradecanoyl-phorbol-13-acetate (TPA) and dimethylbenzanthracene (DMBA). No improvement after conjugation of the particles to anti-EGFR antibody in PDT efficacy. | Gamal-Eldeen et al., 2013 |
| **NanoICG** | 80-150 | - | Human breast cancer cells (MDA-MB-231) | *In vitro* and *in vivo* in mice | Nanoparticles are not toxic in cell culture. Capability of carriers to improve contrast enhancement and depict tumour margins during surgical procedure. | Hill et al., 2015 |
| **POLYMERIC MICELLES** | | | | | | |
| **ICG-PL-PEG** | 17-22 | - | Murine mammary tumour cells (EMT6), human glioma cells (U87MG) and human breast cancer cells (MCF-7) | *In vitro* and *in vivo* in mice | Better efficiency of ICG-PL-PEG in producing temperature increase upon NIR laser than ICG alone. Enhancement of ICG accumulation in tumour cells following i.v. injection after conjugation with integrin αvβ3 monoclonal antibody. | Zheng et al., 2012 |
| **ICG/PEI-encapsulated PNMs** | 80-135 | - | Human cervical carcinoma cells (HeLa) | *In vitro* | Good photothermal effect of the systems ICG/$PEI_{10k}$-loaded PNMs on the tumour cells due to internalization of the particles and preservation of ICG by biodegradation in the acidic environments of endosomes/lysosomes. | Jian et al., 2015 |
| **PEO-PHB-PEO/PF-127 mixed micelles** | 5-6 | - | Mouse colon carcinoma cells (CT-26) | *In vivo* in mice | Maximal ICG fluorescence in the area of the tumour showed by micelles with polymer ratio of 7:3 (PEO-PHB-PEO:PF-127). Mixed micelle formulation shows good circulation time and facilitates the tumour accumulation due to the filamentous structure. | Kim et al., 2012 |
| **PEG-PLL-PLLeu-ICG** | 159.1 | - | Human nonsmall lung cancer cells (H460) | *In vitro* and *in vivo* in mice | Good internalization of the micelles by cancer cells. Photothermal effect under NIR laser irradiation. Extension of the circulation time of ICG inside the micelles, with increasing tumour accumulation during the time. | Wu et al., 2013 |
| **ICGm** | 40-50 | - | Human gastric adenocarcinoma cells (MKN45) | *In vivo* in mice | Visualization of metastatic popliteal lymph nodes with *in vivo* and *ex vivo* imaging. Significant apoptosis and suppression of lymph nodes through PDT. | Tsujimoto et al., 2015 |

| LIPOSOMES | | | | | | |
|---|---|---|---|---|---|---|
| **LPICG** | 70-90 | - | Triple negative breast cancer cells (MDA-MB-468) | *In vivo* in mice | In contrast with free ICG, LPICG showed high fluorescence signal within the tumour tissue up to 48 h. Immediate damage to the tumour site and eradication of the mass after 16 days after i.v administration of LPICG, followed by NIR irradiation. | Shemesh et al., 2015 |
| **Polymer-ICG-HER(II)-liposome** | 117 | DOX | Human cervical cancer cells (HeLa), breast cancer cells (MCF-7), ovarian carcinoma cells (SK-OV3), breast adenocarcinoma cells (SK-BR3) | *In vitro* and *in vivo* in mice | Production of multifunctional liposomes with target specificity (conjugation with trastuzumab) and temperature-responsive drug release. Capability to perform NIR fluorescence-imaging after accumulation. Suppression of SK-OV3 tumour growth in mice due to the administration of liposomes and following mild heating. | Kono et al., 2015 |
| **hCTM01- targeted PEGylated liposome-ICG** | 190 | DOX | Murine breast cancer cells (4T1) and human colon adenocarcinoma cells (HT-29) | *In vitro* and *in vivo* in mice | Tumour accumulation of targeted liposomes (via the hCTM01 surface conjugation) after i.v. administration and visualization using high-resolution optoacoustic imaging. DOX incorporation in order to add a therapeutic functionality to the carriers. | Lozano et al., 2015 |
| **Lipo-ICG** | 170-220 | - | Murine colon adenocarcinoma (C26) | *In vivo* in mice | Study of the biodistribution of liposomal ICG by using optoacoustic tomography. Improved accumulation and retention of Lipo-ICG in tumours compared to free ICG. | Song et al., 2015 |
| **LP-iDOPE** | 191 | - | Adenocarcinomic human alveolar basal epithelial cells (A549) | *In vivo* in mice | Incorporation of iDOPE (conjugation ICG-DOPE) into liposome bilayers. Tumor-specific accumulation of liposomes in vivo xenografts after i.v. injection. | Suganami et al., 2012 |
| **CF800 liposomes** | 85-95 | Iohexol | Human ovarian carcinoma cells (SK-OV3) and human metastatic breast cancer cells (LM2-4H2N)<br>VX-2 tumour cells (buccal mucosa and lung cancer) | *In vivo* in mice<br>*In vivo* in rabbits | After i.v. administration, preoperative localization of tumour nodule in mice and rabbits by computed tomography and intraoperative NIR fluorescence-based lesion confirmation. | Zheng et al., 2015 |

| | | | | | | |
|---|---|---|---|---|---|---|
| **LYPID-POLYMER NANOPARTICLES** | | | | | | |
| **INPs** | 39 (INP-1)<br>68 (INP-2)<br>116 (INP-3) | - | Human pancreatic adenocarcinoma cells (BxPC-3) | *In vitro* and *in vivo* in mice | Good photothermal efficiency *in vitro*. Influence of nanoparticle size on tumour accumulation and photothermal effect *in vivo*. Better tumour growth suppression using INP-2. | Zhao et al., 2014 |
| **FA-ICG-PLGA-lipid NPs** | 118.7 | - | Human breast cancer cells (MCF-7) | *In vitro* and *in vivo* in mice | Enhancement of NPs accumulation due to conjugation with folic acid. Capability to improve photoacoustic contrast in imaging applications. | Wang et al., 2014 |
| **DINPs** | 80-90 (86) | DOX | Human breast adenocarcinoma cells (MCF-7 and MCF-7/ADR) | *In vitro* and *in vivo* in mice | Improvement of ICG stability and high localized temperature produced upon laser irradiation, and cellular uptake of DOX and ICG. Apoptosis and death of the cells *in vitro*, and suppression of tumour growth in vivo, due to efficient cooperation of ICG-mediated thermal toxicity and DOX-mediated cytotoxicity. | Zheng et al., 2013 |
| **INORGANIC PARTICLES** | | | | | | |
| **I-TMSG** | - | - | Human breast cancer cells (MDA-MB-231) | *In vitro* | Nanocarriers possess dual functions as targeting fluorescent probes and targeting PTT agents to tumour cells. Ability to target specific cells due to conjugationwith tLyp-1 peptide. | Liu et al., 2015 |
| **PCSNs** | 30-50 | $^{99m}$Tc | - | *In vivo* in rats | Dual-modality imaging to facilitate sentinel node biopsy examinations, in which NIR fluorescent and radioactive nanoparticles are used to depict sentinel nodes. Lymphoscintigraphy after submucosal injection of PCSNs into the tongue. | Tsuchimochi et al., 2013 |
| **CPNP** | 10-30 | - | Human breast cancer cells (MDA-MB-231) and human pancreatic adenocarcinoma cells (BxPC-3) | *In vitro* and *in vivo* in mice | Bioconjugation of surface-targeting strategies to the CPNPs using human holotransferrin and short gastrin peptides. Diagnostic imaging capability in vivo. | Barth et al., 2013 |

| CARBON NANOMATERIALS | | | | | | |
|---|---|---|---|---|---|---|
| **ICG-CPPDN/rGO** | 210-220 | - | Human breast cancer cells (MDA-MB-231) | *In vitro* and *in vivo* in mice | Photothermal effect causing maximal photothermolysis on treated cells. Targeted toxicity on malignant cells due to pH dependent quenching/relief between the rGO sheet and PDMAEMA in the system. Tumour growth inhibition in vivo under NIR irradiation. | Sharker et al., 2015 |
| **ICG/HArGO** | 110 | - | Human epidermal carcinoma cells (KB) | *In vitro* and *in vivo* in mice | Improvement of photostability and antitumor potency of ICG. The systems provide image-guided and synergistic photothermal anticancer effects in vivo, after i.v. injection and localized irradiation. | Miao et al., 2015 |
| **CSs@PDA-FA@ICG NCs** | - | - | Human cervical carcinoma cells (HeLa) | *In vitro* | Targeted and sensitive switch-control property of the formulation, which can activate fluorescence from "OFF" to "ON" and high specificity for Hela cells due to FA on the surface. PTT/PDT efficiency proved *in vitro*. | Li et al., 2015 |

## 3. LIPOSOMES

Liposomes are spherical vesicular carriers with a small size composed of one or more bilayers, consisting of cholesterol and non-toxic phospholipids (Akbarzadeh et al., 2013). Liposomes are attractive for drug delivery applications for numerous reasons, including biocompatibility and low toxicity, as well as biodegradability and the capacity to load lipophilic and hydrophilic drugs (Bozzuto and Molinari, 2015). These systems show versatile properties that allow the loading of functional drugs in the bilayer or inside the core, or their attachment on the surface of a liposome (Li et al., 2012). Thanks to their numerous advantages, the use of ICG-loaded liposomal formulations has been widely studied with the aimof enhancing the stability of the dye for optical imaging and cancer treatment. The effect of lipid–ICG interactionswas studied in detail by Kraft and Ho (2014) by using spectroscopic techniques. They found that ICG bound to the lipid membrane and itwas completely and stably incorporated into this system. Turner et al. (2012) developed temperature-sensitive liposomes coated with either PEG or dextran to evaluate drug delivery strategy *in vivo*, using ICG as probe to study the biodistribution of liposomes in tumour-bearing mice. In order to find the optimal liposome formulation for optical imaging studies, different formulation parameters such as the presence and the type of co-lipid and the type of coating agent were investigated. The thin film/extrusion method was employed to formulate liposomes. The composition of optimized formulation, having a transition temperature around 42 °C, included L-α-phosphatidylcholine (Soy-PC), cholesterol (Chol), 1.2-dipalmitoyl-sn-glycero-3-phosphocholine (DPPC), and N-(carbonyl-methoxypolyethyleneglycol 2000)-1.2-distearoyl-sn-glycero-3-phosphoethanolamine (DSPE-PEG 2000). At 37 °C liposomal formulation showed good stability but the authors observed burst release at 42 °C. Afterwards, taking into account the previous results, Shemesh et al. (2014) focused their study on theranostic liposomal delivery system for in vivo PDT of breast cancer.

The results from both the MTT ((3-[4,5-dimethylthiazol-2-yl]-2,5 diphenyl tetrazolium bromide) and clonogenic assays showed that the photodynamic effect caused by ICG stopped the growth of TNBC (triple negative breast cancer) cells in vitro. On the basis of these data, the same formulation was also tested in vivo. The human TNBC xenograft in a mice model was used to perform a pharmacokinetic profile and biodistribution. In agreement with other studies, NIRF imaging demonstrated enhanced accumulation of

liposomes within the tumour region. Furthermore, tumour growth in mice treated with liposomes followed by light irradiation was remarkably reduced compared to tumours treated with saline, free ICG and irradiation alone (Shemesh et al., 2015). The efficacy of temperature-sensitive liposomes in anticancer treatment has widely been studied. The combination of temperature sensitive liposomes and target ligands is a good strategy to kill the malignant cells due to tumour accumulation of the liposomes through the EPR effect and target-specific binding. In 2010 Kono et al. developed liposomal carriers composed of egg yolk phosphatidylcholine (EYPC), Chol, and PEG-PE. The authors observed that the attachment of a thermosensitive copolymer onto the liposome surface was advantageous. Indeed, at around 40 °C, poly[2-(2-ethoxy)ethoxyethyl vinyl ether-block-octadecyl vinyl ether (EOEOVE-block-ODVE)] showed lower critical solution temperature. Then, the thermosensitive copolymer provided highly temperature-responsive drug release functionality to PEGylated liposomes. The intravenous administration of these systems loaded with DOX into tumour-bearing mice and subsequent heating at 44–45 °C for 10 min caused significant tumour suppression. Based on these previous results, K. Kono et al. (2015) loaded the thermosensitive liposome with ICG and conjugated them with Tra, which binds to Her-2. In vitro and in vivo studies confirmed the efficacy of the formulation. Indeed, the liposomes showed temperature responsive drug releasing DOX at temperatures above 40 °C and selective targeting to SKOV-3 and SB-BR-3 cells, due to the overexpression of Her-2. In addition, the presence of ICG allowed monitoring liposome accumulation at the tumour site. Therefore, the multifunctional liposomes had a synergistic effect in the tumour treatment. Liposomes containing ICG and Chlorin e6 (Ce6) were proposed for the ablation of cancer cells by Yuan et al. (2015). Ce6 is a promising photosensitizer for PDT. Anyway, this agent is always “ON”, being active even in normal tissue resulting in an undesired phototoxicity. To overcome this drawback, the authors encapsulated Ce6 and ICG into spherical liposomes, prepared through homogeneity and ultrafiltration, finding that the phototoxicity of Ce6 was efficiently inhibited by ICG. As a result of the irradiation, the degradation of ICG caused the switching of Ce6 phototoxicity to status “ON”. Furthermore, the exposure of ICG to NIR laser determined the increase of temperature, involved in a photothermal effect. Targeted PEGylated liposome-ICG was engineered through the hydration method followed by freeze-fracture and extrusion cycles by

Lozano et al. (2015). The anti-MUC-1 mAb hCTM01 was employed to fabricate a cancer-specific theranostic platform. DOX has been loaded inside targeted and non-targeted PEGylated liposomes in order to develop a novel carrier for combined diagnosis and therapy. *In vivo* multispectral optoacoustic tomography (MSOT) imaging was employed to study the delivery of the targeted and non-targeted PEGylated liposome-ICG in HT-29 human colon adenocarcinoma and 4T1 murine breast tumour. ICG-labelled liposomes with and without antibody coupled with MSOT imaging allowed both immediate and long-term detection of liposomes in the tumour. mAb-targeting of liposomes was not able to enhance significantly the accumulationwithin the HT-29 tumours due to their insufficient vascularization. On the other hand, in the case of the highly vascular 4T1model, more rapid accumulationwas observedwith the targeted systems.

Recently, MSOT was also used by another research group to confirm the use of PEGylated liposomes encapsulating ICG (LipoICG) as an optoacoustic agent (Beziere et al., 2015). Using molecular self-assembly principles, the lipid composition consisting of L-a-phosphatidylcholine hydrogenated (HSPC), Chol and DSPE-PEG2000 was combined with increasing ICG amounts, in order to prepare three LipoICG carriers: LipoICG25, LipoICG50 and LipoICG75. Among these formulations, LipoICG75 generated a better optoacoustic signal than gold-nanoparticles (Bao et al., 2013; Herzog et al., 2012), confirming the performance predicted previously. This property was useful for identifying vascular and lymphatic structures in the tumour area. Additionally, specific moieties could be introduced in this system in order to obtain selective agents against different tumours. MSOT technique has been also used by W. Song et al. (2015) to carry out comparative studies between liposomal ICG (LipoICG) and free ICG. Reverse phase evaporation techniquewas employed to design Lipo-ICG, using mPEG2k-stearate (mPEG2k-SA) to protract the circulation lifetime of the liposomes. ICG clearance from blood was slowed by liposome loading. In addition, by using C26 colon adenocarcinoma bearing nude mice it was demonstrated that Lipo-ICG promoted agent accumulation mainly near the tumour vessels at the border. In order to develop multipurpose nanocarriers for optical imaging, PTT and PDT, Suganami et al. (2012) fabricated a novel system in which ICG was conjugated by a covalent approach with 1.2 dioleoyl-sn-glycero-3-phosphoethanolamine (DOPE), named iDOPE. Then, this conjugate was loaded into liposome bilayers, composed of 1.2-dioleoyl-snglycero- 3

phosphocholine (DOPC) to obtain LP-iDOPE. The photothermal effect generated by iDOPEwas proven. Furthermore, iDOPE formulated into a liposomal system seemed to be a stable nanoparticle over 1 week in physiological conditions.Moreover, in in vivo xenografts it showed tumour specific biodistribution. The results confirmed that iDOPE could be a promising optical agent and sensitizer for PTT and PDT. Nevertheless, other *in vivo* studies of LP-iDOPE were required. In a very recent work, an injectable NIRF liposome-based dualmodality (CF800) containing two imaging molecules was proposed (Zheng et al., 2015). CF800 is a nanosystem that co-encapsulates ICG and iohexol, a commercially available CT contrast agent. These liposomes were engineered to allow combining preoperative CT based three-dimensional surgical planning, intraoperative tumour andmalignant lymph node mapping, and NIRF guided resection. In vivo studies revealed that the novel multi-modal systems were able to identify 40 tumour nodules in 8 mice, despite the large variability in liposome accumulationat tumour sites. Promising results have also been achieved with rabbit models of lung, head and neck cancers.

Portnoy et al. (2011) developed a new liposomal agent combining imaging and targeting properties. Although ICG was not covalently bound to the liposome, it was discovered through fluorescence analysis that ICG remained attached to the nanosystems for at least 7 h. In order to obtain active targeting of liposomes, the cetuximab mAb for epidermal EGFR was attached to the liposomal surface by passive adsorption. The results demonstrated that cetuximab-labelled liposomes were uptaken by cancer cells overexpressing EGFR, after specific binding. A new optical contrast agent for SLN and a lymphatic system based on mannosylated liposome-loaded ICG (M-LP-ICG) was prepared by Jeong et al. (2013). M-LP-ICG showed a high uptake in RAW 264.7 macrophage cells, due to the mannose receptor on its surface. The authors confirmed this behaviour through an inhibition study using glucosylated liposome-encapsulated ICG (G-LP-ICG). After either cotreatment or pre-treatment with d-(+)-mannose as an inhibitor, RAW 264.7 cells showed a significant decrease in M-LP-ICG uptake. Compared to LP ICG, the signal generated by M-LP-ICG in SLN occurred and disappeared rapidly after subcutaneous injection in a normal mouse model. Therefore, M-LP-ICG appeared to be a potential contrast agent for optical imaging for SLN detection. Nevertheless, it was observed that LP-ICG accumulated not only in a first draining lymph node but also in a second-tier node in the lower extremities of mice. Taking into account this behaviour,

Toyota et al. (2014) synthesized ICG derivatives by substituting one of the sulfonate groups of the dye with an alkyl chain (ICG-Cn; n=4, 6, 8, 10, and 18). The visualization of lymph nodes was performed by using liposomally formulated ICG-Cn (LP-ICG-Cn), as well as LP-ICG and ICG under a NIRF imaging system. In vitro and in vivo studies were carried out confirming that brilliant fluorescence images came from LP-ICG-C18, which remained only in the popliteal lymph node after injection in a mouse footpad. For this reason, LP-ICG-C18would be a potentially powerful tool to use in non-invasive NIR-bioimaging for SLNs. Taking into consideration the above-mentioned works, liposomes might be a useful vector for ICG encapsulation for tumour diseases. Unfortunately, its application in human clinical practice is still limited. Several risks of the PEGylated liposomes have been also reported. Indeed, on the human body these systems show some side effects such as complement activation (Tanisaka et al., 2007). However, ICG-liposomal carriers have several benefits over free ICG including increased fluorescent signal and improved stability in solution and biological fluids (Beziere et al., 2015; Jeong et al., 2013). Moreover, liposomes are suitable for the conjugation with ligands or antibodies to provide target-specific diagnosis/therapy.

## 4. LIPID–POLYMER NANOPARTICLES

Advantages of polymeric nanoparticles and liposomes such as physical stability and biocompatibility are combined in lipid–polymer nanoparticles. Lipid/lipid–PEG shells and a polymeric core lend nanocarriers the typical core–shell structure (Hadinoto et al., 2013). Due to theirproperties, in latest years these systems have received great attention (Krishnamurthy et al., 2015). Several reports described the loading of ICG into the hybrid platforms. PLGA has been combined with PEG and lipid by Zhao et al. (2014) to develop ICG encapsulated PLGA–lecithin–PEG core–shell nanoparticles (INPs). The biodistribution in nude mice and drug accumulation of INPs in pancreas carcinoma (BxPC-3) xenograft tumours were examined. Using a single-step nanoprecipitation method, nanoparticles with three size distributions (39 nm, 68 nm, and 116 nm) were produced. NIRF imaging and photothermal therapeutic efficiency of ICG was maintained in these particles for cancer theranostics. The strongest efficacy to suppress tumour growth was shown in vivo optical imaging and PTT by 68 nm INPs. On the contrary, *in*

*vitro* experiments proved that pancreatic carcinoma tumour cells absorbed more easily 39 nm INPs, which exhibited better photothermal damage compared with other INPs. Targeting moieties can be linked to ICG-PLGA nanoparticles after appropriate modification, in order to make them tumour-specific. On the basis of this observation, C. Zheng et al. (2012) developed ICGdoped PLGA lipid nanoparticles targeted to the folate receptor (FAICG- PLGA-lipid NPs) through the self-assembly of PLGA, lecithin, andm 1.2-distearoyl-sn-glycerol-3-phosphoethanolamine-N-[folate (polyethylene glycol)-2000] (DSPE-PEG2k-FA), by using a method of nanoprecipitation. In vitro fluorescence properties of FA-ICG-PLGAlipid NPs were investigated. The targeting capability of the FA-ICGPLGA- lipid NPs was confirmed by intracellular uptake, which was more efficient in MCF-7 cells over-expressing the folate receptor compared to A549 cells. Moreover, tumour targeting was performed using the tumour-bearing mice models implanted with MCF-7. Experimental data confirmed excellent optical properties compared to the free ICG, highly selective tumour localization and prolonged circulation time *in vivo*, demonstrating that FA-ICG-PLGA lipid NPs were a promising fluoroprobe for tumour localization and imaging. Wang et al. (2014) proposed FA-ICG-PLGA-lipid NPs for PA imaging of cancer, involving the light conversion to an acoustic wave. After administration in MCF-7 breast carcinoma xenografted mice, FA-ICGPLGA- lipid NPs displayed good optical properties, low toxicity,prolonged circulation time and excellent tumour targeting capability. In addition, these nanocarriers led better PA signals after 24 h in the tumour areas, compared to non-targeted systems. A single hybrid platform that combines chemotherapy and PTT has been realized by Zheng et al. (2013), loading DOX and ICG into PLGA–lecithin–PEG nanoparticles (DINPs). DINPs exhibited high temperature response, rapid DOX release and prolonged retention time in tumour tissue. The combined effects of nanoparticles upon irradiation induced killing cells in DOX-sensitive MCF-7 and DOX-resistant MCF-7/ADR cell lines. In vitro results were confirmed by in vivo studies, which showed the suppression of MCF-7 and MCF-7/ADR tumour growth. Altogether, these hybrid nanocarriers could have a broad clinical impact after further studies on the engineering and pre-clinical valuation in appropriate animal models (Raemdonck et al., 2014).

## 5. INORGANIC PARTICLES

Inorganic nanocarriers, mainly gold, silica (SiO2), iron oxide and calcium phosphate nanoparticles (CPNPs) have been widely employed as fluorophore vectors allowing optical signal improvement. Inorganic matrices for ICG encapsulation can be categorised as $SiO_2$ nanoparticles and CPNPs, which are nontoxic and show good biocompatibility for *in vivo* application. $SiO_2$ has attracted great interest in bioimaging because of its hydrophilic nature and transparency, chemical inertia and ease of surface functionalization (Tu et al., 2015). Moreover, ICG doped $SiO_2$ preserves ICG from photodegradation and photobleaching (Sheng et al., 2013). Mesoporous $SiO_2$ is a mesoporous form of $SiO_2$ introduced in the field of nanomedicine thanks to various advantages. Mesoporous $SiO_2$ nanoparticles (MSN) are chemically and thermally stable nanomaterials with well-defined and controllable morphology and porosity (Lodha et al., 2012). These systems have a large surface area and high pore volume, providing numerous compartmental reservoirs which can be exploited for several functionalities, making MSN a promising tool for various biomedical applications (Taylor et al., 2008). Lee et al. (2009) have proposed MSN modified with trimethylammoniumgroups (MSN-TA) for the entrapment of ICG by electrostatic interactions as an efficient and stable fluorescence contrast agent. This research group was the first to fabricate MSN containing ICG. The co-condensation of tetraethoxysilane (TEOS) with N-trimethoxysilylpropyl-N,N,N-trimethylammonium chloride was employed to prepare these systems. Their efficacy was demonstrated in *in vivo* optical imaging. Furthermore, the nanochannels of MSN provided an immune response decrease as well as protection of ICG molecules from the degradation. Quan et al. (2012) developed newICG doped $SiO_2$ nanoparticles. ICG molecules bound with PEI, a cationic polymer, were incorporated into a $SiO_2$ matrix to obtain $SiO_2$ nanoparticles through the Stöber method (Stöber et al., 1968). In SiO2 nanocarriers self-quenching of fluorescence was reduced because ICG molecules were not able to aggregate thanks to their coupling with PEI. HeLa and HEK293 cells were incubated with three different ICG–PEI doped SiO2 nanoparticles to evaluate the cell viability. Their good biocompatibility was observed while the *in vivo* imaging capability of the systems have been not investigated. However, ICG doped SiO2 nanoparticles exhibited a higher signal through a porcine muscle sample than rhodamine B isothiocyanate doped $SiO_2$ nanoparticles. Taking into account the photostability, success

rates of synthesis and leakages of the dye of different carriers, it was found that ICG–PEI10000 SiO2 nanoparticles were the most appropriate for *in vivo* imaging. Composite systems obtained from the combination of mesoporous silica and GNRs were developed. Liu et al. (2015) fabricated tLyp-1 peptide-functionalized, ICG-containing mesoporous $SiO_2$-coated GNRs which possessed a dual-function as both a tumour cell-targeting NIRF probe and a PTT agent. After the synthesis of GNRs by a seed mediated growth method, the mesoporous $SiO_2$ coating on bare GNRs was achieved by a modified Stöber method. $PEG_{3500}$ was employed asa linker to bind the system with polypeptide (tLyp-1) and ICG was loaded in the mesoporous agent. For PTT, the incubation of MDA-MB-231 cells with these nanoparticles was performed. In addition, the cytotoxicity of PTT was also evaluated by quantification of apoptotic or necrosis tumour cells. Taking into account the data obtained, the authors confirmed that new nanotheranostic agents had the potential to actualize combined diagnosis and PTT treatment in human mammary tumour. ICG-loaded mesoporous $SiO_2$-coated GNRs (ICG-loaded Au@$SiO_2$) were prepared by Luo et al. (2011) for the dual application of fluorescence imaging and X-ray CT. A modified Stöber methodwas used to obtain the coating of the anisotropic GNRs with a $SiO_2$ shell. The efficacy of an ICG-loaded Au@$SiO_2$ as a contrast agentwas tested by intratumoural administration on xenograft mice with gastric cancer. The studies showed for the first time the possibility of combining CT and NIRF using a single nanosized probe, allowing multiple diagnoses, molecular imaging and therapy. Another dual-modality SiO2 vector containing ICG has been proposed by Huang et al. (2011). A self-templated synthetic approach was used to prepare multi-shelled shell-by-shell $SiO_2$ nanospheres. ICG and DOX were encapsulated in a shell-to-shell space. By choosing appropriate pH-dependent molecules, it was found that the structure of multi-shelled $SiO_2$ particles could be used as a multifunctional vector for both drug delivery and imaging. New delivery carriers for ICG, nanoparticle-assembled capsules (NACs), were engineered by Yu et al. (2007), through the combination of an aqueous solution of $SiO_2$ nanoparticles, a phosphate solution and PAH solution. NACs were fabricated via a two-step assembly technique. Polymer chains having a positive charge were combined with anions in order to ionically crosslinked polymer aggregates. Afterwards, $SiO_2$ nanoparticles were combined with preformed aggregates to obtain the NACs. ICG loading within capsules entailed the addition of the dye into the polymer aggregates prior to adding SiO2 nanoparticles inorder

to obtain the shell. Moreover, fibroblasts were used to evaluate the viability of cells exposed to ICG-NACs. After about 30 s of irradiation, ICG-NACs produced heat reaching temperatures higher than 80 °C. The ICG-NACs exhibited several advantages including ease of preparationand high ICG loading without significant leakage of dye. In addition, it was possible to realize targeted PTT thanks to the functionalizable surface. The authors tested ICG-NACs at different concentrations confirming their nontoxicity, making them a promising material for cancer treatment. Sharma et al. (2012) produced small sized ICG-doped $SiO_2$ nanoparticles by using the method of reverse microemulsion. The anionic charges on the dye were manipulated with bivalent cation and aminated silanes in order to encapsulate ICG into $SiO_2$ nanoparticles.

Moreover, paramagnetic gadolinium (Gd) was chelated to ICG-doped $SiO_2$ (Gd-doped ICG–$SiO_2$), imparting a paramagnetic feature to the nanoparticles. *In vitro* and *in vivo* experiments demonstrated the MRI and optical imaging capabilities of the carriers, confirming their possible application in PDT. Recently, ICG-doped SiO2 particles for SLN mapping have been engineered. Tsuchimochi et al. (2013) proposed $SiO_2$ nanoparticles loaded with ICG and technetium-99m (99mTc), coated with polyamidoamine (PAMAM) as a dual imaging system to detect SLN. PAMAM-coated $SiO_2$ nanoparticles showed a mean diameter comprised between 30 and 50 nm. Six male Wistar rats were used for the *in vivo* submucosal administration of the nanoparticle solution into the tongue. The rationale of these systems is that preoperative lymphoscintigraphy can reveal a deeply located SLN, whereas intraoperative NIRF imaging allows visualization during the surgical procedure, following a single injection.

*In vivo* studies demonstrated the potential to reveal SLN during clinical biopsy procedures, clearly identifying them in real time. By virtue of *in vivo* observations, these systems could be proposed as a novel diagnostic and therapeutic platform for targeting metastatic cells. As already mentioned above, in addition to $SiO_2$, calcium phosphate has been suggested as a drug carrier for several applications, thanks to its compatibility, biodegradation and low immune response (He et al., 2000). With the aim of detecting and treating human cancers, bioresorbable CPNPs loadedwith ICG (ICG-CPNPs) were synthesized by Altınoğlu et al. (2008). Spherical CPNPs containing ICG were prepared via a double reverse microemulsion method, involving the coprecipitation of disodium hydrogen phosphate and calcium chloride in the presence of disodium silicate. During the

precipitation process, ICG was added into the microemulsion phase. ICG-CPNPs showed excellent colloidal and optical properties. At the same conditions, the particles exhibited a higher signal compared to the free ICG. In addition, in vivo experiments displayed that PEGylated ICG-CPNPs provided prolonged circulation time in vivo and accumulated in solid xenograft breast adenocarcinoma tumour in a mouse model via a passive effect. The tumour retention persisted for more than 96 h post systematic injection. It has also been possible to reveal a prolonged signal at higher depths compared to the free ICG, confirming the capability of the CPNPs for the detection of solid tumours in diagnostic imaging. Fluorescent calcium phosphosilicate systems were targeted to breast and pancreatic cancer lesions by Barth et al. (2010). In this work, the functionalization of the nanocarriers was realized by using two different coupling strategies. CPNPs were bioconjugated with anti-CD71 antibody, human holotransferrin, and short gastrin peptides in order to target breast cancer and pancreatic cancer, respectively. This study demonstrated that targeting strategies could be realized via two distinct coupling methods, by attaching specific moieties to the CPNPs. For these reasons, developed nanoparticles could be proposed as a theranostic platform in breast and pancreatic cancer tumours, enhancing selective drug delivery and imaging in the single nanoplatform. For this reason, nontoxic and nonaggregating ICG-loaded CPNPs (ICG-CPNPs) have also been suggested as photosensitizers for PDT of leukaemia, despite that it is a tumour not currently treated with this technique (Barth et al., 2011). In the case of non-solid tumours as leukaemia, nanoparticles are not able to accumulate passively via the EPR effect. Bearing in mind this behaviour, a new bioconjugation method was employed to target leukaemia stem cells which express CD117 and CD96 on their surface. ICG-CPNPs showed good optical properties, making them suitable as photosensitizers. A mouse model was used to determine the treatment efficacy of particles against myeloid leukaemia. Targeted ICG CPNPs were found to improve the in vivo efficacy of PDT, decreasing the size of the tumours. Combining different imaging methods such as nuclear, magnetic and NIRF in the same carrier, it could be possible to exploit their specific benefits to enhance diagnosis of diseases. To this end, Ashokan et al. (2013) developed a tri-modal platform based on CPNPs. These particles were loaded with ICG and Gd, and labelled with 99m-Technetiummethylene diphosphonate (99mTc-MDP). In order to protect ICG, an additional coating of PEI was introduced, confining ICG molecules within the amorphous

CPNPs. Several studies were carried out to verify the hemocompatibility of the particles, required for its intravenous administration. *In vivo* imaging confirmed their ability to provide simultaneously NIR, magnetic and nuclear signals. The PEGylation of nanocarriers led to decreased accumulation of particles in the liver after intravenous administration. As already mentioned above, the growing employment of inorganic nanocarriers in medicine led to application of gold systems in tumour diseases in combination with ICG (Luo et al., 2011). Kuo et al. (2012) published a work in which GNRs (Au NRs) and gold nanoparticles (AuNPs) were employed to destroy malignant cells. In order to achieve PDT and PTT, both formulations were conjugated with ICG. In addition to chemical stability, systems conjugated with ICG exhibited good diagnostic properties. Other research groups have proposed gold-base systems containing ICG for future use in cancer theranostics (Bouchard et al., 2014; Luo et al., 2015). Several groups of inorganic nanoparticles have been proposed and examined for the application as contrast agents. Although a few of them have been approved for clinical application, the majority of these formulations are still being tested in vitro or in vivo with animals and the issue concerning potential toxicity will need to be elucidated (Cho et al., 2010). Moreover, the structure of the inorganic nanocarriers is more stable compared to other formulations, such as micelle-based particles, but the presence of a simple functional group on their surface limits a surface functionalization approach (Wu and Zhu, 2015).

## 6. CARBON NANOMATERIALS

Over the last years, carbon based nanosystems have widely been studied as tools for biomedical indications due to their physical and chemical features. The possibility of using carbon nano-sized materials as fluorescent agents is due to their intrinsic optical features and further labeling (Bartelmess et al., 2015). Among many categories of carbon nanomaterials, graphene derivatives and carbon nanotubes are mainly employed in the medical field as drug delivery systems, either as *in vitro* or *in vivo* imaging agents. Graphene represents a promising material for fluorescence imaging and NIR-responsive tumour therapy. In 2014 Chavva et al. reported the fabrication of a magnetic-nanoparticle attached theranostic grapheme oxide (GO) loaded with ICG. These systems were proposed for the targeted capture of prostate cancer circulating tumour cells, accurate diagnosis and therapeutic action on prostate. Experimental data demonstrated that an ICG

containing A9-aptamer-attached theranostic GO is a promising tool for synergistic PTT and PDT of prostate cancer. These theranostic systems could be a potential strategy for real-life applications but the optimization of several parameters are required. Recently, by using electrostatic interaction with ICG, Sharker et al. (2015) have prepared a hybrid NIR-sensitive formulation based on reduced graphene oxide (rGO). These systems, having ICG on a single rGO sheet, exhibited particular features due to quenching effects and pH-dependent relief of poly(2-dimethylamino ethyl methacrylate) [poly(PDMAEMA)], which allowed a specific heat production ability from pH 5.0 to 7.4. This formulation was easily manufactured in aqueous media with sufficient colloidal stability. *In vitro* tests revealed that the hybrid carriers exhibited an enhanced photothermal damage on malignant cells compared to ICG alone. The pH dependent quenching/ relief between the rGO sheet and PDMAEMA in these hybrid nanocomposites represented a barrier between normal cells and malignant tumour cells. As a result, PTT effects showed cytotoxicity on tumour cells but they were relatively inert to normal cells. In vivo studies confirmed the clinical utility of these nanocomposites thanks to specific sensitivity to tumour environments and tumour growth suppression.

rGO has also been utilized by Miao et al. (2015). The authors prepared rGO nanosheets modified with hyaluronic acid (HArGO), suitable for imaging and photothermal therapy of cancer. ICG loading onto both simple rGO (ICG/rGO) and HArGO (ICG/HArGO) notably enhanced the stability of the dye. In this condition, higher intracellular delivery of ICG and cell death in CD44-positive KB cells were provided by HArGO, compared with simple rGO. *In vivo* experiments corroborated that accumulation of ICG/HArGO in KB tumours wasmuch greater than ICG/rGO or ICG alone, following intravenous injection. Local temperatures in tumour areas became suitable to achieve complete tumour ablation. All results indicated that photoresponsive ICG-loaded HArGO nanocarriers were a good candidate for image-guided synergistic PTT. For the first time Nellore et al. (2015) produced a theranostic hybrid platform with magnetic properties based on GO conjugated with an aptamer. The purpose was to perform combined cancer cell detection and antitumoural therapy. The data obtained showed that hybrid graphene could be employed as an agent for specific imaging of human melanoma tumour cells (G361). Moreover, the authors demonstrated that an ICG linked AGE-aptamer attached GO was capable of inducing combined photothermal and photodynamic effects. In

addition to its use as an alternative carrier of therapeutic drugs, the carbon nanotube (CNT) has also received great attention as an optical imaging agent because of its optical properties (Liu et al., 2011). In the literature, a few reports illustrate the use of CNT as an ICG carrier for PA tomography. This innovative modality involves the conversion of light into US waves, following optical absorption of biological samples. The interaction between ICG and a single walled carbon nanotube (SWNT) has been widely studied by Zheng and Zhou (2010). Different spectroscopic techniques including fluorescence and Raman spectroscopy were employed to investigate ICG–SWNT complexes. It was proved that ICG could bind SWNTs without surfactants or covalent approach. Due to the broad absorption spectrum of ICG–SWNT complexes, these formulations were potentially suitable for cancer PTT. On the basis of these results, several research groups focused their attention on nanotubes as a potential tool in the diagnosis and treatment of cancer. Zerda et al. (2010) described a novel CNT system for PA imaging. This platform was obtained by using π–π interactions in order to bind ICG to the surface of the CNTs. Moreover, the contrast agentwas specifically conjugated to target αvβ3 integrins, attaching Arg-Gly-Asp (RGD) peptides to the carrier. The effectiveness of the platform was demonstrated on mice bearing U87MG tumour xenografts. The results proved the ability of this new contrast agent to bind targets, maintaining a very high PA signal. Koo et al. (2012) demonstrated the feasibility of modified SWNTs as a PA contrast agent in SLN and urinary bladder mapping. ICG was conjugated with SWNTs in order to improve the PA sensitivity. In vivo results showed that accumulation of SWNT–ICGs allowed the visualization of the SLN and bladders, distinguishing them from blood vessels. As a consequence, SWNT–ICGs could be a promising tool to monitor vesicoureteral reflux and to detect SLN in breast cancer in combination with PA imaging. Zanganeh et al. (2013) proposed a novel PA contrast agent, obtained from the covalent conjugation between a biscarboxylic acid derivative of ICG and SWNT (ICG/SWNT). In vivo behaviour of the formulation was evaluated in xenograft 4T1 mammary cancer mice. The study was assessed by using the co-registered US and PA imaging system. The signal provided from ICG/SWNT was approximately two times higher compared to free ICG. Due to the size and shape of the nanotubes, the efficacy of ICG/SWNT at the tumour periphery was observed, confirming their potential utility in surgery to assess tumour margins and thus to improve the resection of cancers. Nguyen et al. (2015) revealed the

PA properties of SWNT–ICG for bladder cancer identification. With the aim of obtaining improved contrast and high resolution, PA signals were examined at various concentrations of SWNT–ICG. PA imaging was assessed to visualize the retention of SWNT–ICG in bladder tissue, corroborating the great relevance of the carbon particles in tumour detection. Taking into account their nontoxicity and good PA signals SWNT–ICG could be a useful system for helping in the detection of tissue cancer by PA imaging. Other studies will be carried out to target the monitoring of theranostic applications. In addition to the reports concerning graphene and carbon tubes as components of the carbon group, few works reported surface modification of carbon spheres to obtain a multifunctional platform for cancer imaging and treatment. A novel multifunctional nanoplatform has been engineered by Li et al. (2015). The carrier consisted of carbon nanospheres (CSs) having a polydopamine (PDA) shell as coating. Furthermore, the nanoparticles were functionalized with folic acid (FA). ICG was loaded into the systems through hydrophobic and π–π interactions in order to obtain CSs@PDA-FA@ICG nanocomposites (NCs). These nanocarriers displayed targeted and specific switch-control properties, consisting in high selectivity performed by FA targeting and an activable fluorescent property from "OFF" to "ON", respectively. In addition, a good photoconversion was induced by CSs@PDA-FA@ICG NCs for combined PTT and PDT compared to free ICG. The results confirmed that CSs@PDA-FA@ICG NCs could open new prospects to improve diagnosis and treatment of cancer. Overall, carbon-based carriers are promising ICG vehicles for the detection and treatment of several tumours (Liu et al., 2011). The main limitation in clinical application concerns the potential toxicity of carbon nanostructures because recent studies showed controversial results. Many reports declared the safety of functionalized carbon nanotubes and graphene-based nanosystems, but in vivo studies are assessed in animal models which are different from humans.

## 7. BIOCONJUGATES

### 7.1. Antibody–drug conjugates

ICG is attractive to researchers for the development of platform targeted optical imaging by modification of its structure and conjugation to mAbs or their fragments, producing new systems for cancer diagnosis and treatment. The introduction of active groups on the

ICG molecule is quite difficult because of its symmetrical organization. Recently, some derivatives of ICG have been synthetized. Among them, ICG-N hydroxysulfosuccinimide ester (ICG-sulfo-OSu or ICG-sOSu) is widely used for conjugation with an antibody. An important drawback of mAbs is their prolonged clearance. Consequently, the target-to-background ratio is limited. For this reason, in several works, mAbs have been exposed to enzymatic or genetic modifications in order to develop antigen binding, diabody, minibody, and variable region fragments. However, the tumour uptake is compromised when the fragments are very small because they will be subjected to a fast clearance (Wu and Olafsen, 2008). As previously mentioned, the use of ICG alone for imaging shows some limitations such as loss of fluorescence intensity after the binding of ICG with blood proteins. Nevertheless, this drawback could be overcome using an activatable NIR probe. To this end, Ogawa et al. (2009) reported ICG-sulfo-OSu conjugation to themAbs panitumumab (Pan), Tra and daclizumab (Dac), developing a smart agent which optically "switches on" just in target cells. Indeed, ICG dissociated from its mAb after cell internalization. It was previously proved that these conjugates had very low fluorescence in an aqueous solution. On the contrary, fluorescent intensity increased rapidly by using 2-mercaptoethanol and SDS that released the dye fromthe protein. In vitro studies confirmed activation of the conjugates within the target cells. Animal experiments were carried out in mice with CD25-expressing tumours and HER1 andHER2- overexpressing tumours. The results showed specific imaging-detection of these cancers by the above mentioned formulations. Pan and Tra have been widely employed by other authors for the conjugation with NIR fluorophores. For example, Sano et al. (2012) described the use of two activatable fluorescent probes including Tra-ICG. The systems were evaluated in vitro on cells and in in vivo using an orthotopic mouse model of breast cancer. Sano et al. (2015) evaluated the effectiveness of a PA imaging probe (Pan-EG4-ICG) composed of Pan which is EGFR mAb, marked with an ICG derivative (ICG-EG4-Sulfo-OSu). The Pan-EG4-ICG ability to produce great PA signals in EGFR-positive cells was proved by *in vitro* PA imaging studies. A431 tumour (EGFR positive)-bearing mice were used as animal models to investigate the biodistribution of labelled Pan-EG4-ICG. The authors observed high tumour retention 7 days after administration of Pan-EG4-ICG. Moreover, Pan-EG4-ICG enhanced PA signal in the tumour by 114% at 7th day post-injection compared to preinjection and allowed a clear visualization of EGFR-positive tumours

inoculated in the mammary glands in a breast cancer mouse model. PA signals in the cancer tissues were importantly blocked by co-treatment with a surplus of unconjugated Pan, proving that PA signals partly derived from the Pan-EG4-ICG linked to EGFR expressed in the cancer cells. The results suggested that the ICGlabelled mAb is able to improve a target-specific PA signal, allowing the discrimination of malignant tumours. Nevertheless, the injected dose should be enhanced prior to its application in future clinical trials. Unfortunately, during the fabrication of mAb-ICG conjugates, some ICG molecules are noncovalently bound to the mAb, producing remarkable nonspecific background signals. Indeed, mAb slowly releases this amount of free ICG into the blood. In order to overcome this drawback, different strategies have been proposed to improve the target to background ratio. Sano et al. (2013) demonstrated that the insertion of a linker, such as PEG, between ICG and Sulfo-OSuccinimidyl moiety formed new formulations with more covalent linkage between ICG and mAb. These systems were conjugated to mAb Pan and tested in tumour-bearingmice (MDAMB-468 and 3T3/HER2). The newmAb conjugates showed better target-to-background ratios than conventional ones. Afterwards, Watanabe et al. (2014) conjugated the ICG-sulfo-OSu with two different PEG linkers to an antiprostate specific membrane antigen (PSMA) minibody. These systems visualized PSMA sensitive cancers earlier than conjugates made with mAbs. Furthermore, the authors corroborated that the insertion of PEG linkers in ICG derivatives (ICG-PEG4-Sulfo-OSu and ICG-PEG8-Sulfo-OSu) resulted in the improvement of tumour-to-background ratios in xenografted mice. By virtue of these results, evenminibody-ICG conjugates can be considered an efficient activatable optical probe. PSMA has also been used as target by Nakajima et al. (2011) who developed an activatable mAb fluorophore conjugate starting from ICG-sulfo-OSu and using J591 (a humanized PSMA-specific mAb) and Tra as antibodies. In vivo studies were carried out on mice xenografted with PSMA expressing and non-expressing prostate cancer. Moreover, a comparison with Tra-ICG conjugated which specifically interacts with HER2 expressing tumours was performed. Although this nanosystem required 2 days to be uptaken by the cancer tissue, the activatable antibody was capable of detecting PSMA+ tumours showing a higher fluorescent signal compared to PSMA-tumours for at least 10 days after injection. This result suggested a potential use of the agent prior to a surgical operation. Moreover, activatable J591-ICG is a promising system for the detection of

primary and metastatic PSMA+ prostate tumour and could be employed to perform biopsies and prostatectomies in tumour diseases. Zhou et al. (2014) investigated chemical and biological properties of an ICGsOSu-labelled mAb, Pan. This report provided for the first time a detailed procedure of purification of covalently bound ICG conjugation products. In addition, characterization and application of an ICGsOSuconjugated mAb were investigated. Analysis of the conjugation reaction between an ICG-sOSu dye and Pan revealed the presence of numerous aggregates but they can be removed by purification techniques. The HPLC-purified ICG-sOSu-Pan products were analyzed by native and SDS polyacrylamide gel electrophoresis followed by optical imaging. The results demonstrated that the interaction between ICG-sOSu and Pan was related to both covalent and noncovalent binding of the ICGsOSu to the protein. In addition, a purification step was performed by ethyl acetate extraction, to abrogate noncovalently bound ICG-sOSu prior to in vivo optical imaging studies. The doubly purified bioconjugate exhibited preservation of immunoreactivity and an excellent targetspecific uptakewith lowliver accumulation in athymic nude mice bearing HER1-expressing tumour xenografts. In conclusion, antibody-ICG conjugates could be readily accepted by clinicians thanks to several advantages over other imaging probes. First, these systems are generally quenched, but are activatedwhen cell internalization occurs. Moreover, their components show a good toxicity profile. The FDA already approves ICG and some therapeutic mAbs such as Pan and even PEG has been widely used in clinical products owing to its biocompatibility. These conjugates are promising agents for human clinical use even if more safety studies will be necessary.

### 7.2. HSA-drug conjugates

Sheng et al. (2014) developed HSA-ICG nanoparticles (HSA-ICG NPs). The NPs were obtained via intermolecular disulphide conjugations. The cell uptake behaviour of free ICG and HSA-ICG NPswas investigated through confocal microscopy. The majority of HSA-ICG NPs was uptaken by 4T1 breast cancer cells. On the contrary, a low fluorescent signal was revealed when the HSA-ICG NPs were incubated with normal cells (293T human kidney cells) under the same conditions. Furthermore, the authors demonstrated that the simultaneous PDT/PTT treatment induced more 4T1 cell late apoptosis/necrosis (94.4%) as compared with single PDT (49.3%) or PTT (71.9%). On the basis of the

encouraging result, athymic nude mice with subcutaneous 4T1 breast cancer xenografts were used for in vivo experiments, which confirmed synergistic phototherapeutic efficacy of the formulation. For all these reasons, HSA-ICG NPs could become a theranostic tool for tumour imaging and its margin detection, and for synergistic PDT/PTT.

## 8. OTHER FORMULATIONS

Apart from the widely studied formulations classified above, ICG has been loaded in several other formulations such as hydrogels, nanoemulsions and other systems for diagnosis and therapy of cancers. Salis et al. (2015) proposed in situ gelling thermosensitive chitosan/ glycerophosphate (C/GP) solutions, loaded with ICG, for transartherial embolization and following intraoperative fluorescence imaging of HCC. In order to evaluate the efficacy of these formulations in vitro and *ex vivo* studies were performed. The results demonstrated the capability of solutions to gel in situ.Moreover, the release of ICG fromthe analysed hydrogels was very low, probably due to an electrostatic interaction between chitosan and ICG. *Ex vivo* studies showed the potential of these in situ gelled C/GP formulations to stay in the injection site for a long period as it is required for this kind of therapy (Giunchedi et al., 2013a, b). Considering the data obtained, the system is suitable for local therapy of HCC as an embolic agent, stopping the growth of the tumour and for intraoperative fluorescence imaging thanks to ICG, which could help the following detection of the cancer during surgery. ICG-loaded nanoemulsions showed great promise as a theranostic carrier for both diagnosis and PDT/PTT of lymph node metastasis in cancer patients. Lee et al. (2015) entrapped a cationic lipid stearylamine (SA) with ICG in the shell of a nanoemulsion. The rationale of this work was to improve the cellular uptake of nanoemulsions by changing the surface charge to a positive value, since an ICG-loaded nanoemulsion exhibited a negative surface charge. Loading ICG into SA-incorporated nanoemulsions blocked the aggregation and degradation of ICG compared to loading ICG in SA-free nanoemulsions. SA incorporation also enhanced the tumour cell uptake of the system, resulting in better cell killing upon light irradiation. The positive effects of SA incorporation was also studied *in vivo*, evaluating the nanoemulsion uptake from the popliteal lymph node, after subcutaneous administration into the footpad of a mice model. All results proved that SA-incorporated nanoemulsions were good candidates for combined diagnosis and therapy

of lymph node metastases. A new carrier for contrast agents was proposed by Bae et al. (2014), who developed the multifunctional perfluorocarbon (PFC)/ICG nanoemulsions. The film hydration method followed by microfluidisation was used to formulate PFC/ICG nanoemulsions. These formulations improved ICG properties. The chemical stabilization of the dye into PFC/ICG nanoemulsions was achieved by the interaction of ICG molecules, which reduced the formation of aggregates. Moreover, loading dye into nanoemulsions increased its stability compared to aqueous ICG. HeLa, Raw, or DC2.4 cells were employed in order to measure the MR and NIRF signals and to evaluate nanoemulsion toxicity. In addition, the PFC/ICG bimodal formulation was injected in a mouse model into the footpad of a leg. It was found that PFC/ICG nanoemulsions allowed excellent and prolonged in vivo detection of lymph nodes through 19F-MR imaging and optical imaging. In order to prevent both the decrease of fluorescent signal and the diffusion of free dye, the incision of SLN should be carried out within about 30 min. Similarly, Wang et al. (2013) prepared an oil-in-water ICG-loaded perfluoro-1.5-crown-5-ether (ICG/PFCE) nanoemulsion using Lutrol® F68 as a surfactant. The multifunctional theranostic formulation enabled both bimodal imaging and PDT/PTT of tumour cells. ICG was loaded in the nanoemulsion droplets, with an encapsulation efficiency of 74%. The effectiveness of ICG/PFCE nanoemulsions was evaluated in vitro, confirming the biocompatibility of the dual imaging agent. Moreover, upon light irradiation, necrotic cell death of U87MG glioblastoma cells incubated with ICG/PFCE nanoemulsions occurred, confirming the therapeutic effect of the system. Even peptosomes have been proposed as molecular imaging agents. Tanisaka et al. (2007) prepared vesicular peptosomes (100 nm), obtained by assembling amphiphilic polypeptides. In this study, the authors synthetized block amphiphilic copolypeptides using poly(sarcosine) (PSar) as a hydrophilic block and poly(γ-methyl-L-glutamate) (PMLG) as a hydrophobic portion. The authors chose GA-PSar56-PMLG12 and a mixture of GA-PSar43- PMLG18 and GA-PSar65-PMLG18 (1:1) to prepare peptosomes designed for *in vivo* studies, assessed by injecting ICG-labelled peptosomes in the tail vein of rats. Although peptosomes were partly cleared, the greatest part exhibited a relatively long half-life time. These carriers were compared with peptide micelles prepared with GA-PSar93- PMLG12. The distribution was detected using an optical imaging system and it was found that all ICG loaded systems accumulated in the tumour

tissue by the EPR effect. Furthermore, peptosomes produced better imaging contrast than peptide micelles. Recently, ICG has also been encapsulated into microsystems. With the aim of achieving structural and functional imaging of tumour, Xu et al. (2009) proposed novel ICG-loaded microbubbles as a dualmodal contrast agent. The system was prepared through a modified double emulsion technique, by loading ICG in PLGA microbubbles. The PLGA loading efficaciously preserved ICG fromaggregation and interaction with proteins, leading to better characteristics for quantitative imaging applications. These microbubbles were proposed for the visualization of peritumoural vasculature. Indeed, the injection of microbubbles might act to enhance the ultrasound contrast. Nevertheless, other experiments are required to confirm the efficacy of the system. Useful results about the optimization of microbubbles and their conjugation with ligands to target specific biomarkers have not been published yet. Recently, the improvement of ICG properties due to its loading into cerasome has been demonstrated. Jing et al. (2015) fabricated a theranostic cerasome encapsulating ICG by incorporating 1.2- distearoyl-sn-glycero-3-phosphoethanolamine- N- [carboxy(polyethylene glycol)2000]- 1,4,7,10-tetraazacyclododecane-1,4,7,10-tetraacetic acid monoamide ($DSPEPEG_{2000}$-DOTA) (ICG@DPDCs), followed by chelating the radioisotope of $^{177}Lu$ (ICG@DPDCs-$^{177}Lu$), an attractive agent for theranostic applications. The authors showed that the cerasome could be an efficient agent in optical and nuclear imaging. ICG@DPDCs accumulated at the tumour site into Lewis lung carcinoma tumour bearing mice after intravenous injection, causing the photothermal ablation of tumour by using one-time NIR irradiation. In addition, the strategy of labelling cerasomes with radionuclide $^{177}Lu$ enabled these systems to be used for radionuclide cancer therapy and even for the combined therapy with ICG. All results ensured that ICG@DPDCs could be a safe agent for medical application.

## 9. CONCLUSION

In summary, we have discussed current ICG delivery approaches used for the application in cancer diagnosis and treatment. The papers reviewed demonstrate that the various drug delivery systems are suitable for enhancing ICG chemical stability and extending its half-life. As a non-specific contrast agent, one of the major challenges in the employment of free ICG regards its selective delivery and accumulation in the tumour tissue. Its

incorporation into delivery systems allows better performance in cancer detection and therapy. ICG formulations exhibited a good potential for several applications including the detection of the tumour margin, SLN mapping, and photothermal and photodynamic effects. Taking into account the evolution of nanomedicine in the past years, most of the formulations discussed concern nanosystems. Apart from their composition, ICG-loaded nanocarriers enhance accumulation of the dye in cancer, due to the EPR effect and active targeting, allowing selective diagnosis or treatment. Furthermore, some reviewed nanosystems showed the capability of combining a dual effect in the same platform. Even the other formulations such as microbubbles and hydrogels are suitable agents for these matters. In conclusion, developing ICG platforms could be proposed as a novel tool for image-guided and antitumoural therapy, but so far not one of these systems is under investigation for clinical trials. Indeed, the progress in this field has focused especially on academic research and their regulatory approval is clearly far away. Regardless of the kind of system, indeed few information about biodistribution, in vivo interactions and toxicity are available. Therefore, although many works concerning ICG-loading carriers have been published in the last years and encouraging results have been obtained, further studies are necessary in order to extend their use for human clinical applications.

**References**

Abels, C., 2004. Targeting of the vascular system of solid tumours by photodynamic therapy (PDT). *Photochem. Photobiol. Sci*. 3, 765–771.

Akbarzadeh, A., Rezaei-Sadabady, R., Davaran, S., Joo, S.W., Zarghami, N., Hanifehpour, Y., et al., 2013. Liposome: classification, preparation, and applications. *Nanoscale Res. Lett*. 8, 102.

Alander, J.T., Kaartinen, I., Laakso, A., Pätilä, T., Spillmann, T., Tuchin, V.V., et al., 2012. A review of indocyanine green fluorescent imaging in surgery. *Int. J. Biomed. Imaging* 2012, 1–26.

Altınoğlu, E.I., Russin, T.J., Kaiser, J.M., Barth, B.M., Eklund, P.C., Kester, M., et al., 2008. Near-infrared emitting fluorophore-doped calcium phosphate nanoparticles for in vivo imaging of human breast cancer. *ACS Nano* 2, 2075–2084.

Ashokan, A., Gowd, G.S., Somasundaram, V.H., Bhupathi, A., Peethambaran, R., Unni, A.K.K., et al., 2013. Multifunctional calcium phosphate nano-contrast agent for combined nuclear, magnetic and near-infrared in vivo imaging. *Biomaterials* 34, 7143–7157.

Bae, P.K., Jung, J., Chung, B.H., 2014. Highly enhanced optical properties of indocyanine green/perfluorocarbon nanoemulsions for efficient lymph node mapping using near-infrared and magnetic resonance imaging. *Nano Converg*. 1, 1–10.

Bahmani, B., Guerrero, Y., Bacon, D., Kundra, V., Vullev, V.I., Anvari, B., 2014. Functionalized polymeric nanoparticles loaded with indocyanine green as theranostic materials for targeted molecular near infrared fluorescence imaging and photothermal destruction of ovarian cancer cells. *Lasers Surg. Med*. 46, 582–592.

Bahmani, B., Lytle, C.Y., Walker, A.M., Gupta, S., Vullev, V.I., Anvari, B., 2013. Effects of nanoencapsulation and PEGylation on biodistribution of indocyanine green in healthy mice: quantitative fluorescence imaging and analysis of organs. *Int. J. Nanomedicine* 8, 1609–1620.

Bao, C., Beziere, N., del Pino, P., Pelaz, B., Estrada,G., Tian, F., et al., 2013. Gold nanoprisms as optoacoustic signal nanoamplifiers for in vivo bioimaging of gastrointestinal cancers. *Small* 9, 68–74.

Bartelmess, J., Quinn, S.J., Giordani, S., 2015. Carbon nanomaterials: multi-functional agents for biomedical fluorescence and Raman imaging. *Chem. Soc. Rev*. 44, 4672–4698.

Barth, B.M., Altinoğlu, E.I., Shanmugavelandy, S.S., Kaiser, J.M., Crespo-Gonzalez, D., Di Vittore, N.A., et al., 2011. Targeted indocyanine-green-loaded calciumphosphosilicate nanoparticles for in vivo photodynamic therapy of leukemia. *ACS Nano* 5, 5325–5337.

Barth, B.M., Sharma, R., Altınoğlu, E.I., Morgan, T.T., Shanmugavelandy, S.S., Kaiser, J.M., et al., 2010. Bioconjugation of calcium phosphosilicate composite nanoparticles for selectivetargeting of human breast and pancreatic cancers in vivo. *ACS Nano* 4, 1279–1287.

Bäumler, W., Abels, C., Karrer, S., Weiss, T., Messmann, H., Landthaler, M., et al., 1999. Photo-oxidative killing of human colonic cancer cells using indocyanine green and infrared light. *Br. J. Cancer* 80, 360–363.

Betz, C.S., Zhorzel, S., Schachenmayr, H., Stepp, H., Havel, M., Siedek, V., et al., 2009. Endoscopic measurements of free-flap perfusion in the head and neck region using red excited indocyanine green: preliminary results. *J. Plast. Reconstr. Aesthet. Surg*. 62, 1602–1608.

Beziere, N., Lozano, N., Nunes, A., Salichs, J., Queiros, D., Kostarelos, K., et al., 2015. Dynamic imaging of PEGylated indocyanine green (ICG) liposomes within the tumor microenvironment using multi-spectral optoacoustic tomography (MSOT). *Biomaterials* 37, 415–424.

Boni, L., David, G., Mangano, A., Dionigi, G., Rausei, S., Spampatti, S., et al., 2015. Clinical applications of indocyanine green (ICG) enhanced fluorescence in laparoscopic surgery. *Surg. Endosc*. 29, 2046–2055.

Bouchard, R., Wolfe, T., Thornton, M., Morgan, T., Mitcham, T., Bhattarai, S., et al., 2014. Three-dimensional in vivo photoacoustic tracking of targeted nanoparticles in a pancreatic cancer model. *Cancer Res*. 74, 2051.

Bozzuto, G., Molinari, A., 2015. Liposomes as nanomedical devices. I*nt. J. Nanomedicine* 10, 975–999.

Brouwer, O.R., Buckle, T., Vermeeren, L., Klop,W.M.C., Balm, A.J., van der Poel, H.G., et al., 2012. Comparing the hybrid fluorescent–radioactive tracer indocyanine green–99mTc-nanocolloid with 99mTc-nanocolloid for sentinel node identification: a validation study using lymphoscintigraphy and SPECT/CT. *J. Nucl. Med.* 53, 1034–1040.

Caesar, J., Shaldon, S., Chiandussi, L., Guevara, L., Sherlock, S., 1961. The use of indocyanine green in the measurement of hepatic blood flow and as a test of hepatic function. *Clin. Sci*. 21, 43–57.

Cahill, R.A., Anderson, M., Wang, L.M., Lindsey, I., Cunningham, C., Mortensen, N.J., 2012. Near-infrared (NIR) laparoscopy for intraoperative lymphatic road-mapping and sentinel node identification during definitive surgical resection of early-stage colorectal neoplasia. *Surg. Endosc*. 26 197-4.

Chavva, S.R., Pramanik, A., Nellore, B.P.V., Sinha, S.S., Yust, B., Kanchanapally, R., et al., 2014. Theranostic graphene oxide for prostate cancer detection and treatment. *Part. Part. Syst. Charact.* 31, 1252–1259.

Chen, R., Wang, X., Yao, X., Zheng, X., Wang, J., Jiang, X., 2013. Near-IR-triggered photothermal/photodynamic dual-modality therapy system via chitosan hybrid nanospheres. *Biomaterials* 34, 8314–8322.

Cho, E.C., Glaus, C., Chen, J., Welch, M.J., Xia, Y., 2010. Inorganic nanoparticle-based contrast agents for molecular imaging. *Trends Mol. Med*. 16, 561–573.

Costa, R.A., Farah, M.E., Freymüller, E., Morales, P.H., Smith, R., Cardillo, J.A., 2001. Choriocapillaris photodynamic therapy using indocyanine green. *Am J. Ophthalmol.* 132, 557–565.

Crane, L.M., Themelis, G., Pleijhuis, R.G., Harlaar, N.J., Sarantopoulos, A., Arts, H.J., et al., 2011. Intraoperative multispectral fluorescence imaging for the detection of the sentinel lymph node in cervical cancer: a novel concept. *Mol. Imaging Biol*. 13, 1043–1049.

Desai, N.D., Miwa, S., Kodama, D., Koyama, T., Cohen, G., Pelletier, M.P., et al., 2006. A randomized comparison of intraoperative indocyanine green angiography and transittime flow measurement to detect technical errors in coronary bypass grafts. *J. Thorac. Cardiovasc. Surg*. 132, 585–594.

Desmettre, T., Devoisselle, J.M., Mordon, S., 2000. Fluorescence properties and metabolic features of indocyanine green (ICG) as related to angiography. *Surv. Ophthalmol*. 45, 15–27.

Destro, M., Puliafito, C.A., 1989. Indocyanine green videoangiography of choroidal neovascularization. *Ophthalmology* 96, 846–853.

Dip, F.D., Roy, M., Perrins, S., Ganga, R.R., Menzo, E.L., Szomstein, S., et al., 2015. Technical description and feasibility of laparoscopic adrenal contouring using fluorescence imaging. *Surg. Endosc.* 29, 569–574.

Dorshow, R.B., Bugaj, J.E., Burleigh, B.D., Duncan, J.R., Johnson, M.A., Jones, W.B., 1998. Noninvasive fluorescence detection of hepatic and renal function. *J. Biomed. Opt.* 3, 340–345.

Dougherty, T.J., Gomer, C.J., Henderson, B.W., Jori, G., Kessel, D., Korbelik, M., et al., 1998. Photodynamic therapy. *J. Natl. Cancer Inst.* 90, 889–905.

El-Daly, S.M., Gamal-Eldeen, A.M., Abo-Zeid, M.A., Borai, I.H., Wafay, H.A., Abdel-Ghaffar, A.R.B., 2013. Photodynamic therapeutic activity of indocyanine green entrapped in polymeric nanoparticles. *Photodiagn. Photodyn. Ther*. 10, 173–185.

Engel, E., Schraml, R., Maisch, T., Kobuch, K., König, B., Szeimies, R.M., et al., 2008. Light induced decomposition of indocyanine green. *Invest. Ophthalmol. Vis. Sci.* 49, 1777–1783.

Escobedo, J.O., Rusin, O., Lim, S., Strongin, R.M., 2010. NIR dyes for bioimaging applications. *Curr. Opin. Chem. Biol*. 14, 64–70.

Fischer, T., Ebert, B., Voigt, J., Macdonald, R., Schneider, U., Thomas, A., et al., 2010. Detection of rheumatoid arthritis using non-specific contrast enhanced fluorescence imaging. *Acad. Radiol*. 17, 375–381.

Flower, R., Hochheimer, B., 1976. Indocyanine green dye fluorescence and infrared absorption choroidal angiography performed simultaneously with fluorescein angiography. *Johns Hopkins Med. J*. 138, 33–42.

Fourman, M.S., Phillips, B.T., Fritz, J.R., Conkling, N., McClain, S.A., Simon, M., et al., 2014. Laser-assisted indocyanine green dye angiography accurately predicts the split thickness graft timing of integra artificial dermis. *Ann. Plast. Surg*. 73, 150–155.

Fox, I., Brooker, G., Heseltine, D., Essex, H., Wood, E., 1956. New dyes for continuous recording of dilution curves in whole blood independent of variations in blood oxygen saturation. *Am. J. Phys*. 187, 599–606.

Funayama, T., Sakane, M., Abe, T., Hara, I., Ozeki, E., Ochiai, N., 2012. Intraoperative nearinfrared fluorescence imaging with novel indocyanine green-loaded nanocarrier for spinal metastasis: a preliminary animal study. *Open Biomed. Eng*. J. 6, 80–84.

Gamal-Eldeen, A.M., El-Daly, S.M., Borai, I.H., Wafay, H.A., Abdel-Ghaffar, A.R.B., 2013.

Photodynamic therapeutic effect of indocyanine green entrapped in polymeric nanoparticles and their anti-EGFR-conjugate in skin cancer in CD1 mice. *Photodiagn. Photodyn. Ther*. 10, 446–459.

Gilmore, D.M., Khullar, O.V., Gioux, S., Stockdale, A., Frangioni, J.V., Colson, Y.L., et al., 2013. Effective low-dose escalation of indocyanine green for near-infrared fluorescent sentinel lymph node mapping in melanoma. *Ann. Surg. Oncol*. 20, 2357–2363.

Giunchedi, P., Maestri, M., Gavini, E., Dionigi, P., Rassu, G., 2013a. Transarterial chemoembolization of hepatocellular carcinoma, agents and drugs: an overview. Part 1. *Expert Opin. Drug Deliv*. 10, 679–690.

Giunchedi, P., Maestri, M., Gavini, E., Dionigi, P., Rassu, G., 2013b. Transarterial chemoembolization of hepatocellular carcinoma, agents and drugs: an overview Part 2. *Expert Opin. Drug Deliv.* 10, 799–810.

Gomes, A.J., Lunardi, L.O., Marchetti, J.M., Lunardi, C.N., Tedesco, A.C., 2006. Indocyanine green nanoparticles useful for photomedicine. *Photomed. Laser Surg*. 24, 514–521.

Guo, Z., Park, S., Yoon, J., Shin, I., 2014. Recent progress in the development of nearinfrared fluorescent probes for bioimaging applications. *Chem. Soc. Rev*. 43, 16–29.

Habazettl, H., Athanasopoulos, D., Kuebler,W.M.,Wagner, H., Roussos, C.,Wagner, P.D., et al., 2010. Near-infrared spectroscopy and indocyanine green derived blood flow index for noninvasive measurement of muscle perfusion during exercise. *J. Appl. Physiol.* 108, 962–967.

Hadinoto, K., Sundaresan, A., Cheow,W.S., 2013. Lipid–polymer hybrid nanoparticles as a new generation therapeutic delivery platform: a review. *Eur. J. Pharm. Biopharm.* 85, 427–443.

Hagen, A., Grosenick, D., Macdonald, R., Rinneberg, H., Burock, S.,Warnick, P., et al., 2009. Late-fluorescence mammography assesses tumor capillary permeability and differentiates malignant from benign lesions. *Opt. Express* 17, 17016–17033.

Halle, B.M., Poulsen, T.D., Pedersen, H.P., 2014. Indocyanine green plasma disappearance rate as dynamic liver function test in critically ill patients. *Acta Anaesthesiol. Scand*. 58, 1214–1219.

Handgraaf, H.J., Boogerd, L.S., Verbeek, F.P., Tummers, Q.R., Hardwick, J.C., Baeten, C.I., et al., 2015. Intraoperative fluorescence imaging to localize tumors and sentinel lymph nodes in rectal cancer. *Minim. Invasive Ther*. Allied Technol. 1–6.

Hao, Y., Wang, L., Zhao, Y., Meng, D., Li, D., Li, H., et al., 2015. Targeted imaging and chemophototherapy of brain cancer by a multifunctional drug delivery system. *Macromol. Biosci*. http://dx.doi.org/10.1002/mabi.201500091.

He, Q., Mitchell, A.R., Johnson, S.L., Wagner-Bartak, C., Morcol, T., Bell, S.J., 2000. Calcium phosphate nanoparticle adjuvant. *Clin. Diagn. Lab. Immunol*. 7, 899–903.

Herzog, E., Taruttis, A., Beziere, N., Lutich, A.A., Razansky, D., Ntziachristos, V., 2012. Optical imaging of cancer heterogeneity with multispectral optoacoustic tomography. *Radiology* 263, 461–468.

Hill, T.K., Abdulahad, A., Kelkar, S.S., Marini, F.C., Long, T.E., Provenzale, J.M., et al., 2015. Indocyanine green-loaded nanoparticles for image-guided tumor surgery. *Bioconjug. Chem.* 26, 294–303.

Hirche, C., Dresel, S., Krempien, R., Hünerbein, M., 2011. Sentinel node biopsy by indocyanine green retention fluorescence detection for inguinal lymph node staging of anal cancer: preliminary experience. *Ann. Surg. Oncol*. 18, 2357–2362.

Hirche, C., Mohr, Z., Kneif, S., Doniga, S., Murawa, D., Strik, M., et al., 2012. Ultrastaging of colon cancer by sentinel node biopsy using fluorescence navigation with indocyanine green. *Int. J. Color. Dis*. 27, 319–324.

Holloway, R.W., Bravo, R.A.M., Rakowski, J.A., James, J.A., Jeppson, C.N., Ingersoll, S.B., et al., 2012. Detection of sentinel lymph nodes in patients with endometrial cancer undergoing robotic-assisted staging: a comparison of colorimetric and fluorescence imaging. *Gynecol. Oncol*. 126, 25–29.

Holt, D., Okusanya, O., Judy, R., Venegas, O., Jiang, J., DeJesus, E., et al., 2014. Intraoperative near-infrared imaging can distinguish cancer from normal tissue but not inflammation. *PLoS One* 9, e103342.

Huang, C.C., Huang,W., Yeh, C.S., 2011. Shell-by-shell synthesis ofmulti-shelled mesoporous silica nanospheres for optical imaging and drug delivery. *Biomaterials* 32, 556–564.

Hutteman, M., Choi, H.S., Mieog, J.S.D., van der Vorst, J.R., Ashitate, Y., Kuppen, P.J., et al., 2011. Clinical translation of ex vivo sentinel lymph node mapping for colorectal cancer using invisible near-infrared fluorescence light. *Ann. Surg. Oncol*. 18, 1006–1014.

Hutteman, M., Van Der Vorst, J.R., Gaarenstroom, K.N., Peters, A.A., Mieog, J.S.D., Schaafsma, B.E., et al., 2012. Optimization of near-infrared fluorescent sentinel lymph node mapping for vulvar cancer. *Am. J. Obstet. Gynecol*. 206, e1–e5.

Hwang, S.W., Malek, A.M., Schapiro, R., Wu, J.K., 2010. Intraoperative use of indocyanine green fluorescence videography for resection of a spinal cord hemangioblastoma. *Neurosurgery* 67, 300–303.

Ishizawa, T., Fukushima, N., Shibahara, J.,Masuda, K., Tamura, S., Aoki, T., et al., 2009. Real time identification of liver cancers by using indocyanine green fluorescent imaging. *Cancer* 115, 2491–2504.

Ishizawa, T., Bandai, Y., Ijichi, M., Kaneko, J., Hasegawa, K., Kokudo, N., 2010. Fluorescent cholangiography illuminating the biliary tree during laparoscopic cholecystectomy. *Br. J. Surg.* 97, 1369–1377.

Ishizawa, T., Masuda, K., Urano, Y., Kawaguchi, Y., Satou, S., Kaneko, J., et al., 2014. Mechanistic background and clinical applications of indocyanine green fluorescence imaging of hepatocellular carcinoma. *Ann. Surg. Oncol*. 21, 440–448.

Jeong, H.S., Lee, C.M., Cheong, S.J., Kim, E.M., Hwang, H., Na, K.S., et al., 2013. The effect of mannosylation of liposome-encapsulated indocyanine green on imaging of sentinel lymph node. *J. Liposome Res*. 23, 291–297.

Jewell, E.L., Huang, J.J., Abu-Rustum, N.R., Gardner, G.J., Brown, C.L., Sonoda, Y., et al., 2014. Detection of sentinel lymph nodes in minimally invasive surgery using indocyanine green and near-infrared fluorescence imaging for uterine and cervical malignancies. *Gynecol. Oncol*. 133, 274–277.

Jheng, P.R., Lu, K.Y., Yu, S.H., Mi, F.L., 2015. Free DOX and chitosan-N-arginine conjugate stabilized indocyanine green nanoparticles for combined chemophotothermal therapy. *Colloids Surf. B: Biointerfaces* 136, 402–412.

Jian, W.H., Yu, T.W., Chen, C.J., Huang, W.C., Chiu, H.C., Chiang, W.H., 2015. Indocyanine green-encapsulated hybrid polymeric nano-micelles for photothermal cancer therapy. *Langmuir* 31, 6202–6210.

Jing, L., Shi, J., Fan, D., Li, Y., Liu, R., Dai, Z., et al., 2015. 177Lu-labeled cerasomes encapsulating indocyanine green for cancer theranostics. *ACS Appl. Mater. Interfaces* 7, 22095–22105.

Jones, M.C., Leroux, J.C., 1999. Polymeric micelles — a new generation of colloidal drug carriers. *Eur. J. Pharm. Biopharm*. 48, 101–111.

Kamolz, L.P., Andel, H., Auer, T., Meissl, G., Frey, M., 2006. Evaluation of skin perfusion by use of indocyanine green video angiography: rational design and planning of trauma surgery. *J. Trauma Acute Care Surg*. 61, 635–641.

Kim, G., Huang, S.W., Day, K.C., O'Donnell,M., Agayan, R.R., Day, M.A., et al., 2007. Indocyanine-green-embedded PEBBLEs as a contrast agent for photoacoustic imaging. *J. Biomed. Opt*. 12, 044020.

Kim, S.J., Bae, P.K., Chung, B.H., 2015. Self-assembled levan nanoparticles for targeted breast cancer imaging. *Chem. Commun*. 51, 107–110.

Kim, T.H., Chen, Y., Mount, C.W., Gombotz, W.R., Li, X., Pun, S.H., 2010. Evaluation of temperature-sensitive, indocyanine green-encapsulating micelles for noninvasive near-infrared tumor imaging. *Pharm. Res*. 27, 1900–1913.

Kim, T.H., Mount, C.W., Dulken, B.W., Ramos, J., Fu, C.J., Khant, H.A., et al., 2012. Filamentous, mixed micelles of triblock copolymers enhance tumor localization of indocyanine green in a murine xenograft model. *Mol. Pharm*. 9, 135–143.

Kochubey, V.I., Kulyabina, T.V., Tuchin, V.V., Altshuler, G.B., 2005. Spectral characteristics of indocyanine green upon its interaction with biological tissues. *Opt. Spectrosc.* 99, 560–566.

Kogashiwa, Y., Sakurai, H., Akimoto, Y., Sato, D., Ikeda, T., Matsumoto, Y., et al., 2015. Sentinel node biopsy for the head and neck using contrast-enhanced ultrasonography combined with indocyanine green fluorescence in animal models: a feasibility study. *PLoS One* 10, e132511.

Kokudo, N., Ishizawa, T., 2012. Clinical application of fluorescence imaging of liver cancer using indocyanine green. *Liver Cancer* 1, 15–21.

Kong, S.H., Noh, Y.W., Suh, Y.S., Park, H.S., Lee, H.J., Kang, K.W., et al., 2015. Evaluation of the novel near-infrared fluorescence tracers pullulan polymer nanogel and indocyanine green/γ-glutamic acid complex for sentinel lymph node navigation surgery in large animal models. *Gastric Cancer* 18, 55–64.

Kono, K., Ozawa, T., Yoshida, T., Ozaki, F., Ishizaka, Y., Maruyama, K., et al., 2010. Highly temperature-sensitive liposomes based on a thermosensitive block copolymer for tumor-specific chemotherapy. *Biomaterials* 31, 7096–7105.

Kono, K., Takashima, M., Yuba, E., Harada, A., Hiramatsu, Y., Kitagawa, H., et al., 2015b. Multifunctional liposomes having target specificity, temperature-triggered

release, and near-infrared fluorescence imaging for tumor-specific chemotherapy. *J. Control. Release* 216, 69–77.

Kono, Y., Ishizawa, T., Tani, K., Harada, N., Kaneko, J., Saiura, A., et al., 2015a. Techniques of fluorescence cholangiography during laparoscopic cholecystectomy for better delineation of the bile duct anatomy. *Medicine (Baltimore)* 94, e1005.

Koo, J., Jeon, M., Oh, Y., Kang, H.W., Kim, J., Kim, C., et al., 2012. In vivo non-ionizing photoacoustic mapping of sentinel lymph nodes and bladders with ICG-enhanced carbon nanotubes. *Phys. Med. Biol*. 57, 7853–7862.

Kraft, J.C., Ho, R.J., 2014. Interactions of indocyanine green and lipid in enhancing nearinfrared fluorescence properties: the basis for near-infrared imaging in vivo. *Biochemistry* 53, 1275–1283.

Krishnamurthy, S., Vaiyapuri, R., Zhang, L., Chan, J.M., 2015. Lipid-coated polymeric nanoparticles for cancer drug delivery. *Biomater. Sci.* 3, 923–936.

Kudo, H., Ishizawa, T., Tani, K., Harada, N., Ichida, A., Shimizu, A., et al., 2014. Visualization of subcapsular hepatic malignancy by indocyanine-green fluorescence imaging during laparoscopic hepatectomy. *Surg. Endosc*. 28, 2504–2508.

Kuo, W.S., Chang, Y.T., Cho, K.C., Chiu, K.C., Lien, C.H., Yeh, C.S., et al., 2012. Gold nanomaterials conjugated with indocyanine green for dual-modality photodynamic and photothermal therapy. *Biomaterials* 33, 3270–3278.

Kusano, M., Tajima, Y., Yamazaki, K., Kato, M., Watanabe, M., Miwa, M., 2008. Sentinel node mapping guided by indocyanine green fluorescence imaging: a new method for sentinel node navigation surgery in gastrointestinal cancer. *Dig. Surg.* 25, 103–108.

Lee, B.T.,Matsui, A., Hutteman,M., Lin, S.J., Winer, J.H., Laurence, R.G., et al., 2010. Intraoperative near-infrared fluorescence imaging in perforator flap reconstruction: current research and early clinical experience. J. *Reconstr. Microsurg*. 26, 59–65.

Lee, C.H., Cheng, S.H., Wang, Y.J., Chen, Y.C., Chen, N.T., Souris, J., et al., 2009. Near-infrared mesoporous silica nanoparticles for optical imaging: characterization and in vivo biodistribution. *Adv. Funct. Mater*. 19, 215–222.

Lee, E.H., Kim, J.K., Lim, J.S., Lim, S.J., 2015. Enhancement of indocyanine green stability and cellular uptake by incorporating cationic lipid into indocyanine green-loaded nanoemulsions. *Colloids Surf. B: Biointerfaces* 136, 305–313.

Li, N., Li, T., Hu, C., Lei, X., Zuo, Y., Han, H., 2015. Targeted near-infrared fluorescent turn-on nanoprobe for activatable imaging and effective phototherapy of cancer cells. *ACS Appl. Mater. Interfaces* http://dx.doi.org/10.1021/acsami.5b02037.

Li, S., Goins, B., Zhang, L., Bao, A., 2012. Novel multifunctional theranostic liposome drug delivery system: construction, characterization, and multimodality MR, near-infrared fluorescent, and nuclear imaging. *Bioconjug. Chem.* 23, 1322–1332.

Liberale, G., Vankerckhove, S., Galdon, M.G., Donckier, V., Larsimont, D., Bourgeois, P., 2015. Fluorescence imaging after intraoperative intravenous injection of indocyanine green for detection of lymph node metastases in colorectal cancer. *Eur. J. Surg. Oncol*. 41, 1256–1260.

Lim, C., Vibert, E., Azoulay, D., Salloum, C., Ishizawa, T., Yoshioka, R., et al., 2014. Indocyanine green fluorescence imaging in the surgical management of liver cancers: current facts and future implications. *J. Visc. Surg*. 151, 117–124.

Liu, P., Yue, C., Shi, B., Gao, G., Li, M., Wang, B., et al., 2013. Dextran based sensitive theranostic nanoparticles for near-infrared imaging and photothermal therapy in vitro. *Chem. Commun*. 49, 6143–6145.

Liu, Y., Xu,M., Chen, Q., Guan, G., Hu,W., Zhao, X., et al., 2015. Gold nanorods/mesoporous silica-based nanocomposite as theranostic agents for targeting near-infrared imaging and photothermal therapy induced with laser. *Int. J. Nanomedicine* 10, 4747–4761.

Liu, Z., Yang, K., Lee, S.T., 2011. Single-walled carbon nanotubes in biomedical imaging. *J. Mater. Chem*. 21, 586–598.

Lodha, A., Lodha, M., Patel, A., Chaudhuri, J., Dalal, J., Edwards,M., et al., 2012. Synthesis of mesopourus silica nanoparticles and drug loading of poorlywater soluble drug cyclosporine A. *J. Pharm. Bioallied Sci*. 4, S92–S94.

Lozano, N., Al-Ahmady, Z.S., Beziere, N.S., Ntziachristos, V., Kostarelos, K., 2015. Monoclonal antibody-targeted PEGylated liposome-ICG encapsulating doxorubicin as a potential theranostic agent. *Int. J. Pharm*. 482, 2–10.

Luke, G.P., Yeager, D., Emelianov, S.Y., 2012. Biomedical applications of photoacoustic imaging with exogenous contrast agents. *Ann. Biomed. Eng.* 40, 422–437.

Lund-Johansen, P., 1990. The dye dilution method for measurement of cardiac output. *Eur. Heart J.* 11, 6–12.

Luo, T., Huang, P., Gao, G., Shen, G., Fu, S., Cui, D., et al., 2011. Mesoporous silica-coated gold nanorods with embedded indocyanine green for dual mode X-ray CT and NIR fluorescence imaging. *Opt. Express* 19, 17030–17039.

Luo, T., Qian, X., Lu, Z., Shi, Y., Yao, Z., Chai, X., et al., 2015. Indocyanine green derivative covalently conjugated with gold nanorods for multimodal phototherapy of fibrosarcoma cells. *J. Biomed. Nanotechnol*. 11, 600–612.

Ma, Y., Sadoqi, M., Shao, J., 2012. Biodistribution of indocyanine green-loaded nanoparticles with surface modifications of PEG and folic acid. *Int. J. Pharm*. 436, 25–31.

Ma, Y., Tong, S., Bao, G., Gao, C., Dai, Z., 2013. Indocyanine green loaded SPIO nanoparticles with phospholipid-PEG coating for dual-modal imaging and photothermal therapy. *Biomaterials* 34, 7706–7714.

Makino, A., Yamahara, R., Ozeki, E., Kimura, S., 2007. Preparation of novel polymer assemblies, “lactosome”, composed of poly(L-lactic acid) and poly(sarcosine). *Chem. Lett*. 36, 1220–1221.

Manchanda, R., Fernandez-Fernandez, A., Nagesetti, A., McGoron, A.J., 2010. Preparation and characterization of a polymeric (PLGA) nanoparticulate drug delivery system with simultaneous incorporation of chemotherapeutic and thermo-optical agents. *Colloids Surf. B: Biointerfaces* 75, 260–267.

Meier, R., Boddington, S., Krug, C., Acosta, F.L., Thullier, D., Henning, T.D., et al., 2008. Detection of postoperative granulation tissue with an ICG-enhanced integrated OI-/X ray system. *J. Transl. Med*. 6, 73.

Meijer, D.K.F., Weitering, J.G., Vermeer, G.A., 1983. Pharmacokinetics of biliary excretion in man V. *Eur. J. Clin. Pharmacol*. 24, 549–556.

Miao,W., Shim, G., Kim, G., Lee, S., Lee, H.J., Kim, Y.B., et al., 2015. Image-guided synergistic photothermal therapy using photoresponsive imaging agent-loaded graphene-based nanosheets. *J. Control. Release* 211, 28–36.

Miyashiro, I., Miyoshi, N., Hiratsuka, M., Kishi, K., Yamada, T., Ohue, M., et al., 2008. Detection of sentinel node in gastric cancer surgery by indocyanine green fluorescence imaging: comparison with infrared imaging. *Ann. Surg. Oncol*. 15, 1640–1643.

Miyata, A., Ishizawa, T., Kamiya, M., Shimizu, A., Kaneko, J., Ijichi, H., et al., 2014. Photoacoustic tomography of human hepatic malignancies using intraoperative indocyanine green fluorescence imaging. *PLoS One* 9, 1–8.

Mok, H., Jeong, H., Kim, S.J., Chung, B.H., 2012. Indocyanine green encapsulated nanogels for hyaluronidase activatable and selective near infrared imaging of tumors and lymph nodes. *Chem. Commun*. 48, 8628–8630.

Morita, Y., Sakaguchi, T., Unno, N., Shibasaki, Y., Suzuki, A., Fukumoto, K., et al., 2013. Detection of hepatocellular carcinomas with near-infrared fluorescence imaging using indocyanine green: its usefulness and limitation. *Int. J. Clin. Oncol*. 18, 232–241.

Moroga, T., Yamashita, S.I., Tokuishi, K.,Miyawaki,M., Anami, K., Yamamoto, S., et al., 2012. Thoracoscopic segmentectomy with intraoperative evaluation of sentinel nodes for stage I non-small cell lung cancer. Ann. Thorac. Cardiovasc. Surg. 18, 89–94.

Murawa, D., Hirche, C., Dresel, S., Hünerbein, M., 2009. Sentinel lymph node biopsy in breast cancer guided by indocyanine green fluorescence. Br. J. Surg. 96, 1289–1294.

Nakajima, T., Mitsunaga, M., Bander, N.H., Heston,W.D., Choyke, P.L., Kobayashi, H., 2011. Targeted, activatable, in vivo fluorescence imaging of prostate-specificmembrane antigen (PSMA) positive tumors using the quenched humanized J591 antibodyindocyanine green (ICG) conjugate. *Bioconjug. Chem.* 22, 1700–1705.

Nakamura, T., Kogashiwa, Y., Nagafuji, H., Yamauchi, K., Kohno, N., 2015. Validity of sentinel lymph node biopsy by ICG fluorescence for early head and neck cancer. *Anticancer Res.* 35, 1669–1674.

Nellore, B.P.V., Pramanik, A., Chavva, S.R., Sinha, S.S., Robinson, C., Fan, Z., et al., 2015. Aptamer-conjugated theranostic hybrid graphene oxide with highly selective biosensing and combined therapy capability. *Faraday Discuss*. 175, 257–271.

Newman, M.I., Samson, M.C., 2009. The application of laser-assisted indocyanine green fluorescent dye angiography in microsurgical breast reconstruction. *J. Reconstr. Microsurg*. 25, 21–26.

Nguyen, V.P., Oh, Y., Ha, K., Oh, J., Kang, H.W., 2015. Enhancement of high-resolution photoacoustic imaging with indocyanine green-conjugated carbon nanotubes. *Jpn. J. Appl. Phys.* 54 07HF04.

Noh, Y.W., Park, H.S., Sung, M.H., Lim, Y.T., 2011. Enhancement of the photostability and retention time of indocyanine green in sentinel lymph node mapping by anionic polyelectrolytes. *Biomaterials* 32, 6551–6557.

Ogawa,M., Kosaka, N., Choyke, P.L., Kobayashi, H., 2009. In vivo molecular imaging of cancerwith a quenching near-infrared fluorescent probe using conjugates of monoclonal antibodies and indocyanine green. *Cancer Res*. 69, 1268–1272.

Ott, P., 1998. Hepatic elimination of indocyanine green with special reference to distribution kinetics and the influence of plasma protein binding. *Pharmacol. Toxicol.* 83, 1–48.

Pacheco, P.E., Hill, S.M., Henriques, S.M., Paulsen, J.K., Anderson, R.C., 2013. The novel use of intraoperative laser-induced fluorescence of indocyanine green tissue angiography for evaluation of the gastric conduit in esophageal reconstructive surgery. *Am. J. Surg*. 205, 349–353.

Patel, R.H., Wadajkar, A.S., Patel, N.L., Kavuri, V.C., Nguyen, K.T., Liu, H., 2012. Multifunctionality of indocyanine green-loaded biodegradable nanoparticles for enhanced optical imaging and hyperthermia intervention of cancer. *J. Biomed. Opt.* 17, 046003.

Pauli, J., Brehm, R., Spieles, M., Kaiser, W.A., Hilger, I., Resch-Genger, U., 2010. Novel fluorophores as building blocks for optical probes for in vivo near infrared fluorescence (NIRF) imaging. *J. Fluoresc*. 20, 681–693.

Peloso, A., Franchi, E., Canepa,M.C., Barbieri, L., Briani, L., Ferrario, J., et al., 2013. Combined use of intraoperative ultrasound and indocyanine green fluorescence imaging to detect liver metastases from colorectal cancer. *HPB* 15, 928–934.

Plante, M., Touhami, O., Trinh, X.B., Renaud,M.C., Sebastianelli, A., Grondin, K., et al., 2015. Sentinel node mapping with indocyanine green and endoscopic near-infrared

fluorescence imaging in endometrial cancer. A pilot study and review of the literature. *Gynecol. Oncol*. 137, 443–447.

Poellinger, A., Burock, S., Grosenick, D., Hagen, A., Lüdemann, L., Diekmann, F., et al., 2011. Breast cancer: early-and late-fluorescence near-infrared imaging with indocyanine green—a preliminary study. *Radiology* 258, 409–416.

Polom, K., Murawa, D., Rho, Y.S., Nowaczyk, P., Hünerbein, M., Murawa, P., 2011. Current trends and emerging future of indocyanine green usage in surgery and oncology. *Cancer* 117, 4812–4822.

Portnoy, E., Lecht, S., Lazarovici, P., Danino, D., Magdassi, S., 2011. Cetuximab-labeled liposomes containing near-infrared probe for in vivo imaging. *Nanomedicine: NBM* 7, 480–488.

Quan, B., Choi, K., Kim, Y.H., Kang, K.W., Chung, D.S., 2012. Near infrared dye indocyanine green doped silica nanoparticles for biological imaging. *Talanta* 99, 387–393.

Raabe, A., Beck, J., Gerlach, R., Zimmermann, M., Seifert, V., 2003. Near-infrared indocyanine green video angiography: a newmethod for intraoperative assessment of vascular flow. *Neurosurgery* 52, 132–139.

Raemdonck, K., Braeckmans, K., Demeester, J., De Smedt, S.C., 2014. Merging the best of both worlds: hybrid lipid-enveloped matrix nanocomposites in drug delivery. *Chem. Soc. Rev*. 43, 444–472.

Ranjan, A.P., Zeglam, K.,Mukerjee, A., Thamake, S., Vishwanatha, J.K., 2011. A sustained release formulation of chitosan modified PLCL: poloxamer blend nanoparticles loaded with optical agent for animal imaging. *Nanotechnology* 22, 295104.

Reuthebuch, O., Häussler, A., Genoni, M., Tavakoli, R., Odavic, D., Kadner, A., et al., 2004. Novadaq SPY: intraoperative quality assessment in off-pump coronary artery bypass grafting. *Chest* 125, 418–424.

Riess, G., 2003. Micellization of block copolymers. *Prog. Polym. Sci*. 28, 1107–1170.

Robertson, C.A., Evans, D.H., Abrahamse, H., 2009. Photodynamic therapy (PDT): a short review on cellular mechanisms and cancer research applications for PDT. *J. Photochem. Photobiol. B* 96, 1–8.

Rodriguez, V.B., Henry, S.M., Hoffman, A.S., Stayton, P.S., Li, X., Pun, S.H., 2008. Encapsulation and stabilization of indocyanine green within poly(styrene-alt-maleic anhydride) block-poly(styrene) micelles for near-infrared imaging. *J. Biomed. Opt.* 13, 014025.

Salis, A., Rassu, G., Budai-Szucs, M., Benzoni, I., Csányi, E., Berkó, S., et al., 2015. Development of thermosensitive chitosan/glicerophospate injectable in situ gelling solutions for potential application in intraoperative fluorescence imaging and local therapy of hepatocellular carcinoma: a preliminary study. *Expert Opin. Drug Deliv.* 12, 1583–1596.

Samorani, D., Fogacci, T., Panzini, I., Frisoni, G., Accardi, F.G., Ricci, M., et al., 2015. The use of indocyanine green to detect sentinel nodes in breast cancer: a prospective study. *Eur. J. Surg. Oncol.* 41, 64–70.

Sano, K., Mitsunaga, M., Nakajima, T., Choyke, P.L., Kobayashi, H., 2012. In vivo breast cancer characterization imaging using two monoclonal antibodies activatably labeled with near infrared fluorophores. *Breast Cancer Res*. 14, R61.

Sano, K., Nakajima, T., Miyazaki, K., Ohuchi, Y., Ikegami, T., Choyke, P.L., et al., 2013. Short PEG-linkers improve the performance of targeted, activatable monoclonal antibodyindocyanine green optical imaging probes. *Bioconjug. Chem.* 24, 811–816.

Sano, K., Ohashi, M., Kanazaki, K., Ding, N., Deguchi, J., Kanada, Y., et al., 2015. In vivo photoacoustic imaging of cancer using indocyanine green-labeled monoclonal antibody targeting the epidermal growth factor receptor. *Biochem. Biophys. Res. Commun.* 464, 820–825.

Satou, S., Ishizawa, T., Masuda, K., Kaneko, J., Aoki, T., Sakamoto, Y., et al., 2013. Indocyanine green fluorescent imaging for detecting extrahepatic metastasis of hepatocellular carcinoma. *J. Gastroenterol*. 48, 1136–1143.

Saxena, V., Sadoqi, M., Shao, J., 2003. Degradation kinetics of indocyanine green in aqueous solution. *J. Pharm. Sci*. 92, 2090–2097.

Saxena, V., Sadoqi, M., Shao, J., 2004a. Enhanced photo-stability, thermal-stability and aqueous-stability of indocyanine green in polymeric nanoparticulate systems. *J. Photochem. Photobiol. B* 74, 29–38.

Saxena, V., Sadoqi, M., Shao, J., 2004b. Indocyanine green-loaded biodegradable nanoparticles: preparation, physicochemical characterization and in vitro release. *Int. J. Pharm.* 278, 293–301.

Saxena, V., Sadoqi, M., Shao, J., 2006. Polymeric nanoparticulate delivery system for indocyanine green: biodistribution in healthy mice. *Int. J. Pharm*. 308, 200–204.

Scerrati, A., Della Pepa, G.M., Conforti, G., Sabatino, G., Puca, A., Albanese, A., et al., 2014. Indocyanine green video-angiography in neurosurgery: a glance beyond vascular applications. *Clin. Neurol. Neurosurg*. 124, 106–113.

Schaafsma, B.E., Mieog, J.S.D., Hutteman, M., Van der Vorst, J.R., Kuppen, P.J., Löwik, C.W., et al., 2011. The clinical use of indocyanine green as a near-infrared fluorescent contrast agent for image-guided oncologic surgery. *J. Surg. Oncol*. 104, 323–332.

Schaafsma, B.E., van der Vorst, J.R., Gaarenstroom, K.N., Peters, A.A., Verbeek, F.P., de Kroon, C.D., et al., 2012. Randomized comparison of near-infrared fluorescence lymphatic tracers for sentinel lymph node mapping of cervical cancer. *Gynecol. Oncol*. 127, 126–130.

Sharker, S.M., Lee, J.E., Kim, S.H., Jeong, J.H., In, I., Lee, H., et al., 2015. pH triggered in vivo photothermal therapy and fluorescence nanoplatform of cancer based on responsive polymer-indocyanine green integrated reduced graphene oxide. *Biomaterials* 61, 229–238.

Sharma, P., Bengtsson, N.E., Walter, G.A., Sohn, H.B., Zhou, G., Iwakuma, N., et al., 2012. Gadolinium-doped silica nanoparticles encapsulating indocyanine green for near infrared and magnetic resonance imaging. *Small* 8, 2856–2868.

Shemesh, C.S., Hardy, C.W., David, S.Y., Fernandez, B., Zhang, H., 2014. Indocyanine green loaded liposome nanocarriers for photodynamic therapy using human triple negative breast cancer cells. *Photodiagn. Photodyn. Ther*. 11, 193–203.

Shemesh, C.S., Moshkelani, D., Zhang, H., 2015. Thermosensitive liposome formulated indocyanine green for near-infrared triggered photodynamic therapy: in vivo evaluation for triple-negative breast cancer. *Pharm. Res*. 32, 1604–1614.

Sheng, Z., Hu, D., Xue, M., He, M., Gong, P., Cai, L., 2013. Indocyanine green nanoparticles for theranostic applications. *Nano-Micro Lett.* 5, 145–150.

Sheng, Z., Hu, D., Zheng, M., Zhao, P., Liu, H., Gao, D., et al., 2014. Smart human serum albumin-indocyanine green nanoparticles generated by programmed assembly for dualmodal imaging-guided cancer synergistic phototherapy. *ACS Nano* 8, 12310–12322.

Shimada, S., Ohtsubo, S., Ogasawara, K., Kusano, M., 2015. Macro-and microscopic findings of ICG fluorescence in liver tumors. *World J. Surg. Oncol*. 13, 198.

Situ, J.Q., Ye, Y.Q., Zhu, X.L., Yu, R.S., You, J., Yuan, H., et al., 2015. Specific targeting of A54 homing peptide-functionalized dextran-g-poly (lactic-co-glycolic acid) micelles to tumor cells. *Int. J. Nanomedicine* 10, 665–675.

Skřivanová, K., Škorpíková, J., Švihálek, J., Mornstein, V., Janisch, R., 2006. Photochemical properties of a potential photosensitiserindocyanine green in vitro. *J. Photochem. Photobiol. B* 85, 150–154.

Song, W., Tang, Z., Zhang, D., Burton, N., Driessen, W., Chen, X., 2015. Comprehensive studies of pharmacokinetics and biodistribution of indocyanine green and liposomal indocyanine green by multispectral optoacoustic tomography. *RSC Adv*. 5, 3807–3813.

Song, X., Wu, H., Li, S., Wang, Y., Ma, X., Tan, M., 2015. Ultrasmall chitosan–genipin nanocarriers fabricated from reverse microemulsion process for tumor photothermal therapy in mice. *Biomacromolecules* 16, 2080–2090.

Srinivasan, S.,Manchanda, R., Lei, T., Nagesetti, A., Fernandez-Fernandez, A.,McGoron, A.J., 2014. Targeted nanoparticles for simultaneous delivery of chemotherapeutic and hyperthermia agents—an in vitro study. J. *Photochem. Photobiol. B* 136, 81–90.

Stanga, P.E., Lim, J.I., Hamilton, P., 2003. Indocyanine green angiography in chorioretinal diseases: indications and interpretation: an evidence-based update. *Ophthalmology* 110, 15–21.

Stöber, W., Fink, A., Bohn, E., 1968. Controlled growth of monodisperse silica spheres in the micron size range. *J. Colloid Interface Sci*. 26, 62–69.

Stoffels, I., Leyh, J., Pöppel, T., Schadendorf, D., Klode, J., 2015. Evaluation of a radioactive and fluorescent hybrid tracer for sentinel lymph node biopsy in head and neckmalignancies: prospective randomized clinical trial to compare ICG-

99mTc-nanocolloid hybrid tracer versus 99mTc-nanocolloid. Eur. *J. Nucl. Med. Mol. Imaging* 42, 1631–1638.

Subhash, H.M., Xie, H., Smith, J.W., McCarty, O.J., 2012. Optical detection of indocyanine green encapsulated biocompatible poly (lactic-co-glycolic) acid nanoparticles with photothermal optical coherence tomography. *Opt. Lett.* 37, 981–983.

Suganami, A., Toyota, T., Okazaki, S., Saito, K., Miyamoto, K., Akutsu, Y., et al., 2012. Preparation and characterization of phospholipid-conjugated indocyanine green as a near-infrared probe. *Bioorg. Med. Chem. Lett*. 22, 7481–7485.

Tagaya, N., Yamazaki, R., Nakagawa, A., Abe, A., Hamada, K., Kubota, K., et al., 2008. Intraoperative identification of sentinel lymph nodes by near-infrared fluorescence imaging in patients with breast cancer. *Am. J. Surg.* 195, 850–853.

Takeuchi, H., Kitagawa, Y., 2015. Sentinel lymph node biopsy in gastric cancer. *Cancer J.* 21, 21–24.

Tan, C.,Wang, Y., Fan,W., 2013. Exploring polymeric micelles for improved delivery of anticancer agents: recent developments in preclinical studies. *Pharmaceutics* 5, 201–219.

Tang, Y., Lei, T.,Manchanda, R., Nagesetti, A., Fernandez-Fernandez, A., Srinivasan, S., et al., 2010. Simultaneous delivery of chemotherapeutic and thermal–optical agents to cancer cells by a polymeric (PLGA) nanocarrier: an in vitro study. *Pharm. Res. 27*, 2242–2253.

Tanisaka, H., Kizaka-Kondoh, S.,Makino, A., Tanaka, S., Hiraoka,M., Kimura, S., 2007. Near infrared fluorescent labeled peptosome for application to cancer imaging. *Bioconjug. Chem*. 19, 109–117.

Taylor, K.M., Kim, J.S., Rieter, W.J., An, H., Lin, W., Lin, W., 2008. Mesoporous silica nanospheres as highly efficient MRI contrast agents. *J. Am. Chem. Soc.* 130, 2154–2155.

Toyota, T., Fujito, H., Suganami, A., Ouchi, T., Ooishi, A., Aoki, A., et al., 2014. Near-infrared fluorescence imaging of lymph nodes by using liposomally formulated indocyanine green derivatives. *Bioorg. Med. Chem*. 22, 721–727.

Troyan, S.L., Kianzad, V., Gibbs-Strauss, S.L., Gioux, S., Matsui, A., Oketokoun, R., Ngo, L., et al., 2009. The FLARE™ intraoperative near-infrared fluorescence

imaging system: a first-in-human clinical trial in breast cancer sentinel lymph node mapping. *Ann. Surg. Oncol.* 16, 2943–2952.

Tsuchimochi, M., Hayama, K., Toyama, M., Sasagawa, I., Tsubokawa, N., 2013. Dual modality imaging with 99mTc and fluorescent indocyanine green using surface modified silica nanoparticles for biopsy of the sentinel lymph node: an animal study. *EJNMMI Res*. 3, 33.

Tsujimoto, H., Morimoto, Y., Takahata, R., Nomura, S., Yoshida, K., Hiraki, S., et al., 2015. Theranostic photosensitive nanoparticles for lymph nodemetastasis of gastric cancer. *Ann. Surg. Oncol*. http://dx.doi.org/10.1245/s10434-015-4594-0.

Tsujimoto, H., Morimoto, Y., Takahata, R., Nomura, S., Yoshida, K., Horiguchi, H., et al., 2014. Photodynamic therapy using nanoparticle loaded with indocyanine green for experimental peritoneal dissemination of gastric cancer. Cancer Sci. 105, 1626–1630.

Tsujino, Y.,Mizumoto, K.,Matsuzaka, Y., Niihara, H.,Morita, E., 2009. Fluorescence navigation with indocyanine green for detecting sentinel nodes in extramammary Paget's disease and squamous cell carcinoma. J. Dermatol. 36, 90–94.

Tu, Y., Cheng, K., Shen, B., Cheng, Z., 2015. Near-infrared fluorescence nanoparticle based probes: application to in vivo imaging of cancer. In: Hamblin, R.M., Avci, P. (Eds.), Applications of Nanoscience in Photomedicine, pp. 131–151 Amsterdam.

Turner, D.C., Moshkelani, D., Shemesh, C.S., Luc, D., Zhang, H., 2012. Near-infrared image guided delivery and controlled release using optimized thermosensitive liposomes. *Pharm. Res.* 29, 2092–2103.

Urbanska, K., Romanowska-Dixon, B., Matuszak, Z., Oszajca, J., Nowak-Sliwinska, P., Stochel, G., 2001. Indocyanine green as a prospective sensitizer for photodynamic therapy of melanomas. *Acta Biochim. Pol*. 49, 387–391.

Van den Berg, N.S., Brouwer, O.R., Klop, W.M.C., Karakullukcu, B., Zuur, C.L., Tan, I.B., et al., 2012. Concomitant radio-and fluorescence-guided sentinel lymph node biopsy in squamous cell carcinoma of the oral cavity using ICG-99mTc-nanocolloid. *Eur. J. Nucl. Med. Mol. Imaging* 39, 1128–1136.

Van der Poel, H.G., Buckle, T., Brouwer, O.R., Olmos, R.A.V., van Leeuwen, F.W., 2011. Intraoperative laparoscopic fluorescence guidance to the sentinel lymph node

in prostate cancer patients: clinical proof of concept of an integrated functional imaging approach using a multimodal tracer. *Eur. Urol*. 60, 826–833.

van der Vorst, J.R., Schaafsma, B.E., Hutteman, M., Verbeek, F.P., Liefers, G.J., Hartgrink, H.H., et al., 2013a. Near-infrared fluorescence-guided resection of colorectal liver metastases. *Cancer* 119, 3411–3418.

van der Vorst, J.R., Schaafsma, B.E., Verbeek, F.P.R., Swijnenburg, R.J., Hutteman, M., Liefers, G.J., et al., 2013b. Dose optimization for near-infrared fluorescence sentinel lymph node mapping in patients with melanoma. *Br. J. Dermatol*. 168, 93–98.

Verbeek, F.P., Troyan, S.L.,Mieog, J.S.D., Liefers, G.J.,Moffitt, L.A., Rosenberg,M., et al., 2014. Near-infrared fluorescence sentinel lymph node mapping in breast cancer: a multicentre experience. *Breast Cancer Res. Treat*. 143, 333–342.

Vogiatzis, I., Habazettl, H., Louvaris, Z., Andrianopoulos, V.,Wagner, H., Zakynthinos, S., et al., 2015. A method for assessing heterogeneity of blood flow and metabolism in exercising normal human muscle by near-infrared spectroscopy. *J. Appl. Physiol*. 118, 783–793.

Vollrath, A., Schubert, S., Schubert, U.S., 2013. Fluorescence imaging of cancer tissue based on metal-free polymeric nanoparticles—a review. *J. Mater. Chem. B* 1, 1994–2007.

Vos, J.J., Wietasch, J.K.G., Absalom, A.R., Hendriks, H.G.D., Scheeren, T.W.L., 2014. Green light for liver function monitoring using indocyanine green? An overview of current clinical applications. *Anaesthesia* 69, 1364–1376.

Wan, Z., Mao, H., Guo, M., Li, Y., Zhu, A., Yang, H., et al., 2014. Highly efficient hierarchical micelles integrating photothermal therapy and singlet oxygen-synergized chemotherapy for cancer eradication. *Theranostics* 4, 399–411.

Wang, H., Liu, C., Gong, X., Hu, D., Lin, R., Sheng, Z., et al., 2014. In vivo photoacoustic molecular imaging of breast carcinoma with folate receptor-targeted indocyanine green nanoprobes. *Nanoscale* 6, 14270–14279.

Wang, Y.G., Kim, H., Mun, S., Kim, D., Choi, Y., 2013. Indocyanine green-loaded perfluorocarbon nanoemulsions for bimodal 19F-magnetic resonance/nearinfrared fluorescence imaging and subsequent phototherapy. *Quant. Imaging Med. Surg*. 3, 132–140.

Watanabe, R., Sato, K., Hanaoka, H., Harada, T., Nakajima, T., Kim, I., et al., 2014. Minibody indocyanine green based activatable optical imaging probes: the role of short polyethylene glycol linkers. *ACS Med. Chem. Lett.* 5, 411–415.

Werner, S.G., Langer, H.E., Schott, P., Bahner, M., Schwenke, C., Lind-Albrecht, G., et al., 2013. Indocyanine green-enhanced fluorescence optical imaging in patients with early and very early arthritis: a comparative study with magnetic resonance imaging. *Arthritis Rheum*. 65, 3036–3044.

Wu, A.M., Olafsen, T., 2008. Antibodies for molecular imaging of cancer. *Cancer J*. 14, 191–197.

Wu, H., Zhao, H., Song, X., Li, S., Ma, X., Tan,M., 2014. Self-assembly-induced near-infrared fluorescent nanoprobes for effective tumor molecular imaging. *J. Mater. Chem. B* 2, 5302–5308.

Wu, L., Fang, S., Shi, S., Deng, J., Liu, B., Cai, L., 2013. Hybrid polypeptide micelles loading indocyanine green for tumor imaging and photothermal effect study. *Biomacromolecules* 14, 3027–3033.

Wu, X., Zhu, W., 2015. Stability enhancement of fluorophores for lighting up practical application in bioimaging. *Chem. Soc. Rev*. 44, 4179–4184.

Xie, J., Lee, S., Chen, X., 2010. Nanoparticle-based theranostic agents. *Adv. Drug Deliv. Rev*. 62, 1064–1079.

Xu, R.X., Huang, J., Xu, J.S., Sun, D., Hinkle, G.H.,Martin, E.W., et al., 2009. Fabrication of indocyanine green encapsulated biodegradable microbubbles for structural and functional imaging of cancer. *J. Biomed. Opt*. 14, 034020.

Xu, W., Ling, P., Zhang, T., 2013. Polymeric micelles, a promising drug delivery system to enhance bioavailability of poorly water-soluble drugs. *J. Drug. Delivery* 2013. http://dx.doi.org/10.1155/2013/340315.

Yamamichi, T., Oue, T., Yonekura, T., Owari, M., Nakahata, K., Umeda, S., et al., 2015. Clinical application of indocyanine green (ICG) fluorescent imaging of hepatoblastoma. *J. Pediatr. Surg*. 50, 833–836.

Yamashita, S.I., Tokuishi, K., Anami, K., Miyawaki, M., Moroga, T., Kamei, M., et al., 2011. Video-assisted thoracoscopic indocyanine green fluorescence imaging

system shows sentinel lymph nodes in non-small-cell lung cancer. *J. Thorac. Cardiovasc. Surg.* 141, 141–144.

Yan, L., Qiu, L., 2015. Indocyanine green targeted micelles with improved stability for near-infrared image-guided photothermal tumor therapy. *Nanomedicine* 10, 361–373.

Yang, H., Mao, H., Wan, Z., Zhu, A., Guo, M., Li, Y., et al., 2013. Micelles assembled with carbocyanine dyes for theranostic near-infrared fluorescent cancer imaging and photothermal therapy. *Biomaterials* 34, 9124–9133.

Yanina, I.Y., Tuchin, V.V., Navolokin, N.A., Matveeva, O.V., Bucharskaya, A.B., Maslyakova, G.N., et al., 2012. Fat tissue histological study at indocyanine green-mediated photothermal/photodynamic treatment of the skin in vivo. *J. Biomed. Opt.* 17, 058002.

Yokoyama, N., Otani, T., Hashidate, H., Maeda, C., Katada, T., Sudo, N., et al., 2012. Realtime detection of hepatic micrometastases from pancreatic cancer by intraoperative fluorescence imaging. *Cancer* 118, 2813–2819.

Yoon, H.K., Ray, A., Lee, Y.E.K., Kim, G.,Wang, X., Kopelman, R., 2013. Polymer–protein hydrogel nanomatrix for stabilization of indocyanine green towards targeted fluorescence and photoacousticbio-imaging. *J. Mater. Chem. B* 1, 5611–5619.

Yu, J., Javier, D., Yaseen, M.A., Nitin, N., Richards-Kortum, R., Anvari, B., et al., 2010. Self assembly synthesis, tumor cell targeting, and photothermal capabilities of antibody-coated indocyanine green nanocapsules. *J. Am. Chem. Soc.* 132, 1929–1938.

Yu, J., Yaseen, M.A., Anvari, B., Wong, M.S., 2007. Synthesis of near-infrared-absorbing nanoparticle-assembled capsules. *Chem. Mater.* 19, 1277–1284.

Yuan, A., Tang, X., Qiu, X., Jiang, K.,Wu, J., Hu, Y., 2015. Activatable photodynamic destruction of cancer cells by NIR dye/photosensitizer loaded liposomes. *Chem. Commun.* 51, 3340–3342.

Yuan, L., Lin, W., Zheng, K., He, L., Huang, W., 2013. Far-red to near infrared analyte responsive fluorescent probes based on organic fluorophore platforms for fluorescence imaging. *Chem. Soc. Rev*. 42, 622–661.

Zanganeh, S., Li, H., Kumavor, P.D., Alqasemi, U., Aguirre, A., Mohammad, I., et al., 2013. Photoacoustic imaging enhanced by indocyanine green-conjugated single-wall carbon nanotubes. *J. Biomed. Opt*. 18, 096006.

Zerda, A.D.L., Liu, Z., Bodapati, S., Teed, R., Vaithilingam, S., Khuri-Yakub, B.T., et al., 2010. Ultrahigh sensitivity carbon nanotube agents for photoacoustic molecular imaging in living mice. *Nano Lett*. 10, 2168–2172.

Zhao, P., Zheng, M., Yue, C., Luo, Z., Gong, P., Gao, G., et al., 2014. Improving drug accumulation and photothermal efficacy in tumor depending on size of ICG loaded lipid–polymer nanoparticles. *Biomaterials* 35, 6037–6046.

Zheng, C., Zheng, M., Gong, P., Jia, D., Zhang, P., Shi, B., et al., 2012. Indocyanine green loaded biodegradable tumor targeting nanoprobes for in vitro and in vivo imaging. *Biomaterials* 33, 5603–5609.

Zheng, J., Muhanna, N., De Souza, R., Wada, H., Chan, H., Akens, M.K., et al., 2015. A multimodal nano agent for image-guided cancer surgery. *Biomaterials* 67, 160–169.

Zheng, M., Yue, C., Ma, Y., Gong, P., Zhao, P., Zheng, C., et al., 2013. Single-step assembly of DOX/ICG loaded lipid–polymer nanoparticles for highly effective chemophotothermal combination therapy. *ACS Nano* 7, 2056–2067.

Zheng, M., Zhao, P., Luo, Z., Gong, P., Zheng, C., Zhang, P., et al., 2014. Robust ICG theranostic nanoparticles for folate targeted cancer imaging and highly effective photothermal therapy. *ACS Appl. Mater. Interfaces* 6, 6709–6716.

Zheng, X., Xing, D., Zhou, F.,Wu, B., Chen,W.R., 2011. Indocyanine green-containing nanostructure as near infrared dual-functional targeting probes for optical imaging and photothermal therapy. *Mol. Pharm*. 8, 447–456.

Zheng, X., Zhou, F., Wu, B., Chen, W.R., Xing, D., 2012. Enhanced tumor treatment using biofunctional indocyanine green-containing nanostructure by intratumoral or intravenous injection. *Mol. Pharm.* 9, 514–522.

Zheng, X., Zhou, F., 2010. Noncovalent functionalization of single-walled carbon nanotubes by indocyanine green: potential nanocomplexes for photothermal therapy. *J. X-Ray Sci. Technol*. 19, 275–284.

Zhong, J., Yang, S., Zheng, X., Zhou, T., Xing, D., 2013. In vivo photoacoustic therapy with cancer-targeted indocyanine green-containing nanoparticles. *Nanomedicine* 8, 903–919.

Zhong, J., Yang, S., 2014. Contrast-enhanced photoacoustic imaging using ICG-containing nanoparticles. *J. Innov. Opt. Health Sci*. 07, 1350029.

Zhou, Y., Kim, Y.S., Milenic, D.E., Baidoo, K.E., Brechbiel, M.W., 2014. In vitro and in vivo analysis of indocyanine green-labeled Panitumumab for optical imaging—a cautionary tale. *Bioconjug. Chem*. 25, 1801–1810.

# 2.3 Development of thermosensitive chitosan/glycerophosphate injectable *in situ* gelling solutions for potential application in intraoperative fluorescence imaging and local therapy of hepatocellular carcinoma: a preliminary study

*Adapted from:*

**Development of thermosensitive chitosan/glicerophospate injectable in situ gelling solutions for potential application in intraoperative fluorescence imaging and local therapy of hepatocellular carcinoma: a preliminary study**

Andrea Salis, Giovanna Rassu, Maria Budai-Szűcs, Ilaria Benzoni, Erzsébet Csányi, Szilvia Berkó, Marcello Maestri, Paolo Dionigi, Elena Piera Porcu, Elisabetta Gavini, Paolo Giunchedi.

*Expert Opinion on Drug Delivery*. May 2015, Volume 12, Issue 10, pages 1583-1596.

License Number: **LA/IEDD/P9147**

## 1. INTRODUCTION

Hepatocellular carcinoma (HCC) is an important cause of cancer deaths: each year > 600,000 people die from HCC in the world [1]. The hepatic resection represents the initial treatment for localized HCCs in patients without vascular invasion and with preserved hepatic functions [2]: the precise imaging of HCC nodules is clearly important for the success of the surgical procedure.

HCC is classified as a highly chemoresistant disease and conventional systemic chemotherapy plays almost no role in the treatment of advanced HCCs. For these reasons, localized anticancer therapies must be taken into account [3]. Among several locoregional ablative methods, transarterial embolization (TAE) consists of embolization of the artery feeding the tumor, which results in ischemia and subsequent tumor necrosis, whereas transarterial chemoembolization (TACE) implies the localized delivery of chemotherapeutic drugs combined with the use of embolic materials. The rationale is based on the fact that normal liver tissue receives its blood supply from the portal vein,

whereas liver tumors mostly from the hepatic artery [4,5]: a combination of concentrated chemotherapy and local ischemia within the tumor can be synergistic in achieving tumor necrosis [6].

Nowadays, microparticles are used both as embolic agents (TAE), and as embolic drug carriers (TACE). In humans microparticles of size larger than 10 μm are used considering that the capillary diameter is ~ 6 – 8 μm. Diameters from 40 to almost 1000 μm are suitable. Particles greater than 1000 μm can determine catheter clogging during the intra-arterial administration [3].

The microparticles can be classified as non-biodegradable (e.g., polyvinyl-alcohol [PVA] microspheres) or biodegradable (e.g., microspheres based on natural polymers such as starch, gelatin, chitosan or on synthetic polymers such as polylactic-co-glycolic acid. Commercial products are available constituted by calibrated microspheres (drug empty particles to be loaded before use) that have changed the conditions of embolization: radiologists can adapt the size of microspheres to the size of the vessels to be occluded, in such a way to obtain an accurate targeting [7]. Several agents can be used for hepatic embolization; they have been recently reviewed [8]. Briefly, there are microspheres available on the market for so-called bland embolization or TAE. These include Bead Block®, Embospheres®, Embozene® and Contour SE®. DC Bead® was designed to load therapeutic agents to enable one-step TACE and consists of PVA hydrogel modified with sulfonate groups that were first to demonstrate the ability to load and release chemotherapeutics in a controlled manner – a concept known as a drug-eluting bead (DEB). Other DEB systems are also now commercially available but based on microspheres with carboxylic acid functionality instead (HepaSphere® and Tandem®) [9]. All these commercial products are quite successful in the clinic, even if the intra-arterial local administration of microparticles can present some difficulties (such as catheter clogging). There is therefore the need of new embolizing systems, possibly not based on the intra-arterial administration of particles.

Indocyanine green (ICG) is a water-soluble, amphiphilic tricarbocyanine dye that has a broad range of clinical applications due to its low toxicity and capacity to absorb and emit in the near-infrared (NIR) spectral range [10]. Human tissue has the lowest absorption coefficient in the NIR part of the spectrum; therefore this dye is utilized for diagnostic and therapeutic applications.

Recent studies report the usefulness of ICG-based intraoperative fluorescence imaging for the detection of HCC nodules. HCC tumors show very strong fluorescent signals in patients who had been given an ICG bolus several days before surgery as a routine preoperative liver function test [11-14]. The real mechanisms that mediate the preferential accumulation of ICG in HCC nodules instead of the normal liver tissue are still unknown. A hypothesis could be that ICG accumulates in regions of tissue possessing leaky capillaries of vessels [15] or disturbance of bile secretion [11].

As reported in the literature [11,12,16], fluorescent nodules can be examined by an NIR camera system named PDE (photo dynamic eye, Hamamatsu Photonics K.K. Hamamatsu, Japan), that activates ICG with emitted light at a wavelength of 760 nm and filters out light with a wavelength < 820 nm [17]. The light source is a light emitting diode, and the detector is a charge-coupled device camera. The camera unit of the device is directly handled and real-time fluorescence images can be observed on the monitor in the operating room. Thus, either nodules detection or hepatic resection could be performed under the guide of the PDE.

'Smart' hydrogels are constituted by polymer solutions, which exhibit sol–gel phase transition in response to environmental stimuli such as pH, temperature, ionic strength, electric field, magnetic fields [18].

In situ thermo-sensitive hydrogels use temperature as the trigger of the gelation. Hence, it is possible to obtain hydrogels that are solutions at room temperature, but under physiological conditions (i.e., the body temperature) they form gels [19]. They can be designed as fluids that can be introduced into the desired tissue, organ or body cavity by simple syringe injection.

The viscosity of solutions can be low enough to allow direct blood administration. Thus after intra-arterial injection the solutions quickly form a gelled structure able to embolize the tumor [8,20] and to deliver imaging agents and/or drugs (if loaded in the precursor solution) [21]. Chitosan (C) is a cationic polysaccharide obtained by partial N-deacetylation of chitin. This polymer is widely used in the field of controlled drug release for its gelling properties, biodegradability and high biocompatibility [22-24].

The major issue concerning the applicability of C formulations is the impossibility of maintaining C in solution up to physiological pH due to its pKa (~ 6.3). Above pH 6, C has no charge and it forms a gel-like precipitate [25].

Chenite et al.[25] developed a thermosensitive neutral aqueous solution based on C and glycerophosphate (GP), which exhibit sol–gel transition around body temperature. The addition of polyol salts, such as GP, leads to the transformation of pH-dependent C solutions into thermally sensitive pH-dependent solutions. In the presence of GP, C solutions remain liquid below room temperature, even with pH values within a physiologically acceptable neutral range from 6.8 to 7.2 [25]. These nearly neutral C/GP aqueous solutions gel when heated [26]. The neutralization behavior of GP determines C/GP solubility and phase transition phenomena. GP presents a mild alkalinity (pKa ~ 6.34) providing correct buffering without inducing immediate precipitation or gelation when the temperature provided is between 4 and 15°C [26].

Taking into account these considerations, the aim of this work was the design and preparation of polymeric platforms based on C/GP and loaded with ICG that might be used in the field of TAE and following intraoperative fluorescence imaging of HCC.

## 2. MATHERIALS AND METHODS

### 2.1 Materials

C was obtained from Primex ehf (Oslo, Norway). The deacetylation degree was 94% and the molecular weight was 103 kDa. GP, hydrated disodic salt, was purchased from Sigma Aldrich (St. Louis, USA). ICG Pulsion was obtained from SEDA (Trezzano, Italy). The molecular weight was 774.96 Da. All other chemicals were of analytical grade.

### 2.2 Preparation of C/GP blank solutions

C/GP blank solutions at different concentrations (Table 1) were prepared according to the method of Kashyap et al. [27]. C was dissolved in 18 ml HCl 0.1 N and GP was solubilized in 2 ml of bidistilled water, at room temperature. The two solutions were put into an ice bath until the temperature of 4°C was reached. Thereafter, the GP solution was dropwise added, under vigorous magnetic stirring, into the C solution. The final solution was then left under stirring into the ice bath for 15 min, at 4°C. As reported in the literature, in order to obtain liquid C/GP systems below room temperature a pH range of 6.8 – 7.2 is required [25]. For this reason the pH of all solutions was measured (pH meter 510, XS instruments) (Table 1).

**Table 1.** Composition and pH of C/GP blank solutions prepared for the evaluation of gel formation.

| C (%w/v) | GP (%w/v) | pH |
|---|---|---|
| 2.0 | 12.0 | 7.31 |
| 2.0 | 10.0 | 7.25 |
| 2.0 | 7.0 | 7.21 |
| 2.0 | 6.0 | 7.17 |
| 2.0 | 5.0 | 6.98 |
| 2.0 | 4.0 | 6.98 |
| 2.0 | 3.5 | 6.95 |
| 2.0 | 3.0 | 6.95 |
| 1.6 | 18.0 | 7.42 |
| 1.6 | 15.0 | 7.34 |
| 1.5 | 7.0 | 7.29 |
| 1.5 | 6.0 | 6.98 |
| 1.5 | 5.0 | 6.96 |
| 1.5 | 4.0 | 6.96 |
| 1.5 | 3.5 | 6.85 |
| 1.5 | 3.0 | 6.81 |
| 1.0 | 7.0 | 6.89 |
| 1.0 | 6.0 | 6.88 |
| 1.0 | 5.0 | 6.86 |
| 1.0 | 4.0 | 6.84 |
| 1.0 | 3.5 | 6.80 |
| 1.0 | 3.0 | 6.80 |

C/GP: Chitosan/glycerophosphate.

### 2.3 Gel formation

In order to assess their thermo-sensitivity at 37°C, the C/GP blank solutions obtained (Table 1) were placed inside a plastic syringe, conveniently cut and isolated with a rubber cap and Parafilm®. The syringe was then emerged in a temperature-controlled water bath

at 37°C (±1°C). The solutions were left there for 20 min in order to make a preliminary assessment of their gelation behavior.

### 2.4 Gelation time of C/GP blank solutions

Gelation time of C/GP blank solutions was studied using the inverted tube test method, according to the methodology described by Gupta et al. [28]. The inverted tube test was performed with the solutions that exhibited gel formation in 20 min with the previous method (Table 2). Two ml chromatographic glass tubes were thermo-stabilized in a temperature-controlled bath at 37°C (±1°C). Five hundred µl of the sample solution were placed into the tubes and incubated in the bath.

At predetermined time intervals of 30 s, the tubes were taken out of the water bath and horizontally inverted in order to verify the solution flowability. If the solution did not flow within 15 s, the time is recorded as gelation time. Inverted tube tests were carried out immediately after the preparation of the solutions, which were then stored at 4°C. New measurements were taken the day after the preparation and every week through 3 weeks, in order to evaluate the solution stability and the possible changes of the gelation time over that period.

**Table 2**.Composition and gelation time of C/GP blank solutions (S) and formulations (F) performed with inverted tube test.

| ***Composition*** | | ***Gelation time (min:s)*** | | | | | | | | | |
|---|---|---|---|---|---|---|---|---|---|---|---|
| **C (%w/v)** | **GP (%w/v)** | **after prep.** | | **1 day** | | **1 week** | | **2 weeks** | | **3 weeks** | |
| | | **S** | **F** | **S** | **F** | **S** | **F** | **S** | **F** | **S** | **F** |
| 2.0 | 12.0 | 06:00 | 06:00 | 06:00 | 06:30 | 06:00 | 06:00 | 05:30 | 05:30 | 05:00 | 05:30 |
| 2.0 | 10.0 | 07:00 | 07:00 | 07:00 | 07:00 | 07:00 | 07:30 | 04:30 | 04:30 | 04:00 | 04:00 |
| 2.0 | 7.0 | 14:00 | 14:30 | 03:00 | 03:00 | 02:00 | 02:30 | 01:30 | 01:30 | 01:00 | 01:00 |
| 2.0 | 6.0 | 16:30 | 16:00 | 04:30 | 05:00 | 01:00 | 01:00 | 00:30 | 00:30 | 00:30 | 00:30 |
| 2.0 | 5.0 | 18:00 | 18:00 | 07:30 | 07:30 | 00:30 | 01:00 | 00:30 | 00:30 | 00:30 | 01:00 |
| 1.6 | 18.0 | 02:00 | 02:00 | 02:00 | 02:00 | 02:00 | 02:00 | 02:00 | 02:00 | 01:30 | 01:30 |
| 1.6 | 15.0 | 03:00 | 03:00 | 03:00 | 03:00 | 03:00 | 02:30 | 03:00 | 03:00 | 02:30 | 02:30 |

C/GP: Chitosan/glycerophosphate.

### 2.5 Preparation of formulations and determination of their gelation time

ICG was incorporated in the C/GP solutions; composition is reported in Table 2. About 5 mg of ICG were dissolved in each C/GP solution (20 ml) under stirring condition at 4°C. Gelation time of formulations was determined following the inverted tube test method previously reported. The rationale was the assessment of the dye influence in the gelling properties of these thermosensitive fluids. Inverted tube tests were performed considering the same time intervals carried out for C/GP blank solutions.

### 2.6 Biodegradability

The leader solutions and formulations that exhibited the best gelation time were selected for further studies and named as reported in Table 3.

Biodegradability studies were conducted following the method of Zang et al. [29]. Hydrogels formed from blank solutions and formulations were prepared at 0.6 cm3 volume and 1 cm diameter and immersed in 2 ml of DMEM medium with 0.1% sodium azide containing 1.91 µg/ml chicken egg white lysozyme. Samples were placed in incubator thermostabilized at 37°C for 14 days. The medium was replenished every week of storage. Dried weights of the samples were measured on the 1st, 4th, 7th and 14th days of incubation. Degradation was determined by percentage of weight loss [29].

**Table 3.** Composition of leader solutions and formulations.

| Code | C (% w/v) | GP (% w/v) | ICG (% w/v) |
|---|---|---|---|
| C2/GP12 | 2.0 | 12.0 | - |
| C2/GP12d | 2.0 | 12.0 | 25 |
| C2/GP10 | 2.0 | 10.0 | - |
| C2/GP10d | 2.0 | 10.0 | 25 |
| C2/GP7 | 2.0 | 7.0 | - |
| C2/GP7d | 2.0 | 7.0 | 25 |
| C1.6/GP18 | 1.6 | 18.0 | - |
| C1.6/GP18d | 1.6 | 18.0 | 25 |
| C1.6/GP15 | 1.6 | 15.0 | - |
| C1.6/GP15d | 1.6 | 15.0 | 25 |

C: Chitosan; GP: Glycerophosphate; ICG: Indocyanine green.

## 2.7 Rheological characterization

Leader solutions (Table 3) and their corresponding hydrogels were analyzed by rheological methods. The gelling and rheological properties were performed with a Physica MCR101 rheometer (Anton Paar, Austria). The measuring system was parallel-plate type (diameter 50 mm, gap 0.2 mm). Each type of rheological measurement was performed immediately after the preparation of solutions and after 1 week of storage at 4 and 20°C. Data were expressed as mean ± standard deviation (n = 3).

### 2.7.1 Viscosity measurements

Viscosity measurements of solutions were carried out at 4°C applying a shear rate from 0 to 100 1/s. For all curves the slope (n) was determined in order to evaluate the changes of the viscosity increasing the shear rate.

### 2.7.2 Frequency sweep measurements

Dynamic frequency sweep tests were performed at constant temperature (37°C) and strain (1%) in the limit of the linear viscoelastic region. The storage (G′), and loss moduli (G″) damping factors were determined for angular frequencies (ω) between 0.1 and 100 1/s. The viscoelastic behavior on the hydrogels was analyzed via their corresponding damping factors (tan(δ)) at ω = 10 1/s.

### 2.7.3 Gelation time performed with rheometer

Gelation time was determined at 37°C at a constant angular frequency (ω) of 1.0 1/s at a constant strain of 1 % measuring the G′ and G″ as a function of time. Gelation time of the samples was established at the time of the intersection of G′ and G″, where tanδ = 1. The differences between gelation time values gained by the rheometer and the inverted tube test were assessed.

## 2.8 *In vitro* dye release studies

Each formulation (Table 3) was filled in a dialysis bag previously activated with ethylene diamine tetra-acetic acid. The molecular weight cut off of the dialysis bag was 12,000 – 14,000 and higher than the molecular weight of the dye. The dye release was studied by

using the USP dissolution apparatus (DT70, Erweka GmbH, Germany). Each dialysis bag was fixed to the rotating bar of the dissolution tester and lowered into the dissolution vessel containing 900 ml of phosphate buffer (PBS) at pH = 6.5, 37°C (±1°C). The rotation speed of the dialysis bag was 100 rpm. The dissolution test was performed up to 16 h. At each prefixed time point, the medium (1 ml) was removed for analysis and it was replaced with the corresponding volume of fresh PBS. The samples removed from the medium were immediately analyzed spectrophotometrically (λ=779 nm) (ThermoSpectronic, Helios, UK). The dissolution studies were conducted in triplicate (mean values are reported). The dye contents of the samples were measured from the reference absorption–concentration curve of the dye that was constructed by using standard solutions of known ICG concentration in PBS. The same test was performed filling 10 mg of ICG in the aqueous solution in another dialysis bag in order to make a comparison with the release behavior of C/GP systems loaded with ICG.

### 2.9 Dye uptake from a preformed hydrogel

The eventual ability of blank hydrogels to up-take ICG dispersed in the liver was investigated filling a preformed blank hydrogel (C1.6/GP15) into a solution of known ICG concentration (0.01 mg/ml) in PBS pH = 6.5, 37°C (±1°C). The variation of ICG concentration in the medium was analyzed via the UV spectrophotometer (λ = 779 nm) (ThermoSpectronic, Helios, UK) removing samples (1 ml) from the medium at 15, 30, 45, 60 and 90 min. The medium removed for analysis was always replaced with the corresponding volume of fresh PBS.

### 2.10 *Ex vivo* embolization procedure

*Ex vivo* studies were carried out on a bovine liver (weight of ~ 8 kg), thermostabilized at 37°C in a saline bath. The experiments were carried out in standard conditions, with the organ preserved outside of the body. It was flushed at a low pressure saline solution (NaCl 0.9%) and immersed into ~ 10 – 15 cm of $H_2O$.

The leader formulations were selected for these studies (Table 3).

The hepatic artery was surgically exposed and then catheterized with a catheter (CVC 14 Gauge). Successively, 5 ml of formulation was slowly injected till a predetermined area

of the organ through the distal branches of the hepatic artery (in the right lateral lobe) to selectively embolize an area of 3 – 4 $cm^2$. Selective visualization of the injection site with an NIR fluorescence imaging system (PDE; Hamamatsu Photonics K.K. Hamamatsu, Japan) and intraoperative ultrasound (Flexfocus 800, BK medical) were performed in order to assess the localization and gelation of the solutions and the occlusion of the artery. Our group has previously described the combined use of ICG fluorescence and ultrasounds as a useful combine technique to detect small nodules into a liver [16]. In this experiment the probe could allow us to confirm the site of gelation shown by fluorescence detection. The site visualized by PDE was then cut open in order to evaluate the hydrogel formation.

## 3. RESULTS

### 3.1 Preparation of C/GP blank solutions and gel formation

Twenty-two C/GP blank solutions, characterized by different C/GP weight ratios, were prepared (Table 1). Solutions with the highest concentrations of GP (12 – 18% w/v) were clear solutions at 4°C when polyol salt was dropwise added. On the contrary, solutions with the lowest concentration of GP (3.0 – 7.0% w/v) showed a different behavior at 4°C: the formation under stirring of a milky suspension was observed, whereas a gel-like milky precipitate formed without stirring. However, by shaking or intense stirring, the milky suspension was again obtained.

Gelation of the solutions was assessed through their incubation in a plastic syringe inside a thermo-stabilized bath (37 ± 1°C) and left there for 20 min. Solutions which displayed gelation within that time interval are showed in Table 2. An increase in the hydrogel compactness was found by rising the concentration of C and GP. For the same amount of C, hydrogels with higher amounts of GP were more opaque and they presented a stronger milk coloration, which was in conformity with the observations reported by Ahmadi and De Bruijn [30].

### 3.2 Gelation time of C/GP blank solutions and formulations

Figure 1 shows gel set in the inverted tube of a formulation chosen as an example Gelation time results following the inverted tube test method are presented in Table 2. After the

preparation, solutions with 2% of C showed the increase of gelation time as the GP concentration decreases from 6 min (12% w/v) to 18 min (5% w/v). When C concentration is lowered to 1.6%, higher GP concentrations are necessary to obtain more rapid gelation time: 2 min (18% w/v) and 3 min (15% w/v) were gained.

A decrease in the gelation time values taken 1 day after the preparation was observed for 2% C solutions with the lowest amount of GP (5.0 – 7.0%) till 7 – 3 min, respectively; this behavior was observed also along the time as a further remarkable decrease in the gelation time from the first to the third week was observed.

The incorporation of ICG into C/GP blank solutions did not display any significant change in the gelation rates of these systems (Table 2). Even after 3 weeks of storage at 4°C, all of the C/GP solutions analyzed remained temperature-sensitive.

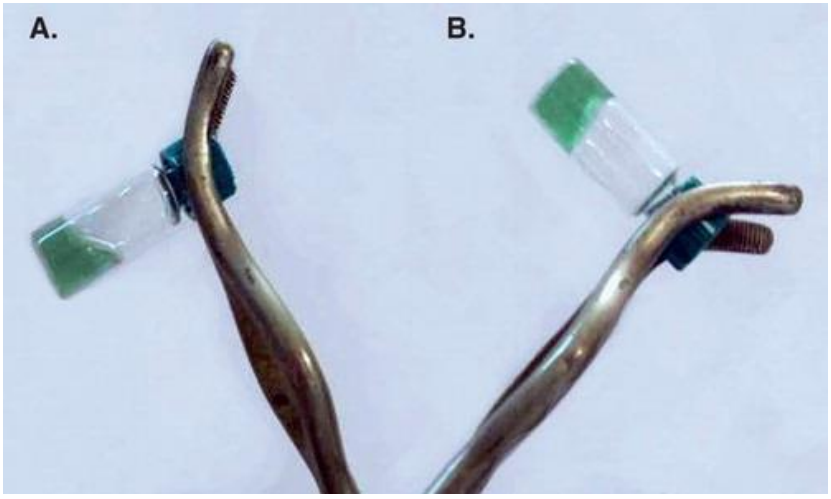


**Figure 1.** Photographs of the gelation process observed by the inverted tube test. Formulation is a flowable liquid at room temperature (A) and it is transformed to a rigid hydrogel at 37°C (B).

### 3.3 Biodegradability

Figure 2 shows the degradation rate of blank hydrogels or containing ICG. The degradation rate was independent of dye loading and decreased as the C concentration in the solution increased. Over the 14 days of degradation, formulations with 2% C concentration were degraded no more than 54%, whereas formulations with 1.6% C concentration exhibited a degradation rate > 60% (Figure 2B). Nevertheless, the cross-

link density between C and GP did not affect the degradation rate in the case of formulations with 2% C concentration. The only exception was formulation C2/GP7d that exhibited the lowest degradation rate despite the lowest concentration of GP (lowest cross-link density between C and GP). As concerning 1.6% C concentration, the formulation degradation rate increased as the cross-link density decreased.

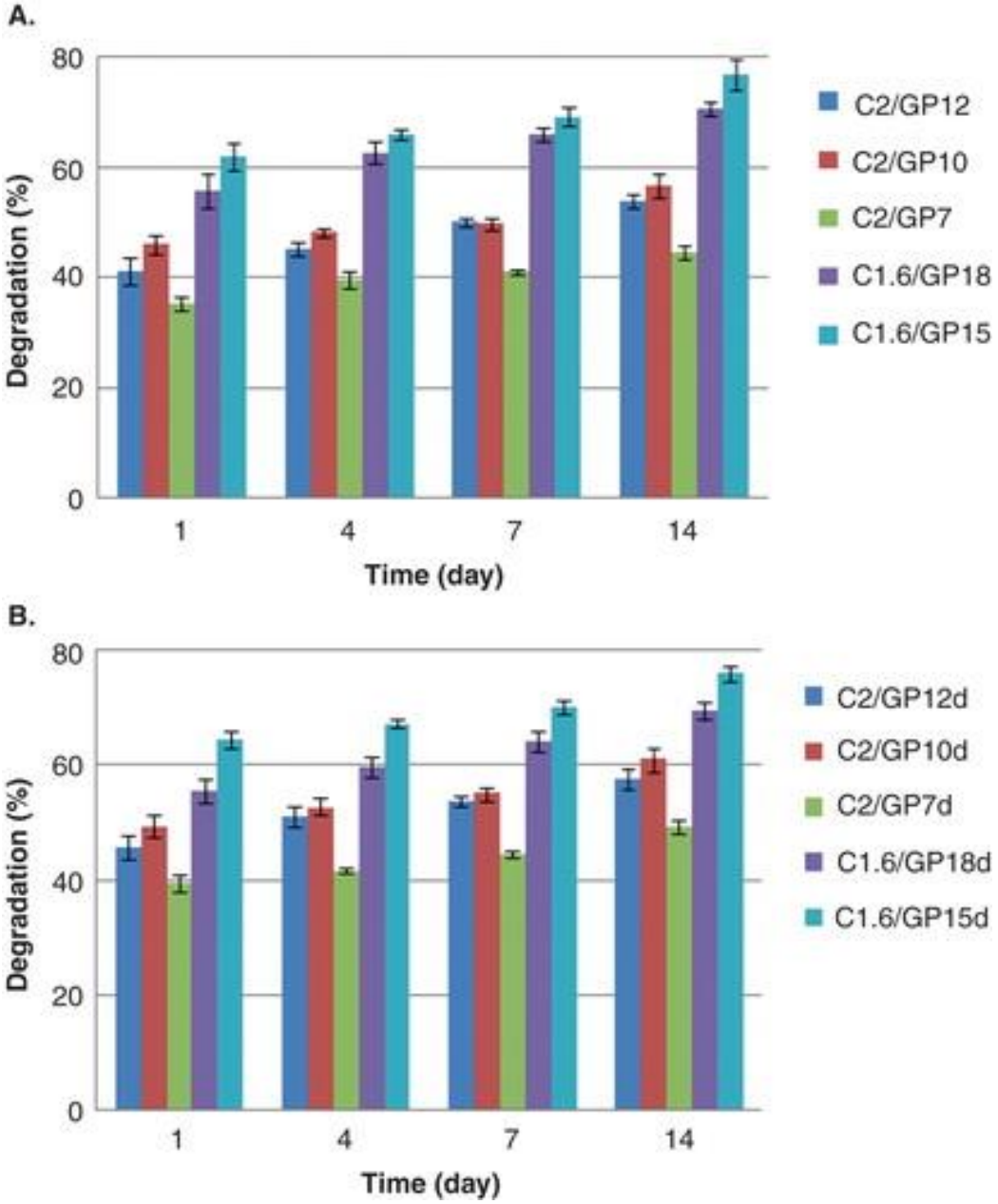


**Figure 2.** Degradation of hydrogel obtained from blank solutions (A) and formulations (B) > 14 days. Data are depicted as mean ± SD (n = 3).

### 3.4 Rheological characterization

#### 3.4.1 Viscosity measurements

For all solutions, the viscosity curve was determined at 4°C. In this type of diagram, viscosity is plotted versus shear rate in order to get information about the flow behavior of polymer solutions. Figure 3 shows viscosity of C1.6/GP18, chosen as example. This formulation exhibited a shear-thinning behavior showing viscosity decreases when the shear rate has increased. Furthermore, the storage time and temperature had also an effect on the viscosity. Other solutions displayed similar viscosity performance.

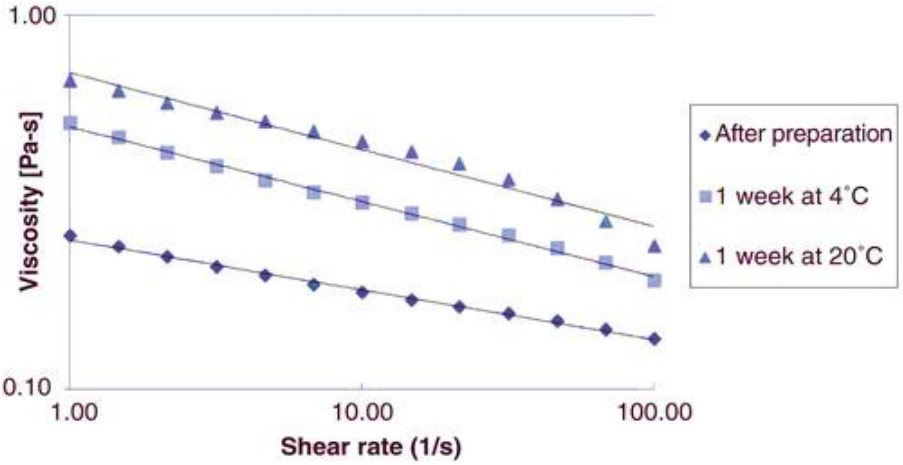


**Figure 3.** Viscosity curves of C1.6/GP18, chosen as example, after preparation and after 1 week of storage at 4 and 20°C.

Data in Table 4 show the viscosity values at the shear rate of 100 1/s. Solutions with high cross-link density between C and GP (formulation C1.6/GP18 and C1.6/GP 15) exhibited an increase of the viscosity during the storage, as already reported in the literature [31].
For all viscosity curves, the slope (n) was determined. Table 4 shows that the solution with the lowest cross-link density between C and GP (C2/GP7) exhibited the highest value of n. Solutions with the highest cross-link density (formulation C1.6/GP18 and C1.6/GP15) displayed the lowest values of n as it was expected. The slopes were quite independent from storage temperature (data not shown).

**Table 4.** Viscosity, η, at shear rate of 100 1/s of solutions stored at 4°C and 20°C.

| Solution | η (Pa × s) | | | Slopes (n) after preparation |
|---|---|---|---|---|
| | Storage at 4°C | | Storage at 20°C | |
| | after preparation | 1 week | 1 week | |
| **C2/GP12** | 0.476 ± 0.06 | 0.412 ± 0.05 | 1.040 ± 0.07 | 0.379 ± 0.09 |
| **C2/GP10** | 0.358 ± 0.03 | 0.302 ± 0.08 | 0.710 ± 0.10 | 0.333 ± 0.08 |
| **C2/GP7** | 0.205 ± 0.02 | 0.370 ± 0.03 | 0.152 ± 0.03 | 1.163 ± 0.10 |
| **C1.6/GP18** | 0.157 ± 0.02 | 0.244 ± 0.03 | 0.317 ± 0.05 | 0.125 ± 0.01 |
| **C1.6/GP15** | 0.160 ± 0.01 | 0.274 ± 0.03 | 0.270 ± 0.07 | 0.129 ± 0.01 |

### 3.4.2 Frequency sweep measurements

Figure 4 displays the frequency dependency of G′ of hydrogels. High gel strengths (high G′) were obtained increasing the cross-link density between C and GP. The only exception was solution C2/GP7 that exhibited a good gel structure despite the lowest cross-link density. Data in Table 5 show the damping factor of hydrogels at ω of 10 1/s. The lowest values of tan (δ) are related to solutions with the highest molar ratio GP/C. This tendency was general at 4 and 20°C. The tan (δ) slightly changed during the storage time (at 4 and 20°C) except for C2/GP7 whose tan (δ) was similar and even lower than tan (δ) plotted for C2/GP10 and C2/GP12, made with the same concentration of C but with higher concentration of GP.

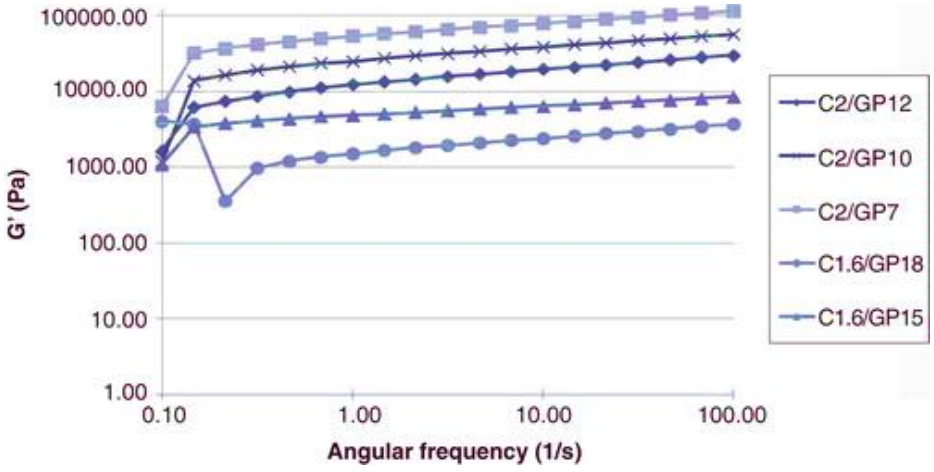


**Figure 4.** Frequency dependence of hydrogels after preparation.

**Table 5.** Damping factors (tan (δ)) at 10 1/s of hydrogels, obtained from solutions stored at 4 and 20°C.

| Solution | tan (δ) | | |
|---|---|---|---|
| | Storage at 4°C | | Storage at 20°C |
| | after preparation | 1 week | 1 week |
| **C2/GP12** | 0.28 ± 0.01 | 0.29 ± 0.02 | 0.26 ± 0.01 |
| **C2/GP10** | 0.29 ± 0.03 | 0.30 ± 0.01 | 0.28 ± 0.01 |
| **C2/GP7** | 0.30 ± 0.03 | 0.27 ± 0.02 | 0.24 ± 0.01 |
| **C1.6/GP18** | 0.19 ± 0.02 | 0.17 ± 0.03 | 0.16 ± 0.04 |
| **C1.6/GP15** | 0.22 ± 0.03 | 0.24 ± 0.03 | 0.22 ± 0.03 |

### 3.4.3 Gelation time performed with rheometer

The dynamic viscoelastic functions G′ and G″ were measured as a function of time at 37°C. Gelation time ($t_g$) is defined as the crossing point between G′ and G″. Figure 5 shows the changes of the storage and the loss modulus as a function of time at 37°C of C1.6/GP18, chosen as an example. The gelation point of the samples was established at the intersection of G′ and G″.

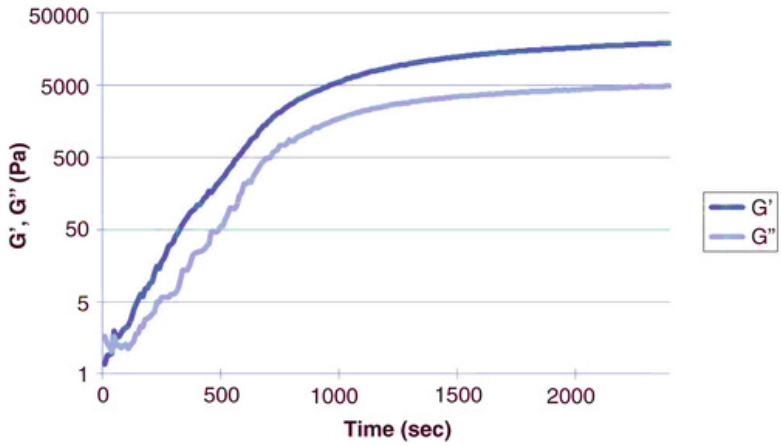


**Figure 5.** Sol–gel transitions versus time of C1.6/GP18 at 37°C after preparation, chosen as example.

Values of $t_g$ of all samples extrapolated from sol–gel transitions versus time curves (data not shown) are quite similar to gelation time values carried out with inverted tube test. Thus, there was a good correspondence between the two methodologies.

For C2/GP7, it was not possible to identify the crossing point, and consequently the tg because G′ was always higher than G″ during the time.

From G′ versus time curves (Figure 6), the gelation speed of the samples necessary to reach an adequate gel structure can be evaluated, through the slopes of those curves (Table 6). The slopes were dependent on the cross-link density between C and GP and on C and GP concentrations. The only exception was C2/GP7 that exhibited a rapid gelling despite the lowest cross-link density between C and GP.

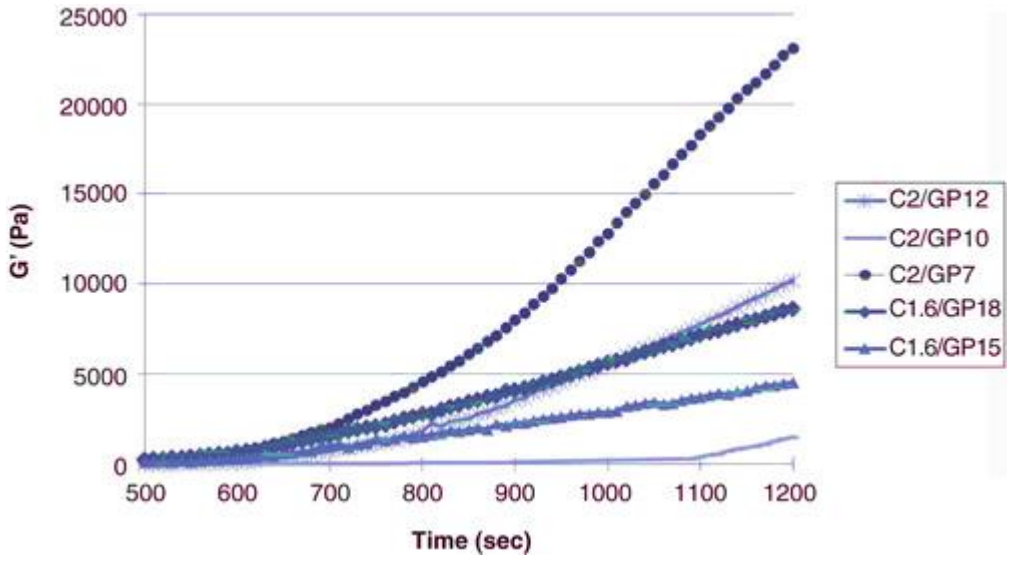


**Figure 6.** Comparison of the slopes of solutions after preparation

| *Solution* | *Slope (n)* |
|---|---|
| **C2/GP12** | 21.75 ± 6.53 |
| **C2/GP10** | 13.80 ± 4.00 |
| **C2/GP7** | 47.70 ± 4.31 |
| **C1.6/GP18** | 16.80 ± 2.11 |
| **C1.6/GP15** | 6.84 ± 1.05 |

**Table 6.** Slopes (n) of G′ versus time curves of solutions after preparation.

### 3.5 *In vitro* dye release studies

Release of ICG from hydrogels into PBS at 37°C over the course of 16 h was measured spectrophotometrically. The results are displayed in Figure 7. The dye in the aqueous solution was able to diffuse across the membrane. On the contrary, no significant release of ICG from C1.6/GP15d hydrogel occurred. Indeed, ICG cross through the cutoff of the dialysis bag neither in the first minutes when formulation was still in solution, nor when it gelled. No difference in the release profile was found in the case of other formulations.

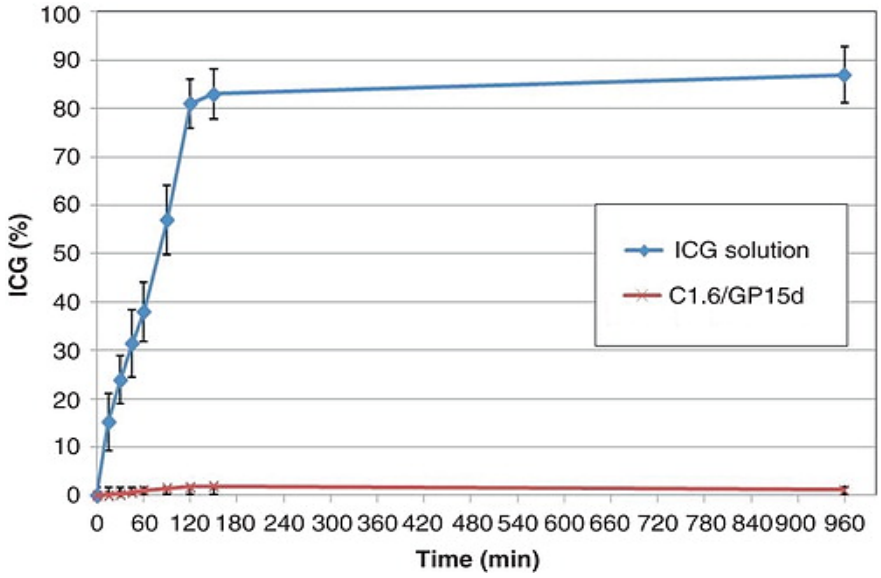


**Figure 7.** *In vitro* release profile of ICG from C1.6/GP15d, chosen as example, compared with that of diffusion from the ICG water solution. Data were expressed as mean ± SD (n = 3).

### 3.6 Dye uptake from preformed hydrogel

Considering the results from *in vitro* release studies, which showed the ability of hydrogels to retain ICG, the present test was done to confirm the strong affinity between ICG and hydrogels. A preformed hydrogel (C1.6/GP15) was immersed into the PBS solution of known ICG concentration (Figure 8A); the variation of ICG concentration was measured spectrophotometrically at different time intervals. It was observed a loss of dye absorbance in the PBS solution just only after 15 min from 0.952 to 0.294 and decreased till 0.092 after 60 min (Figure 8B). The observed loss of dye absorbance could be correlated with the strong interaction between C and ICG [32]. As the hydration of

C1.6/GP15 hydrogel occurs, an interaction between chitosan and the dye could be hypotized: in fact, green gelled clots were observed suspended into the PBS solution, which appeared decolored (Figure 8C).

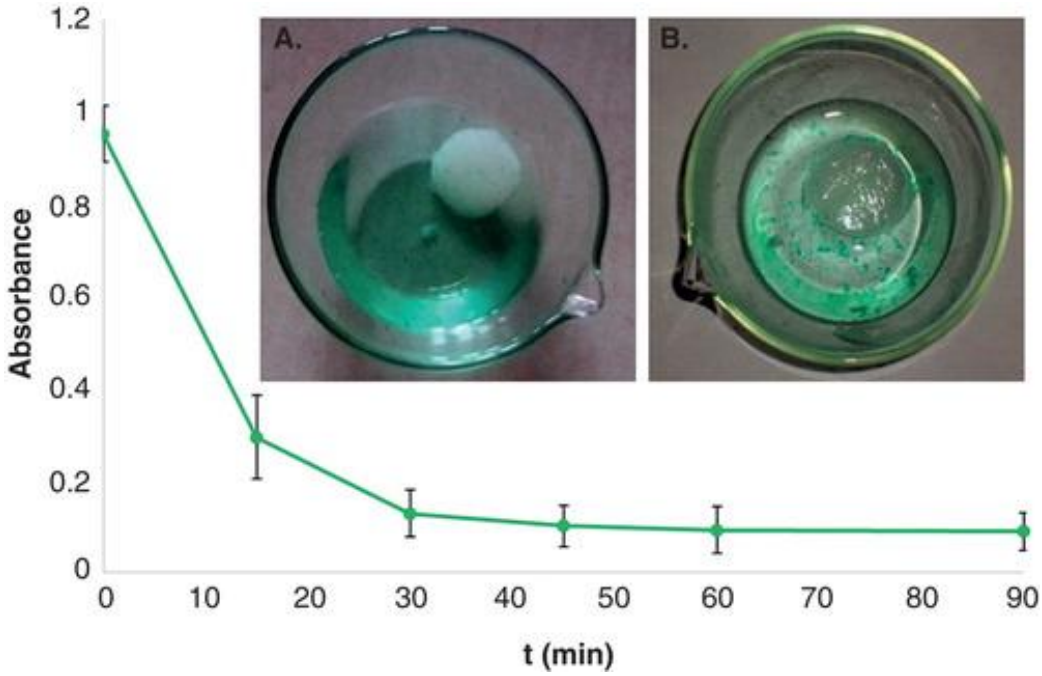


**Figure 8.** Absorbance curve of ICG solution versus time during dye uptake from preformed hydrogel; picture of ICG solution immediately after the immersion of C1.6/GP15 hydrogel. (A) and after 90 min (B).

### 3.7 *Ex vivo* embolization procedure

The injection of the leader formulations (Table 3) through the hepatic artery was performed as previously described. Considering the results gained from the inverted tube test, C2/GP7d was injected the day after the preparation in order to achieve a faster gelation inside the artery.

In all cases the formation of a stable gelled clot was macroscopically observed at the site of embolization in the hepatic parenchyma, due to the rapid gelation of the injected solution, containing the thermosensitive polymer. In this set of experiments, the hydrogel was apparently completely stabilized after 1 – 5 min at 37°C. The same clot was evident

at PDE examination (Figure 9). Furthermore, sections of the liver in correspondence of the injected site confirmed the presence of the gelled clot (Figure 10).

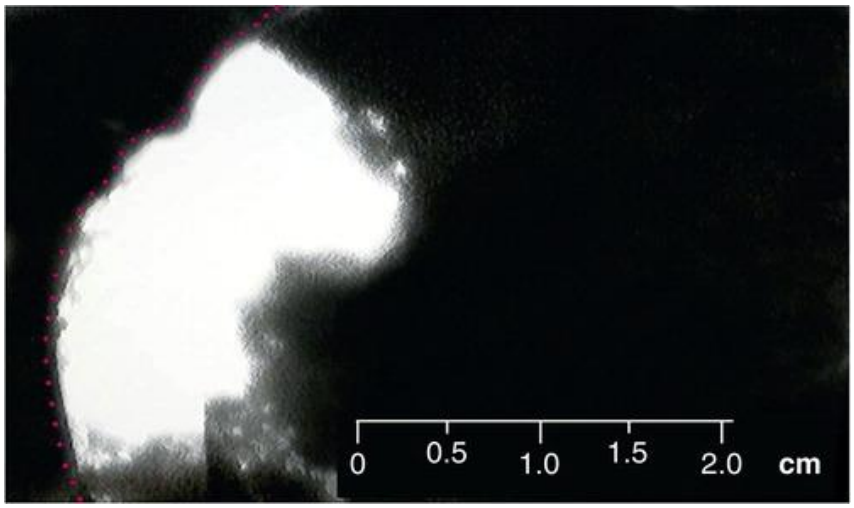


**Figure 9.** Selective visualization of the injection site with a near-infrared fluorescence imaging system PDE. The embolizing formulation was injected through the hepatic artery in the right lateral lobe. The figure shows the bright fluorescence of ICG under the infrared PDE camera and its neat localization into the injection site. The dotted line indicates the limit of the organ.

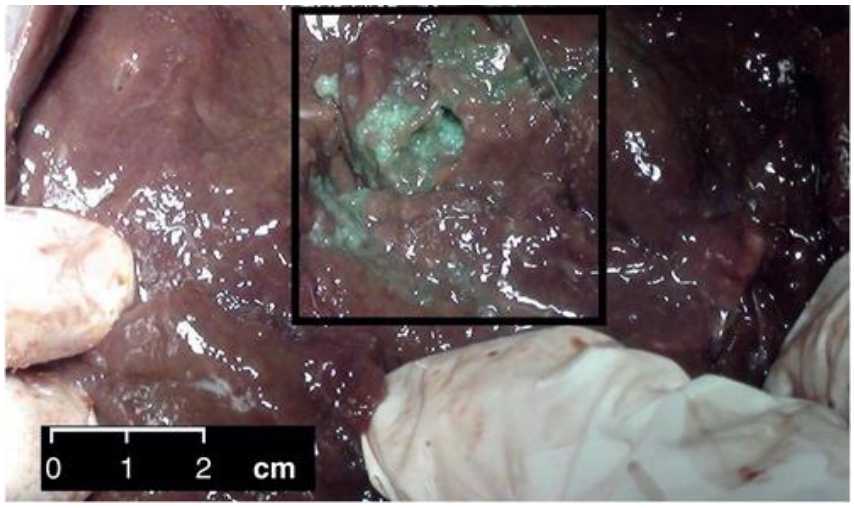


**Figure 10.** Section of the liver after the in situ gelation of C1.6/GP15d. The picture demonstrates gelled clots at the site of injection after cutting open the area previously localized by PDE and showed in Figure 9.

## 4. DISCUSSION

C/GP solutions were prepared to develop a class of ICG-loaded injectable hydrogels, whose potential application is the loco-regional detection and treatment of HCC nodules. Particularly, the solution should be injected down a catheter, which is selectively placed into the arterial branches of a predetermined liver area, similarly to the technique used for superselective TACE. The polymeric compound should be delivered close to the tumor and saturate its vessels. The sol–gel transition should be fast enough to allow a saturation of the microcirculation. These solutions should be able to exhibit an adequate viscosity to be injected and gelation behavior at physiological temperature (about 37°C). The formed gel should have suitable viscosity to embolize and avoid that hydrogel fragments can flow in the blood circulation. Any peripheral escape of the dye should not be observed.

Most of the solutions prepared are characterized by low concentrations of GP, ranging from 3 to 7% w/v (Table 1); in spite of its endovenous use being approved by the Food and Drug Administration, certain GP toxicity issues have been arisen: after gelation GP starts diffusing out of the physically cross-linked network, resulting in a linear increase of the extraction medium osmolality, which results in possible local cytotoxic effects [33]. Therefore the rationale was the preparation of in situ gelling solutions containing the minimum GP amount. In C/GP systems three types of interactions may be involved in the gelation process: i) hydrogen bonding between C chains, as a consequence of reduced electrostatic repulsion after neutralization with GP; ii) electrostatic attraction between C ammonium groups and GP phosphate groups; iii) C–C hydrophobic interactions [25,34]. Although sol–gel phase transition is driven by hydrophobic interactions, gelation would not occur without mechanisms i) and ii). This explains the role of pH in the temperature-controlled gelation of C/GP aqueous systems [25]. At low temperatures, C/GP solutions with a pH around 7 do not immediately turn into a gel suggesting that repulsive forces between the C chains are stabilized at low temperatures and destabilized at high temperatures. Ruel-Gariépy et al.[35] hypothesized that GP prevents or slows down gelation at low temperature. In fact, polyols are known to stabilize several compounds in aqueous solutions, promoting the formation of a shield of water around some macromolecules in polyol-water mixtures [36]. Accordingly, the presence of GP into the C solution promotes the protective hydration of C chains, preventing at low temperatures

their association and consequently gelation. C chain hydration is then dependent on the amount of GP added to the C solution. If GP concentration is too low, as in the solutions prepared, the formation of a water shield around C chains and their neutralization is only partial, preventing just part of their association and leading to a gel-like precipitate at low temperatures. The gel-like precipitate formation at 4°C is reversible. At 4°C hydrogen bonding between C–C and C–water are predominant and there is not enough energy for hydrophobic bonds to be established, resulting in a reversible gelation process. Gelation time values obtained immediately after the preparation of the final solutions (Table 2) are in accordance with the results reported by Chenite [25]. In order to achieve a physiologically acceptable pH range and fast gelation at 37°C, high concentrations of C and GP are required. As a consequence, gelation time increased with the decreasing of GP and C amounts. The increase of the gelation rate observed for solutions with the lowest amount of GP (5.0 – 7.0%) during the storage, at 4°C, could be explained in the following way: as we previously reported, low proportions of GP lead to a reversible gelation of C solutions at low temperature even if the pH of the formulations is neutral. Although the hydrogels turned back into a solution under stirring, the presence of small gel nucleus dispersed into the C/GP solutions was observed. As a result, shear stress allows the breaking of the gel network and the formation of small gel nucleus of C/GP, which are suspended in the aqueous solution. Gel nucleus can aid and accelerate the final gelation induced by temperature through a mechanism of nucleation and growth. The small increase in the gelation rate for the formulations with the highest GP concentrations after 3 weeks of storage was also dependent on the high deacetylation degree of C used for the preparation of these formulations. The combination of high deacetylation degree with high GP concentration leads to high cross-link density between the phosphate groups of GP and the ammonium groups of C [34].

Although all solutions and formulations (Table 2) gel at body temperature, the solutions that exhibited slow gelation cannot be considered suitable for local treatment of HCC as embolic agents.

The C/GP solution should form a gel quickly in order to provide good occlusion of blood flow [37]. The viscosity and compactness of the corresponding hydrogels that strictly depend on C and GP concentrations could be further critical parameters [36]. High viscosity may help to control injection, to avoid dilution of the solution and to limit the

possibility of migration into collateral arteries [31]. In the latter case, if the arterial blood flow disperses the embolic agent, cardiopulmonary embolism may occur [38-42]. However, too fast gelation may be problematic because it could determine catheter occlusion. Accordingly, five leader solutions and formulations were selected for further in vitro and ex vivo studies (Table 3). By virtue of the high viscosity, high compactness and adequate gelation rate, these formulations are supposed to remain in the injection site, filling and gelling in vessel cavities. In all cases, formulations remained easily injectable through (CVC 14 Gauge) catheters. Data in Table 4 show the viscosity values at the shear rate of 100 1/s in order to make a comparison with the high shear rate evolving during a hypothetical injection of our solutions. Thus, it is possible to evaluate the injectability of these systems immediately after the preparation and after 1 week of storage. These systems could be considered still injectable, nevertheless an increase of the viscosity during the storage was observed for solutions with high cross-link density between C and GP. The determination of the slope (n) of viscosity curves is a useful approach to understand the resistance to flow of our solutions and consequently the injectability of such systems. The high slope determines low resistance to flow, which indicates a good injectability for these pseudoplastic liquids and, in terms of applicability, a good fit to the desired blood vessel or body cavity. As shown in Table 4 the solution with the lowest cross-link density between C and GP (C2/GP7) exhibits the best injectability despite the formation of a gel-like precipitate at 4°C. This because the gel-like precipitate structure is quite easy to be destroyed during the injection procedure.

Frequency sweep tests were used to characterize the final gel-structure of the five solutions at body temperature. The gels can be described as systems in which the G′ are higher than the G″ and/or they are relatively independent from frequency. Lapasin and Pricl [43] classified gels into two classes: strong gels, where the moduli are relatively independent from frequency and weak gels, where the moduli are slightly dependent from frequency. Frequency sweep measurements were carried out in the limit of the linear viscoelastic range, in order to evaluate the frequency dependency of the G′ and G″. The high gel strengths (high G′) showed by solutions with high cross-link density between C and GP were in conformity with the results previously reported in the literature [35]. The unexpected result of C2/GP7, which exhibited a good gel structure despite the lowest cross-link density, could be explained with the presence of the gel-like precipitation at

4°C. The gel-like precipitate can aid the reaching of a strong gel structure thanks to a nucleation mechanism.

The damping factor reveals the ratio of the viscous and the elastic portion of the viscoelastic deformation behavior. In the hydrogel field, the determination of this value is an important criterion to assess gel formation and the hardening process. Therefore, tan (δ) > 1 defines the liquid state and tan (δ) < 1 defines the gel state. Furthermore, tan (δ) indicates the elasticity property of the hydrogels: the low tan (δ) determines strong gel structure and, as a consequence, good gel resistance and stability inside the desired tissue, organ, or body cavity.

Data in Table 5 show that the lowest values of tan (δ) are related with solutions with the highest molar ratio GP/C, due to a better neutralization of C chains that leads to an improvement of the interactions involved in the gelation process (hydrogen bonding and hydrophobic interactions). The unexpected tan (δ) of C2/GP7 displayed during the storage time (at 4 and 20°C) could be explained by the nucleation growth mechanism previously supposed. As previously reported, it was not possible to extrapolate the tg from sol–gel transitions versus time curves for C2/GP7: G′ was always higher than G″ during the time. This comportment is probably due to the presence of the gel-like precipitation at 4°C that leads to an elastic response of the material and that is stronger than the viscous response. As described before, low proportions of GP lead to a reversible gelation of C solutions at low temperature.

The unexpected result for formulation C2/GP7 is found and it is in contrast with the theories reported in the literature [25,35]. C2/GP7 exhibited a rapid gelling despite the lowest cross-link density between C and GP. This performance could be explained by the gel-like precipitation at 4°C. For the other solutions, the slopes are dependent on the cross-link density between C and GP and on C and GP concentrations as we expected.

The degradation rate of C/GP hydrogels with lower concentration of C was faster than those with higher concentrations of this polymer. This behavior was in accordance with previous studies [29,44]. As concerning as the cross-link density, the literature reports that hydrogels with high cross-link density have strong gel intensity prohibiting enzyme permeation and causing less degradation [44,45]. However, our results demonstrated that C concentration mainly affects the degradation rate as C1.6/GP15d and C1.6/GP18d (although they have high cross-link density) showed higher weight loss compared to 2%

C formulations. It can be attributed to the susceptibility of C toward lysozyme [46]. The lowest degradation rate observed for formulation with the lowest cross-link density (C2/GP7d) was also supported by our frequency sweep experiments. This hydrogel exhibited a good gel structure that can be attributed to the nucleation growth mechanism previously mentioned.

The release of ICG from formulations analyzed was not significant. This behavior could be due to an electrostatic interaction between C and ICG [32]. In the aqueous solution, the dye is negatively charged thanks to its sulphonic groups, whereas C is cationic. Therefore, the molecular weight of the ionic complex is bigger than cutoff of dialysis membrane used in our release study and ICG is not quantified in the dissolution medium.

A final consideration must be done about the sterilization of these systems: the formulations described in this preliminary work are not sterile because the kind of experiments performed (in vitro and ex vivo) does not require sterile systems. The literature shows that steam sterilization of chitosan may have different effects depending on whether sterilization was performed during its dry state or after it was in solution. Results show that autoclaving the dry chitosan power had no effect on viscosity and thus chitosan dry after sterilization does not undergo any structural changing. Thus, sterile hydrogel can be obtained by treating the dry material and working in aseptic environment [29].

At the current point of this research, we have demonstrated that a polymeric platform can be loaded with a dye to mark a liver area. Considering the results gained from the ex vivo procedure, these in situ gelled C/GP formulations have the potential to remain in correspondence of the injected site for a long period of time. As we reported before, the time of gelation of these hydrogels was a matter of second, and the process starts immediately at contact with the warmth of blood resulting in an embolization effect of the tumor. Such an approach could stop the growth and shrink the tumor burden, while leaving on site a marker, to help the following intraoperative detection of the cancer. At the same time, the removal of the fluorescent tissue would be guided throughout the operation by a real time observation of the parenchymal margins. The final result could be a better outcome for the patients, with an advantage offered by the pre-treatment of the tumor and a resulting aid during the resection. However, this preliminary study is a ‘proof of concept’ and its clinical use still requires further experiments.

## 5. CONCLUSIONS

Thermosensitive C/GP platforms were prepared and loaded with ICG, which did not interfere with their gelation process. C2/GP7d thanks to a gel-like precipitation, rapidly forms in situ compact gels and represents a good candidate for filling vessels. Taking into tumor nodules; as the solution gels in these areas, a prolonged visualization of these nodules can be achieved in 'real time imaging' during the embolization and the following hepatic resection of HCC.

## References

[1] Ferenci P, Fried M, Labrecque D, Hepatocellular carcinoma (HCC): a global perspective. *J Clin Gastroenterol*. 2010; 44:239–45.

[2] Tam KY, Leung KC, Wang YX. Chemoembolization agents for cancer treatment. *Eur J Pharm Sci*. 2011; 44:1–10.

[3] Giunchedi P, Maestri M, Gavini E, Transarterial chemoembolization of hepatocellular carcinoma. Agents and drugs: an overview. Part 1. *Expert Opin Drug Deliv*. 2013; 10:679–90.

[4] Breedos C, Young G. The blood supply of neoplasms in the liver. Am J Pathol. 1954; 30:969–77.

[5] Kemeny NE, Niedzwiecki D, Hollis DR, Hepatic arterial infusion versus systemic therapy for hepatic metastases from colorectal cancer: a randomized trial of efficacy, quality of life, and molecular markers (CALGB 9481). *J Clin Oncol*. 2006; 24:1395–403.

[6] Raoul JL, Heresbach D, Bretagne JF, Chemoembolization of hepatocellular carcinomas. A study of the biodistribution and pharmacokinetics of doxorubicin. *Cancer*. 1992; 70:585–90.

[7] Laurent A. Microspheres and nonspherical particles for embolization. *Tech Vasc Interv Radiol*. 2007; 10:248–56.

[8] Giunchedi P, Maestri M, Gavini E, Transarterial chemoembolization of hepatocellular carcinoma. Agents and drugs: an overview. Part 2. *Expert Opin Drug Deliv*. 2013; 10:799–810.

[9] Lewis AL, Gonzalez MV, Lloyd AW, DC Bead: in vitro characterization of a drug-delivery device for transarterial chemoembolization. *J Vasc Interv Radiol*. 2006; 17:335–42.

[10] Landsman ML, Kwant G, Mook G. A, Light-absorbing properties, stability, and spectral stabilization of indocyanine green. *J Appl Physiol*. 1976; 40:575–83.

[11] Gotoh H, Yamada T, Ishikawa O, A Novel Image-Guided Surgery of Hepatocellular Carcinoma by Indocyanine Green Fluorescence Imaging Navigation. *J Surg Oncol*. 2009; 100:75–9.

[12] Ishizawa T, Fukushima N, Shibahara J, Real-time identification of liver cancers by using indocyanine green fluorescent imaging. *Cancer*. 2009; 115:2491–504.

[13] Kokudo N, Ishizawa T. Clinical application of fluorescence imaging of liver cancer using indocyanine green. *Liver Cancer*. 2012; 1:15–21.

[14] Ishizawa T, Masuda K, Urano Y, Mechanistic background and clinical applications of indocyanine green fluorescence imaging of hepatocellular carcinoma. *Ann Surg Oncol*. 2014; 21:440–8.

[15] Alacam B, Yazici B, Intes X, Extended Kalman filtering for the modeling and analysis of ICG pharmacokinetics in cancerous tumors using NIR optical methods. *IEEE Trans Biomed Eng*. 2006; 53:1861–71.

[16] Peloso A, Franchi E, Canepa MC, Combined use of intraoperative ultrasound and indocyanine green fluorescence imaging to detect liver metastases from colorectal cancer. *HPB (Oxford).* 2013; 15:928–34.

[17] Unno N, Inuzuka K, Suzuki M, Preliminary experience with a novel fluorescence lymphography using indocyanine green in patients with secondary lymphedema. *J Vasc Surg.* 2007; 45:1016–21.

[18] Qiu Y, Park K. Environment-sensitive hydrogels for drug delivery. *Adv Drug Deliv Rev*. 2001; 53:321–39.

[19] Klouda L, Mikos AG. Thermoresponsive hydrogels in biomedical applications. *Eur J Pharm Biopharm.* 2008; 68:34–45.

[20] Wang J, Pang Q, Liu Z, A new liquid agent for endovascular embolization: initial clinical experience. *ASAIO J*. 2009; 55:494–7.

[21] Weng LN, Zantek ND, Rostamzadeh P, An in situ forming biodegradable hydrogel-based embolic agent for interventional therapies. *Acta Biomater*. 2013; 9:8182–91.

[22] Muzzarelli RAA. Human enzymatic activities related to the therapeutic administration of chitin derivatives. *Cell Mol Life Sci*. 1997; 53:131–40.

[23] Hirano S, Seino H, Akiyama Y, Chitosan: a biocompatible material for oral and intravenous administrations. In: Progress in biomedical polymers. Springer; USA: 1990. p. 283–90.

[24] Rassu G, Gavini E, Mattana A, Improvement of antiamoebic activity of rokitamycin loaded in chitosan microspheres. *Open Drug Deliv*. J 2008; 2:38–43.

[25] Chenite A, Chaput C, Wand D, Novel injectable neutral solutions of biodegradable gels in situ. *Biomaterials*. 2000; 1:2155–61.

[26] Chenite A, Buschmann MD, Wang D, Rheological characterisation of thermogelling chitosan/glycerol-phosphate solutions. *Carbohydr Polym*. 2001; 46:39–47.

[27] Kashyap A, Viswanad B, Sharma G, Design and evaluation of biodegradable, biosensitive in-situ gelling system for pulsatile delivery of insulin. *Biomaterials*. 2007; 28:2051–60.

[28] Gupta D, Tator CH, Shoichet MS. Fast-gelling injectable blend of hyaluronan and methylcellulose for intrathecal, localized delivery to the injured spinal cord. *Biomaterials*. 2006; 27:2370–9.

[29] Zang S, Dong G, Peng B, A comparison of physicochemical properties of sterilized chitosan hydrogel and its applicability in a canine model of periodontal regeneration. *Carbohydr Polym*. 2014; 113:240–8.

[30] Ahmadi R, De Bruijn JD. Biocompatibility and gelation of chitosan-glycerol phosphate hydrogels. *J Biomed Mater Res A*. 2007; 86A:824–32.

[31] Ruel-Gariépy E, Leclair G, Hildgen P, Thermosensitive chitosan-based hydrogel containing liposomes for the delivery of hydrophilic molecules. *J Control Release.* 2002; 82:373–83.

[32] Wu H, Zhao H, Song X, Self-assembly-induced near-infrared fluorescence nanoprobes for effective tumor molecular imaging. *J Mater Chem B*. 2014; 2:5302–8.

[33] Jauhari S, Dash AK. A mucoadhesive in situ gel delivery system for paclitaxel. *AAPS PharmSciTech*. 2006; 7:154–9.

[34] Zhou HY, Chen XG, Kong M, Preparation of chitosan-based thermosensitive hydrogels for drug delivery. *J Appl Polym Sci.* 2009; 112:1509–15.

[35] Ruel-Gariépy E, Chenite A, Chaput C, Characterization of thermosensitive chitosan gels for the sustained delivery of drugs. *Int J Pharm*. 2000; 2 03:89–98.

[36] Back JF, Oakenfull D, Smith MB. Increased thermal stability of proteins in the presence of sugars and polyols. *Biochemistry*. 1979; 18:5191–6.

[37] Coutu JM, Fatimi A, Berrahmoune S, A new radiopaque embolizing agent for the treatment of endoleaks after endovascular repair: influence of contrast agent on chitosan thermogel properties. *J Biomed Mater Res B Appl Biomater*. 2013; 101B:153–61.

[38] Khan I, Vasudevan V, Nallagatla S, Acute lung injury following transcatheter hepatic arterial chemoembolization of doxorubicin-loaded LC beads in a patient with hepatocellular carcinoma. *Lung India*. 2012; 29:169–72.

[39] Wu JJ, Chao M, Zhang GQ, Pulmonary and cerebral lipiodol embolism after transcatheter arterial chemoembolization in hepatocellular carcinoma. *World J Gastroenterol.* 2009; 15:633–5.

[40] Shiah HS, Liu TW, Chen LT, Pulmonary embolism after transcatheterarterial chemoembolization. *Eur J Cancer Care (Engl).* 2005; 14:440–2.

[41] Naorungroj T, Naksanguan T, Chinthammitr Y. Pulmonary lipiodol embolism after transcatheter arterial chemoembolization for hepatocellular carcinoma: a case report and literature review. *J Med Assoc Thai.* 2013; 96:270–5.

[42] Zhao H, Wang HQ, Fan QQ, Rare pulmonary and cerebral complications after transarterial chemoembolisation for hepatocellular carcinoma: a case report. *World J Gastroenterol.* 2008; 14:6425–7.

[43] Lapasin R, Pricl S. Rheology of industrial polysaccharides: theory and applications. Springer, London: 1995.

[44] Ganji F, Abdekhodaie MJ, Ramazani ASA. Gelation time and degradation rate of chitosan-based injectable hydrogel. *J Sol-Gel Sci Techn*. 2007; 42:47–53.

[45] Dang QF, Yan JQ, Li JJ, Controlled gelation temperature, pore diameter and degradation of a highly porous chitosan-based hydrogel. *Carbohydr Polym*. 2011; 63:171–8.

[46] Drury JL, Mooney DJ. Hydrogels for tissue engineering: scaffold design variables and applications. *Biomaterials*. 2003; 24:4337–51.

# 2.4 Indocyanine green-chitosan complexes loaded in polymeric microspheres as potential systems for transarterial embolization and intraoperative imaging of HCC: preliminary evaluation

## 1. INTRODUCTION

Hepatocellular carcinoma (HCC) is the most common type of liver cancer, with an increasing incidence in developed countries during the past 20 years [1]. Palliative, potentially curative and symptomatic treatment modalities are available for this malignancy [2]. Although the surgery remains the main approach to treat HCC, the most patients are not qualified for surgical resection [3]. Indeed, the surgical method is the primary method for early- and early-stage HCC, but the majority of tumours are diagnosed at intermediate and advanced stages, for which this curative treatment is not feasible [2,4,5]. In this case, the options are limited to palliative treatments, including transcatheter intraarterial therapies and systemic chemotherapy [4,6].

Transarterial embolization (TAE) and chemoembolization (TACE) are loco-regional approaches, widely used to treat HCC [7]. TACE involves the localized injection of chemotherapeutic agents combined with the use of embolic materials, whereas TAE consists of embolization without chemotherapy [5,8]. Although normal liver tissue receives its nutrient supply mainly from the portal vein, most HCCs are mostly vascularized by the hepatic artery [7,9,10]. The embolic agents are injected to the target site with a minimally invasive procedure, through a catheter causing artery occlusion. This allows for localized therapy directly to hepatic cancers, leading to tumour destruction and protecting the rest of the hepatic parenchyma against necrosis [11,12]. Over the years, several embolic systems has been employed, as coils, liquids and particulate agents, classified in spherical and non-spherical [13].

Permanent or temporary occlusion can be achieved using polymeric microparticles or other embolic agents, depending on their nature. Natural polymers, such as gelatin, starch and chitosan and synthetic polymers such as polylactic-co-glycolic acid (PLGA) have been employed for their fabrication [8,14].

The shape and size of embolic microparticles are critical parameters for their embolizing efficacy. Microspheres have precisely controlled sizes and show a smooth and homogeneous surface. Due to this structure, particle aggregation during the injection is avoided and compression of particles into microcatheter is feasible [13].

With regard to the sizes, microparticles ranging from 40 to 1000-1200 μm in diameter are required [8]. Usually, larger particles occlude mainly proximal vascular regions, increasing the risk of reflux and non-specific embolization. Therefore, small particles (less than 100 μm) are more favourable than larger particles because they are able to block terminal vessels, producing higher hypoxia rate [15,16].

Microparticles less than 40 μm in diameter can reach non-targeted organs, such as the lungs [17]. Different commercial systems have been successful in human embolization [18,19], but they still exhibit some disadvantages. One of the main limitations of these products is the lack of imaging capability, which would be advantageous to detect the location and distribution of embolic material. For this reason, it is necessary to explore a new type of multi-functional embolizing systems. During the last years, several researchers have focused their attention on the development of detectable embolic agents by using different traceability modalities [20-23].

Indocyanine green (ICG) is a cyanine dye that displays fluorescent properties in the near infrared region [24]. This compound has been employed in many clinical fields due its favourable properties [25]. During the last years, ICG has been employed for the identification of HCC during surgical procedures [26-28] proving that ICG is a valuable tool during hepatic resection. ICG fluorescence can be detected by using different instruments, including Photodynamic Eye (PDE) [29-32].

In 2015, *in situ* gelling thermosensitive chitosan/glycerophosphate solutions have been proposed by Salis et al. [33] for TAE application and following intraoperative fluorescence imaging of HCC. A strong interaction between chitosan and ICG loaded in the systems have been proved.

Taking into account this observation, we decided to develop a novel microparticulate system containing ICG-chitosan complexes (ICG-Cs), with the aim of obtaining suitable embolic agents in size with fluorescent properties for the treatment and the intraoperative visualization of HCC. Chitosan, a biopolymer with a wide range of biomedical applications, has been proven to be biocompatible and biodegradable [34]. The

crosslinking of chitosan with sodium tripolyphosphate (TPP), a very popular and non-toxic compound [35], has been reported in several studies. Indeed, it is possible to obtain different and safe polymeric systems through electrostatic interactions [36-40].

Cellulose acetate butyrate (CAB), used to fabricate several delivery systems [41-43] was chosen to form particle matrix due to its biocompatibility. It is a hydrophobic and thermoplastics polysaccharide obtained by esterification of hydroxyl groups of cellulose [44].

In this research work, ICG-CS complexes, prepared through spray-drying technique, have been subsequently incorporated into CAB-based microspheres (ICG-Cs-CAB), obtained by emulsion solvent extraction method.

After preparation, final microparticles were characterized for size distribution, morphology, loading and release properties. In addition, the capability for fluorescence detection of embolic microparticles was tested *in vitro* by using plasma as release medium and PDE as imaging system.

## 2. MATERIALS AND METHODS

### Materials

Chitosan (Cs) was supplied from Primex Ltd (Iceland). The material was used to prepare the corresponding hydrochloride salt.

Sodium triphosphate pentabasic (TPP), corn oil, Tween 80, N-methyl-2-pyrrolidone (NMP) and Cardiogreen® (ICG) were obtained from Sigma Aldrich (St. Louis, USA). Cellulose acetate butyrate (CAB) was an Eastman Chemical Company (Kingsport, USA) product. Plurol diisostearique CG was gently provided by Gatefossé (Saint Priest, France). All other chemicals and reagents were of analytical grade. Drug free plasma from healthy patients was kindly provided by IRCCS Fondazione Policlinico San Matteo, Pavia.

### Preparation of formulations

*Preparation of ICG-Cs complexes*

ICG-Cs complexes were prepared by ionic gelation technique [45] using TPP as cross-linking agent. Briefly, 0.06 % w/v Cs hydrochloride was dissolved in bistilled water by

magnetic stirring and after its complete dissolution, aqueous ICG (0.03 w/v) was dispersed uniformly into the polymer solution. After that, a volume of TPP (0.1% w/v), corresponding to a Cs-TPP ratio of 4:1 (w/w), was added dropwise to mixture under magnetic stirring at room temperature.

The green suspension obtained was then centrifuged at 4400 rpm for 20 mins at room temperature (Centrifuge 5702 R, Eppendorf, Hamburg, Germany) and washed several times with distilled water and then freeze-dried with Lio 5P Cinquepascale (Trezzano sul Naviglio, Italy). The freeze-dried complexes (ICG-Cs(L)) thus obtained were stored in dark within a desiccator for further use.

*Preparation of microspheres from ICG-Cs complexes*

Spherical particles were obtained from the suspension containing ICG-Cs complexes by using the emulsification/spray drying method. The previously prepared ICG-Cs suspension was concentrated until a fifth of initial volume and mixed with dichloromethane (ratio 1:2 v/v) under homogenization at 12,000 rpm (Ultra-Turrax T25 basic, IKA, Germany) in an ice bath. The emulsion, kept under magnetic stirrer, was then sprayed through the nozzle of a spray dryer model Mini Spray Dryer Büchi B-191 (Büchi Labortechnik-Technik AG, Flawil, Switzerland), within the nebulization chamber. After preparation, microspheres (ICG-Cs(SP)) were collected and stored in desiccators at 20 °C in dark conditions.

*Preparation of ICG-Cs-CAB formulation*

The formulation ICG-Cs-CAB was obtained as follows. The organic phase was prepared by dissolving CAB (0.250 g) in a mixture of NMP (2.375 g) and Tween 80 (0.166 g) under magnetic stirring in a glass vial. After dissolution of the polymer, 25 mg of CS-ICG were suspended in the organic phase. In another glass vial, Plurol diisoestearique CG was dispersed in corn oil, with magnetic stirring, to form the oil phase. After that, it was proceeded to the dropwise addition of the oil phase to the organic phase, under magnetic stirring (1000 rpm for 15 mins). The final emulsion was injected in the phosphate buffer (PB) pH 7.4, in a proportion of 1 mL of emulsion to 1 mL of buffer. Once the microspheres were formed, vacuum filtration was used in order to extract them

from the PB. The sample was rinsed with PB, collected in a cellulose acetate filter (pore size 0.2 μm), and then freeze-dried.

CAB-based microspheres containing only free ICG (ICG-CAB) were prepared following the same procedure described above, dissolving 10 mg of ICG in the organic phase instead of ICG-Cs complexes.

## Microparticles characterization

*Yield of production*

All formulations (n=3) were accurately weighed after preparation. The yields of production were calculated as the weight percentage of the final product, with respect to the initial total amount of all components, used for the preparation of samples:

$$\text{Yield (\%)} = \frac{\text{mass of microparticles}}{\text{mass of materials}} \times 100 \quad (1)$$

*Particle size analysis*

The particle size of the microparticles was determined with a Coulter LS 100Q Laser diffractometric equipment (Coulter LS 100Q Laser sizer, Beckman Coulter, Miami, USA). Different formulations (2 mg) were suspended in the medium, sonicated for 5-10 s and analyzed under gentle magnetic stirring. 2-Propanol was used as dispersion fluid for ICG-Cs(L) analysis while ICG-Cs(SP), ICG-CAB and ICG-Cs-CAB were dispersed in water. Three different dispersions were prepared for each formulation and the results are reported as the averages of three values for each dispersion (n = 9). The average particle size of the microspheres was reported as the mean size (μm).

*Drug content and encapsulation efficiency*

Real drug content of particles loaded with ICG was determined by two direct and indirect methods, depending on the formulation.

The ICG content of particles was defined as the spectrophotometrically detected amount of ICG with respect to the real amount of total materials used for the preparation. The real drug content (DC) was expressed in percent:

$$DC\ (\%) = \frac{\text{real ICG content}}{\text{total mass of components}} \times 100 \quad (2)$$

The encapsulation efficiency (EE) was expressed as the ratio of the real amount of encapsulated ICG over the total amount of ICG used, through the following equation:

$$EE\ (\%) = \frac{\text{real ICG content}}{\text{total amount of ICG}} \times 100 \quad (3)$$

The result obtained was the average of three determinations (n = 3; ± standard deviation, SD).

● *ICG-Cs(L) complexes*

The amount of loaded ICG in ICG-Cs(L) was determined indirectly by quantifying the differences between total amount of ICG and free amount of ICG in supernatant after centrifugation of final suspension obtained after the addition of TPP in ICG-Cs suspension. The sample was assayed spectrophotometrically (Thermo Spectronic; Helios Gamma, UK) at 779 nm to determine unloaded ICG. The absorbance results were correlated with ICG concentration through a calibration curve determined earlier from the standard solutions of the dye. The same solvent was used as a reference.

● *ICG-Cs(SP)*

10 mg of CS-ICG(SP) were dissolved in 100 ml HCl solution 0.1 M under stirring for 30 min. Solution was diluted in bidistilled water and ICG content analysed spectrophotometrically at 779 nm.

● *ICG-CAB*

20 mg of CAB-ICG were dissolved in 20 ml EtOH 96%. Absorption of solution was checked by UV spectroscopy at 787 nm and ICG content was determined from standard calibration curve in EtOH.

● *ICG-Cs-CAB*

The drug content of ICG-Cs-CAB microspheres was determined by dissolving 20 mg of the formulation in 10 mL of EtOH and then centrifuging the solution at 4400 rpm for 10 mins. The supernatant was analysed by spectrophotometer at 787 nm and the pellet, not solubilized in EtOH, was dissolved in 3 ml HCl 0.1 M. After that, the obtained solution

was further centrifuged and examined as above described in order to calculate ICG content.

*Morphological analysis*

Shape and surface characteristics of all formulations were studied by scanning electron microscopy (SEM). The analysis was performed using a Zeiss EVO MA10 (Zeiss, Germany) on gold sputtered samples.

### *In vitro* drug release studies

*In vitro* release studies were performed using a shaker incubator (Orbital Incubator, SI 50, Stuart Scientific, Redhill, UK) at 37 ± 0.5 °C. To detect the amount of ICG released from the different particles, ICG-Cs(SP), ICG-CAB and ICG-Cs-CAB were placed in bidistilled water pH 7.4 and stirred at 80 rpm using the horizontal shaker bath. At predetermined time intervals (0h, 1h, 3h, 6h, 8h, 24h, 1 day, 3 days, 7 days, 14 days, 21 days, 28 days) the medium (1 ml) was removed for analysis and it was replaced with the corresponding volume of water. Collected samples were centrifuged at 13000 rpm and immediately analysed spectrophotometrically ($\lambda$ = 779 nm). The same test was carried out filling ICG powder in the aqueous solution in order to make a comparison with the release behaviour of microparticles loaded with ICG. *In vitro* release studies were performed in triplicate (n=3).

### Fluorescence analysis by PDE

The potential fluorescence of ICG-Cs-CAB was evaluated *in vitro* by using plasma to simulate physiological conditions after particles administration. In order to simulate intraoperative "real time" imaging of ICG in liver, Photodynamic Eye (Hamamatsu Photonics, Hamamatsu, Japan) was used to capture the fluorescence level of microspheres.

Briefly, sample was suspended in plasma medium and then centrifuged at 4400 rpm. Fresh plasma was replaced every week for 4 weeks. Images were taken with the camera positioned about 20 cm from the sample. During the experiments, the camera light level was kept constant and the resulting images have been enhanced with the same level of

contrast and brightness.

### Injectability

The injectability of leader formulation (ICG-Cs-CAB) was evaluated by using a device made from a syringe and a pan resting on the piston of the syringe [46]. The microspheres, suspended in 4 mL NaCl 0.9% was transferred into 5-mL glass syringe equipped with 21G × 1 ½ needle, avoiding the appearance of air bubbles. Different masses (20g, 50g, 100g and 200g) were placed on the pan and the time necessary to finish the injection of the volume of formulation through the syringe was recorded. Three different concentrations of sample were tested (12.5 mg/ml, 25 mg/ml, 37.5 mg/ml). The injection flow rate was expressed as the ratio of the injection volume to the injection time. All measurements were repeated at least six times. The injectability was measured as:

$$\text{Injectability (ml/sec)} = \frac{\text{syringe volume (ml)}}{\text{time (sec)}} \quad (4)$$

## 3. RESULTS AND DISCUSSION

### Microsphere preparation and characterization

*Evaluation of yield of production, drug content and encapsulation*

The leader formulation ICG-Cs-CAB was prepared through a multi-step process. First, spherical CS-ICG complexes were prepared through spray-drying method in order to obtain small and spherical particles to be load in CAB-based microspheres. Microparticles prepared by emulsion solvent extraction method (ICG-CAB and ICG-Cs-CAB) showed highest yields of production, close to 100%, whereas ICG-Cs(L) and ICG-Cs(SP) resulted in yields about 70% and 40%, respectively (Tab. 1).

Spray-drying is a good technique for the preparation of suitable microsystems but the deposition of materials in nebulization apparatus causes low yield of production [47]. On the contrary, emulsion solvent extraction method allowed for the solidification of the majority of polymer.

Although the yield was low, ICG-Cs complexes showed the best EE, due to the strong interaction between the polymer and the dye. Non-spherical complexes having high ICG content were spray-dried, obtaining microspheres with EE about 96%.

In both formulations prepared by emulsion solvent extraction method (ICG-CAB and ICG-Cs-CAB), the amount of ICG entrapped in microspheres was lower than the theoretical value. These results indicate that some complexes ICG-Cs or free ICG were lost during the process of encapsulation. In ICG-CAB, during the extraction step, ICG quickly moves to the water phase due to its hydrophilic nature, leading to low encapsulation. In the other case, the amount of dispersed powder (ICG-Cs(SP)) was very small compared to the total volume of the emulsion, determining a low drug content.

ICG-Cs(L) particles measured between 250 and 300 nm in diameter (Tab. 1). Indeed, the microparticles were agglomerated with a broad size distribution (from 1 to 1000 μm) and large particle size.

The nebulization of ICG-Cs suspension before the lyophilisation led to the formation of smaller particles (~ 3 μm), with a narrow distribution. This size is not suitable for the embolization as reported previously [17] because the use of small particles, especially in the solid organs such as the liver, may lead to focal necrosis and abscess formation [48]. In addition, a mean particle diameter of at least 40 μm is required for embolization because smaller particles may distribute in other organs, such as lung and spleen [8], with fatal complications.

CAB-based formulations, loaded with free ICG and ICG-Cs(SP) complexes, obtained through extraction solvent method, were homogeneous mixtures of particles having a mean diameter of 65 and 70 μm, respectively.

Therefore, the composition of loaded system did not influence the size of the final systems, which showed comparable sizes. Taking into account these results, ICG-Cs-CAB could be a promising embolic system because small particles (less than 100 μm) can prevent the development of collateral arterial flow to a tumour, embolizing end-branches of the hepatic artery [49].

**Table 1.** Yields of production, encapsulation efficiency and mean size of all formulations. All results are expressed as mean ± SD.

| Formulation | Yield of production (%) | Encapsulation efficiency (%) | Mean size (µm ± SD) |
|---|---|---|---|
| **ICG-Cs(L)** | 70.89 ± 0.75 | 98.82 ± 0.23 | 275.5 ± 64.28 |
| **ICG-Cs(SP)** | 39.57 ± 2.78 | 96,11 ± 1,82 | 3.232 ± 2.277 |
| **ICG-CAB** | 95.08 ± 2.10 | 7,12 ± 0,064 | 64.57 ± 22.23 |
| **ICG-Cs-CAB** | 92.95 ± 3.09 | 12,17 ± 0.58 | 69.42 ± 24.69 |

*Morphological analysis*

The morphology and the shape of different formulations were examined by SEM. As shown in Fig. 1, the structure of ICG-Cs particles before and after the spray-drying process was drastically different (Fig 1A-1B). Indeed, ICG-Cs(L) obtained after freeze-drying showed non-homogeneous structure, due to the high concentration of TPP [50] required for substantial encapsulation efficiency.

The surface of ICG-Cs(L) formulation was irregular and it was not possible to identify individual particles (Fig. 1A), because a spongy aggregate was obtained (Fig. 1B). After nebulization of the emulsified ICG-Cs complexes, discrete particles, heterogeneous in size, were obtained (Fig. 1C). The roundness of the microspheres became better (Fig. 1D), but the surface of ICG-Cs(SP) was still clearly rough with numerous wrinkles (Fig. 1E).

The emulsion solvent extraction method led to microspheres with smooth and dense surface, without any porous structures. In addition, SEM photographs revealed that CAB-based microspheres were spherical (Fig. 1F and G), as required for the embolization procedure. Indeed, advantages of using microspheres instead of nonspherical particles for embolization purpose were reported in several experimental studies [51]. In order to examine the internal structure, ICG-Cs-CAB particles were fractured and then analysed. It was observed that smaller spherical particles (ICG-Cs(SP) complexes) were entrapped

in porous internal structure of CAB matrix, confirming the encapsulation of CS-ICG(SP) complexes inside the system (Fig. 1H).

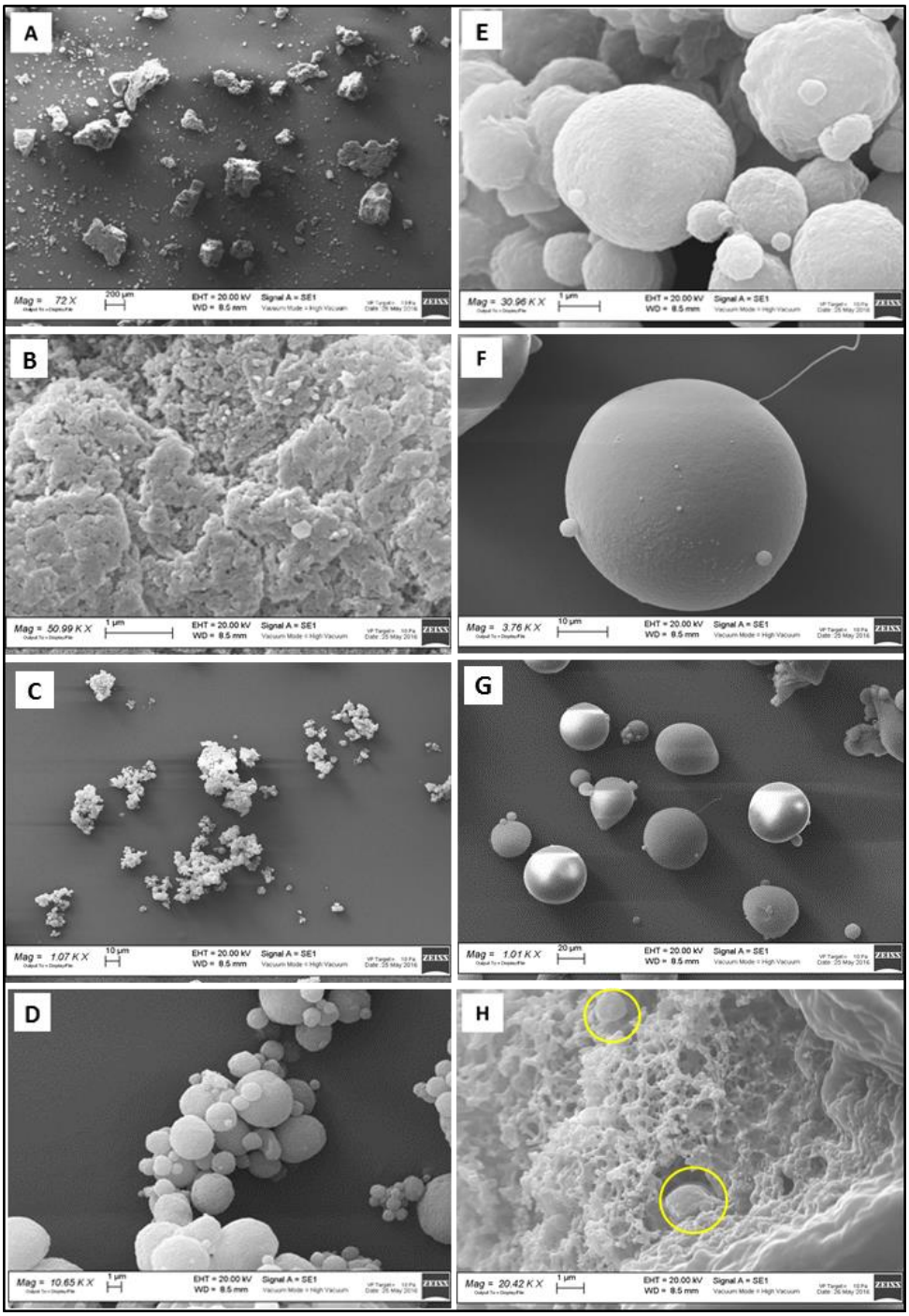


**Figure 1.** SEM images of all formulations prepared. **A**,**B**: ICG-Cs(L). **C**,**D**,**E**: shape and surface of ICG-Cs(SP). **F**: ICG-CAB. **G**: ICG-Cs-CAB. **H**: porous internal structure of CAB matrix containing ICG-Cs(SP) complexes, indicated by yellow circles.

***In vitro* drug release studies**

Release studies of ICG from different formulations were carried out in water (pH 7.4) at 37°C and the amount of released drug was measured spectrophotometrically. In order to evaluate the degradation of ICG in solution over time, standard ICG solutions were stored in the same conditions. Degradation of ICG was observed, in according to Saxena et al. [52]. Indeed, at the end of the experiment, the concentration of ICG in solution was very low. As reported in Fig. 2, ICG-CAB particles showed high initial release, suggesting a burst release, with a concomitant degradation over time.

On the contrary, ICG-Cs complexes and ICG-Cs-CAB curves displayed low release of the fluorescent dye, confirming the results obtained previously [33].

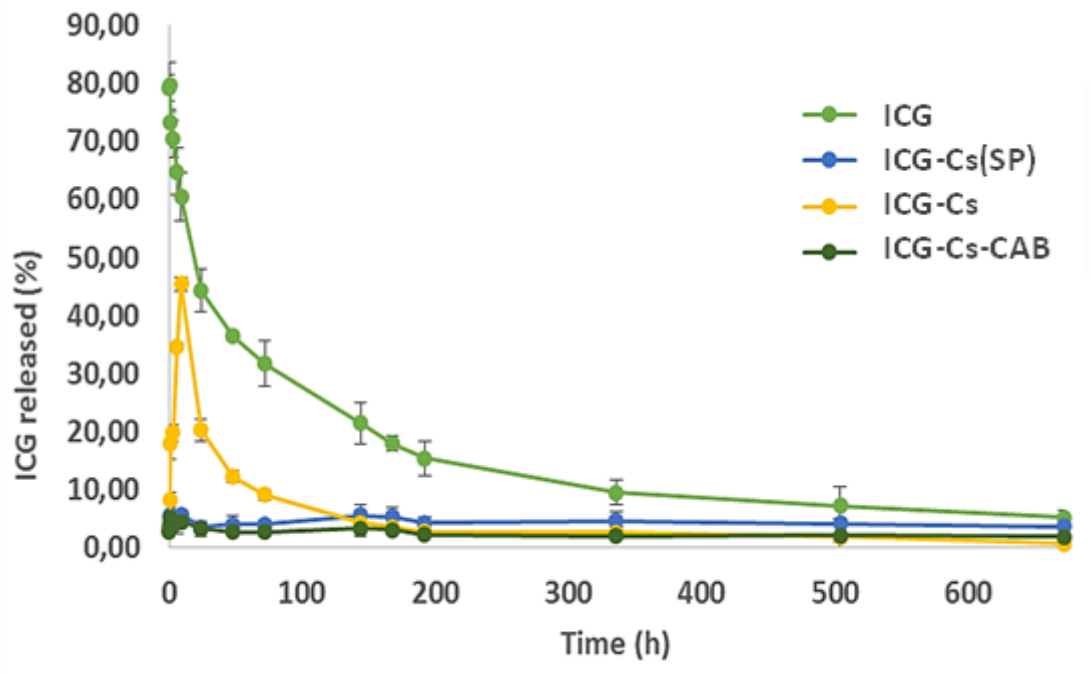


**Figure 2.** The cumulative release curves of ICG-Cs(SP) complexes, ICG-CAB and ICG-Cs-CAB particles, compared to standard solution of ICG.

This behaviour could be related with a strong interaction between chitosan and ICG [33,53], that was preserved also after incorporation of smaller complexes inside CAB-based microspheres. Both formulations showed a sustained and controlled release of the dye over the course of the test. The controlled release of ICG avoided the remarkable degradation of the cynine, because the amount constantly released was very low. In the case of ICG-Cs-CAB, dye release was delayed further by CAB matrix. The results

confirmed the capability of these systems to aid the following intraoperative detection of the cancer, thanks to the permanence of ICG inside the microspheres. The release profile of ICG-Cs-CAB was corroborated by fluorescence analysis with PDE.

**Fluorescence analysis by PDE**

ICG-Cs-CAB particles were chosen for *in vitro* fluorescence imaging studies and NIR light with wavelengths at 760 was employed for their visualization. In order to evaluate the fluorescence over time, these particled were immersed in plasma (Fig. 3A) for 4 weeks and PDE was used to visualize their fluorescence changes. Fresh plasma were replaced every week in order to simulate physiological condition. The results confirmed the capability of particles to maintain selective fluorescence until 4 weeks. No significant differences were revealed after 2 weeks and 4 weeks before plasma replacement (Fig. 3B1 and 3C1) and after this procedure (Fig. 3C1 and 3C2), demonstrating that the amount of ICG released from the system was very low in comparison with ICG entrapped in the systems. Although a low rate of ICG was released over the time, confirmed by a weak fluorescence in the plasma medium (Fig. 3B1 and 3C1), fluorescent pictures demonstrated that ICG-Cs-CAB were capable to maintain the fluorescence selectivity for 4 weeks, allowing for the clear visualization of the systems over the surrounding tissue. This represents a positive result because confirms the possibility to employ this multi-functional platform as embolic system, filling specific liver vessels that feed the tumour and as imaging tool during surgical procedure. Indeed, as reported previously [33], fluorescence of ICG loaded in the carrier could be exploited to identify tumoural region during its resection, after the shrink of cancer caused by embolization.

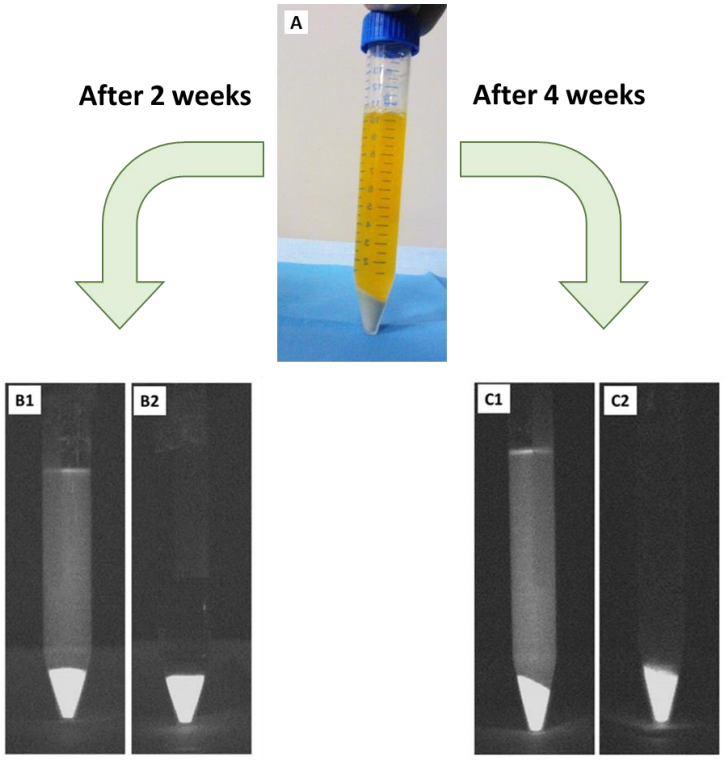


**Figure 3.** *In vitro* visualization of ICG-Cs-CAB by using PDE system.
**A**: Particles freshly incubated in plasma; **B1, C1**: ICG-Cs-CAB after 2 and 4 weeks of incubation, respectively, before plasma replacement; **B2, C2**: particles after 2 and 4 weeks of incubation before plasma replacement.

**Injectability**

The injectability of leader formulation ICG-Cs-CAB was evaluated by using the method reported by Schuetz et al. [46], with some modification. The obtained results proved the good injectability of the dried formulation suspended in 4 ml of physiological saline at different concentration, through a needle 21 $G^{1/2}$. As reported in Fig. 4, injection speed rate depended on the concentration of samples. Indeed, increasing concentration of microsphere required more time to pass in the needle, but in all cases (12.5 mg/ml, 25 mg/ml, 37.5 mg/ml), particles did not meet any resistance and no needle occlusion was found. The force needed for their injection was similar to that required for injection of saline solution in the same conditions. To prevent needle occlusion and then catheter clumping, a good suspension without aggregates had to be prepared.

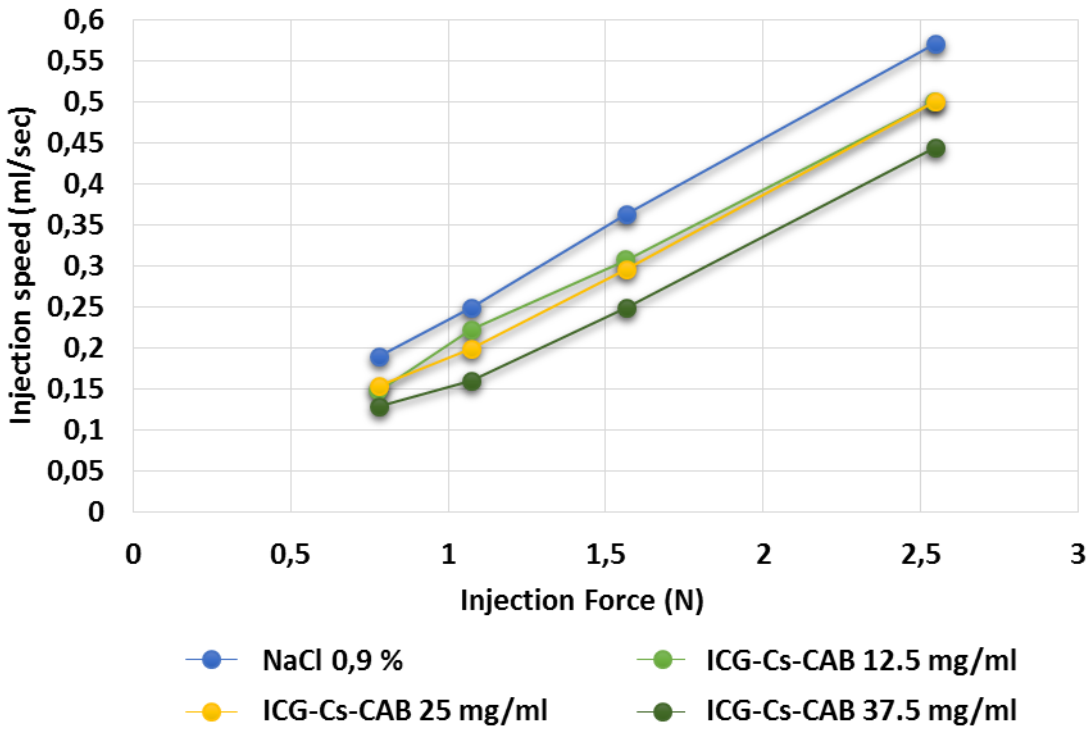


**Figure 4.** Injection speed (ml/sec) *vs* injection force (N) of ICG-Cs-CAB formulation at three different concentrations (12.5 mg/ml, 25 mg/ml, 37.5 mg/ml) compared to saline solution.

## 4. CONCLUSION

In summary, the results reported in the present work demonstrated that CAB-based microspheres loaded with ICG-Cs complexes are suitable for TAE application. Indeed, these particles showed a desirable particle size for embolic treatment. In addition, ICG release profile proved the capability of the systems to retain the dye, releasing very low ICG amount after 4 weeks. This property was also confirmed by *in vitro* PDE studies, which confirmed the selective fluorescence of particles over time. The prolonged visualization of microspheres for several weeks could be useful during the surgical resection of the liver tumour embolized previously with the same particles.

All these results suggested that ICG-Cs-CAB could be proposed as multifunctional platforms, which could perform embolization of HCC, followed by intraoperative visualization. Further *in vivo* studies are required to confirm the real potential of these systems.

**References**

[1] B. Njei, Y. Rotman, I. Ditah, J. K. Lim, Emerging trends in hepatocellular carcinoma incidence and mortality. *Hepatology*, 61 (2015) 191.

[2] S. Lin, K. Hoffmann, P. Schemmer, Treatment of hepatocellular carcinoma: a systematic review. *Liver cancer*, 1 (2012) 144.

[3] M. Maluccio, A. Covey, Recent progress in understanding, diagnosing, and treating hepatocellular carcinoma. *CA Cancer J. Clin*., 62 (2012) 394.

[4] J. A. Davila, Z. Duan, K. A. McGlynn, H. B. El-Serag, Utilization and outcomes of palliative therapy for hepatocellular carcinoma: a population-based study in the United States. *J. Clin. Gastroenterol*. 46 (2012) doi:10.1097/MCG.0b013e318224d669.

[5] P. Giunchedi, M. Maestri, E. Gavini, P. Dionigi, G. Rassu, Transarterial chemoembolization of hepatocellular carcinoma. Agents and drugs: an overview. Part 1. *Expert Opin. Drug Deliv*., 10 (2013) 679.

[6] M. Kumar, D. Panda, Role of supportive care for terminal stage hepatocellular carcinoma. *J Clin Exp Hepatol*, 4 (2014) S130-S139.

[7] Z. B. Xie, L. Ma, X. B. Wang, T. Bai, J. Z. Ye, J. H. Zhong, L. Q. Li, Transarterial embolization with or without chemotherapy for advanced hepatocellular carcinoma: a systematic review. *Tumor Biology*, 35 (2014) 8451-8459.

[8] P. Giunchedi, M. Maestri, E. Gavini, P. Dionigi, G. Rassu, Transarterial chemoembolization of hepatocellular carcinoma - agents and drugs: an overview. Part 2. *Expert Opin. Drug Deliv.*, 10 (2013) 799.

[9] C. Breedis, G. Young, The blood supply of neoplasms in the liver. Am. J. Pathol., 30 (1954) 969.

[10] J. Cazejust, B. Bessoud, N. Colignon, C. Garcia-Alba, O. Planché, Y. Menu, Hepatocellular carcinoma vascularization: from the most common to the lesser known arteries. *Diagn. Interv. Imaging*, 95 (2014) 27.

[11] R. J. Lewandowski, J. F. Geschwind, E. Liapi, R. Salem, Transcatheter intraarterial therapies: rationale and overview. *Radiology*, 259 (2011) 641.

[12] E. A. Tsochatzis, E. Fatourou, J. O'Beirne, T. Meyer, A. K. Burroughs, Transarterial chemoembolization and bland embolization for hepatocellular carcinoma. *World J. Gastroenterol.*, 20 (2014) 3069.

[13] J. J. Leyon, T. Littlehales, B. Rangarajan, E. T. Hoey, A. Ganeshan, Endovascular embolization: review of currently available embolization agents. *Curr. Probl. Diagn. Radiol.*, 43 (2014) 35.

[14] A. Poursaid, M. M. Jensen, E. Huo, H. Ghandehari, Polymeric materials for embolic and chemoembolic applications. *J. Control Release*, 240 (2016) 414-433.

[15] P. Bastian, R. Bartkowski, H. Köhler, T. Kissel, Chemo-embolization of experimental liver metastases. Part I: distribution of biodegradable microspheres of different sizes in an animal model for the locoregional therapy. *Eur. J. Pharm. Biopharm*., 46 (1998) 243.

[16] Y. Kumar, P. Sharma, N. Bhatt, K. Hooda, Transarterial Therapies for Hepatocellular Carcinoma: a Comprehensive Review with Current Updates and Future Directions (2016). *Asian Pac. J. Cancer Prev.,* 17(2), 473-478.

[17] Y. X. J. Wáng, T. De Baere, J. M. Idée, S. Ballet, Transcatheter embolization therapy in liver cancer: an update of clinical evidences. Chin. J. Cancer Res., 27(2015) 96.

[18] J. Kettenbach, A. Stadler, I. V. Katzler, R. Schernthaner, M. Blum, J. Lammer, T. Rand, Drug-loaded microspheres for the treatment of liver cancer: review of current results. *Cardiovasc. Intervent. Radiol.*, 31 (2008) 468.

[19] K. Osuga, N. Maeda, H. Higashihara, S. Hori, T. Nakazawa, K. Tanaka, M. Nakamura, K. Kishimoto, Y. Ono, N. Tomiyama, Current status of embolic agents for liver tumor embolization. *Int. J. Clin. Oncol.*, 17 (2012) 306.

[20] Choi, S. Y., Kwak, B. K., Shim, H. J., Lee, J., Hong, S. U., & Kim, K. A. (2015). MRI traceability of superparamagnetic iron oxide nanoparticle-embedded chitosan microspheres as an embolic material in rabbit uterus. *Diagnostic and Interventional Radiology*, 21(1), 47.

[21] K. V. Sharma, Z. Bascal, H. Kilpatrick, K. Ashrafi, S. L. Willis, M. R. Dreher, A. L. Lewis, Long-term biocompatibility, imaging appearance and tissue effects associated with delivery of a novel radiopaque embolization bead for image-guided therapy. *Biomaterials*, 103 (2016) 293.

[22] R. Tang, W. Huang, F. Yan, Y. Lu, W. M. Chai, G. Y. Yang, K. M. Chen, In-line phase contrast imaging of hepatic portal vein embolization with radiolucent embolic agents in mice: a preliminary study. *PloS one,* 8 (2013) e80919.

[23] M. van Elk, B. Ozbakir, A. D. Barten-Rijbroek, G. Storm, F. Nijsen, W. Hennink, T. Vermonden, R. Deckers, Alginate microspheres containing temperature sensitive liposomes (TSL) for MR-guided embolization and triggered release of doxorubicin. *PloS one,* 10 (2015) e0141626.

[24] J.T. Alander, I. Kaartinen, A. Laakso, T. Pätilä, T. Spillmann, V.V. Tuchin, M. Venermo, P. Valisuo, A review of indocyanine green fluorescent imaging in surgery. *Int. J. Biomed. Imaging*, 2012 (2012) 7.

[25] E. P. Porcu, A. Salis, E. Gavini, G. Rassu, M. Maestri, P. Giunchedi, Indocyanine green delivery systems for tumour detection and treatments. *Biotechnol. Adv*., 34 (2016) 768.

[26] K. Gotoh, T. Yamada, O. Ishikawa, H. Takahashi, H. Eguchi, M.Yano, H. Ohigashi, Y. Tomita, Y. Miyamoto, S. Imaoka, A novel image-guided surgery of hepatocellular carcinoma by indocyanine green fluorescence imaging navigation. *J. Surg. Oncol.*, 100 (2009) 75.

[27] T. Ishizawa, N. Fukushima, J. Shibahara, K. Masuda, S. Tamura, T. Aoki, , K. Hasegawa, Y. Beck M. Fukayama, N. Kokudo, Real-time identification of liver cancers by using indocyanine green fluorescent imaging. *Cancer*, 115 (2009) 2491.

[28] T. Ishizawa, K. Masuda, Y. Urano, Y. Kawaguchi, S. Satou, J. Kaneko, K. Hasegawa, J. Shibahara, M. Fukayama, S. Tsuji, Y. Midorikawa, H. Aburatani, N. Kokudo, Mechanistic background and clinical applications of indocyanine green fluorescence imaging of hepatocellular carcinoma. *Ann. Surg. Oncol*., 21 (2014) 440.

[29] T. Abo, A. Nanashima, S. Tobinaga, S. Hidaka, N. Taura, K. Takagi, J. Araia, H. Miyaakib, H. Shibatab, T. Nagayasua, Usefulness of intraoperative diagnosis of hepatic tumors located at the liver surface and hepatic segmental visualization using indocyanine green-photodynamic eye imaging. *Eur. J. Surg. Oncol*., 41 (2015) 257.

[30] M. Kaibori, M. Ishizaki, K. Matsui, A. H. Kwon, Intraoperative indocyanine green fluorescent imaging for prevention of bile leakage after hepatic resection. *Surgery*, 150 (2011) 91.

[31] S. Noura, M. Ohue, Y. Seki, K. Tanaka, M. Motoori, K. Kishi, I. Miyashiro, H. Ohigashi, M.Yano, O. Ishikawa, Y. Miyamoto, Feasibility of a lateral region sentinel node biopsy of lower rectal cancer guided by indocyanine green using a near-infrared camera system. *Ann. Surg. Oncol.*, 17 (2010) 144.

[32] Y. M. Zhang, R. Shi, J. C. Hou, Z. R. Liu, Z. L. Cui, Y. Li, Z. Y. Shen, Liver tumor boundaries identified intraoperatively using real-time indocyanine green fluorescence imaging. *J. Cancer Res. Clin. Oncol.*, 143 (2017) 51-58.

[33] A. Salis, G. Rassu, M. Budai-Szűcs, I. Benzoni, E. Csányi, S. Berkó, M. Maestri, P. Dionigi, E.P. Porcu, E. Gavini, P. Giunchedi, Development of thermosensitive chitosan/glicerophospate injectable in situ gelling solutions for potential application in intraoperative fluorescence imaging and local therapy of hepatocellular carcinoma: A preliminary study. *Expert Opin. Drug Deliv.*, 12 (2015) 1583.

[34] S. K. Shukla, A. K. Mishra, O. A. Arotiba, B. B. Mamba, Chitosan-based nanomaterials: A state-of-the-art review. *Int. J. Biol. Macromolec*., 59 (2013) 46.

[35] J. Antoniou, F. Liu, H. Majeed, J. Qi, W. Yokoyama, F. Zhong, Physicochemical and morphological properties of size-controlled chitosan–tripolyphosphate nanoparticles. *Colloids Surf. A Physicochem. Eng. Asp.*, 465 (2015) 137.

[36] Y. Huang, Y. Lapitsky, On the kinetics of chitosan/tripolyphosphate micro-and nanogel aggregation and their effects on particle polydispersity. *J. Colloid Interface Sci.*, 486 (2017) 27-37.

[37] E. M. Hejjaji, A. M. Smith, G. A. Morris, Designing chitosan-tripolyphosphate microparticles with desired size for specific pharmaceutical or forensic applications. Int. *J. Biol. Macromolec.*, 95, (2017) 564-573.

[38] S. Hassani, A. Laouini, H. Fessi, C. Charcosset, Preparation of chitosan–TPP nanoparticles using microengineered membranes–Effect of parameters and encapsulation of tacrine 482 (2015) 34.

[39] A. F. Martins, D. M. de Oliveira, A. G. Pereira, A. F. Rubira, E. C. Muniz, Chitosan/TPP microparticles obtained by microemulsion method applied in controlled release of heparin. Int. J. Biol. Macromolec., 51 (2012) 1127.

[40] M. L. Kang, J. Y. Ko, J. E. Kim, G. I. Im, Intra-articular delivery of kartogenin-conjugated chitosan nano/microparticles for cartilage regeneration. Biomaterials, 35 (2014) 9984.

[41] V. R. Babu, K. K. Rao, Y. I. Lee, Preparation and characterization of nifedipine-loaded cellulose acetate butyrate based microspheres and their controlled release behavior. Polym. Bull., 65 (2010) 157.

[42] N. S. Barakat, A. A. Ahmad, Diclofenac sodium loaded-cellulose acetate butyrate: Effect of processing variables on microparticles properties, drug release kinetics and ulcerogenic activity. J. Microencapsul., 25 (2008) 31.
[43] G. Fundueanu, M. Constantin, E. Esposito, R. Cortesi, C. Nastruzzi, E. Menegatti, Cellulose acetate butyrate microcapsules containing dextran ion-exchange resins as self-propelled drug release system. Biomaterials, 26 (2005) 4337.
[44] G. Fundueanu, M. Constantin, C. Stanciu, G. Theodoridis, P. Ascenzi, pH-and temperature-sensitive polymeric microspheres for drug delivery: the dissolution of copolymers modulates drug release. J. Mater. Sci. Mater. Med., 20 (2009) 2465.
[45] P. Calvo, C. Remunan-Lopez, J. L. Vila-Jato, M. J. Alonso, Novel hydrophilic chitosan-polyethylene oxide nanoparticles as protein carriers. J. Appl. Polym. Sci., 63 (1997) 125.
[46] Y. B. Schuetz, R. Gurny, O. Jordan, A novel thermoresponsive hydrogel based on chitosan. Eur. J. Pharm. Biopharm., 68 (2008) 19.
[47] A. Sosnik, K. P. Seremeta, Advantages and challenges of the spray-drying technology for the production of pure drug particles and drug-loaded polymeric carriers. Adv. Colloid. Interface Sci., 223 (2015) 40.
[48] M. Lubarsky, C. E. Ray, B. Funaki, Embolization agents—which one should be used when? Part 1: large-vessel embolization. Semin. Intervent. Radiol., 26 (2009) 352.
[49] Y. X. J. Wáng, T. De Baere, J. M. Idée, S. Ballet, Transcatheter embolization therapy in liver cancer: an update of clinical evidences. Chin. J. Cancer Res., 27 (2015) 96.
[50] L. Y. Wang, Y. H. Gu, Z. G. Su, G. H. Ma, Preparation and improvement of release behavior of chitosan microspheres containing insulin. Int. J. Pharm., 311, (2006) 187.
[51] A. Laurent, Microspheres and nonspherical particles for embolization. Techniques in vascular and interventional radiology, 10 (2007) 248-256.
[52] V. Saxena, M. Sadoqi, J. Shao, Degradation kinetics of indocyanine green in aqueous solution. J. Pharm. Sci., 92 (2003) 2090.
[53] H. Wu, H. Zhao, X. Song, S. Li, X. Ma, M. Tan, Self-assembly-induced near-infrared fluorescent nanoprobes for effective tumor molecular imaging. J. Mater. Chem. B, 2 (2014) 5302.

# *2.5 In situ* forming microspheres based on poly(ε-caprolactone) and ibuprofen sodium for the treatment of advanced stages of hepatocellular carcinoma

## 1. INTRODUCTION

Hepatocellular carcinoma (HCC) is one of the most common cancer in the world. It is usually diagnosed at advanced stages and patients are not suitable for curative therapies such as resection, liver transplantation and percutaneous treatments [1]. For this reason, locoregional therapies play a key role in the treatment of liver cancer [2]. Among them, transarterial embolization (TAE) is the most widely used for the treatment of advanced stages of HCC. TAE consists of injection of an embolic material in the hepatic artery cutting off the tumour's main blood supply. Ischemia and subsequent tumour necrosis can be achieved [3,4].

This therapy can cause side effects such as "post embolization syndrome" characterised by pain, sickness, and a raised temperature for several days after TAE treatment.

The most effective embolizing agents are microparticles. Calibrated PVA (polyvinylalcohol) based microspheres are available on the market [5]. All commercial products are quite successful in the clinic, even if the intra-arterial local administration of microparticles can present some difficulties such as catheter clogging [6]. There is therefore the need of new embolizing systems, possibly not based on the intra-arterial administration of preformed particles. In situ forming microspheres (ISM) could be suggested as a novel tool for the TAE treatment of HCC. They consist of injectable emulsions in which an internal organic polymer phase is emulsified in an oil phase resulting in a stable dispersion of polymer–organic solvent solution microglobules (premicrospheres) dispersed in a continuous oil phase [7]. Upon injection into the body, the system is exposed to the water from body fluids and the microglobules hardens to solid microspheres due to the diffusion of solvent out of the microglobules [8,9].

The aim of this work was the development of a novel in situ forming microsphere system based on poly(ε-caprolatone) (PC) (PCISM) that can be suggested as a novel embolic

formulation for TAE treatment of HCC. PCL is a biodegradable polymer [10] and it has not yet been used as embolic material.

Furthermore, ibuprofen sodium salt was loaded in these systems in order to evaluate their potential for the treatment of embolization post syndrome. The influence of various formulation parameters on the technological properties of our PCISM (triangular phase diagrams, size, shape, drug content, drug release) was investigated by using an experimental design.

Preliminary *in vivo* studies have been done with blank PCISM in order to evaluate the *in situ* formation of the microspheres.

## 2. MATERIALS AND METHODS

### 2.1 Materials

Polycaprolactone (PC) (MW 45000 Da), corn oil, tween 80, amaranth trisodium, ibuprofen sodium, N-methyl-2-pyrrolidone (MP) were obtained from Sigma Aldrich (St. Louis, USA). Plurol diisostearique CG was gently provided by Gatefossé (France). All other chemicals were of analytical grade.

### 2.2 Triangular phase diagrams

PC solutions in MP, with different concentrations **(**4, 6, 8, 10, 12, 14, 16% w/w) were prepared and poured in beakers equipped with magnetic stirrers. The coacervation process of PC was gained through the progressive addition of aliquots of 1 ml (0.9 g) corn oil under magnetic stirring (1000 rpm) for 1 minute. Amaranth trisodium dye was dissolved in these organic phases in order to make a distinction between the organic polymer phase and the oily phase. After each addition, progress of the coacervation process was observed by using an optical microscopic image analysis system (Quantimet 500, Leica, Cambridge, UK). The phase diagram was obtained using a 5 mL PC solution.

Following the same method, two more phase diagrams were established in order to evaluate the influence of surfactants and hydrophilic model drug in the coacervation process: In the second phase diagram, the organic phase, in which PC is dissolved, was MP and Tween 80 2% (w/w). In the third diagram the organic phase was MP with Tween

80 2% (w/w) and ibuprofen sodium salt 2% (w/w). The oil phase was corn oil with Plurol diisostearique CG 2% (w/w) for both diagrams.

### 2.3 Experimental Design

D-optimal mixture design was used to study the influence of the formulation composition on the PCISM properties. Five factors were studied and expressed as weights of PCISM: PC (A), MP (B), corn oil (C), Tween 80 + Plurol diisostearique CG weight ratio 1:1 (D) and ibuprofen sodium (E).

These factors are ingredients of an ISM formulation and their sum adds up to 100%:

$$X_1 + X_2 + X_3 + X_4 + X_5 = 10g \quad \text{(Eq.1)}$$

Furthermore, constraints were put for the amounts of each factor: PC $0.3g \leq X_1 \leq 0.5g$, MP $4.3g \leq X_2 \leq 5.1g$, corn oil $4.2g \leq X_3 \leq 4.8g$, Tween 80 + Plurol diisostearique CG $0.2g \leq X_4 \leq 0.6g$ and ibuprofen sodium $0.2g = X_5$.

Constraints for the factors were established based on our previous ternary phase diagram studies, on the limit of the stability window of our ternary systems in the presence of hydrophilic surfactants and hydrophilic drug (Figure 1 C).

Design Expert® was used to produce the experimental design (Table 1).

The experimental D-optimal plan design consisted of 17 experiments in total. It enabled application of the quadratic model for quantification of formulation factors effects and interactions on the properties of the ISM and derivation of regression models.

Quadratic Scheffé models in the mixture design comprises both linear and interaction terms and the interaction and quadratic effects are combined [11]. These models (Eq. 2) were applied in order to derive relationships between the responses (PCISM properties) and factors (mixture composition) through the statistical analysis (ANOVA).

$$Z_i = a_1X_1 + a_2X_2 + a_3X_3 + a_4X_4 + a_5X_1X_2 + a_6X_1X_3 + a_7X_1X_4 + a_8X_2X_3 + a_9X_2X_{14} + a_{10}X_3X_4 + a_{11}X_1X_2X_3 + a_{12}X_1X_2X_4 + a_{13}X_1X_3X_4 + a_{14}X_2X_3X_4 \quad \text{(Eq. 2)}$$

The responses were the particle size ($Z_1$), the roundness ($Z_2$) the encapsulation efficiency ($Z_3$), the drug released after 0.5 h, 24 h and 48 h ($Z_4 – Z_6$).

### 2.3.1 Preparation of PCISM loaded with ibuprofen sodium

The formulations reported in table 1 were prepared as follows. The organic phase was prepared by dissolving PC in a mixture of MP and Tween 80 under magnetic stirring and heating to 50°C in a glass vial. The solution was cooled to room temperature and then ibuprofen sodium was dissolved. Simultaneously, in a separate glass vial, Plurol diisoestearique CG was dispersed in corn oil, with magnetic stirring, to form the oil phase of the PCISM emulsion. When the dissolution of the drug in the organic phase was complete, it was progressed to the dropwise addition of the oil phase to the organic phase, under magnetic stirring (1000 rpm for 15 minutes), in order to form the PCISM emulsion. The amount of each compound used for the preparation of these formulations were established as a result of the previous ternary phase diagram study.

### 2.3.2 Preparation of microspheres from ISM emulsions

Each emulsion prepared by the above mentioned method was injected in the phosphate buffer 7.4 (PB), in a proportion of 1 mL of emulsion to 10 mL of buffer, contained in glass beaker.

Once the microparticles were formed, it was proceeded to their extraction from the PB by vacuum filtration. In this step of the process, each sample was rinsed several times with PB (in order to completely remove the organic and oil phase from the microspheres), collected in a cellulose filter (pore size = 0.2 μm,), and afterwards stored in a desiccator for 24h, before further analysis.

### 2.3.3 Size and roundness of microspheres

In the present work, the 17 batches of microspheres obtained from the particle hardening of the PCISM formulations reported in Table 1, were characterized for size and shape using an optical microscopic image analysis system. The system comprised of an optical microscope (Olympus BX4, Japan and Highlight 3100, Olympus Optical), video camera (Leica DF295, Germany) and software (Leica Imaging Ltd, Cambridge, England). At least each batch was analized in triplicate (500 microspheres per sample) and data were expressed as mean $\pm$SD.

Circle equivalent diameter was used to express the microsphere size and roundness to express the shape.

### 2.3.4 Drug loading and encapsulation efficiency of PCISM

In order to establish the amount of ibuprofen sodium encapsulated in the microspheres formed from the PCISM formulations under investigation (Table 1), it was performed an experiment regarding the drug loading. For this matter, 1 mL of emulsion was injected in a beaker containing 100 mL of PB, to allow the particle formation. At this point, the obtained mixture underwent a vacuum filtration, without further rinsing, collecting the microparticles in a cellulose acetate filter, as previously described. After completing the filtration, 1 mL sample was withdrawn from the filtrate, with regard to perceive the amount of ibuprofen sodium that was not encapsulated inside the microparticles. In this sense, the collected samples of filtrate were centrifuged at 13 000 rpm for 5 min, thus allowing the separation of the oil phase from the organic-aqueous phases, being the remaining ibuprofen sodium salt dissolved in the latter. The organic-aqueous phase was, then, collected, filtered using an appropriate filter, and analyzed by spectrofluorimeter (λexc= 263 nm, λem= 290 nm).

Simultaneously, for the assessment of the amount of drug encapsulated, the particles were dissolved in a 5 mL of chloroform under stirring. About 100 mL of PB was added to the above solution and chloroform was vaporized by continuous stirring at 50°C. The aqueous solution was then analyzed by spectrofluorimeter ($\lambda_{exc}$= 263 nm, $\lambda_{em}$= 290 nm).

Drug loading and encapsulation efficiency (values expressed as percentages) were estimated by using the following equations:

$$\%\ \text{Drug loading} = \frac{\text{amount of drug loaded in particles}}{\text{amount of particles}} \times 100 \qquad \text{(Eq. 3)}$$

$$\%\ \text{Encapsulation efficiency} = \frac{\text{actual amount of drug loaded in particles}}{\text{theorical amount of drug loaded in particles}} \times 100 \qquad \text{(Eq. 4)}$$

### 2.3.5 Ibuprofen sodium release studies

Drug release studies of PCISM formulations were performed by USP paddle method.
1 mL of PCISM emulsion was directly injected in PB pH 7.4 at 37°C. The rotation speed of the apparatus was 100 rpm.
At predetermined time intervals, 1 mL sample was withdrawn and immediately replaced with fresh medium. The samples removed from the medium were immediately analysed by spectrofluorimeter ($\lambda_{exc}$= 263 nm, $\lambda_{em}$= 290 nm) for the quantitation of ibuprofen sodium in our formulations. The dissolution studies were conducted in triplicate (mean values ±SD are reported).

## 2.4 Differential scanning calorimetry (DSC)

Thermal analysis were carried out on a DSC 204F1 Phoenix® differential scanning calorimeter (NETZSCH, Germany).The samples analyzed were: ibuprofen sodium salt, PC, microspheres from PCISM without drug, microspheres from PCISM with the lowest and the highest ibuprofen sodium loading.
Non-isothermal experiments were performed in the temperature range 20 – 250 °C at a heating rate of 10 °C/min and under a nitrogen purge gas flow of 50 ml/min. The samples size was 10 mg.
The onset of melting was taken as the extrapolated onset of the bulk melting endotherm. The heat of fusion of each sample was calculated as from the area of the endothermic peak.

## 2.5 X-ray diffraction

X-ray diffraction (XRD) measurements were carried out with X-ray Diffractometer (XRD) (X'Pert Pro, Philips, Netherlands) using Cu Kα radiation. Crystallographic assays were performed on Ibuprofen sodium, PC, microspheres from PCISM without drug, microspheres from PCISM with the lowest and the highest ibuprofen sodium loading.

## 2.6 Evaluation of particle hardening of PCISM emulsions by *ex vivo* studies

*Ex vivo* studies were carried out on three livers from Sprague–Dawley rats following the procedure previously reported by Salis and co-workers [12]. Briefly, each rat liver was

thermostabilized at 37°C in a plasma bath and flushed at a low pressure plasma solution. The proper hepatic artery was exposed and incised, and a polyethylene catheter inserted until resistance was met. The PCISM formulation (0,5 mL) was injected into the catheter. Then, the rat livers were fixed with paraformaldehyde 10% (w/V) in order to make histological studies.

Histological examinations of the rat livers were done to evaluate the formation of solid microspheres from the injected PCISM emulsion and their localization in the hepatic vascular bed. After paraformaldehyde fixation, the livers were washed in PB pH 7.4 and conserved at 4°C for 2 daysvin a cryoprotective solution. Then the samples were frozen in Tissue-Tek® O.C.T (optimum cutting temperature embedding medium, Sakura Finetek, Torrance, CA, USA) and sectioned with a cryostat at the temperature of -20°C into slices of 10-25 microns. The slices were observed by an Optical microscope (Zeiss, Oberkochen, Germany) equipped with a digital camera.

## 3. RESULTS

### 3.1 Triangular phase diagrams

The phase diagrams were constructed in order to determine the phase separation region where stable coacervates exist. Figure 1 shows the 3 triangular phase diagrams of our ternary systems. The phase separation process can be divided in 4 steps. The area marked in red, the added quantity of oil was sufficient to allow a stable dispersion of coacervate PC droplets where the agglomeration was very slow.

Coacervate droplets presented lower size and better homogeneity. As it is reported in the literature [13,14], well defined microspheres are formed when the conditions correspond to this step ( also called “stability window”). For lower quantity of oil added to the organic polymeric phase, the coacervate droplets were not stable and rapidly merged together to give large agglomerates which also bursted.

For higher quantity of oil, the coacervate droplets showed an extensive aggregation with irreversible precipitation.

From figure 1 A it can be observed that PC concentration affected the coacervation process. Increasing the concentration of PC in the organic phase, the stability window decreased.

The microscopical observations of the coacervation process exhibited that the incorporation of the non ionic surfactants in the mixture increased the stability of microglobules cutting down the slow agglomeration process observed in the stability window. Furthermore, PC microglobules were more spherical.

The presence of ibuprofen sodium in the organic phase decreased the stability window (Figure 1 C).

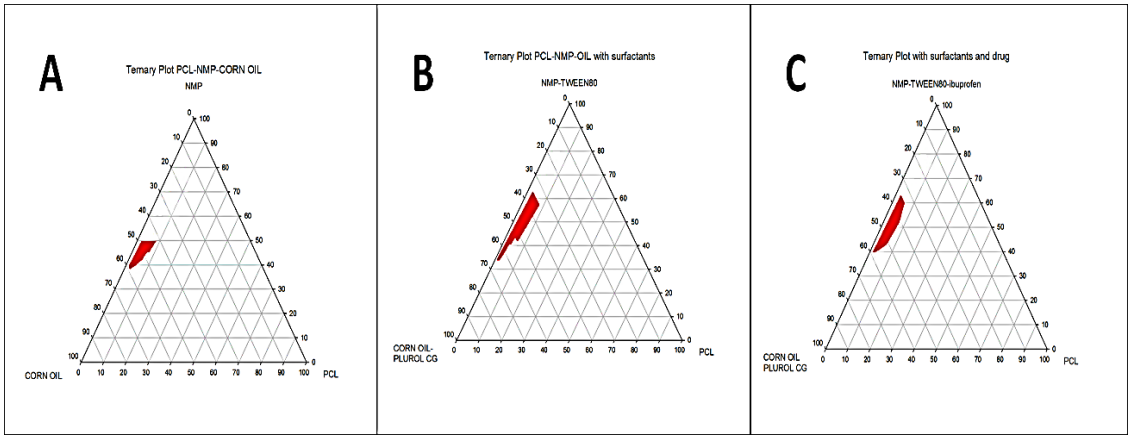


**Figure 1.** Triangular phase diagrams: A) MP-corn oil-PC; B) MP-corn oil-PC-surfactant; C) MP-corn oil-PC-surfactant-ibuprofen sodium.

### 3.2 Experimental Design

The amount of each dependant variable used to prepare the PCISM systems and the observed responses are reported in Table 1 and 2, respectively.

The responses ($Z_1$-$Z_6$) were fitted to linear-, quadratic-, special cubic- and cubic models using Design Expert® and the results of regression analysis are reported in Table 3.

**Table 1**. Experimental design of PCISM formulations.

| Batch | $X_1$ PC (g) | $X_2$ NMP (g) | $X_3$ Corn oil (g) | $X_4$ Surfactants (g) (PlurolCG:Tween 80 1:1) | $X_5$ Ibuprofen sodium (g) |
|---|---|---|---|---|---|
| **A** | 0.3 | 4.7 | 4.6 | 0.2 | 0.2 |
| **B** | 0.5 | 4.9 | 4.2 | 0.2 | 0.2 |
| **C** | 0.3 | 4.7 | 4.2 | 0.6 | 0.2 |
| **D** | 0.3 | 4.3 | 4.8 | 0.4 | 0.2 |
| **E** | 0.5 | 4.3 | 4.8 | 0.2 | 0.2 |
| **F** | 0.3 | 4.3 | 5.0 | 0.2 | 0.2 |
| **G*** | 0.3 | 5.1 | 4.2 | 0.2 | 0.2 |
| **H** | 0.4 | 4.8 | 4.2 | 0.4 | 0.2 |
| **I** | 0.4 | 4.3 | 4.5 | 0.6.00 | 0.2.00 |
| **J*** | 0.5 | 4.5 | 4.2 | 0.6.00 | 0.2.00 |
| **K** | 0.4 | 4.5 | 4.45 | 0.4.00 | 0.2.00 |
| **L** | 0.5 | 4.3 | 4.6 | 0.4.00 | 0.2.00 |
| **M** | 0.5 | 4.6 | 4.5 | 0.2.00 | 0.2.00 |
| **N** | 0.3 | 4.5 | 4.4 | 0.6.00 | 0.2.00 |
| **O** | 0.4 | 4.425 | 4.675 | 0.3.00 | 0.2.00 |

*with repetition

**Table 2.** Experimental design of PCISM systems and the observed responses with statistically significant model.

| Batch | $Z_1$ (particle size, μm) | $Z_3$ (encapsulation efficiency%) | $Z_4$ (Cumulative release g at 0.5h) | $Z_5$ (Cumulative release g at 48h) |
|---|---|---|---|---|
| **A** | 377.8 | 32.32 | 0.005 | 0.189 |
| **B** | 450.2 | 56.4 | 0.003 | 0.180 |
| **C** | 122.8 | 30.79 | 0.095 | 0.201 |
| **D** | 160.9 | 31.35 | 0.017 | 0.169 |
| **E** | 276.6 | 57.02 | 0.007 | 0.201 |
| **F** | 256.8 | 56.64 | 0.009 | 0.191 |
| **G** | 243.9 | 43.65 | 0.027 | 0.196 |
| **H** | 171.2 | 42.97 | 0.076 | 0.200 |
| **I** | 185.6 | 33.50 | 0.137 | 0.201 |
| **J** | 174.9 | 40.50 | 0.065 | 0.205 |
| **K** | 200.4 | 55.95 | 0.061 | 0.202 |
| **L** | 248.9 | 52.80 | 0.021 | 0.198 |
| **M** | 372.5 | 48.45 | 0.003 | 0.201 |
| **N** | 207.5 | 37.53 | 0.121 | 0.185 |
| **O** | 201.0 | 50.30 | 0.044 | 0.200 |

**Table 3.** Results of regression analysis for responses with statistically significant model.

| Responses | $R^2$ | Adjusted $R^2$ | Predicted $R^2$ | *p* value | Lack of it (*p*-value) |
|---|---|---|---|---|---|
| $Z_1$ (size) | 0.9049 | 0.8097 | 0.3152 | 0.0023 | 0.1375 |
| $Z_3$ (encapsulation efficiency) | 0.9887 | 0.9638 | 0.7859 | 0.0004 | 0.4689 |
| $Z_4$ (release % at 0.5 h) | 0.9977 | 0.9926 | 0.8087 | < 0.0001 | 0.1488 |
| $Z_6$ (release % at 48 h) | 0.9910 | 0.9711 | 0.8471 | 0.0002 | 0.8862 |

**Regression equations of the fitted model**

$Z_1 = 4519.47X_1-156.59X_2-150.48X_3+513.79X_4-42.52X_1X_2-53.34X_1X_3-64.55X_1X_4+6.72X_2X_3-7.93X_2X_4$

$Z_3 = -437.78X_1+83.68X_2+103.17X_3+2202.77X_4+5.93X_1X_2+2.32X_1X_3+69.45X_1X_4-3.89X_2X_3-52.92X_2X_4-60.34X_3X_4-1.45X_1X_2X_4+1.39X_2X_3X_4$

$Z_4 = -165.44X_1+20.40X_2-1.31X_3+2141.09X_4 -1.70X_1X_2+4.08X_1X_3-467.81X_1X_4-0.30X_2X_3-29.05X_2X_4-19.69X_3X_4+6.61X_1X_2X_4+4.10X_1X_3X_4$

$Z_5 = 226.08X_1+28.13X_2+30.41X_3+102.82X_4-10.66X_1X_2-10.78X_1X_3-11.96X_1X_4-1.19X_2X_3-0.37X_2X_4-2.57X_3X_4+0.35X_1X_2X_3+0.39X_1X_3X_4$

From Table 3 it can be seen that response $Y_1$ was found to follow modified quadratic model while responses $Y_3$, $Y_4$ and $Y_5$ fitted modified special cubic model. These models are modified because no significant model terms (*p* value > 0.05) were excluded from the fitting.

The high $R^2$ values and the *p*-values of lack of fit (> 0.1) achieved by the fitted models are synonymous with reliability of the design.

No significant model was found for response $Y_2$ (roundness) and $Z_5$ (drug release at 24 h). The values of roundness measured were almost similar for all formulations of the experimental design.

The short range of values (1.534-1.220) does not imply relationships between this response and factors selected for the generation of the experimental design. Furthermore, considering the short range of roundness values, the microspheres obtained from all PCL-ISM formulations of the mixture design displayed similar spherical shape.

Considering the regression equations reported in Table 3, it can be observed the presence of coefficients with more than one factor term in all of them that means interaction terms. Consequently, the value of the response variables depends highly on the quantities of all components in the PCISM system.

The interaction effect of $X_1$ was seen with $X_2$, $X_3$ and $X_4$ for response $Z_1$ (size). In addition, factor $X_2$ showed an interaction with $X_3$ and $X_4$. Responses $Z_3$, $Z_4$ and $Z_5$ displayed coefficients with three factor terms. For example, there is an interaction effect between factor $X_1$, $X_2$ and $X_4$, and between $X_2$, $X_3$ and $X_4$ for response $Z_3$.

### 3.2.1 Preparation of microspheres

The injection of 1 ml of emulsion in 10 mL of phosphate buffer lead to a fast hardening process of the PC microglobules into solid microspheres. For all formulations reported in table 1 the hardening rate was no more than 5-10 seconds. Regarding the ability of PC microglobules to form microspheres in situ, the fast hardening process showed by PCISM systems with surfactants could be explained by the presence of Tween 80% that allowed consistent extraction of the organic and oily vehicles in water [7].

### 3.2.2 Size of microspheres

From Table 2 as well as from the regression equation, it can be stated that particle size of PCISM systems is highly and negatively affected by surfactants. An increase in the amount of surfactants leads to a linear decrease of particle size. It can be also observed that microspheres with the highest values of mean diameter can be achieved at surfactants level of about 0.2g.

Another important factor that influence this response is the concentration of PC. For surfactants level of about 0.2 and 0.4g, it can be noticed that the mean particle diameter decreases when the concentration of PC increases up to 0.4g and after that increasing the component content (PC quantity higher than 0.4g) leads to the decrease in the response value.

From Table 2 it can be seen that, at fixed level of surfactants of about 0.2g, the response $Z_1$ increases when PC increase from 0.4 to 0.5g and MP increases from 4.3 to 4.9g while corn oil decreases from 5.0 to 4.2g. When the level of surfactants is fixed at 0.4g, higher values of size can be obtained when PC decreases from 0.4 to 0.3g and MP increases from 4.3 to 4.7g while corn oil decreases from 4.6 to 4.2g. In the same way, this response increases even when PCL increases from 0.4 to 0.5g, NMP decreases from 4.89 to 4.7 and corn oil increases from 4.2 to 4.5g.

### 3.2.3 Drug content and Encapsulation Efficiency

Summary of the results obtained are showed in Table 2. It can be observed that our systems exhibited an encapsulation efficiency ranging from 26.52 to 57.02 %.

Formulations with the lowest amount of PC (0.3g) showed the lowest ability to entrap the drug. The opposite behaviour can be observed for formulation with the highest amount of PC (0.5g).

Formulations with the same quantity of PC displayed an increase of encapsulation efficiency increasing the polymer phase: oil phase ratio and/or decreasing the amount of surfactants.

### 3.2.4 Ibuprofen sodium release studies

Drug release studies of PCISM systems are reported in Figure 2. No significant model was found for drug cumulative release at 24h. On the contrary, statistically significant models were found for responses $Y_4$ (drug cumulative release at 30 min) and $Y_6$ (drug cumulative release at 48 h). The release at 30 min is highly influenced by the surfactants quantity. The amount of drug released increases when surfactants quantity moves from 0.2g to 0.6g.

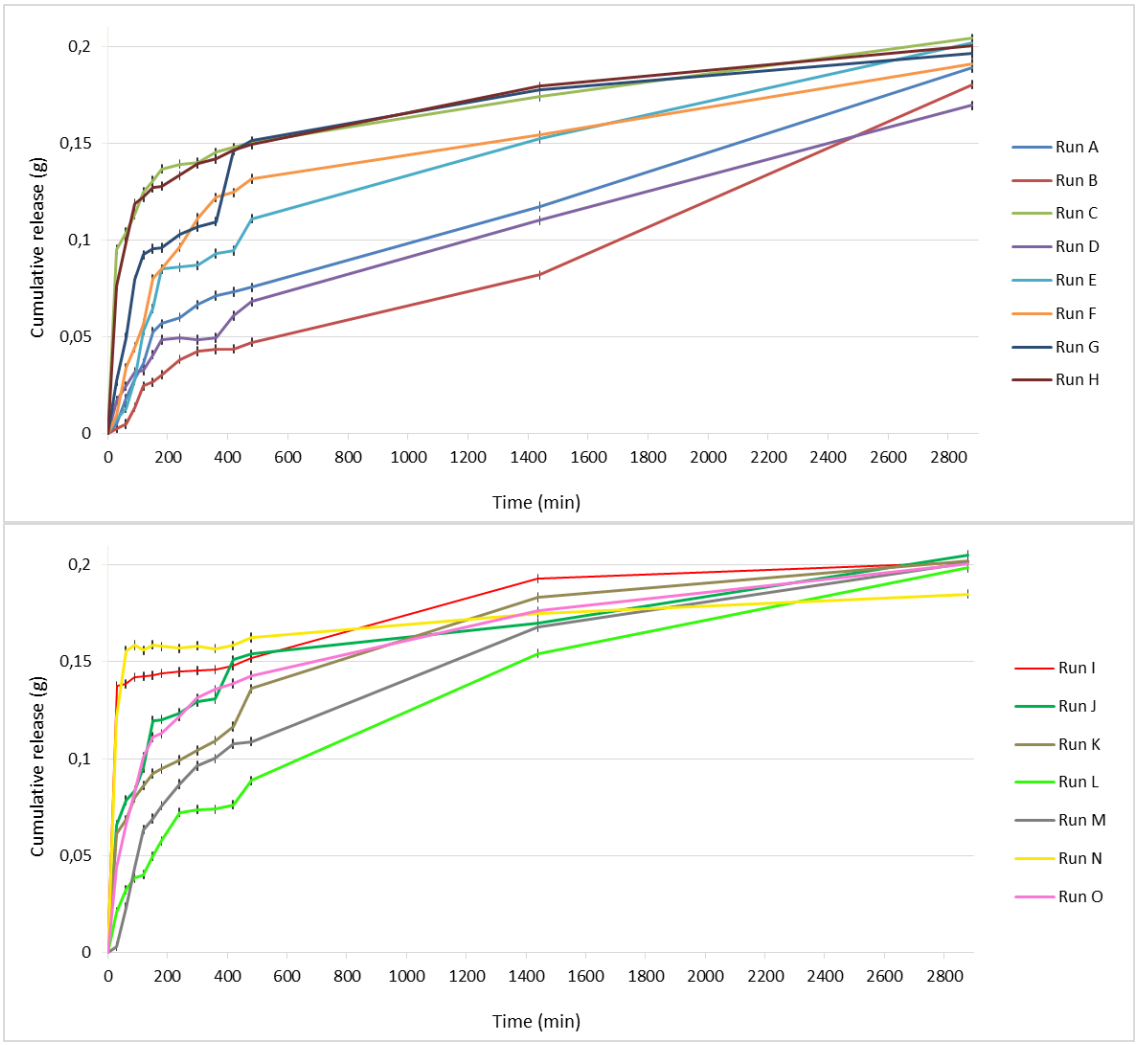


**Figure 2.** Drug release studies of PCISM formulations of the experimental design.

### 3.3 Differential Scanning Calorimetry

DSC analysis showed the absence of the characteristic endotermic peak of crystalline ibuprofen sodium (that melts at 197.8 °C, Figure 3A) in both formulations loaded with this drug (Figure 3D-E).

The amorphous state of the drug could be related with the fast particle hardening process of PCISM which does not allow the recrystallization of the drug.

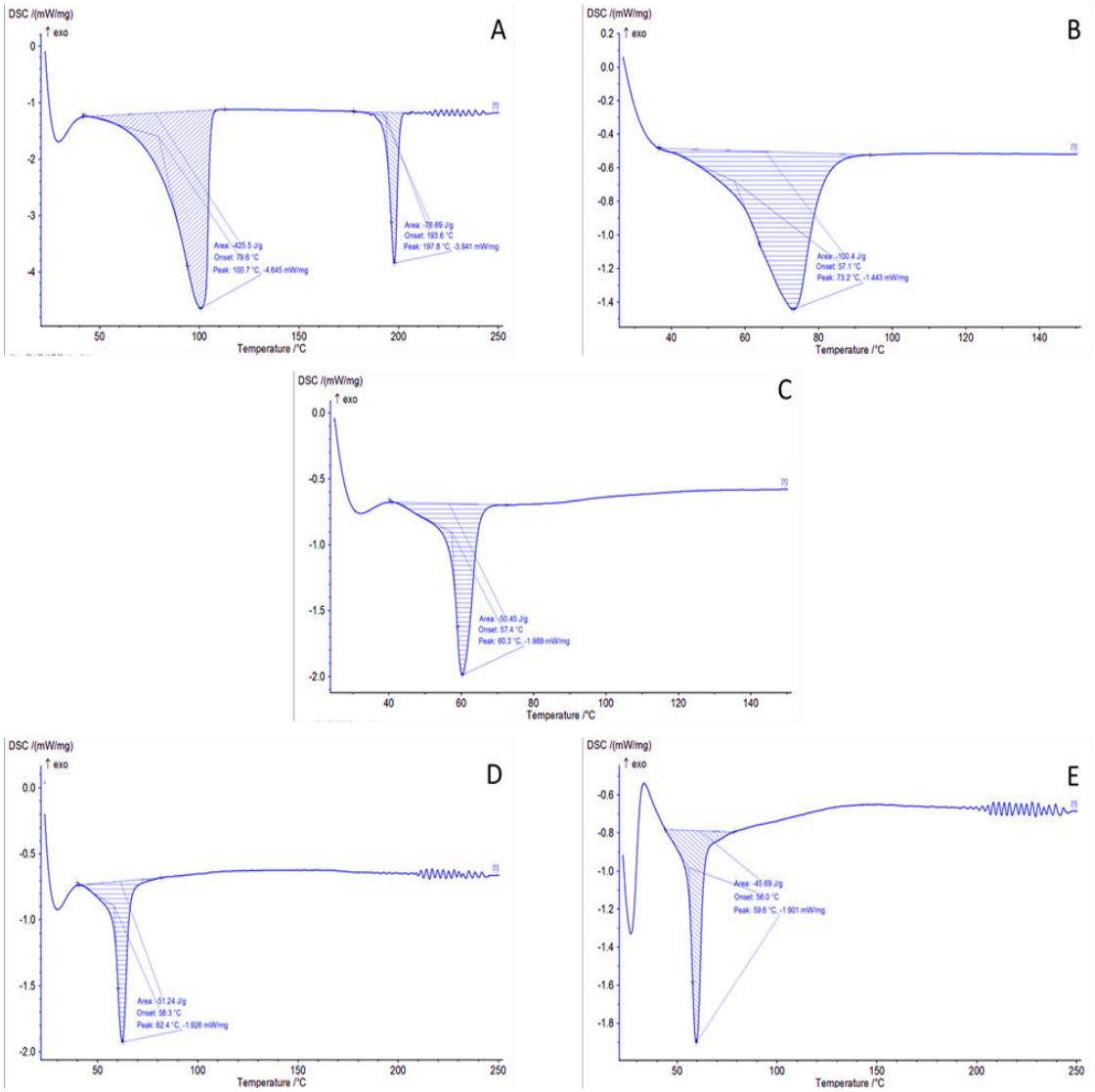


**Figure 3.** DSC thermograms of: A) ibuprofen sodium; B) PC; C) blank PCISM; D) PCISM loaded with 12.93% ibuprofen sodium; E) PCISM loaded with 18.63% ibuprofen sodium.

### 3.4 X-ray diffraction

From Figure 4, characteristic diffraction peaks of ibuprofen sodium are noticed in both spectrum of PC microspheres loaded with 18.63% and 12.93 % of ibuprofen sodium salt. Anyway, X-ray assays showed that the drug loaded in the PC microspheres lost most of its cristallinity, clearly evident in the X-ray diffraction spectra of ibuprofen sodium (Figure 4).

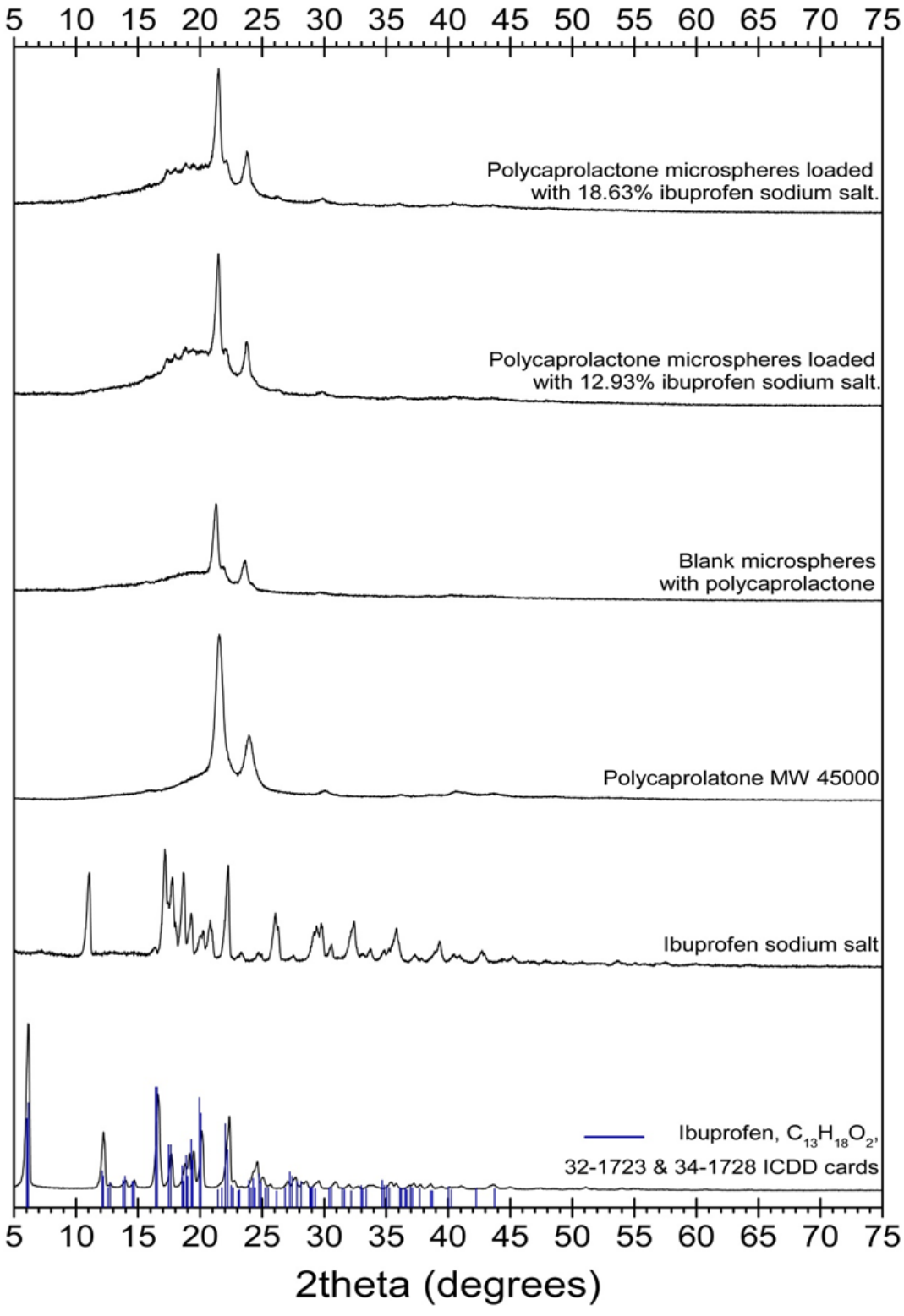


**Figure 4.** X-ray diffraction spectra of ibuprofen; ibuprofen sodium; PC; blank PCISM; PCISM loaded with 12.93% ibuprofen sodium; PCISM loaded with 18.63% ibuprofen sodium.

### 3.5 Evaluation of particle hardening of PCISM emulsions by *ex vivo* studies

The injection of the selected PCISM emulsion was performed as previously reported. The formulation was injected through the catheter without any substantial resistance and there was no clogging.

Sections of the liver around the injected site revealed the presence of solid PC particles inside the vessels. From Figure 5 it can be seen PC microsphere within a vessel of the portal space. The particle seems to occlude the lumen of the blood vessel.

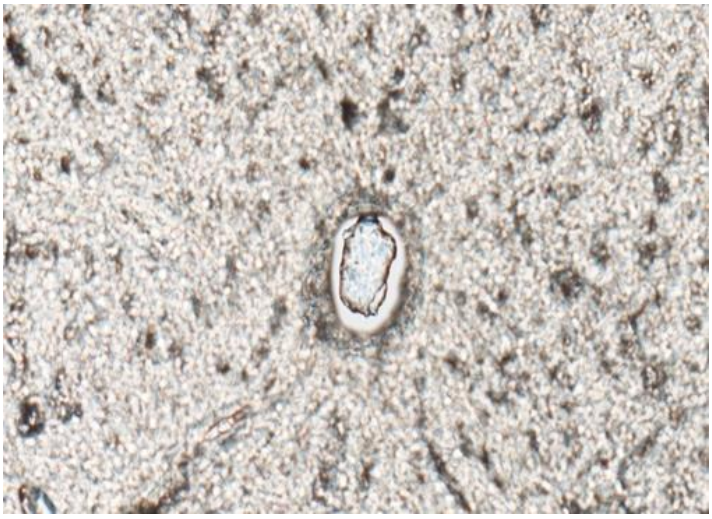

**Figure 5.** Liver section and particle hardening assessment from *ex vivo* embolization studies (magnification 10X).

## 4. DISCUSSIONS

### 4.1 Triangular phase diagrams

A phase diagram of a ternary mixture oil-organic solvent-polymer generally represents a usefull approach for the determination of the phase separation region where stable coacervates exist. In our studies we have also considerated the possible effect of non ionic surfactants and hydrophilic drug incorporated in these type of ternary mixtures. The rationale was the influence of these parameters on the characteristics of ISM based on PLGA previously reported in literature [7,15]. Briefly, the incorporation of non ionic surfactant with low HLB in the oil phase prevented the adhesion of PLGA microglobules to each other. The addition of a non ionic surfactant with high HLB in the organic phase

improved the spherical shape of PLGA microglobules and the extraction of the organic and oily vehicles in fisiological fluids. In this way, well fined and disaggregated microspheres could be obtained avoiding the formation of agglomerated PLGA mass.
The influence of PCL concentration in the stability of coacervates (Figure 1) could be explained as follow: higher polymer concentration lead to higher viscosity of the organic phase. As a consequence, the microglobules are bigger and more unstable.
The decrease of the stability window due to the incorporation of the drug in the organic phase could be considered reasonable. The PCL coacervate droplets are more concentrated because of the presence of the drug.
The incorporation non ionic surfactants in the ternary system produced PCL microbules more spherical. This behaviour could be explained by the presence of the surfactant with high HLB (Tween 80) in the organic phase as it reported by Jain and coworkers [7] for ISM based on PLGA. Furthermore, the increased stability of microglobules could be explained by the presence of the surfactant with low HLB (Pluroldiisostearique CG) in the oil phase.

### 4.2 Experimental Design

In order to assure the desired product quality, it is important to analyze the influence of the formulation factors on the properties of ISM formulations and to develop quantitative regression models. When the examined factors are ingredients of a formulation, their amounts cannot be varied independently of the others, since they add up to 100%, and a mixture experimental design is recommended [16]. From the different types of the mixture experimental designs, the D-optimal mixture design offers greater flexibility in the choice of the levels of the factors [17]. For this reason, a D-optimal mixture design with upper-bound and lower-bound constraints was used to assess the influence of the formulation composition on the PCISM properties.

#### 4.2.1 Preparation of microspheres

The fast hardening process observed during the injection of our ISM emulsion in PB pH 7.4 could be considered an efficient property in terms of an eventual application of these formulations as embolic agents.

The ISM emulsion could be delivered close to the tumor and the fast in situ microspheres formation can fill its vessels. The microspheres will be formed just in these vessel cavities avoiding migration into collateral arteries.

### 4.2.2 Size of microspheres

From the regression model related to the mean particle diameter, it can be concluded that variable surfactants show more significant effect than the other variables. It can be explained with the importance of these excipients for the stability of coacervates reducing the surface tension of PC microglobules. As a result, low surface tension allow to small particle hardened from these systems. Another important component is PC. The increase of particle size for PC quantity beyond the level of 0.4g can be related to a beginning of instability of coacervate droplets of our PCISM formulations. This phenomenon can be also highlighted with the studied triangular phase diagrams (Figure 1) where it can be observed that PCISM mixtures with PC amount in the range of 0.4 to 0.5g are close to the boundary (limit) of the stability window (stable coacervate phase).

### 4.2.3 Drug content and Encapsulation Efficiency

As it is reported in Table 2 (and confirmed by regression models), increasing PC amount increased the amount of drug entrapped into the polymer matrix. The rationale of this behaviour is that the particle hardening rate increases when polymer microglobules are more concentrated [7].

The increase of encapsulation efficiency for formulations with the same amount of PC but with higher polymer phase: oil phase ratio could be due to the increase of the oily barrier (increasing with decreasing polymer:oil phase ratio) between the aqueous buffer and the internal polymeric solution [15]. The hydrophilic drug dissolved in the polymer phase does not have affinity to the external oil phase. Thus, the drug will stay more in the inner polymer phase and more encapsulation can be achieved.

The oil formed a partial barrier (increasing when polymer:oil phase ratio decreases) between the aqueous medium and the internal polymer solution. The low solubility of the active agent in the external oil phase caused the drug to stay in the inner polymer phase as it was encapsulated within the precipitated microparticles.

The increase of encapsulation efficiency for formulations with the same amount of PC but with lower amount of surfactants, could be considered a result of the low quantity of Tween 80. It slows down the extraction of the organic and oily vehicles made by the aqueous buffer and as a concequence, the transportation of the drug to the aqueous phase is slower.

The high hydrophility of ibuprofen sodium can be considered another parameter that affect the encapsulation efficiency. The high affinity of this drug to the aqueous buffer accelerates its diffusion during the hardening of PCL microglobules.

### 4.2.4 Ibuprofen sodium release studies

The treatment of post embolization syndrome requires the use of anti-inflammatory drugs to relieve the pain. As it is reported in the literature, it is required to release and delivery a large quantity of anti-inflammatory drug within the first hour of therapy, followed by a slower release over a period of 24-48 h [18]. As a result, the PCISM systems developed have the potential to be used for the treatment of post embolization syndrome. Indeed, Figure 2 shows that PCISM systems are capable to release a big amount of ibuprofen sodium in 30 min. Furthermore, the complete release of this drug can be achieved in 48 h.

## 4.3 Differential Scanning Calorimetry

DSC analysis of the PCISM formulations loaded with ibuprofen sodium (with the highest and lowest drug loading) displayed the loss of typical ibuprofen sodium crystallinity, by the absence of the peak characteristic of the crystalline ibuprofen sodium salt. This behaviour means that the drug is entrapped in the polymer matrix in the amorphous state. The amorphous state of the drug could be related with the fast particle hardening process of PCISM, which does not allow the recrystallization of the drug.

## 4.4 X-ray diffraction

From X-ray spectra of PCISM loaded with ibuprofen sodium, it can be observed the presence of diffraction peaks of ibuprofen. This behavior implies that the drug was molecularly incorporated in PC microspheres. Furthermore, X-ray assays (Figure 4)

showed the lost of cristallinity of ibuprofen sodium salt when it is loaded into the PCISM. The drug is entrapped in the PC microspheres in the amorphous state confirming the results obtained with DSC studies. The fast release of this hydrophilic drug from our formulations can be also considerate dependent on the amorphous state of the drug in our microspheres. The amorphous form may improve the dissolution rate of the drug in the aqueous medium.

### 4.5 Evaluation of particle hardening of PCISM emulsions by *ex vivo* studies

The ex vivo studies were performed to evaluate the usefulness of PCISM formulations as embolic platforms. The PCISM emulsion selected for this experiment was formulation C from the experimental design reported in Table 1. The particle hardening of this mixture lead to microspheres with mean particle diameter of about 120 μm. As it is reported in literature, it is usually suggested to use embolic agents with size similar to formulation C in order to reach the smallest cancer-feeding blood vessels [18,19].
The results showed that the selected PCISM emulsion used for these experiments was capable to harden into solid microspheres in the hepatic arterial bed after coming into contact with the plasma. Histochemical studies showed that our systems could be retained by the arterial system due to the fast hardening of PC microglobules into well-defined microspheres. Taking into account this result, the distribution of the microspheres in the blood circulation and subsequent cardiopulmonary embolism can be avoided [20,21].

## 5. CONCLUSIONS

Taking into account the obtained results, PCISM system represent a good candidate for the treatment of advanced stages of HCC. It could be injected through a catheter into tumor nodules and as the emulsion hardens into solid microspheres, an embolization in the artery feeding the tumour will occur. In addition, the efficient loading of ibuprofen sodium into PCISM systems and the release of this drug within 2 days are important accounts for the use of these platforms in the treatment of post embolization syndrome.

## References

[1] Tam KY, Leung KC, Wang YX. Chemoembolization agents for cancer treatment. *Eur J Pharm Sci* 2011; 44:1-10.

[2] Giunchedi P, Maestri M, Gavini E, et al. Transarterial chemoembolization of hepatocellular carcinoma. Agents and drugs: an overview. Part 1. *Expert Opin Drug Deliv* 2013; 10:679-90.

[3] Breedos C, Young G. The blood supply of neoplasms in the liver. Am J Pathol 1954; 30:969-77.

[4] Kemeny NE, Niedzwiecki D, Hollis DR, et al. Hepatic Arterial Infusion Versus Systemic Therapy for Hepatic Metastases From Colorectal Cancer: A Randomized Trial of Efficacy, Quality of Life, and Molecular Markers (CALGB 9481). *J Clin Oncol* 2006; 24:1395-1403.

[5] Giunchedi P, Maestri M, Gavini E, et al. Transarterial chemoembolization of hepatocellular carcinoma. Agents and drugs: an overview. Part 2. *Expert Opin Drug Deliv* 2013; 10:799-810.

[6] Lewis AL, Gonzalez MV, Lloyd AW, et al. DC Bead: in vitro characterization of a drug-delivery device for Transarterial Chemoembolization. *J Vasc Interv Radiol* 2006; 17:335-42.

[7] Jain RA, Rhodes CT, Railkar AM, et al. Controlled release of drugs from a novel injectable in situ formed biodegradable PLGA microsphere system. *J Microencapsul* 2000; 17:343-62.

[8] Jain RA, Rhodes CT, Railkar AM, et al. Controlled release of drugs from injectable in situ formed biodegradable PLGA microspheres: effect of various formulation variables. Eur J Pharm Biopharm 2000; 50:257-62.

[9] Kranz H, Bodmeier R. A biodegradable in situ forming system for controlled drug release. *Pharm Sci Suppl* 1998; 1:414.

[10] Woodroof MA, Hutmacher DW. The return of a forgotten polymer—Polycaprolactonein the 21st century. *Prog Polym Sci* 2010; 35:1217-56.

[11] Esbensen KH, Guyot D, Westad F, et al. Multivariate Data Analysis - in Practice: An Introduction to Multivariate Data Analysis and Experimental Design. CAMO Software, Aalborg University: Esbjerg 2002.

[12] Salis A, Rassu G, Budai-Szűcs M, et al. Development of thermosensitive chitosan/glicerophospate injectable in situ gelling solutions for potential application in intraoperative fluorescence imaging and local therapy of hepatocellular carcinoma: A preliminary study. *Expert Opin Drug Deliv* 2015; 12: 1583-96.

[13] Ruiz JM, Tissier B, Benoit JP. Microencapsulation of peptide: a study of the phase separation of poly( D,L-lactic acid-co-glycolic acid) copolymers 50/50 by silicone oil. *Int J Pharm* 1989; 49:69-71.

[14] Stassen S, Nihant N, Martin V, et al. Microencapsulation by coacervation of poly(lactide-co-glycolide): Physicochemical characteristics of the phase separation process. *Polymer* 1994; 35:777-85.

[15] Kranz H, Bodmeier R. A biodegradable in situ forming system for controlled drug release. *Pharm Sci Suppl* 1998; 1:414.

[16] Hinkelmann, K., Kempthorne, O. Designs and Analysis of Experiments. Volume 1, John Wiley and Sons Inc., New York (2007).

[17] Lewis, G.A., Mathieu, D., Phan-Tan-Luu, R. Mixtures in a constrained region of interest. In Pharmaceutical Experimental Design (J. Swarbrick, ed.), pp. 413-454. Marcel Dekker, New York (1999).

[18] Borovac T, Pelage JP, Kasselouri A, et al. Release of ibuprofen from beads for embolization: in vitro and in vivo studies. *J Control Release* 2006; 115:266-74.

[19] Kettenbach J, Stadler A, Katzler IV, et al. Drug-loaded microspheres for the treatment of liver cancer: review of current results. *Cardiovasc Inter Rad* 2008; 31:468-76.

[20] Bastian P, Bartkowski R, Köhler H. et al. Chemo-embolization of experimental liver metastases. Part I: distribution of biodegradable microspheres of different sizes in an animal model for the locoregional therapy. *Eur J Pharm Biopharm* 1998; 46: 243-54.

[21] Brown KT. Fatal pulmonary complications after arterial embolization with 40–120-μm tris-acryl gelatin microspheres. *J Vasc Inter Radiol* 2004; 15:197-200.

# CHAPTER 3

## Drug delivery strategies for therapeutic applications

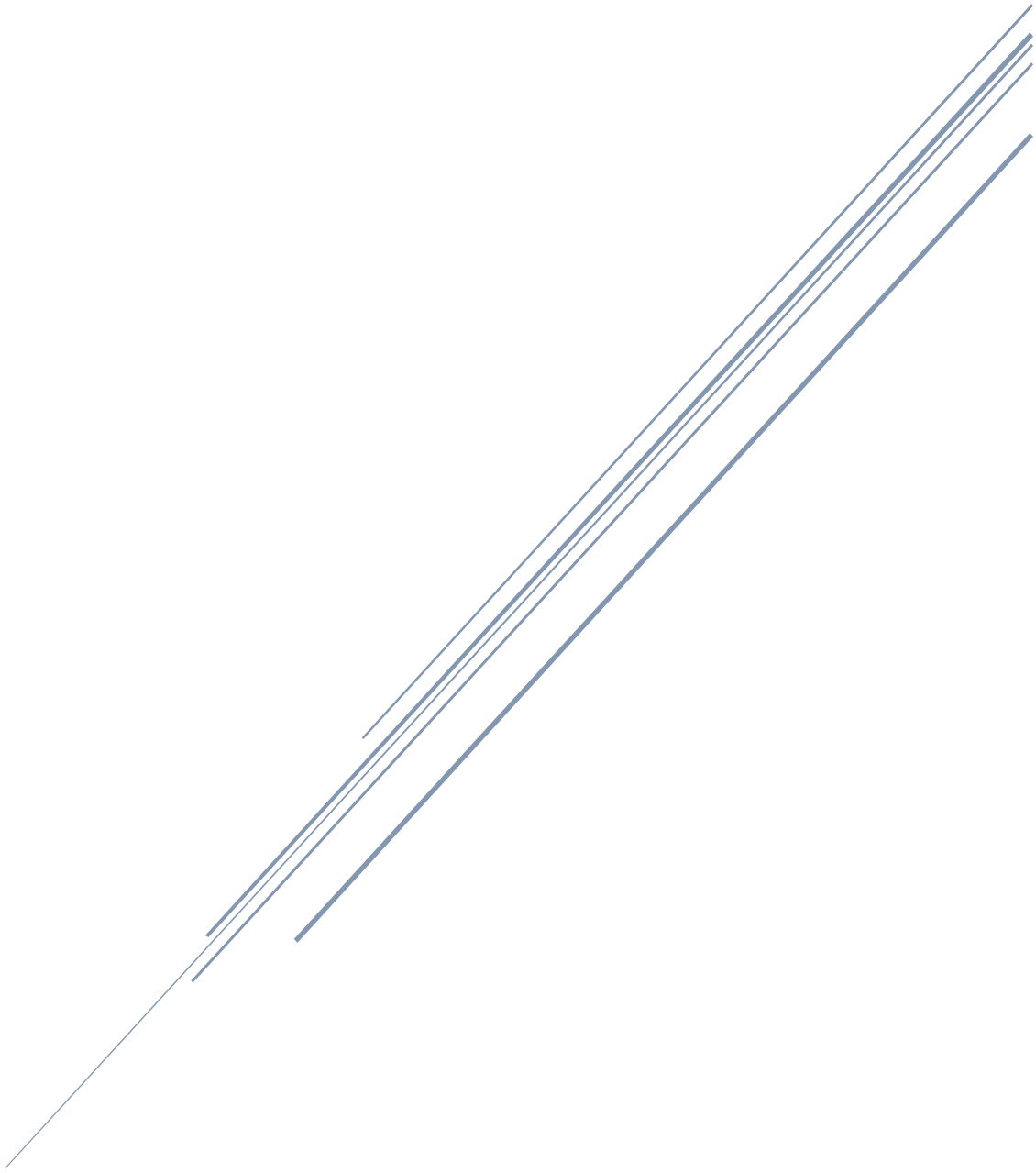

# 3.1 Engineered microparticles based on drug–polymer coprecipitates for ocular-controlled delivery of Ciprofloxacin: influence of technological parameters

*Adapted from:*

**Engineered microparticles based on drug–polymer coprecipitates for ocular-controlled delivery of Ciprofloxacin: influence of technological parameters**

Elisabetta Gavini, Maria Cristina Bonferoni, Giovanna Rassu, Giuseppina Sandri, Silvia Rossi, Andrea Salis, Elena Piera Porcu, Paolo Giunchedi. *Drug Development and Industrial Pharmacy*. 42(4), 554-562.



## 1. INTRODUCTION

Topical eye drops represent a remarkable part of ophthalmic medications present in the market for treating diseases of the anterior segment of the eye. The rapid ocular clearance is however a remarkable limit of this kind of formulations. The bioavailability of the drug administered topically is consequently very low because once the drops are placed onto the eye surface; they are rapidly diluted and washed out by tearing and blinking. Most of the liquid ocular formulations are consequently drained away from the precorneal area in few minutes. The preparation of ocular solutions containing a drug overdose can be a method to compensate these effects, but this is not the optimal choice because greater doses can also determine increased side effects and toxicity [1].The therapeutic effect of an ocular drug formulation can be improved by prolonging its contact with the corneal surface.

Fluoroquinolones are characterized by a remarkable activity against the most frequent Gram-positive and Gram-negative ocular pathogens. They are broad spectrum bactericidal agents with activity against many important corneal pathogens including staphylococci, Neisseria gonorrhea, Haemophilus influenzae, Enterobacteriaceae and Pseudomonas aeruginosa [2,3]. Bacterial keratitis is an important infective pathology

because it may arise secondary to corneal epithelial breakdown associated with dry eye, use of contact lens and trauma. The optimal therapeutic approach should firstly require the identification of the causative microorganism; however, the etiological agent could be rarely identified in time for the selection of the correct antibiotic therapy. For a rapid and successful therapeutic treatment, the empirical choice of a wide broad-spectrum agent can therefore be very important3. Recently, an interesting paper has been published regarding the surveillance of the activity of fluoroquinolones against ophthalmic pathogens in Europe in the 2010–2011 period [4]. Ciprofloxacin, a fluoroquinolone antibiotic, is active against a broad spectrum of aerobic Gram-positive and Gram-negative bacteria. Its partition coefficient (log P, octanol-Tris model) is –1.31 [5]. The resistance to this drug is developed slowly, with aminimal toxicity associated with its use. For all these reasons, this drug can be currently considered the anti-bacterial agent of choice for the eye [6,7] and it is often utilized for the treatment of ocular pathologies, such as bacterial infections and/or corneal ulcers. However, the ocular treatment with this antibiotic is characterized by low compliance because it requires frequent drug administrations. It is reported that ciprofloxacin eye drops need to be administered every 15–30 min in acute infections and at least 6–7 times daily in severe pathologies [8]. Furthermore, ciprofloxacin presents a pH-dependent solubility, which becomes very low at the pH of tears [9,10] with consequent possible problems of low bioavailability.

The development of topical controlled release formulations of ophthalmic drugs can be a way to improve their low ocular bioavailability with respect to the traditional eye drops, in particular by decreasing the clearance rate of the formulation from the precorneal area [11] and by controlling as much as possible drug release in this more prolonged time of contact. Therefore, ciprofloxacin is a good candidate for the preparation of ocular controlled release formulations to be administered in the precorneal site. The preparation of drug delivery systems for the sustained release of actives to the precorneal regions of the eye is a field of general and remarkable interest for the design of an ocular therapy. The main challenge of such treatments is to sustain sufficiently high concentrations of the drug in the corneal region.

In order to enhance the bioavailability of the drugs administered by the ocular route and to improve their compliance, the design and preparation of different delivery systems and/or new strategies are possible. Early examples of improvement of the ocular

bioavailability concerned the use of hydrogels or solutions that change to a gel after instillation, such as those based on Gelrite [12,13] or poly(vinylalcohol) and polymethacrylic acid

Derivatives [14]. Vesicular systems, such as liposomes [14–19], chitosan coated liposomes [20] and niosomes [11] have also been prepared. Recently, gel-forming ocular films based on xyloglucan for the ocular delivery of ciprofloxacin have been proposed [21]. Moreover, the preparation of microparticles with suitable size can be a way to achieve a precorneal prolonged residence time. These microparticles are polymeric microspheres, constituted by biodegradable and/or mucoadhesive polymers [22–30]. Microspheres based on ion-exchange resins for ocular drug administration have been used, even if until now there are very few examples of this kind of controlled release formulations designed for the ophthalmic route [31–33]. The ionic interaction between polymers (polyelectrolytes) and oppositely-charged drugs has been previously proposed by our group as a way to develop ocular controlled release drug formulations. The drug–polymer interaction results in insoluble coprecipitates that dissociate only in the presence of the medium's counterions, thus slowly releasing the drug. Once the drug is released, the polymer dissolves, leaving no residues in the site of administration [34–37]: this is particularly important in the case the route is constituted by the eye.

The aim of this work was the study of the influence of the technological parameters on the particle size of drug/polymer

coprecipitates obtained by a procedure of ionic interaction and engineered for ocular administrations. Ciprofloxacin was chosen as a model alkaline drug. The polyelectrolytes used are two anionic polymers able to interact with alkaline drugs: lambdacarrageenan and chondroitin sulfate. Lambda carrageenan is anatural hydrocolloid, already proposed as viscolyser in eye-drop formulations [38]. Chondroitin sulfate is a polysaccharide similar to hyaluronic acid in its properties [36,37], already used as lubricant for the treatment of dry eye [39]. The final goal was to obtain aqueous suspensions containing microparticulate coprecipitates engineered with a size suitable for ocular controlled drug administrations. This size should be lower than 25 mm40 limit that fulfills requirements of American Pharmacopeia for ophthalmic formulations.

In some suspensions, Carbomer (Carbopol 934P) was added to improve the mucoadhesive behavior of the microparticles. This polymer has good and well-known

mucoadhesive properties and it has been already used for the preparation of ocular formulations [41,42].

Different technological parameters were taken into account for the preparation of the suspensions: concentration of the solutions of drug and polymer, temperature, kind and concentration of surfactant(s), stirring. A light scattering technique was used for the studies of particle size of the coprecipitates. Mucoadhesion tests were carried out using the ‘‘inclined plane’’ method [43,44], in order to characterize the capability of these systems to be retained in the precorneal region.

## 2. MATHERIALS AND METHODS

### 2.1 Materials

Ciprofloxacin HCl (CPX) was a generous gift from Bayer, Milan, Italy. Chondroitin 6 sulfate (CS) was purchased from Fluka Chemie (Buchs, AG CH). Lambda-carrageenan (CR) Viscarin GP Q1 109 NF (FMC Corporation) was donated by Prodotti Gianni, Q1 Milan, Italy. Carbomer (CB) (Carbopol 934P, BF Goodrich, Brecksville, OH).Polyoxyethylene 20 sorbitan monooleate (Tween 80), Aldrich Chemie Gmbh, Steinheim, Germany. Sorbitan monooleate (Span 80) Aldrich Chemie Gmbh, Steinheim, Germany. Mucin type II crude from porcine stomach was purchased from Sigma Chemical Co., St Louis, MO. All of the other solvents and chemicals used were of reagent grade.

### 2.2 Preparation of the CPX/CS and CPX/CR microparticle systems

Solutions of the two polyelectrolytes, CS and CR, were prepared separately in distilled water at the concentration of 0.5% w/v. These solutions were then slowly added dropwise into an equal volume of 1% w/v CPX solution in distilled water, under magnetic stirring and at room temperature. This slow addition determined the formation of microparticles represented by coprecipitates, due to the ionic interaction that happens between drug and polyelectrolytes.

The resulting formulations (constituted by suspensions) are named hereafter as COP 1 and COP 2, respectively. An aqueous solution of CB at the concentration of 0.25% w/v (pH 7.5, adjusted with triethanolamine) was then added at room temperature to samples

of the two suspensions, achieving two other suspensions named COP 3 and COP 4, respectively. Table 1 summarizes the compositions (expressed as percentage w/v) of all the suspensions prepared.

On the basis of the experimental results obtained in the particle size characterization (carried out as below described), the suspension more suitable in terms of size of particles for ocular administration (COP 1, based on CS), was used as reference formulation for the further studies of formulation parameters.

**Table 1.** Compositions (% w/v) of CPX suspensions prepared.

| Suspensions | CPX (% w/v) | CS (% w/v) | CR (% w/v) | CB (% w/v) |
|---|---|---|---|---|
| **1** | 0.50 | | | |
| **2** | 0.50 | | 0.25 | |
| **3** | 0.25 | | | 0.125 |
| **4** | 0.25 | | 0.125 | 0.125 |

The influence of the following parameters on the particle size of the coprecipitates in suspension was studied: (a) concentrations of drug (CPX) and polymer (CS) solutions; (b) possible use of surfactants (kind and concentration); (c) temperature; (d) stirring. Concentrations of the solutions: aqueous solutions of CPX and CS at different concentrations (w/v) were prepared and mixed together with the method previously described, in such a way to obtain suspensions (named A1–4) of drug/polymer (CPX/CS) coprecipitates of different final concentrations. The concentrations of the solutions are reported in Table 2, while the concentrations of the corresponding suspensions obtained from these solutions are reported in Table 3. In all these preparations, the drug/polymer weight ratio was always maintained 2/1.

Use of surfactants: the kind and amount of surfactant(s) were evaluated as a possible formulation parameter. Tween 80 was used alone or in combination with Span 80 in two different weight ratios, named Mix 1 (72:28 w/w) and Mix 2 (53:47 w/w), respectively. The surfactants were dissolved in the CPX and CS solutions, to obtain the suspensions T1–T3, whose final composition is reported in Table 4. Temperature: an aqueous solution of CS (0.5% w/v) was added dropwise, as previously described, to a solution of CPX (1% w/v) maintained under magnetic stirring, at a temperature of 40 °C. The obtained

suspension is named as B1 (final concentration 0.5%w/v). Stirring: CS solution (0.5% w/v) was dropwise added to CPX solution (1% w/v), sonicated and stirred by paddle. The obtained suspension was named C1 (final concentration 0.5% w/v).

**Table 2.** Compositions (% w/v) of the solutions of CPX and CS used for the preparation of the suspensions A1–4.

| **Components** | ***Solution A1*** | ***Solution A2*** | ***Solution A3*** | ***Solution A4*** |
|---|---|---|---|---|
| ***CPX*** | 0.250 | 0.50 | 1.00 | 1.50 |
| ***CS*** | 0.125 | 0.25 | 0.50 | 0.75 |

**Table 3.** Compositions (% w/v) of the CPX/CS suspensions A1–4.

| **Components** | ***A1*** | ***A2*** | ***A3*** | ***A4*** |
|---|---|---|---|---|
| **CPX** | 0.125 | 0.250 | 0.50 | 0.750 |
| **CS** | 0.075 | 0.125 | 0.25 | 0.375 |
| **Final total concentration** | 0.200 | 0.370 | 0.75 | 1.130 |

**Table 4.** Compositions (% w/v) of the suspensions T1–3 containing surfactants.

| **Components** | **T1** | **T2** | **T3** |
|---|---|---|---|
| **CPX** | 0.500 | 0.500 | 0.500 |
| **CS** | 0.250 | 0.250 | 0.250 |
| **Tween 80** | 0.100 | - | - |
| **Mix 1** | - | 0.100 | - |
| **Mix 2** | - | - | 0.020 |

### 2.3 Resuspension test

To determine the resuspendability of the formulations, a test was carried out as follows: a sample of A3 suspension was centrifuged, the supernatant was then eliminated, and the coprecipitate resuspended in distilled water to obtain the original concentration (0.50% w/v CPX and 0.25 w/v CS) giving the suspension named C2.

### 2.4 Particle-size analysis

Particle size and particle-size distributions were determined and studied by the method of laser diffractometry, using the Colter Laser Diffraction apparatus (Colter LS 100Q Laser Sizer, Beckman Colter, Miami, FL). Particle size analyses were performed, at room temperature, on different samples of the prepared suspensions constituted by the drug/polymer coprecipitates. The samples of the suspensions were always manually stirred (for about 5 s) before analysis. The average particle sizes were expressed as volume-surface diameters (dvs, mm) [45]. The results were calculated as a mean of six determinations (SD50.30). Particle size distributions were expressed as percentage distribution by volume. The results of the particle size distributions were also expressed in terms of SPAN factor (mm), which was calculated as follows:

$$SPAN = (d_{90} - d_{10}) / d_{50} \quad (1)$$

where $d_{10}$, $d_{50}$ and $d_{90}$ are the diameter sizes and the given percentage value (by volume) is the percentage of particles smaller than that size. A high SPAN value indicates a wide particle size distribution [46,47].

### 2.5 Morphological analysis

SEM microphotographs (Zeiss DSM 962, Zeiss, Germany) of the coprecipitate were taken as follows: after freeze-drying, the samples were placed on double-sided tape, which had been previously secured to aluminum stubs, and then analyzed at 20 kV acceleration voltage after gold spattering in an argon atmosphere.

### 2.6 Evaluation of mucoadhesion by means of the ‘‘inclined plane’’

Mucoadhesion was measured using the method of the ‘‘inclined plane’’, as previously described [43,44]. Briefly, the ‘‘inclined plane’’ apparatus basically consisted of an inclined plane (angle of inclination = 60°, surface area = 28 $cm^2$) thermostated at 37 °C and of an electronic microbalance (Sartorius L420P, Germany) Q1 connected with a personal computer. Porcine gastric mucin (Sigma, Italy) was used as a biological substrate. Mucin films Q1 were prepared directly on the plane: 2.5 ml of an aqueous 8% w/w mucin dispersion were placed on the plane, which was kept horizontal at 45 °C for 45 min to dry, and 250 mg of formulation (suspension) was placed on the plane previously coated with the biological substrate and kept horizontal. The plane was then inclined and the amount of formulation dropped on the microbalance was recorded: the mucoadhesivity was expressed as percentage of formulation remained on the surface of the plane. As a comparison, measurements without mucin were also carried out using the inclined plane as such, at the same experimental conditions employed in presence of the biological substrates. The results are expression of three measurements (SD <4%). The ‘‘inclined plane’’ method aimed to evaluate the contribution of rheology of formulation to the mucoadhesive potential.

### 2.7 Statistical analysis

Statistical analysis of data was performed using analysis of variance (ANOVA) followed by a post-hoc Tukey’s All Pairs Comparison (Graph-Pad Prism, version 2.01; GraphPad Software Incorporated). Significance was taken as $p < 0.05$.

### 2.8 Stability test

The stability of the leader formulation (A3) was carried out as follows: the aqueous suspension of methylparaoxybenzoate (0.08% w/v) and propylparaoxybenzoate (0.02% w/v) was added and stored at 4–8 °C and 25 °C for 6 months. The morphology of the microparticles was checked by an optical microscope.

## 3. RESULTS AND DISCUSSION

The results of particle size analyses of COP 1–4 suspensions, expressed as percentage distribution by volume are reported in Table 5. Among all the suspensions, COP 1 (prepared using CS as polyelectrolyte) presents the best results in terms of particle size suitable for ocular administration. In fact 97% of the population of particles has a size <25 mm and 100% of particles have a size <<50 mm. The polyelectrolyte CR leads to particles of larger size: COP 2 presents in fact only 13.6% of particles with a size <25 mm and about 44% with a size<50 mm. This result is probably due to the formation of aggregates among the microparticles, whose size becomes lower after prolonged sonication (data not reported). SEM pictures confirmed that the process of coprecipitation creates almost spherical particles with rough surface, as previously reported [36]. The roughness of the microparticles depends on the technique of preparation, which involves the precipitation of self-assembled polymer chains, more hydrophobic owing to the interaction with the drug [36]. In order to keep the ocular formulation in the conjunctive area as long as possible, a mucoadhesive polymer was added. However, the addition of the mucoadhesive polymer CB determines different consequences on the particle size of the suspensions, depending on the polyelectrolyte used for the formation of the coprecipitates. The suspension based on CS (COP 3) is characterized by particles with a larger size with respect to the corresponding suspension without CB (COP 1) (about 49% <25 mm versus 97%, respectively). The suspension based on CR (COP 4) has particles with lower size with respect to the corresponding suspension without CB (COP 2) (47% <25 mm versus about 13%,respectively). As a consequence of this different effect of CB on the size of the suspensions based on the two polymers (CS and CR), COP 3 and COP 4 present a similar particle size distribution. The modification of the particle size of the suspensions that is found after the addition of the mucoadhesive polymer CB could be due to the adsorption of this polymer onto the surface of the microparticles made by the preformed coprecipitates. However, also a possible chemical interaction between the drug and the polyelectrolyte (CB) should be taken into account. Sahoo et al. [48] in fact recently prepared an oral controlled release gastro-retentive dosage form constituted by mucoadhesive suspensions of CPX with Carbopol 934, using a method of ultrasonication. Results from FTIR and Raman spectroscopic analyses carried out by the authors, suggested that in these formulations the carboxylic groups of CPX and hydroxyl groups

of Carbopol undergo a chemical interaction, probably leading to esterification and hydrogen bonding, even if they do not report any influence of this chemical interaction on the particle size of the suspensions [48].

**Table 5.** Percentage distribution by volume ($d_{vs}$, µm).

| | *% by volume* | | |
|---|---|---|---|
| *Suspensions* | **< 25 µm** | **< 50 µm** | **< 90 µm** |
| *COP 1* | 97.0 | 100.0 | 100.0 |
| *COP 2* | 13.6 | 43.8 | 81.0 |
| *COP 3* | 49.0 | 81.1 | 99.1 |
| *COP 4* | 47.3 | 80.2 | 99.6 |

Starting from the results of particle size analyses and from the consideration that the suspension containing CS has a good mucoadhesive behavior itself, even without the addition of Carbopol, it was decided to use CS as polyelectrolyte for the further preparation of the ocular suspensions, without any addition of CB to the formulations. The parameter evaluated was then the concentration of CPX and CS solutions used for the preparation of the microparticulate coprecipitates. Four different suspensions (A1–4) were prepared and characterized in terms of particle size, starting from four different combinations of CPX and CS concentrations (solutions A1–4, Table 2). The results were expressed as mean volume-surface diameter ($d_{vs}$) [45] and SPAN values, calculated using Equation (1). The concentrations of the CPX and CS solutions used for the preparation of the suspensions have a remarkable influence in determining the particle size and particle size distributions. As shown in Figure 2 (where mean diameters dvs are reported), the solutions A2 and A3 lead to the suspensions A2 and A3, which are characterized by the lowest mean diameters ($d_{vs}$ about 3 µm). The solutions A4, characterized by higher CPX and CS concentrations with respect to A2 and A3, lead to the formation of A4 suspension, which has particles with a bigger size ($d_{vs}$ 4.25 µm; $p < 0.0001$). The use of more diluted concentrations (A1 solutions), leads to the highest mean diameter ($d_{vs}$8.5 mm; $p < 0.0001$).

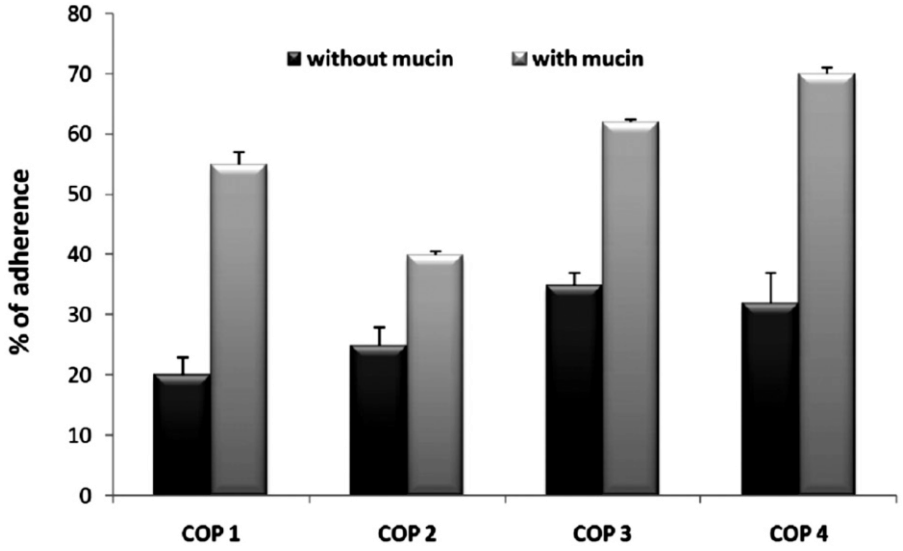


**Figure 1.** Mucoadhesive properties of COP 1–4 suspensions.

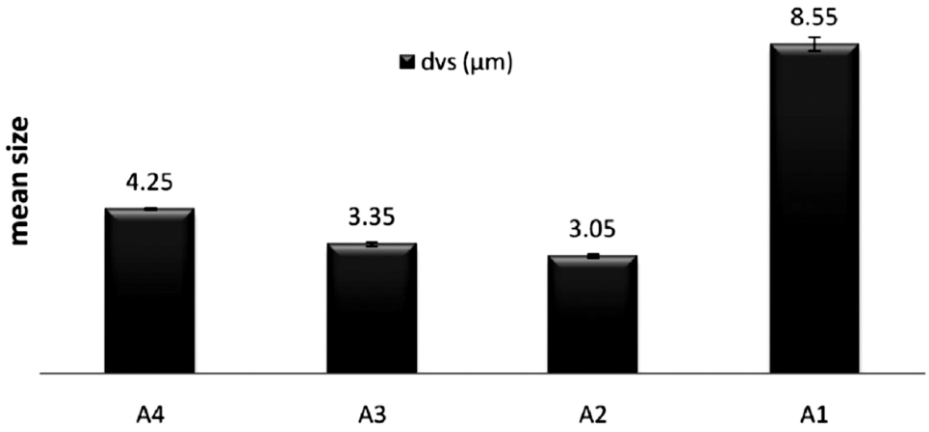


**Figure 2.** Mean diameters ($d_{vs}$, µm) of A1–4suspensions.

This latter result is probably due to the formation of aggregates among the microparticles, as suggested by the comparison between the particle size distributions of A3 (d90 = about 13 µm) and A1 (d90 = about 40 µm) suspensions, reported in Figure 3. A1 suspension in fact presents a typical bimodal profile, with a second peak located at higher $d_{vs}$ values, probably due to the presence of the aggregates, while A3 has a substantially monomodal profile.

The comparison among SPAN values of A1–4 suspensions (Figure 4) shows that A3 suspension has the lowest SPAN value (1.94), thus corresponding to the narrowest particle size distribution, while A1 suspension (prepared from the more diluted CPX and CS solutions) has the highest SPAN value. A possible explanation of this behavior could be that drug and polymer concentrations influence the rate of the interaction process that leads to the formation of the microparticles, consequently the interaction rate is responsible of the final size of the microparticles formed. As a matter of fact, the more dilute solution determines the formation of microparticles with a larger particle size distribution.

Therefore, A3 suspension presents the lower dvs and the lower SPAN value at the same time with respect to the other suspensions and for these reasons, it can be considered the formulation with the best characteristics for a potential ocular administration of CPX. It has a final concentration of drug–polymer product of interaction of 0.75% w/v (corresponding to 0.50% w/v of drug and 0.25% w/v of polymer).

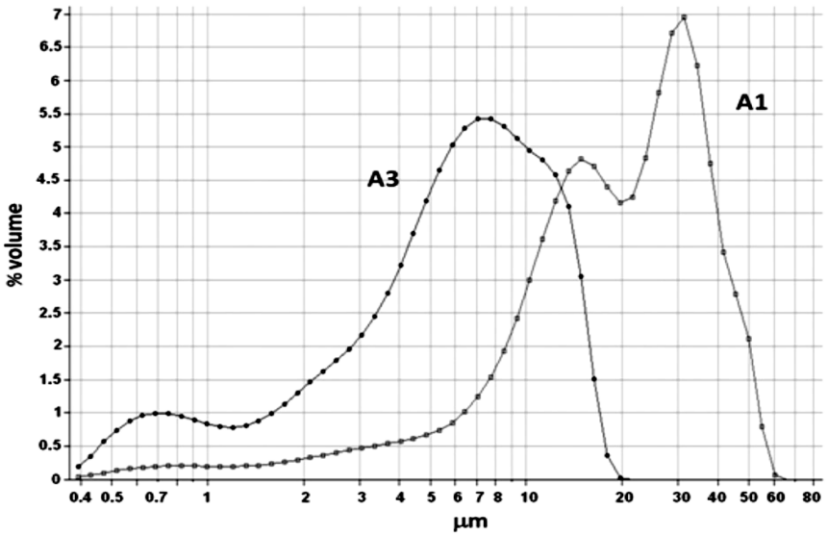


**Figure 3.** Particle size distributions of A1 and A3 suspensions.

Therefore, this suspension was chosen as reference formulation for the further study concerning the influence of the addition of surfactants on the size of the coprecipitates. Surfactants are in fact important additional excipients, which may be included in

ophthalmic suspensions to disperse the microparticles during the product use and for this reason their addition can be an additional parameter to be evaluated in the preparation of an ocular formulation. Non-ionic surfactants are used in this study. Three different samples of A3 suspension were added of 0.100% w/v of Tween 80 (obtaining T1 suspension), of 0.100% w/v or0.020% w/v of different weight ratios of Tween 80 and Span 80(Mix1 and Mix2, as previously reported) leading to T2 and T3suspensions, respectively.

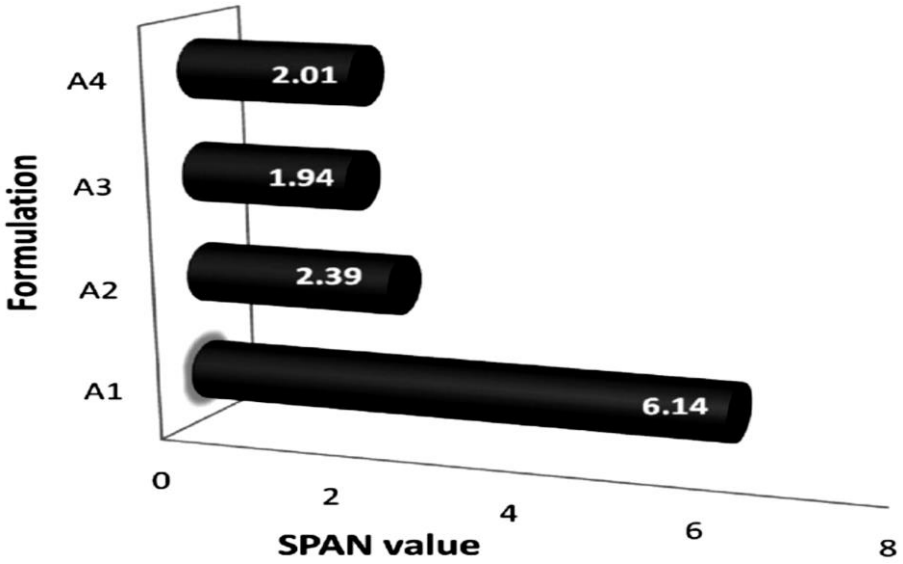


**Figure 4.** SPAN values of A1–4 suspensions.

Figure 5 reports the mean diameters ($d_{vs}$, µm) of T1–3 compared to the mean diameter of reference A3. As shown by this comparison, T1 (0.1% w/v concentration of Tween 80) has the lowest mean diameter ($d_{vs}$ 2.67 µm), even lower with respect to the reference formulation A3 ($d_{vs}$ 3.35 µm) ($p < 0.0001$). T2 suspension (0.1% w/v of a mixture of Tween 80 and Span 80) has a $d_{vs}$ of 3.20 µm, while T3 suspension (0.02% w/v of surfactant mixture) presents the highest dvs value (5.13 mm) ($p < 0.0001$). The comparison among SPAN values (Figure 6) shows that this parameter is low for T1 and T3 (1.75 and 1.78 µm, respectively) and very close to that of A3 (1.94 µm), meaning that a narrow particle size distribution is maintained. On thecontrary, T2 suspension has a SPAN value quite increased (6.96 µm), meaning that its particle size distribution is quite larger with respect to A3 and T1, despite mean diameters are similar (dvs of about 3 µm).

These data show that Tween 80 alone (present in T1 formulation) gives the best results in terms of particle size suitable for ocular administration, preventing the formation of aggregates. The characteristics of A3 formulation are therefore even improved in T1 formulation, characterized by lower values of $d_{vs}$ and SPAN with respect to this reference formulation. The lower concentration of Tween 80, despite the presence of Span 80, always determines worse particle size characteristics, in terms of dvs and/or particle size distributions.

Both surfactants are non-ionic; however, Tween 80 is characterized by a higher hydrophilicity with respect to Span 80 and for this reason it is more suitable for the prevention of formation of aggregates in an aqueous suspension. This probably occurs by a process of interfacial adsorption of the surfactant onto the surface of drug/polymer coprecipitates.

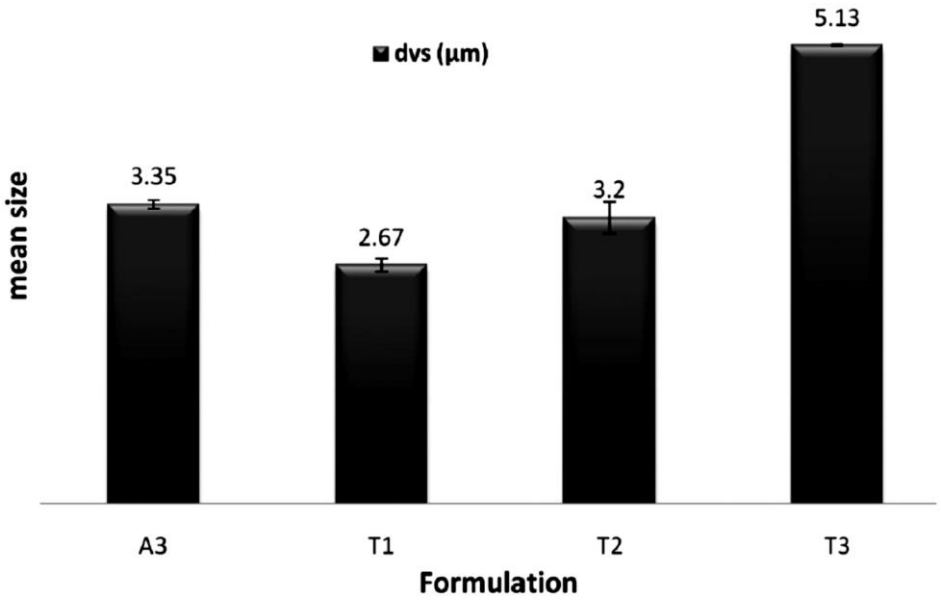


**Figure 5.** Mean diameters ($d_{vs}$, µm) of T1–3 suspensions, compared to the suspension A3.

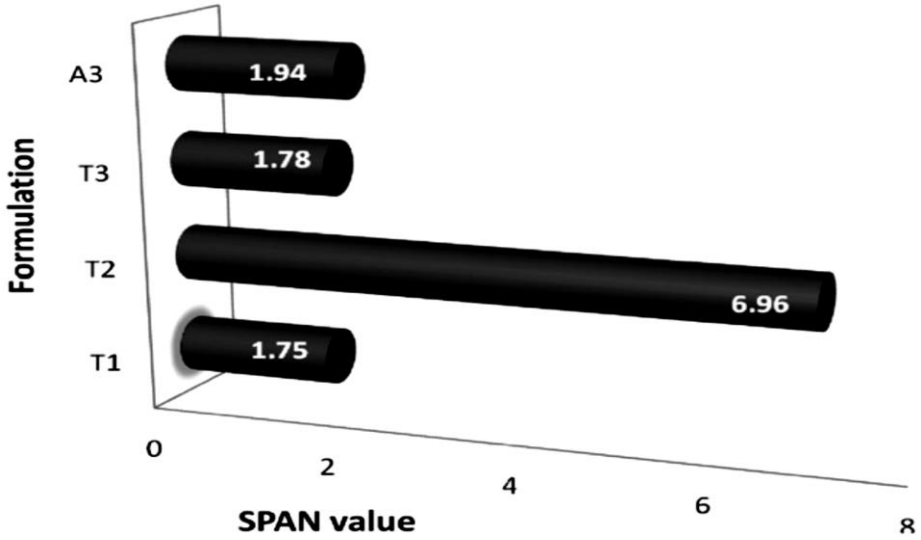


**Figure 6.** SPAN values of T1–3 suspensions, compared to the suspension A3.

The fact that Tween 80 gives the best results in terms of particle size and stabilization of the suspension is particularly important for an ocular formulation because this non-ionic surfactant is widely utilized in ophthalmic formulations, due to its safety [49,50]. It is listed in the US Pharmacopeia-NationalFormulary, in the European Pharmacopeia and in the Japanese Pharmacopeia [49,50]. Furthermore, Tween 80 has been classified as practically non-irritant as shown by an interesting test of evaluation of ocular irritation, set up and described by Alany et al. [51].

Other suspensions were prepared using different conditions of preparation, in terms of temperature (B1) and stirring (C1). Moreover, the sedimentation of A3, followed by its resuspension led to the formation of the suspension named C2. Figure 7 showsthe corresponding mean diameters (dvs) compared to reference formulation A3.

B1 and C1 present mean diameters (dvs 4.88 and 3.65 mm, respectively), which are higher than the mean diameter of A3 ($d_{vs}$3.35 µm) ($p < 0.0001$ and <0.006, respectively), while C2 has a mean diameter lower ($d_{vs}$ 2.03 µm) ($p < 0.0001$). B1 and C2 are characterized by SPAN values higher with respect to A3, while C1 has a lower parameter (Figure 8). In the case of B1, an improvement of both mean particle size ($d_{vs}$) and SPAN value with respect to A3 can be therefore found, meaning that in the preparation of the suspension the use of a higher temperature (40 °C), with respect to the room temperature, leads to worse characteristics of the suspensions.

The sonication of the drug solution during the addition of polymer solution does not lead to any further improvement ofparticle size characteristics of the suspension (C1). The results obtained from the analyses carried out on C2 show that the sedimentation of the coprecipitates, followed by their resuspension with fresh medium leads to a new homogeneous suspension that maintains the good particle size characteristics, suitable for an ocular administration.

Owing to its good characteristics, A3 formulations were chosen for preliminary stability tests. The morphology of the microparticles was not changed before and after the storage period: as shown by microscope pictures (not reported), no aggregation was found and no formation of drug crystals. This is particularly important because, as previously reported [36], CPX instability results in the precipitation of the drug in large acicular crystals (length of a few hundred microns) than can cause discomfort and/or damage.

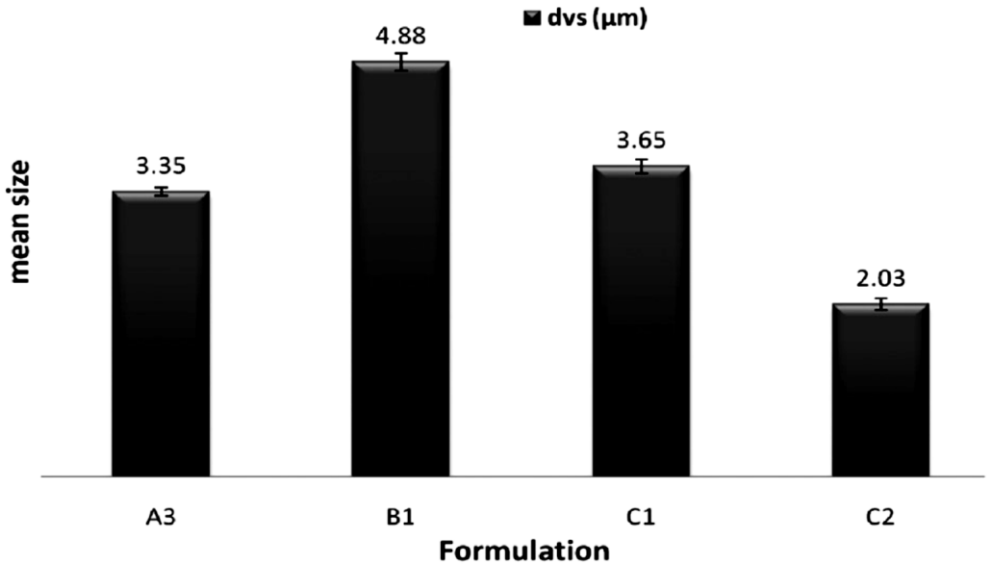


**Figure 7.** Mean diameters ($d_{vs}$, µm) of B1 and C1–2 suspensions, compared to the suspension A3.

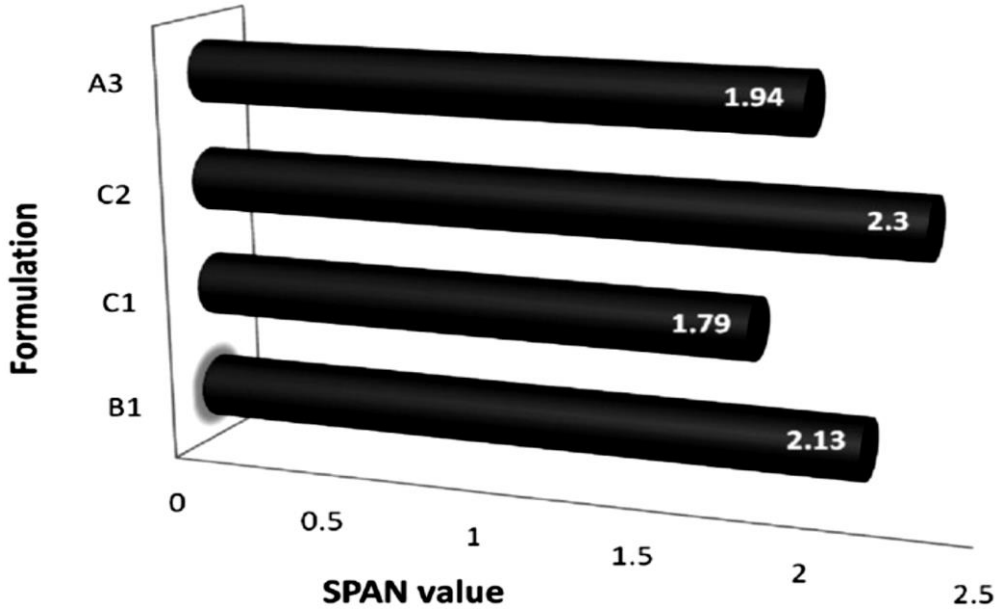


**Figure 8.** SPAN values of B1 and C1–2 suspensions, compared to the suspension A3.

## 4. CONCLUSIONS

Particle size in suspensions for ocular drug delivery is a critical parameter determining the quality of the preparation. For this reason, the study of the influence of the technological parameters on the size of the microparticles is very important.

The results obtained from this study show that all the suspensions based on the drug/polyelectrolyte product of interaction are characterized by a positive mucoadhesivity, particularly those based on chondroitin sulfate. The addition of Carbopol obviously improves this property, but it determines a modification of particle size.

Furthermore, chondroitin sulfate coprecipitates the best characteristics in terms of particle size suitable for ocular administration.

As shown by comparison of dvs values, reduction in concentration of the solutions used to obtain the coprecipitates determines the formation of particles with smaller size but after a critical size reduction is achieved, agglomerates are formed, probably due to high surface energy. In the present case, the best formulation is characterized by 0.5% w/v concentration of drug and 0.25% w/v final concentration of polymer (A3).

A further improvement of the particle size characteristics was found with the addition of Tween 80 at the concentration of 0.1% w/v as surfactant, corresponding to T1

formulation. The presence of the surfactant also improves the resuspension properties of the formulation prepared and thus its conditions of use.

## References


[1] Teng W, Cappello J, Wu W. Physical crosslinking modulates sustained drug release from recombinant silk-elastin like protein polymer for ophthalmic applications. *J Control Release*. 2011; 156:186–94.

[2] Blondeau JM. Fluoroquinolones: mechanism of action, classification, and development of resistance. *Surv Ophthalmol*. 2004; 49:S73–8.

[3] Diamond JP, White L, Leeming JP, et al. Topical 0.3% ciprofloxacin, norfloxacin, and ofloxacin in treatment of bacterial keratitis: a new method for comparative evaluation of ocular drug penetration. *Br J Ophthalmol*. 1995; 79:606–9.

[4] Sanfilippo CM, Morrissey I, Janes R, Morris TW. Surveillance of the activity of aminoglycosides and fluoroquinolones against ophthalmic pathogens from Europe in 2010–2011. *Curr Eye Res*. 2015; 22:1–9.

[5] Montero MT, Vazquez JL, Hernandez-Borrell J, Keough KMW. 2. In: Carmona P, et al. (eds). Spectroscopy of biological molecules: Q2 modern trends. 2: Kluwer Academic Publishers. 1997:311–12.

[6] Appelbaum PC, Hunter PA. The fluoroquinolone antibacterials: past, present, and future perspectives. *Int J Antimicrob Agents*. 2000; 16:5–15.

[7] Campoli-Richards DM, Monk JP, Price A, et al. Ciprofloxacin. A review of its antibacterial activity, pharmacokinetic properties and therapeutic use. *Drugs*. 1988; 35:373–447.

[8] Mundada AS, Shrikhande BK. Formulation and evaluation of Ciprofloxacin hydrochloride soluble ocular drug insert. *Curr Eye Res*. 2008; 33:469–75.

[9] Parks DJ, Abrams DA, Sarfarazi FA, Katz HR. Comparison of topical ciprofloxacin to conventional antibiotic therapy in the treatment of ulcerative keratitis. *Am J Ophthalmol*. 1993; 115:471–7.

[10] Firestone BA, Dickason MA, Tran T. Solubility characteristics of three fluoroquinolone ophthalmic solutions in an in vitro tear model. *Int J Pharm.* 1998; 164:119–28.

[11] Abdelbary G, El-Gendy N. Niosome-encapsulated Gentamicin for ophthalmic controlled delivery. *AAPS Pharm Sci Tech*. 2008; 9: 740–7.

[12] Sintzel MB, Bernatchez SF, Tabatabay C, Gurny R. Biomaterials in ophthalmic drug delivery. *Eur J Pharm Biopharm*. 1996; 42:358–74.

[13] Rozier A, Mazuel C, Grove J, Plazonnet B. Gelrite: a novel, ionactivated, in situ gelling polymer for ophthalmic vehicles. Effect on bioavailability of Timolol. *Int J Pharm*. 1989; 57:163–8.

[14] Budai L, Hajdu M, Budai M, et al. Gels and liposomes in optimized ocular drug delivery: studies on Ciprofloxacin formulations. *Int J Pharm* 2007; 343:34–40.

[15] Kaur IP, Garg A, Singla AK, Aggarwal D. Vesicular systems in ocular drug delivery: an overview. *Int J Pharm*. 2004; 269:1–14.

[16] Hosny KM. Ciprofloxacin as ocular liposomal hydrogel. *AAPS Pharm Sci Tech*. 2010; 11:241–6.

[17] Taha EI, El-Anazi MH, Mel-Bagory I, Bayomi MA. Design of liposomal colloidal systems for ocular delivery of Ciprofloxacin. *Saudi Pharm J.* 2014; 22:231–9.

[18] Li H, Liu Y, Zhang Y, et al. Liposomes as a novel ocular delivery system for Brinzolamide: in vitro and in vivo studies. *AAPS Pharm Sci Tech.* 2015; Sep 3 [Epub ahead of print].

[19] Chetoni P, Monti D, Tampucci S, et al. Liposomes as a potential ocular delivery system of Distamycin A. *Int J Pharm*. 2015; 492: 120–6.

[20] Abdelbary G. Ocular ciprofloxacin hydrochloride mucoadhesive chitosan-coated liposomes. *Pharm Dev Technol*. 2011; 16:44–56.

[21] Mahajan HS, Deshmukh SR. Development and evaluation of gelforming ocular films based on xyloglucan. *Carbohydr Polym*. 2015; 122:243–7.

[22] Huang YY Chung TW. Microencapsulation of gentamicin in iodegradable PLA and/or PLA/PEG copolymer. *J Microencapsul*. 2001; 18:457–65.

[23] Giunchedi P, Conte U, Chetoni P, Saettone MF. Pectin microspheresas ophthalmic carriers for Piroxicam: evaluation in vitro and in vivo in albino rabbits. *Eur J Pharm Sci*. 1999; 9:1–7.

[24] Giunchedi P, Chetoni P, Conte U, Saettone MF. Albumin microspheres for ocular delivery of Piroxicam. *Pharm Pharmacol Commun*. 2000; 6:149–53.

[25] Gavini E, Chetoni P, Cossu M, et al. PLGA microspheres for the ocular delivery of a peptide drug, Vancomycin using emulsification/ spray-drying as the preparation method: in vitro/in vivo studies. *Eur J Pharm Biopharm*. 2004; 57:207–12.

[26] Rassu G, Gavini E, Jonassen H, et al. New chitosan derivatives for the preparation of Rokitamycin loaded microspheres designed for ocular or nasal administration. *J Pharm Sci*. 2009; 98:4852–65.

[27] Park CG, Kim MJ, Park M, et al. Nanostructured mucoadhesive microparticles for enhanced preocular retention. *Acta Biomater*. 2014; 10:77–86.

[28] Shinde UA, Shete JN, Nair HA, Singh KH. Design and characterization of chitosan-alginate microspheres for ocular delivery of azelastine. *Pharm Dev Technol*. 2014; 19: 813–23.

[29] Addo RT, Yeboah KG, Siwale RC, et al. Formulation and characterization of atropine sulfate in albumin-chitosan microparticles for in vivo ocular drug delivery. *J Pharm Sci.* 2015; 104:1677–90.

[30] Cadinoiu AN, Peptu CA, Fache B, et al. Microparticulated systems based on chitosan and poly(vinyl alcohol) with potential ophthalmic applications. *J Microencapsul.* 2015; 32:381–9.

[31] Jani R, Gan O, Ali Y, et al. Ion exchange resins for ophthalmic delivery. *J Ocul Pharmacol.* 1994; 10:57–67.

[32] Li J, Liu H, Liu LL, et al. Design and evaluation of a brinzolamide drug-resin in situ thermosensitive gelling system for sustained ophthalmic drug delivery. *Chem Pharm Bull.* 2014; 62:1000–8.

[33] Qin F, Zeng L, Zhu Y, et al. Preparation and evaluation of a timolol maleate drug-resin ophthalmic suspension as a sustained-release formulation in vitro and in vivo. *Drug Dev Ind Pharm*. 2015; 1–11. Sep 14:[Epub ahead of print].

[34] Bonferoni MC, Chetoni P, Giunchedi P, et al. Carrageenan-gelatin mucoadhesive systems for ion-exchange based ophthalmic delivery: in vitro and preliminary in vivo studies. *Eur J Pharm Biopharm* 2004; 57:465–72.

[35] Sandri G, Bonferoni MC, Chetoni P, et al. Ophthalmic delivery systems based on drug-polymer-polymer ionic ternary interaction: in vitro and in vivo characterization. *Eur J Pharm Biopharm*. 2006; 62:59–69.

[36] Bonferoni MC, Sandri G, Gavini E, et al. Microparticle systems based on polymer-drug interaction for ocular delivery of ciprofloxacin I. In vitro characterization. *J Drug Del Sci. Tech* 2007; 17:57–62.

[37] Bonferoni MC, Sandri G, Chetoni P, et al. Microparticle systems based on polymer-drug interaction for ocular delivery of ciprofloxacin II. Precorneal residence times. *J Drug Del Sci Tech.* 2007; 17:63–8.

[38] Verschueren E, VanSantvliet L, Ludwig A. Evaluation of various carrageenans as ophthalmic viscolysers. *STP Pharma Sci.* 1996; 6:203–10.

[39] Moon JW, Lee HJ, Shin KC, et al. Short term effects of topical cyclosporine and viscoelastic on the ocular surfaces in patients with dry eye. *Korean J Ophthalmol.* 2007; 21:189–94.

[40] Baranowski P, Karolewicz B, Gajda M, Pluta J. Ophthalmic drug dosage forms: characterisation and research methods. *Scientific World J.* 2014; 2014:861904. doi: 10.1155/2014/861904. Q3.

[41] Qi H, Chen W, Huang C, et al. Development of a poloxamer analogs/carbopol-based in situ gelling and mucoadhesive ophthalmic delivery system for puerarin. *Int J Pharm*. 2007; 337:178–87.

[42] Aburahma MH, Mahmoud AA. Biodegradable ocular inserts for sustained delivery of brimonidine tartarate: preparation and in vitro/in vivo evaluation. *AAPS Pharm Sci Tech.* 2011; 12:1335–47.

[43] Sandri G, Rossi S, Ferrari F, et al. Mucoadhesive and penetrationenhancement properties of three grades of hyaluronic acid usingporcine buccal and vaginal tissue, Caco-2 cell lines, and rat jejunum. *J Pharm Pharmacol*. 2004; 56:1083–90.

[44] Sandri G, Bonferoni MC, Ferrari F, et al. An in situ gelling buccal spray containing platelet lysate for the treatment of oral mucositis. *Curr Drug Discov Technol*. 2011; 8:277–85.

[45] Edmundson IC. 2. In: Bean HS, Carless JE, Beckett AH, eds. Advances in pharmaceutical sciences. Vol. 2. New York, NY: Q4 Academic Press; 1967:2.

[46] Gavini E, Rassu G, Muzzarelli C, et al. Spray-dried microspheres based on methylpyrrolidinone chitosan as new carrier for nasal administration of Metoclopramide. *Eur J Pharm Biopharm.* 2008; 68:245–52.

[47] Rassu G, Gavini E, Spada G, Giunchedi P. Ketoprofen spray-dried microspheres based on Eudragit RS and RL: study of the manufacturing parameters. *Drug Dev Ind Pharm.* 2008; 34:1178–87.

[48] Sahoo S, Chakraborti CK Mishra SC. Qualitative analysis of controlled release Ciprofloxacin/Carbopol 934 mucoadhesive suspension. *J Adv Pharm Technol Res.* 2011; 2:195–204.

[49] Ammar HO, Salama HA, Ghorab M, Mahmoud AA. Nanoemulsion as a potential ophthalmic delivery system for dorzolamide hydrochloride. *AAPS Pharm Sci Tech.* 2009; 10:808–19.

[50] Yamaguchi M, Yasueda S, Isowaki A, et al. Formulation of an ophthalmic lipid emulsion containing an anti-inflammatory steroidal drug, difluprednate. *Int J Pharm.* 2005; 301:121–8.

[51] Alany RG, Tucker IG, Davies NM, Rades T. Characterizing colloidal structures of pseudoternary phase diagrams formed by oil/water/amphiphile systems. *Drug Dev Ind Pharm.* 2001; 27:31–8.

# 3.2 Composite chitosan/alginate hydrogel for controlled release of deferoxamine: A system to potentially treat iron dysregulation diseases

*Adapted from:*

**Composite chitosan/alginate hydrogel for controlled release of deferoxamine: A system to potentially treat iron dysregulation diseases**

Giovanna Rassu, Andrea Salis, Elena Piera Porcu, Paolo Giunchedi, Marta Roldo, Elisabetta Gavini. *Carbohydrate polymers*, 136, 1338-1347.

License Number: **3967570187803**

## 1. INTRODUCTION

Iron is a redox active metal, essential for life and indispensable for several biological reactions [1]. Nevertheless, its excess is toxic due to the release of reactive oxygen species (ROS) [1-3]. The hydroxyl radical is very reactive and can cause oxidative damage to various cell components, including lipid membranes, DNA, and proteins, thereby causing cell damage [2,4].Disruption of iron regulation plays a key role in the etiology of neurological disorders, cancer, stroke, muscle diseases such as Duchenne's muscular dystrophy, and aging [3,5]. Iron overload in the cytoplasm of hepatocytes contributes to hepatocellular damage and hepatocarcinogenesis [4]. In the skin, excess iron combined with UV radiation exerts pro-oxidant effects [3]. Furthermore, it is hypothesized that iron may contribute to the pathogenesis of ocular diseases [2].

Iron chelators are currently being investigated for their benefit in limiting iron-induced oxidative damage. The best known iron chelator in clinical use is deferoxamine (DFO, Desferal™) [2]. DFO as mesylate salt is the treatment of choice for acute iron intoxication and chronic iron overload due to transfusion-dependent anemia [6]. Data to support DFO use in other disorders associated with iron overload are growing. Several studies have shown the beneficial effects of DFO in reducing skin necrosis [7-11]. DFO appears to

mitigate radiation-induced hypovascularity and improve tissue elasticity in a rat model [12]. DFO can prevent liver injury and development of preneoplastic lesions in rats [13,14], and it was proposed as an anticancer agent for the therapy of advanced hepatocellular carcinoma (HCC) [4,15]. Over the past few years, a variety of studies have been conducted on DFO demonstrating some positive effects on fracture healing [16-21]. Unfortunately, DFO has properties that significantly limit its usefulness in a clinical setting. Administration of this drug is limited to the parenteral route due to its poor absorption in the gut. Furthermore, DFO has a very short plasma half-life because of rapid renal excretion; thus, repetitive or continuous subcutaneous infusions are necessary to maintain its effective therapeutic levels [1,22]. These are associated with toxic effects [23]. Furthermore, repeated injection of DFO at the bony injury may not be practical or effective clinically [19]. In most studies DFO was administered in solution [4,12,15,16], and to date, very few formulation strategies have been developed in order to improve DFO biopharmaceutical properties: (i) conjugation to hydroxyethyl starch (Hespan) [24] or to hyperbranched polyglycerol (HPG) [25] for increasing plasma half-life; (ii) formulation in nasal microparticulate delivery systems to improve the nose to brain transport [26]; (iii) loading in morselized beads of calcium sulfate [27] or in true bone ceramic scaffolds [21] for the treatment of bone defects.

Hydrogels are widely used as debriding agents, moist dressings, components of pastes for wound care, as well as ocular drug delivery carriers, and subcutaneous inserts. Furthermore, hydrogels are able to both locally embolize the hepatic tumor and deliver drugs in a controlled manner [28,29]. Tissue engineering is one of the most recent applications of hydrogels as space filling agents, delivery vehicles for bioactive substances or as three-dimensional structures that organize cells and ensure the development of a required tissue [30].

Composite hydrogels are a co-formulation of particulate systems incorporated into the hydrogel matrix forming “plum pudding” hydrogel networks [31]. Incorporating degradable micro- or nanoparticles loaded with a drug in the hydrogel can further extend the possibilities for controlling drug delivery [32]. This can have the added benefits of reducing burst release commonly displayed in microsphere formulations and can prevent microsphere displacement away from the site of action [31].

In order for DFO therapy to progress to clinical treatment, methods of delivery, timing, and dosage need to be considered and optimized [14,18,20]. In this study, the feasibility of hydrogel as prolonged delivery systems of DFO, useful for solving the criticalities common to several iron dysregulation diseases, was investigated.

Physical chitosan/alginate hydrogel was selected in order to obtain a carrier able to control the delivery of this drug to the target site, and at the same time, depending on the disease, to serve as structural support (e.g. on fracture healing) or embolic agent (e.g. in the therapy of advanced hepatocellular carcinoma).

Finally, it should be reabsorbed after it has served its function. This system should be entirely biocompatible and biodegradable, no toxic, injectable or implantable. The materials used well correspond to the characteristic quality of the required drug delivery systems making alginate and chitosan more suitable carriers than others. The advantages of chitosan/alginate hydrogel alone or co-formulated with PLGA microparticles were evaluated in vitro.

## 2. MATERIALS AND METHODS

### 2.1 Materials

Sodium alginate (Protanal LF 120 L, batch: 907788; MW: 221 kDa; viscosity (1% sol): 93 cP; Seaweed species: *Lessonia nigrescens;* $F_G$: 0.41; $F_M$: 0.59; $F_{GG}$: 0.22; $F_{GM}$: 0.19; $F_{MM}$: 0.40; $F_{GGM}$: 0.05; $F_{MGM}$: 0.14; $F_{GGG}$: 0.17; $N_{G>1}$: 5.6 [33] was purchased from FMC BioPolymer, now FMC Health and Nutrition (Philadelphia, USA). Chitosan (ChitoClear TM 1358, deacetylation degree: 95%; viscosity (1% sol): 63 cP; MW: 103 kDa; ash residue: 0.9% (according to the manufacturer's specifications)) was acquired from PRIMEX EHF, Siglufjordur, Island. Poly(d,l-lactide-co-glycolide) (PLGA) RG502 (viscosity: 0.16–0.24 dl/g (50:50), MW: 7000–17,000), RG504 (viscosity: 0.45–0.60 dl/g, MW: 38,000–54,000), and deferoxamine mesylate salt (DFO) were purchased from Sigma–Aldrich, St. Louis, USA. All other solvents and chemicals were of analytical grade.

## 2.2 Hydrogel preparation

Unloaded hydrogel characterized by a molar ratio 1/1 between alginate and chitosan and 2.5% (w/v) concentration of polymers, in the final volume, were prepared. Sodium alginate solution (2.44% w/v) was made dissolving alginate powder in water with the aid of a magnetic stirrer at room temperature. Separately, chitosan (2.75% w/v) was dissolved in hydrochloric acid solution pH 0.7, under magnetic stirring. Then, 1.25 mL of chitosan solution was added to 3.75 mL alginate solution (pH 7.0) and stirred vigorously in order to obtain the final pH of 3.0. Loaded hydrogels were prepared by dissolving DFO (3 mg) in chitosan solution before mixing polymer solutions.

## 2.3 Microsphere preparation

Microspheres, composed by PLGA, hydrophobic polymer, and DFO, hydrophilic drug, were prepared by using the emulsification/spray drying method previously described [34]. After preliminary studies, the total solid (drug + polymer) concentrations of 4% w/v was selected; drug to polymer ratios of 1:4 and 1:10 were considered. Table 1 lists the formulations prepared. Briefly, w/o emulsion was prepared by dissolving DFO in water and PLGA in 25 mL of dichloromethane. The aqueous solution was added dropwise to the organic one within 5 min, under homogenization at 10,000 rpm (Ultra-Turrax T25 basic, IKA, Germany). The w/o emulsion was then sprayed through the nozzle (0.7 mm) of a spray-dryer, co-current flow type (Buchi Mini Spray Dryer B-191, Milano, Italy). The process conditions are shown in Table 1. The temperature of emulsion was maintained at about 5°C throughout the process. No phase separation during the spray-drying process was observed in the emulsion, thus rendering unnecessary the use of surfactants (Figure S1). Microspheres were collected and kept under vacuum for 48 h at room temperature. Blank microspheres were produced as control by dissolving PLGA in dichloromethane.

**Table 1.** Microsphere formulations: composition and spray-dryer manufacturing parameters. Mean diameter and d90/d10 ratio were also reported.

| | Microspheres composition[a] | | Spray dryer parameters | | Particle size and distribution | |
|---|---|---|---|---|---|---|
| **Formulation** | **DFO (g)** | **water (mL)** | **Air In (°C)** | **Air Out (°C)** | **dm[b] (µm)** | **d90/d10** |
| **502** | - | - | 50 | 41 | 5.63±0.31 | 8.33 |
| **504** | - | - | 50 | 41 | 8.19±2.09 | 15.95 |
| **D502 4** | 0.250 | 5 | 80 | 55 | 33.13±23.75 | 10.37 |
| **D504 4** | 0.250 | 5 | 80 | 51 | 66.38±11.86 | 9.10 |
| **D502 10** | 0.100 | 1.5 | 50 | 39 | 18.21±3.2 | 8.62 |
| **D504 10** | 0.100 | 1.5 | 50 | 42 | 21.93±17.76 | 13.08 |

a Drug to polymer ratio of 1:4 and 1:10 were used; The following conditions were also used during spray-drying: drying airflow, 31.3 m3/h; spraying airflow, 500 L/h; solution feed rate, 4.09 ± 0.05 mL/min. b Mean ± standard deviation, SD (n = 15).

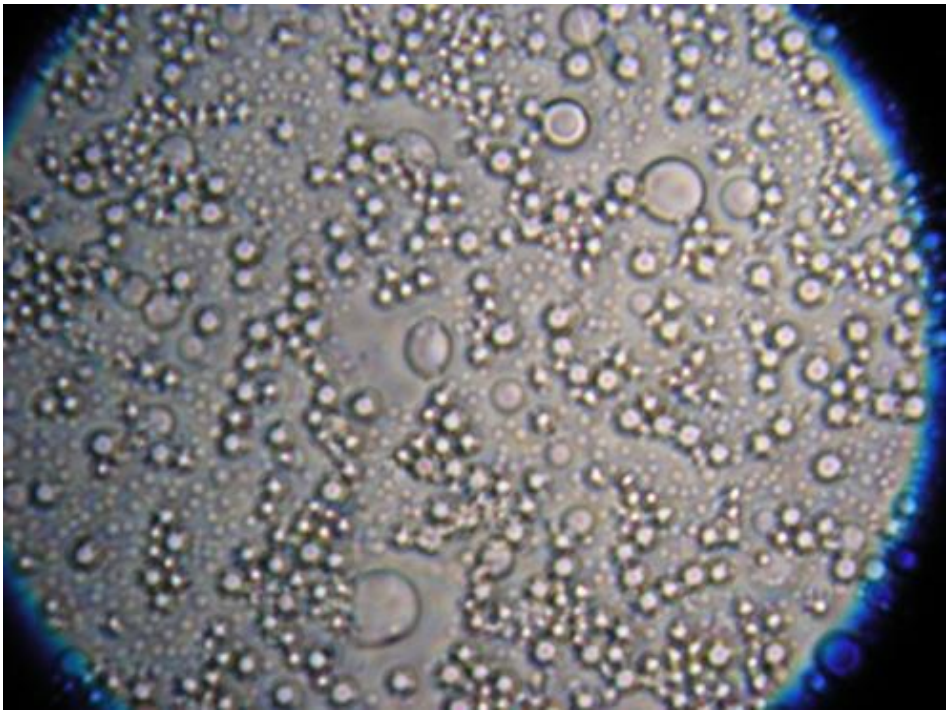

**Figure S1.** Photomicrograph of emulsion almost at the end of spray-drying process. Magnification 80x.

### 2.4 Composite hydrogel preparation

Composite hydrogels were prepared by combining the microspheres and the hydrogel. Two methods were tested: (1) PLGA microspheres (30mg) were added into the chitosan solution; which was then loaded onto the alginate solution and stirred vigorously; and (2) the addition of microspheres was performed after the formation of chitosan/alginate hydrogel.

### 2.5 Microsphere characterization

#### *2.5.1 Yield of production*

The yield of production was calculated as percentage of the weight of the final product with respect to the total solid (drug and polymer) solubilised in the feed solutions.

### *2.5.2 Particle size analysis using a suspension method*

The particle size and particle size distribution of the microspheres were determined with a Coulter LS 100Q Laser diffractometric equipment (Beckman Coulter Particle Characterization, Miami, FL, USA). For particle size analysis using a suspension method, microspheres (2 mg) were suspended in 1 mL of Tween 80 solution (0.1% w/v); the suspension was further diluted and dispersed by vortexing for 10min in case of formulation based on RG502 and vortexing for 10 min and sonication for 2 min in case of RG504. Values reported are the averages of three determinations for five samples of each formulation (standard deviation, SD, $n = 15$).

### *2.5.3 Powder particle size analysis*

The particle size in the dry powder was measured by an HELOS Particle Size Analyser from Sympatec GMbH, fitted with an Aspiros doser (pressure, 2.00 bar; vacuum, 36.00 mbar; feed velocity; 25.00 mm/s). A lens able to detect particles in the size range 0.9–175 μm was fitted.

### *2.5.4 Drug content*

DFO loaded microspheres (15 mg) were dissolved in 2–4 mL dichloromethane with the aid of magnetic stirring. The solution was then diluted with 40 mL of water and the organic phase was evaporated using a rotavapor at 35°C before transferring the remaining aqueous solution into a volumetric flask (50 mL) and analyzed by HPLC as described below. One extraction was enough for complete DFO recovery.
Loading efficiency (LE), as percentage, was calculated by using the following equation:

$$LE = \frac{DC_A}{DC_T} \times 100 \quad (1)$$

where $DC_A$ and $DC_T$ are the amount of drug loaded into the polymer matrix and the expected theoretical value, respectively. $DC_A$ was calculated as previously reported [35].

### *2.5.5 Drug burst test*

Microspheres (15 mg) were suspended in 50 mL of water, at either 37 °C or at room temperature. The samples were then vortexed for 10 s before centrifugation (3000 rpm for 5 min) and then analyzed by HPLC.

### *2.6 HPLC analysis of deferoxamine mesylate*

For the quantification of DFO in buffer samples, a Varian ProStar 210 with AutoSampler 410 and a PDA photodiode array detector (Varian Inc Scientific Instruments, Walnut Creek, CA, USA) was employed. The chromatographic separation was performed as previously reported [26]. Briefly, separation was performed at room temperature on a C18 column with polar endcapping (Phenomenex Synergi Hydro-RP 80A, 150 × 4.6 mm I.D. and 4 μm of particle size). Twenty microliters of samples were directly injected into the column and eluted with a binary mixture consisting of acetonitrile (pH 4.6 with 0.5 M $H_3PO_4$) and a 0.1 M $KH_2PO_4$ (3.4 g/250 mL), 120 mg/L (30 mg/250 mL) 1-eptane sulfonic acid sodium salt solution ratio 17:83 (v/v) adjusted to pH 4.6 by 0.5 M phosphoric acid. DFO was detected by UV at 210 nm wavelength. Concentrations of analyte were calculated by interpolation of DFO standard curves.

## 2.7 Hydrogel characterization

### *2.7.1 Viscosity measurement*

Viscosity of unloaded hydrogel as well as polymer solutions was measured, at room temperature, by rotational viscometer (Alpha-L, Fungilab, Barcelona, Spain) at a constant rotation speed of 60 rpm or 100 rpm, respectively.

### *2.7.2 Porosity measurement*

The solvent replacement method was used to determine the porosity of the hydrogel samples [36]. Freeze-dried hydrogels (unloaded, loaded and composite) were immersed in absolute ethanol overnight and weighed after blotting excess ethanol on the surface. The porosity was calculated from the following equation:

$$\text{Porosity} = \frac{(M_2 - M_1)}{\rho V} \times 100 \quad (2)$$

where$M_1$ and $M_2$ are the masses of the hydrogel before and after immersion in ethanol, respectively, $\rho$ is the density of absolute ethanol and $V$ is the volume of the hydrogel.

### *2.7.3 Water uptake and swelling*

Hydrated and freeze-dried hydrogels (unloaded, loaded and composite) were weighed and fully immersed in a sealed container with phosphate buffered saline (PBS; pH 7.4) for 24 h at 37°C [37] to study the water uptake (WU%) and swelling characteristics. Then, samples were taken out, wiped with paper and weighed. The water uptake percentage was determined gravimetrically using following equation:

$$\text{WU} = \frac{(M_2 - M_1)}{M_1} \times 100 \quad (3)$$

where$M_1$ is the dry weight and $M_2$ is the saturated weight.
Similarly, the swelling ratio was calculated from the volume of dry and saturated hydrogel.

### *2.7.4 Dynamic vapor absorption (DVS) studies*

Dynamic vapor sorption (DVS) analysis of the freeze-dried hydrogels (unloaded, loaded and composite) was carried out with a Surface Measurement Systems DVS Advantage instrument. Using nitrogen as the carrier gas; the mass change of samples subjected to a changing water vapor partial pressure at 25°C was recorded. The partial pressure was increased from 0 to 90% in 10% increments; the partial pressure was increased to the next step either after equilibrium or after a maximum time of 360 min. A full adsorption/desorption cycle was performed; the data collected were used to calculate the adsorption and desorption isotherms as well as the hysteresis. The data were further analyzed according to the following equation:

$$W_p = K_p t^{np} \quad (4)$$

where $W_p$ is the weight gain; $K_p$ is the kinetic constant of water penetration into the composite material; $n_p$ is the exponent describing the mechanism of water penetration.

### *2.7.5 Biodegradability*

The weight loss of the composite hydrogels was monitored as a function of incubation time in PBS (pH 7.4) at 37°C for 24 days [37]. Weights of the samples were measured at 10, 17 and 24 days of incubation, after freeze-drying. Degradation was determined by percentage of weight loss ($W_L$) using following equation:

$$W_L(\%) = \frac{W_L - W_0}{W_0} \times 100 \quad (5)$$

where $W_0$ was the initial weight and $W_L$ was the weight after degradation. Each experiment was repeated three times, and the value is reported as mean ± SD ($n$ = 3). No significant change in pH was found during the test.

### *2.8 Drug release studies*

Release studies of DFO from microspheres, loaded and composite hydrogels were carried out. Microspheres or hydrogels were put in 50 mL of PBS containing 0.01% Tween 80 and shaken at 80 rpm, 37°C for 10 days.

At predetermined time points, 1 mL of medium was withdrawn and centrifuged at 13,000 rpm for 10 min, the supernatant was removed and stored at −20°C until HPLC analysis. Pellets eventually obtained after centrifugation were resuspended in 1 mL PBS and poured back into the release medium to restore the initial volume. Standard DFO solutions (60 mg/L) were stored in the same conditions in order to check the possible degradation of DFO during the time.

Release profiles were corrected to remove the degradation aspect and analyzed with regards to release kinetics and mechanism of release. The following equation describes the method used for the corrections. Ftn is the corrected percentage release, Ft is the cumulative percentage release, $t$ is the time at which Ft level was taken.

$$\mathrm{Ftn} = \mathrm{Ft} \times \left( \frac{100}{-0.2428 \times t + 107.31} \right) \quad (6)$$

The corrected data were then investigated for fit into various release models. Zero order is demonstrated by plotting the corrected cumulative release fraction versus time. Zero order describes the concentration-independent drug release rate from a formulation:

$C=k_0t$ (7)

First order release is described by plotting log cumulative drug fraction versus time and describes concentration-dependent drug release from the system:

$$\log C = \log C_0 - \frac{kt}{2.303} \quad (8)$$

The Hixson–Crowell cube root law describes the release from systems where there is a change in surface area and diameter of particles (therefore applies to microsphere only formulations). As described by Eq. (9), a straight line will confirm this type of release.

$$Q_0^{1/3} - Q_t^{1/3} = K_{HC}\, t \quad (9)$$

The Korsmeyer–Peppas equation as shown in Eq. (10), describes the mechanism of drug release. The release exponent can be used to characterize different release mechanisms [38].

$$\frac{M_t}{m_\infty} = K_{kp}\, t^n \quad (10)$$

where $M_t/M_\infty$ is the fraction of drug released at time $t$, $K_{kp}$ is the rate constant and $n$ is the release exponent.

At the end of test, the microspheres, loaded and composite hydrogel were recovered, frozen at −80°C and freeze-dried for morphological examination.

### 2.9 Scanning electron microscope (SEM) studies

he morphology of microspheres and freeze-dried hydrogels was analyzed by SEM. A Jeol JSM-6060LV Scanning Electron Microscope was used and samples were coated with gold using a Quorum Q 150RES spatter coater.

### 2.10 Statistical analysis

Data were analyzed using the nonparametric Kruskal–Wallis test; individual differences were evaluated using a post hoc Dunn's multiple comparison test (GraphPad Prism, version 6.02; GraphPad Software Incorporated). When suitable, analysis of variance (ANOVA) followed by a Tukey test was done.

# 3. RESULTS

## 3.1 Microsphere preparation and characterization

### *3.1.1 Yield of production*

Microspheres were produced by spray-drying technique using RG502 and RG504 as polymers. Spray-drying appears to be a suitable method for the preparation of unloaded and DFO loaded microspheres, but with yield of production ranging from 34% to 67%. Loss of yield was due to deposition in the spray-drying apparatus. This is a common problem with small drying chambers and does not normally occur in industrial scale spray-drying due to the large cyclone area [39].

### *3.1.2 Particle size analysis*

The particle size and particle size distribution of the microspheres were determined by analyzing the powder in the dry state or in suspension. When measured in suspension (Table 1) there was no significant difference in particle size between the two unloaded formulations (502 versus 504, $p = 0.423$), that differed only in molecular weight of the polymers used. The skewness in 502 is slightly more to the right with almost double the leptokurtic value compared to 504. 502 also had smaller d90/d10 showing reduced distribution (Table 1).

The loading of DFO in the polymer matrix determined an increase of particles size regardless of the PLGA used mainly when the highest drug amount was employed. In fact, the loaded D502 4 and D504 4 compared to the unloaded samples, 502 and 504, were significantly larger in size ($p<0.05$). Significant difference between particle sizes of 502 versus D502 10 and 504 versus D504 10 were also observed ($p> 0.05$) (Table 1). Both unloaded and loaded samples were skewed to the right with leptokurtic properties.

The increase in particle size of all 504 formulations can be attributed to the increase in water/DCM ratio ($p = 0.0029$) (Figure S2). The distribution also narrows with increasing water content (d90/d10 = 15.95, 14.00 and 8.74). Less evident but significant is the change of size of 502 formulations according to the ratio drug polymer used (Table 1, $p<0.05$).

In order to observe whether an improvement in particle size distribution with reduced aggregation was observed using a dry method, samples were analyzed using this method as a qualitative assessment.

The mean particle size was mostly larger using the dry method (Figure S3), which could indicate that sample preparation for the suspension method for 502, 504, D502 4 and D502 10 broke aggregates and reduced the average particle size.

In comparison of the two particle size analysis methods, it is evident that suspending the microspheres in solution containing surfactant as well as vortexing and sonicating is beneficial in reducing aggregation which is advantageous to creating a true distribution curve of particle sizes.

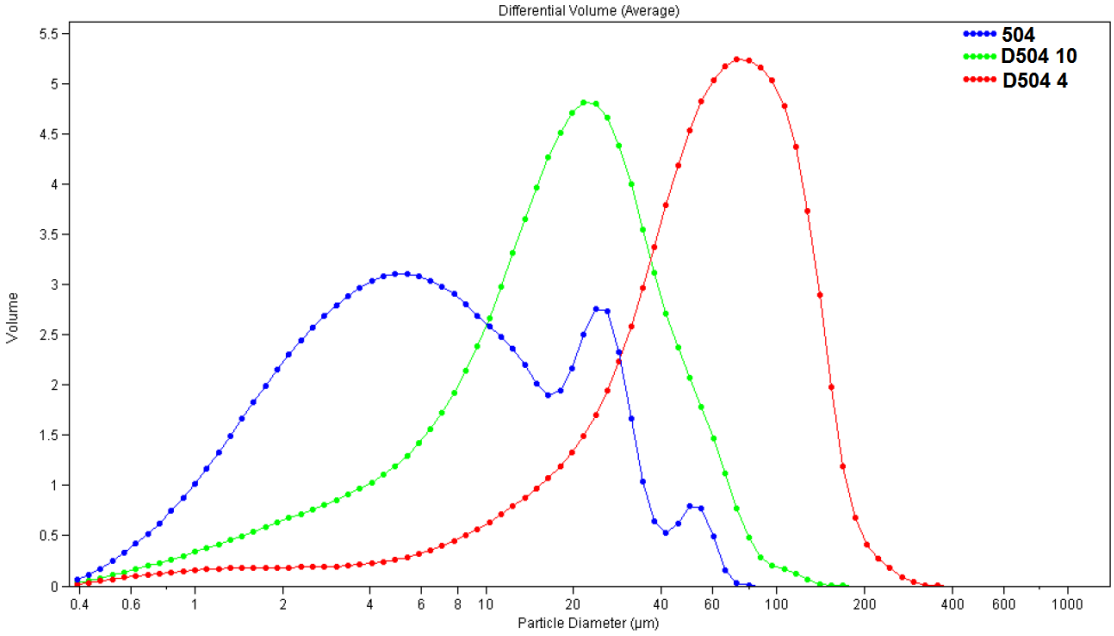


**Figure S2.** Comparative overlay of 504 (blue), D504 10 (green) and D504 4 (red) in order of increasing water content.

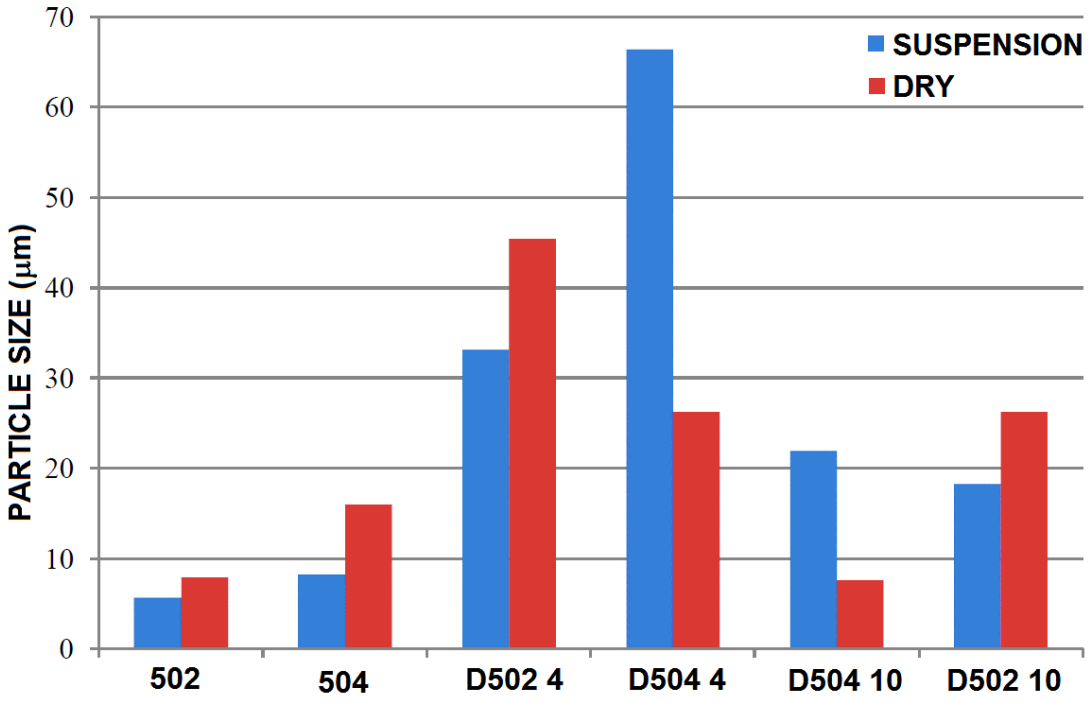


**Figure S3.** Comparison of mean particle size diameter of microsphere formulations using the suspension and the dry methods.

### *3.1.3 Drug content and drug burst release*

In order to accurately determine drug loading efficiency and drug release of PLGA particles, the actual drug content of the microspheres was investigated as well as the burst release. Burst release as a proportion of actual drug content will help to determine which formulation manages to sustain drug release. All loading efficiency (LE) were above 83% of theoretical values (Figure 1). LE depends on factors such as kind of PLGA and drug to polymer ratio. When 1:4 drug to polymer ratio was used, LE increased if PLGA with high molecular weight was used (D502 4 versus D504 4 $p$ = 0.0068); no significant differences were observed when high concentration of polymer was used (D502 10 versus D504 10 $p$>0.05). The drug to polymer ratio affected the LE only in the case of 502 formulations (D502 4 versus D502 10 $p$ = 0.0310). Higher molecular weight formulations tended to have a significant reduction in burst release (D504 4 versus D504 10, $p$>0.05). Figure 1 shows a significant difference between D502 4 and D504 4, D502 10 and D504 10 and between D502 4 versus D502 10. Temperature did not significantly affect the burst test.

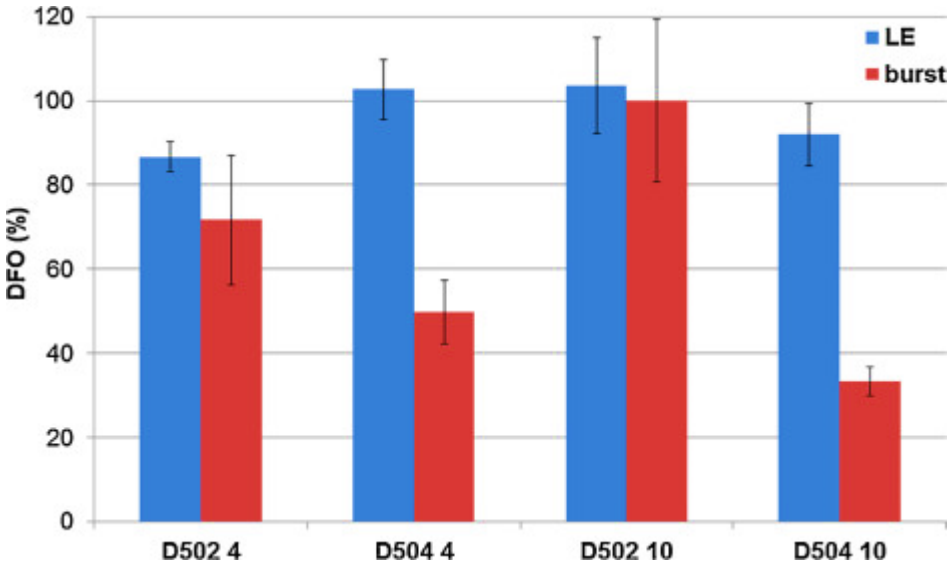


**Figure 1.** Loading efficiency (LE) of formulations and the percentage of DFO released during the burst test.

### *3.1.4 Microspheres morphology by (SEM)*

The image of unloaded 502 microspheres in Figure 2A and C concurs with the particle size distribution profiles discussed above. Figure 2 shows not only the wide range of particle size present in the formulations but it also provides evidence that agglomeration is the cause for anomalous spikes that occur in the distribution graphs (Figure S2). In contrast, 504 presented less visible aggregation between the microspheres which is likely due to the higher glass transition temperature of the polymer. Figure 2 also shows the presence of fibrous polymer between microspheres; this could be due to the difficulty in separating the longer strands of polymer for incorporation in individual spheres during the preparation process. Studies found that increasing the drying gas flow rate will reduce this fibrous formation and therefore increase efficiency due to better separation in the cyclone [40].

504 microspheres also had a comparatively more textured surface than 502. As all other manufacture and formulation parameters, apart from the molecular weight of the polymer, were kept constant, it is hypothesized that the more amorphous nature of the RG502 allowed the formation of a smoother surface.

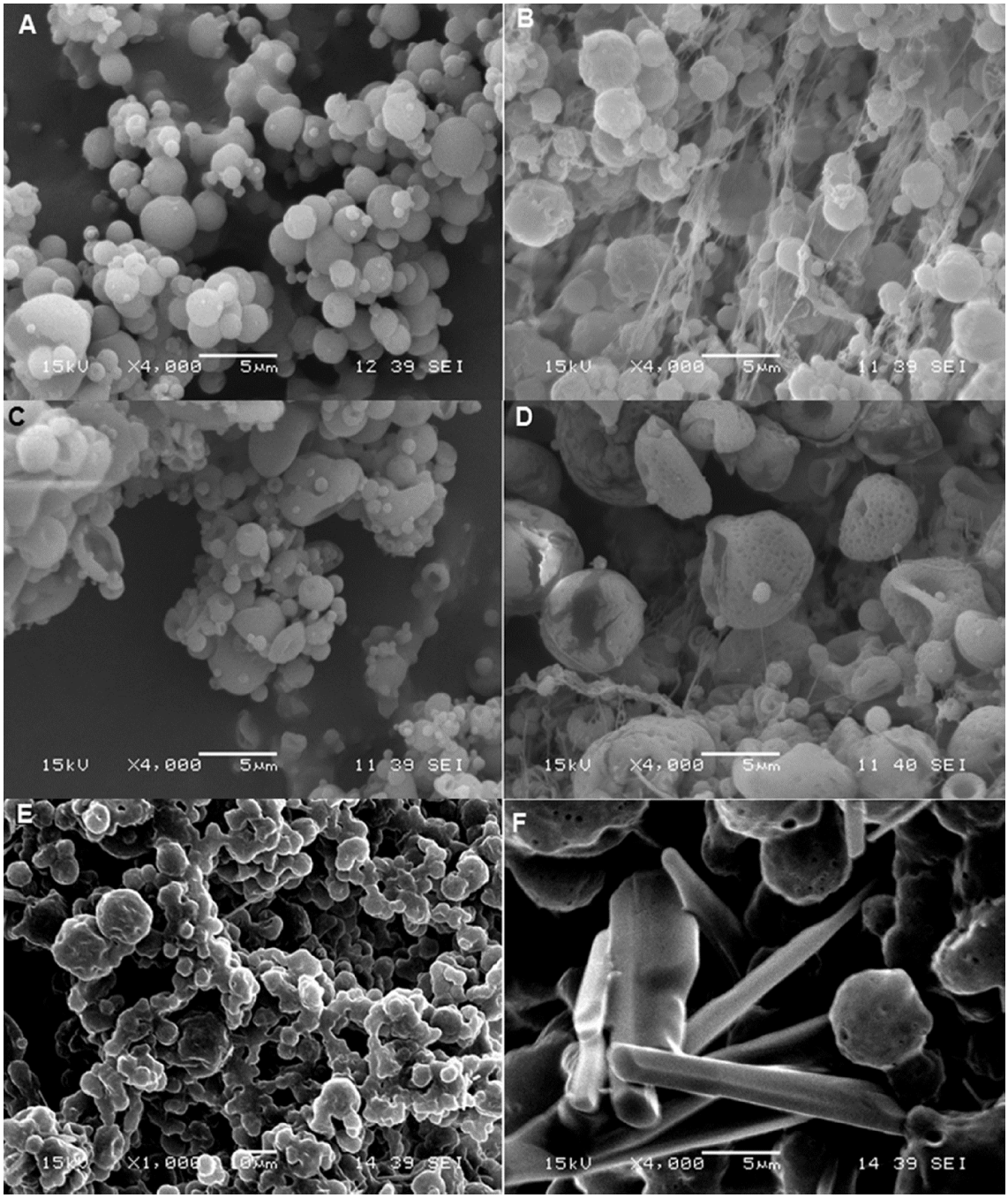


**Fig. 2.** SEM pictures showing morphology of unloaded microspheres: 502 (A) and 504 (B), D502 10 (C) and D504 10 (D), chosen as example (magnification 4000×). E and Fpictures showing morphology of D504 10 after drug release studies (magnification 1000× and 4000×, respectively).

Regardless of the polymer used, unloaded microspheres appeared to have a better spherical appearance compared to loaded microspheres (Figure 2A–D). The difference could be due to the use of water in the formulation of loaded microspheres, this could cause disruption during structural formation [41]. On examination of the manufacturing parameters, the increase in outlet temperature from unloaded batches to loaded batches could also contribute to the large morphological change.

The surface of loaded microspheres appeared to be smooth with pores and did not show presence of crystallized drug on the surface. This opposes theories that indicate drug deposited on the surface as the reason for the burst release observed. The filamentous appearance of 504 is still present in the loaded microspheres D504 10 (Figure 2D). Morphology of D504 10 was observed also after drug release studies. Samples analyzed after release tended to show more agglomerated and fused particles (Figure 2E). This occurrence is explained by the reduction in glass transition temperature and therefore the increase in rubbery nature of the PLGA in the presence of water. The filamentous structures disappeared after dissolution, possibly due to degradation. Pores are present in this formulation which alongside microsphere collapsing is the primary cause for burst release. There is some evidence of the presence of drug after dissolution, indicating there is good internalization of the drug in the dry microspheres (Figure 2F).

### *3.1.5 Drug release studies*

Release studies of DFO from microspheres were carried out. Standard deferoxamine solutions (60 mg/L) were stored in the same conditions in order to check the degradation of DFO in solution during the time.

Degradation of DFO over time was observed in DFO solution. Whereas D502 4 and D504 4 curves displayed concomitant release and degradation and had no significant difference in gradient (1–250 h) when compared to the standard (Figure S4). The high initial release of the microspheres (86% and 90%) indicated a burst release, followed by a negative correlation to the same degree as the DFO standard indicative of drug degradation with time.

In an attempt to reduce the burst release of the microspheres, an increase in the ratio of polymer to drug was used as well as a reduction in water content in the preparation

process. D504 10 shows a high initial release followed by non-significant difference in degradation gradient (time 1–240 h, $p$ = 0.11629) when compared to the DFO solution. D502 10 was not tested because of the very high percentage of DFO released during the burst test.

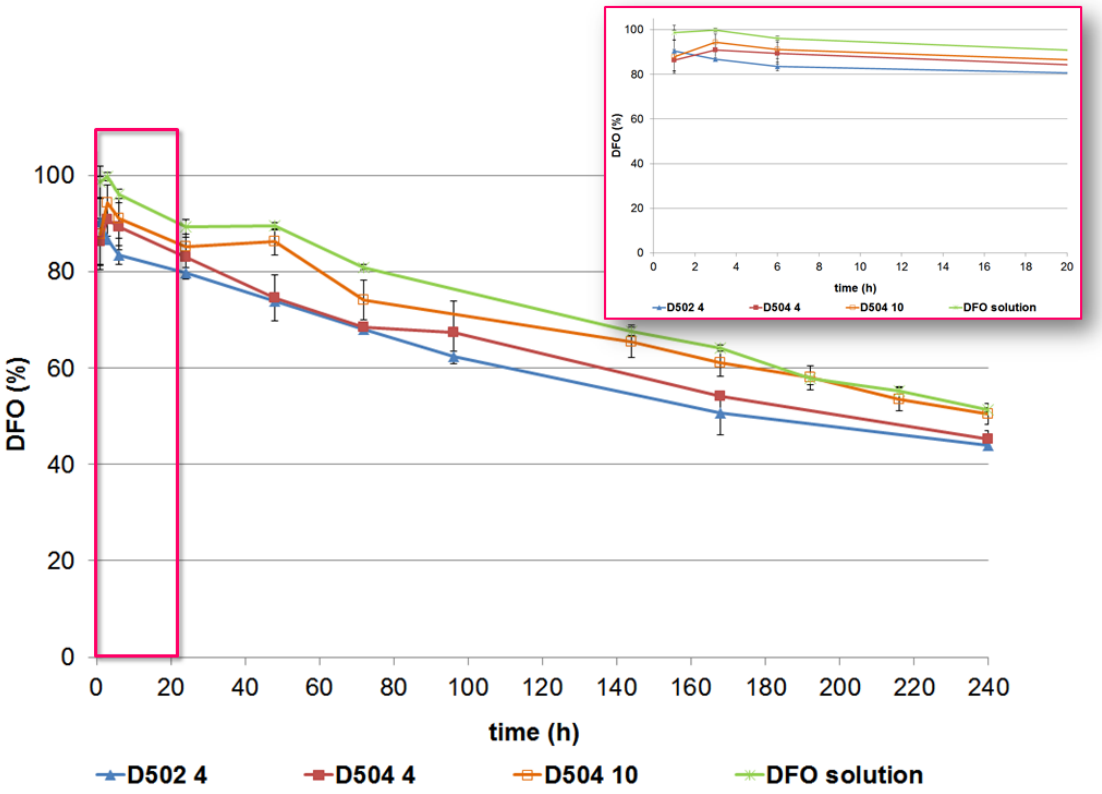


**Figure S4.** DFO release from microspheres and concomitant degradation of DFO solution, without corrected data of degradation.

Even though the release profile was similar, they could be the result of a different ratio of drug being released and being degraded. In order to examine the release profile, data points were corrected to remove the degradation aspect. Most microsphere batches on their own exhibited very little correlation with any of the kinetic or mechanistic equations ($R^2$<0.9). It was found that D502 4 had strong correlation with first order (concentration dependent), Hixson–Crowell and Korsmeyer–Peppas at 1–6 h. The application of the Hixson–Crowell equation shows that there is a change in surface area and diameter of particles in the time frame 1–6 h and from the close fit to the Korsmeyer–Peppas equation, it can be deduced that D502 4 releases the drug with diffusion as the rate controlling factor ($n$<0.45).

### 3.2 Preparation of hydrogels and characterization

Unloaded and DFO loaded hydrogels as well as composite hydrogel were prepared. The molar ratio 1/1 and pH of 3.0 were found to be critical to formation of alginate and chitosan hydrogel. The gelation was immediate after vigorously stirring the chitosan and alginate solutions at room temperature (Figure S5).

**Figure S5.** Photographs of chitosan solution added to alginate solution (left) and gel instantaneously formed after stirring (right).

#### *3.2.1 Viscosity measurement*

The viscosity of alginate and chitosan solutions employed for hydrogel formation was 460.3 ± 8.7 cP and 658.1 ± 59.1 cP, respectively. The viscosity of hydrogel was 10-fold higher (4470.1 ± 458.9 cP).

#### *3.2.2 Porosity measurement*

Porosity of unloaded, loaded and composite hydrogels was measured by the solvent replacement method. Results demonstrate that the porosity of the system remains unchanged regardless the presence of DFO and microspheres and the preparation method of composite hydrogel ($p$>0.05). The porosity of unloaded and loaded hydrogels was 84.86 ± 4.23%, and 82.11 ± 7.32% respectively. D502 hydrogel produced by 2nd method, showed a porosity of 78.68 ± 2.00%. No significant differences in porosity were found in case of other composite hydrogels.

### *3.2.3 Water uptake and swelling*

In order to study the water uptake (WU, %) and swelling characteristics, the weight and volume variations of hydrated and freeze-dried hydrogels were measured (Table 2)). Freeze-dried hydrogels absorbed a considerable amount of water and the unloaded ones showed the highest WU percentage.

The presence of microspheres reduces the WU value compared with the unloaded hydrogel ($p$<0.05). After water absorption, the hydrogels obtained have a bigger volume than freeze-dried forms. In particular the hydrogels containing DFO showed a 54% volume increase, a much higher value compared to any other ($p$<0.05).

**Table 2.** Water uptake (WU,%) and swelling ratio (SW,%) of unloaded, loaded and composite hydrogels both hydrated and freeze-dried.

| Hydrogel | freeze-dried | | hydrated | |
|---|---|---|---|---|
| | WU (%) ± SD | SW (%) | WU (%) | SW (%) |
| unloaded | 2759.9 ± 246.9$^{\$}$ | 3.6 ± 0.7* | -16.9 ± 2.2$^{\$}$* | -8.3 ± 2.8* |
| loaded | 2379.2 ± 151.4 | 54.2 ± 6.7*$^{\S}$ | -1.04 ± 1.5*$^{\S}$ | -32.3 ± 3.0*$^{\S}$ |
| D502(2$^{nd}$method) | 1954.1 ± 139.8$^{\$}$ | 16.1 ± 1.5$^{\S}$ | 7.9 ± 0.2$^{\$\S}$ | -0.3 ± 3.7$^{\S}$ |

*p < 0.05. §p < 0.05. $p < 0.05.

When the test was performed with the hydrated hydrogel, no water absorption was observed. On the contrary, weight loss was observed as well as volume contraction. As a consequence, negative WU and SW values were obtained. As concerning the preparation method, the composite hydrogel obtained by 1st method did not differ from loaded hydrogel. On the contrary, the composite hydrogel from the 2nd method absorbed smaller amount of water but did not change in volume.

No significant differences in water uptake and swelling were observed when different microspheres were incorporated.

### *3.2.4 Dynamic vapor absorption (DVS) studies*

Dynamic vapor sorption (DVS) studies describe the mechanism of water sorption by the gels. The unloaded hydrogel (Figure 3A) showed a profile typical of bulk water absorption; the hysteresis is due to the reversible and elastic swelling deformations caused by the introduction of water molecules within the polymeric network. This hydrogel fits the type II model according to the BDDT classification, indicative of a multilayer mechanism of absorption. Loaded and composite hydrogels (Figure 3B and C), presented a type III isotherm: this profile is generally observed when the interaction between vapor/surface and vapor/vapor are similar so only a few molecules of vapor adsorb on the surface at low partial pressure followed by condensation when higher humidity is reached. For all hydrogels, hysteresis was greatly reduced for RH values greater than 60%, indicating this value as a critical RH after which no further structure deformation is occurring.

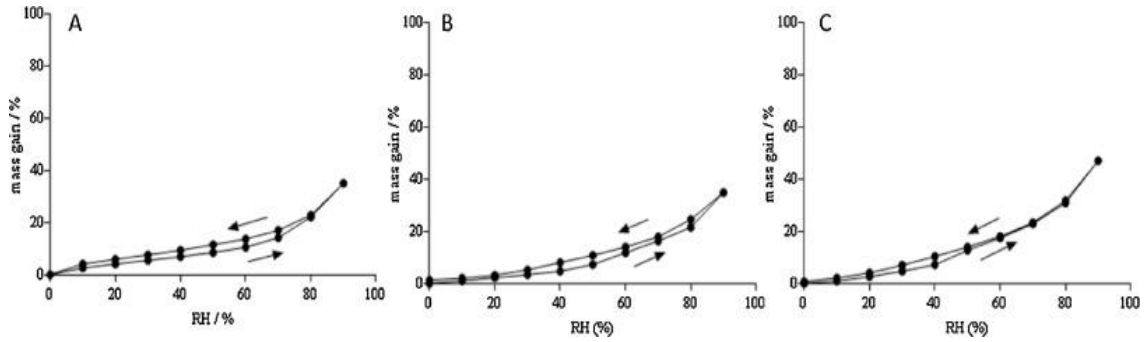


**Figure 3.** Isotherm curves for unloaded (A), loaded (B) and composite (C) hydrogels.

By applying the Korsmeyer–Peppas equation to the plots of percentage water sorbed versus time, the mechanism of hydration can be further understood. By comparing the diffusion exponent, it is evident that the unloaded hydrogel ($n_p$ = 1.018) presents a Case-II transport mechanism where the rate limiting factor is relaxation and chain disentanglement. For all loaded hydrogels (0.45 <$n_p$<0.89) diffusion is controlled by a combination of Fickian diffusion and gel deformation.

### *3.2.5 Hydrogels morphology by SEM*

The morphology of the hydrogels was evaluated in order to observe their overall structural characteristics, the presence of microspheres, the presence of the drug and also the changes after drug release.

The unloaded hydrogel (Figure 4A) presented a layered structure, whereas porous appearance was observed for the loaded hydrogel. Furthermore, crystals of DFO were evident on the structure of the loaded hydrogel (Figure 4B).

Observing the composite hydrogel prepared with the two methods, the included microspheres were clearly visible. Figure 4C shows the composite hydrogel produced by the 1st method, chosen as example; it can be seen that particles included in the gel showed integral spherical shape without collapse phenomena.

After dissolution, crystals were found in the hydrogel indicating that the composite hydrogel is able to entrap the drug released from the microspheres further delaying its release (Figure 4D). Greater drug crystallization on composite hydrogel obtained with the 2nd method occurred. Microspheres are visible after dissolution too (Figure 4D).

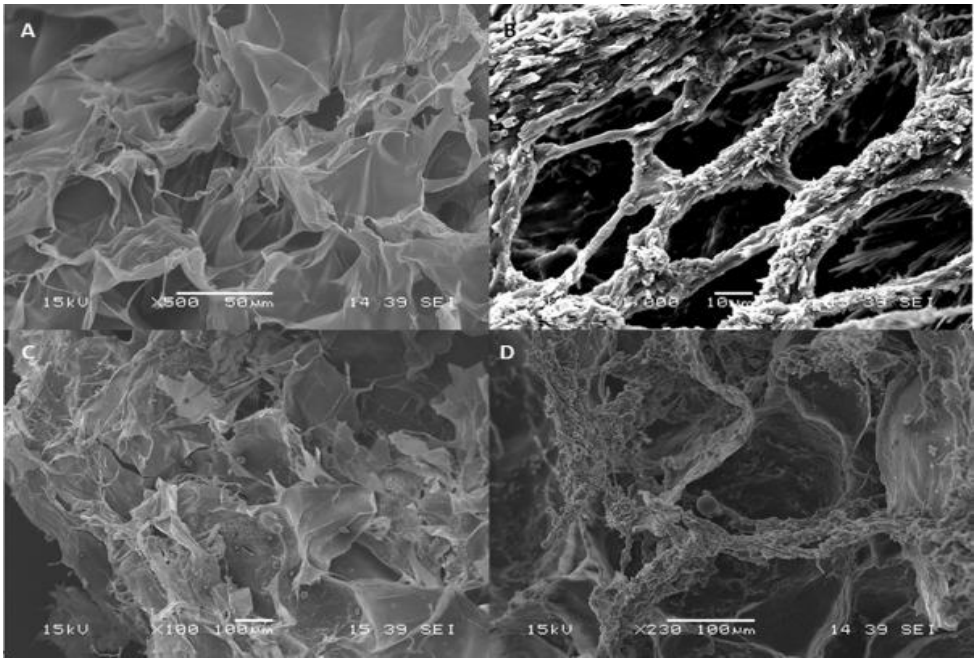


**Figure 4.** SEM pictures showing morphology of unloaded (A) and loaded (B) hydrogel (magnification 500× and 1000×). SEM pictures showing morphology of D502 10 composite hydrogel, produced by 1st method, before (C) and after (D) drug release studies (magnification 100× and 230×), chosen as examples.

### 3.2.6 Drug release studies

Figure 5 shows the release of DFO from loaded and composite hydrogels. Loaded chitosan/alginate hydrogel was able to control the release of DFO incorporated: 46% of the drug was quickly released within 1 h, the release continued gradually till reaching a plateau at 72% after 48 h. After 144 h, no statistical differences are observed between profiles of loaded hydrogel and standard DFO solution.

Data obtained are affected by the degradation process of DFO and therefore Figure 5 shows release profiles corrected and not corrected to account for the degradation. The release of DFO from the composite hydrogels was affected by the method of incorporation of the microspheres.

If microspheres were added into the chitosan solution before hydrogel formation, the resulting hydrogel showed a DFO release profile superimposable to the loaded hydrogel ($p$>0.05) during the first 48 h. Afterwards, the concentration of released DFO from the composite hydrogel declined indicating degradation exceeding release.

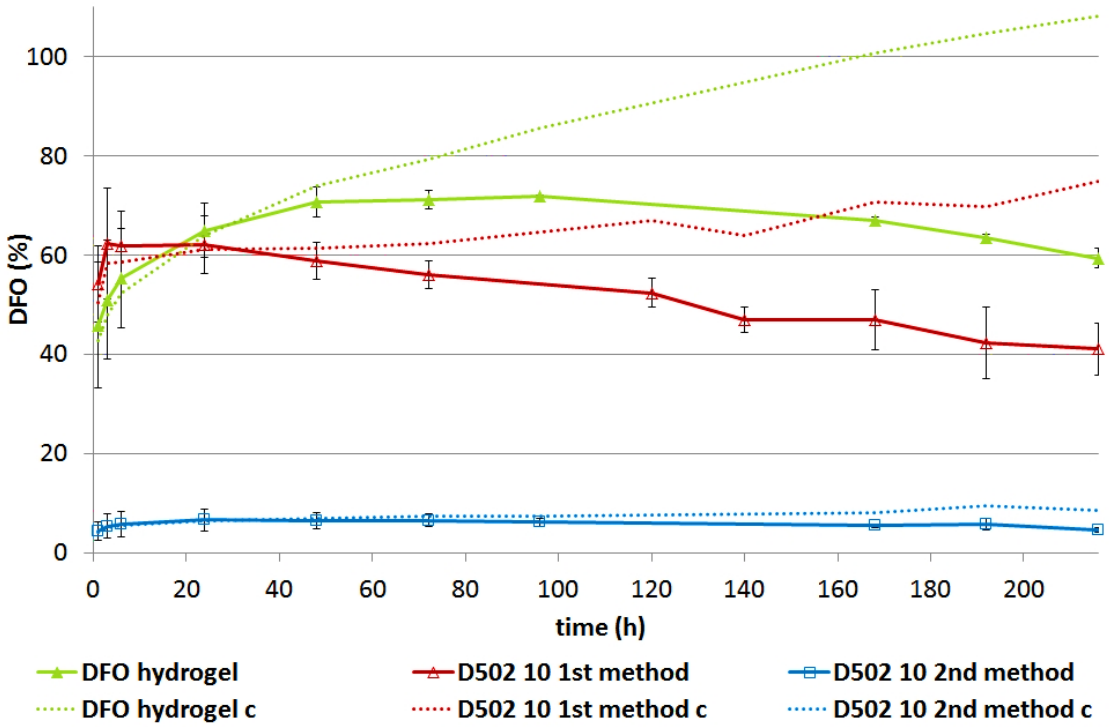


**Figure 5.** DFO release from composite hydrogel with incorporated D502 10 prepared adding microspheres into the chitosan solution before hydrogel formation (1st method) or at preformed hydrogel (2nd method). Data corrected (dotted lines) and not corrected (continuous lines).

When microspheres were incorporated into the preformed hydrogel, a much more sustained release profile was observed (Figure 5): 4% of drug incorporated in the microspheres was released within 1 h and no further release was observed until 216 h. The ability of this composite hydrogel to provide a more sustained release was attested also by the higher amount of DFO observed by SEM after dissolution test, as above described.

It must be kept in mind that the release profile of all systems is the result of two different phenomena occurring at the same time: release and degradation.

In order to examine the release profile, data points were corrected to remove the degradation aspect using Eq. (6). The D502 10 composite hydrogel formulation prepared with the 1st method did not show a strong relationship with either zero or first order overall, however, there was indication of a first order release (concentration dependent) after 48 h. This hydrogel also fits with Korsmeyer–Peppas to show Fickian diffusion as the mechanism of drug release ($n$< 0.45) (Table 3).

**Table 3.** Table showing significant $R^2$ values for the release kinetics and mechanism of release models for microspheres and composite hydrogels. $R^2$ was taken for the whole experimental time frame, from points at the beginning and toward the end of the dissolution duration.

| | t (h) | Zero Order | First Order | Hixson-Crowell | Korsmeyer-Peppas |
|---|---|---|---|---|---|
| **D502 4** | 1≤ t <240 | 0.0857 | 0.0727 | 0.1345 | 0.0465 |
| | 1≤ t <6 | 0.969 | 0.9724 | 0.9581 | 0.9940 |
| | 1≤ t <24 | 0.4785 | 0.483 | 0.4651 | 0.8401 |
| | 48≤ t <240 | 0.6221 | 0.6165 | 0.6359 | 0.4182 |
| **D502 10 1st method** | 1≤ t <216 | 0.8658 | 0.8474 | - | 0.9437 |
| | 1≤ t <24 | 0.7934 | 0.78 | - | 0.9918 |
| | 48≤ t <216 | 0.947 | 0.9477 | - | 0.9568 |
| **D502 10 2nd method** | 1≤ t <216 | 0.7562 | 0.6873 | - | 0.9612 |
| | 1≤ t <24 | 0.8017 | 0.7368 | - | 0.978 |
| | 48≤ t <216 | 0.6816 | 0.7115 | - | 0.7183 |

D502 10 composite hydrogel obtained with the 2nd method did not fit strongly to either zero or first order overall or at selected time intervals. Korsmeyer–Peppas in this composite hydrogel shows overall Fickian diffusion as the mechanism of drug release ($n$< 0.45) (Table 3).

No statistical differences were observed regardless the microspheres formulation employed. The different behavior of the composite hydrogel, can be attributed to the diverse water uptake and swelling capability. The hydrated hydrogel from 2nd method, indeed, absorbed water but did not reduce in volume whereas the other formulations significantly decreased in volume loosing water entrapped into the hydrogel network. As a consequence the drug dissolved in water is released from the hydrogel.

### 3.2.7 Biodegradability

Since ionically crosslinked alginate hydrogels do not specifically degrade but undergo slow, uncontrolled dissolution [42], biodegradability in PBS (pH 7.4) at 37°C was studied. Figure S6 shows the percentage of degradation measured for the composite hydrogel obtained with the 1st method, containing microspheres characterized by 1:10 drug–polymer ratio. At the end of the drug release studies, the hydrogel biodegraded by approximately 32–34% on the first day. No significant difference was observed regardless the kind of microspheres included in the hydrogel ($p$>0.05) at each time point. Concerning D502 10 and D504 10 composite hydrogels, a significant increase of degradability was observed between 10 and 24 days ($p$<0.05), reaching 53% and 49% respectively.

The biodegradability of chitosan/alginate hydrogel studied was independent of the preparation method employed.

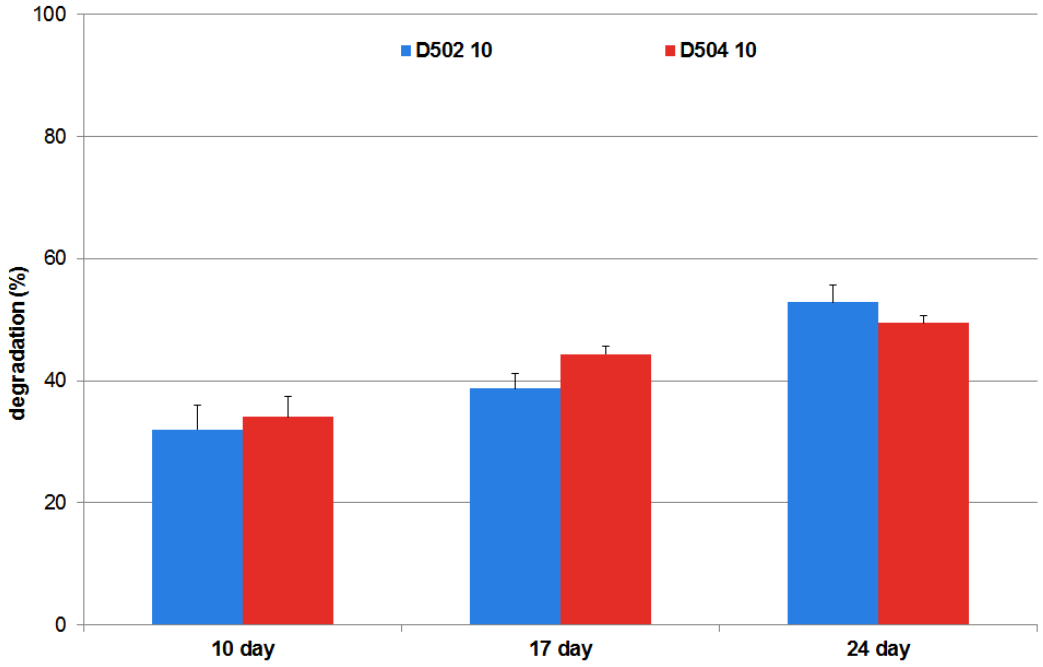


**Figure S6.** Degradation degree of composite hydrogels obtained with the 1st method

## 4. CONCLUSION

In this work, we proposed a new application of physical chitosan/alginate hydrogel and PLGA microspheres for the modified release of DFO, for which there is a therapeutic demand. These formulations produced can represent one of the few formulative approaches of DFO exploited. DFO, highly water soluble drug, can be encapsulated in biodegradable microspheres of PLGA; nevertheless, formulation into a composite hydrogel is necessary in order to obtain sustained drug release: hydrogel is better capable to control the DFO release compared to PLGA microspheres and thus absolutely necessary for achieving the prearranged aim; the composite chitosan/alginate hydrogel gave the most efficient delivery system. Furthermore, the preparation method affected the performance of the obtained systems, the DFO release from them and consequently the kind of therapeutic application. As example, hydrogel prepared by the first method can be formed in situ after injection of both solutions/suspension; on the other hand, the second method gives an implantable hydrogel.

In conclusion, disruption of iron regulation plays a key role in the etiology of several diseases (neurological disorders, cancer, stroke, skin, muscle and bone diseases), which

require different approaches, methods and time of treatment. The prepared systems not only could solve the criticalities common to several iron dysregulation diseases, but show versatility and usefulness with regard to the disease and/or administration route.

## References


[1] Camaschella C, Strati P. Recent advances in iron metabolism and related disorders. *Internal and Emergency Medicine*. 2010; 5:393–400.

[2] Loh A, Hadziahmetovic M, Dunaief JL. Iron homeostasis and eye disease. *Biochim Biophys Acta.* 2009; 1790:637–49.

[3] Pouillot A, Polla A, Polla BS. Iron and iron chelators: a review on potential effects on skin aging. *Curr Aging Sci*. 2013; 6:225–31.

[4] Yamasaki T, Sakaida I. Hepatic arterial infusion chemotherapy for advanced hepatocellular carcinoma and future treatments for the poor responders. *Hepatol Res* 2012; 42:340–48.

[5] Jomova K, Valko M. Importance of iron chelation in free radical-induced oxidative stress and human disease. *Curr Pharm Design*. 2011; 17:3460–73

[6] Hua Y, Keep RF, Hoff JT, Xi G. Deferoxamine therapy for intracerebral haemorrhage. *Act Neur S*. 2008; 105:3–6.

[7] Angel M, Narayanan K, Swartz W, Ramasastry SS, Kuhns DB, Basford RE, Futrell JW. Deferoxamine increases skin flap survival: additional evidence of free radical involvement in ischemic flap survival. *Brit J Plast Surg*.1986; 9:469–72.

[8] Diaz DD, Freeman SB, Wilson JF, Parker GS. Hematomainduced flap necrosis and free radical scavengers. *Archiv Otolaryngol*. 1992; 118:516–8.

[9] Hom DB., Goding GS. Jr, Price JA, Pernell KJ, Maisel RH. The effects of conjugated deferoxamine in porcine skin flaps. *Head Neck*. 2000; 22:579–84.

[10] Morris SF, Pang CY, Lofchy NM, Davidson G, Lindsay WK, Zuker RM, Boyd B. Deferoxamine attenuates ischemia- induced reperfusion injury in the skin and muscle of myocutaneous flaps in the pig. *Plast Reconstr Surg*. 1993; 92:120–32.

[11] Weinstein G, Maves M, McCormack M. Deferoxamine decreases necrosis in dorsally based pig skin flaps. *Otolaryngol. Head Neck Surg*. 1989; 10:559–61.

[12] Mericli AF, Das A, Best R, Rodeheaver P, Rodeheaver G, Lin KY. Deferoxamine mitigates radiation-induced tissue injury in a rat irradiated tram flap model. *Plast Reconstr Surg*. 2015; 135:124e–134e.

[13] Jin H, Terai S, Sakaida I. The iron chelator deferoxamine causes activated hepatic stellate cells to become quiescent and to undergo apoptosis. *J Gastroenterol*. 2007; 42:475–484.

[14] Sakaida I, Hironaka K, Uchida K, Okita K. Iron chelator deferoxamine reduces preneoplastic lesions in liver induced by choline-deficient L-amino acid-defined diet in rats. *Digest Dis Sci.* 1999; 44:560–9.

[15] Yamasaki T, Terai S, Sakaida I. Deferoxamine for advanced hepatocellular carcinoma. *The New Engl J Med*. 2011; 365:576–8.

[16] Farberg AS, Sarhaddi D, Donneys A, Deshpande SS, Buchman SR. Deferoxamine enhances bone regeneration in mandibular distraction osteogenesis. *Plas Reconstr Surg*. 2014; 133:666–71.

[17] Felice PA, Ahsan S, Donneys A, Deshpande SS, Nelson NS, Buchman SR. Deferoxamine administration delivers translational optimization of distraction osteogenesis in the irradiated mandible. *Plast Reconstr Surg*. 2013; 132:542e–48e

[18] Grewal BS, Keller B, Weinhold P, Dahners LE. Evaluating effects of deferoxamine in a rat tibia critical bone defect model. *J. Orthop*. 2014; 11:5–9.

[19] Hertzberg BP, Holt JB, Graff RD, Gilbert SR, Dahners LE. An evaluation of carrier agents for deferoxamine, an upregulator of vascular endothelial growth factor. *J Biomate Appl*. 2013; 27:1046–54.

[20] Stewart R, Goldstein J, Eberhardt A, Chu GT, Gilbert S. Increasing vascularity to improve healing of a segmental defect of the rat femur. *J Orthop Trauma* 2011; 25:472–6.

[21] Zhang W, Li G, Deng R, Deng L, Qiu S. New bone formation in a true bone ceramic scaffold loaded with desferrioxamine in the treatment of segmental bone defect: a preliminary study. *J Orthop Sci.* 2012; 17:289–98.

[22] Allain P, Mauras Y, Chaleil D, Simon P, Ang KS, Cam G, Le Mignon L, Simon M. Pharmacokinetics and renal elimination of desferrioxamine and ferrioxamine in healthy subjects and patients with haemochromatosis. *Brit J Clin Pharm*. 1987; 4:207–12.

[23] Cappellini MD, Pattoneri P. Oral iron chelators. *Annu Revi Med*. 2009; 60:25–38.

[24] Hallaway PE, Eaton JW, Panter SS, Hedlund BE. Modulation of deferoxamine toxicity and clearance by covalent attachment to biocompatible polymers. *P Natl Acad Sci USA*. 1989; 86:10108–12.

[25] Imran ul-haq M, Hamilton JL, Lai BF, Shenoi RA, Horte S, Constantinescu I, Leitch HA, Kizhakkedathu JN. Design of long circulating nontoxic dendritic polymers for the removal of iron in vivo. *ACS Nano*. 2013; 7:10704-16.

[26] Rassu G, Soddu E, Cossu M, Brundu A, Cerri G, Marchetti N, Ferraro L, Regan RF, Giunchedi P, Gavini E, Dalpiaz A. Solid microparticles based on chitosan or methyl-β-cyclodextrin: A first formulative approach to increase the nose-to-brain transport of deferoxamine mesylate. *J Control Release*. 2015; 68–77.

[27] Grewal BS, Keller B, Weinhold P, Dahners LE. Evaluating effects of deferoxamine in a rat tibia critical bone defect model. *J. Orthop*. 2014; 11:5–9

[28] Giunchedi P, Maestri M, Gavini E, Dionigi P, Rassu G. Transarterial chemoembolization of hepatocellular carcinoma – Agents and drugs: An overview. Part 2. *Expert Opin Drug Del*. 2013; 10:799–810

[29] Salis A, Rassu G, Budai-Szűcs M, Benzoni I, Csányi E, Berkó S, Maestri M, Dionigi P, Porcu EP, Gavini E, Giunchedi P. Development of thermosensitive chitosan/glicerophospate injectable in situ gelling solutions for potential application in intraoperative fluorescence imaging and local therapy of hepatocellular carcinoma: a preliminary study. *Expert Opin Drug Del*. 2015; In Press doi:10.1517/ 17425247.2015.1042452 .

[30] Caló E, Khutoryanskiy VV. Biomedical applications of hydrogels: A review of patents and commercial products. *Eur Polym J*. 2015; 65:252–67.

[31] Hoare TR, Kohane DS. Hydrogels in drug delivery: Progress and challenges. *Polym.* 2008; 49:1993–2007.

[32] Buwalda SJ, Boere KW, Dijkstra PJ, Feijen J, Vermonden T, Hennink WE. Hydrogels in a historical perspective: From simple networks to smart materials. *J Control Release.* 2014; 190:254–73

[33] Hartmann M, Dentini M, Draget KI, Skjåk-Bræk G. Enzymatic modification of alginates with the mannuronan C-5 epimerase AlgE4 enhances their solubility at low pH. *Carbohyd Polym*. 2006; 63.257–62.

[34] Gavini E, Chetoni P, Cossu M, Alvarez MG, Saettone MF, Giunchedi P. PLGA microspheres for the ocular delivery of a peptide drug, vancomycin using emulsification/spray-drying as the preparation method: in vitro/in vivo studies. *Eur J Pharm Biopharm*. 2004; 57:207–12.

[35] Rassu G, Nieddu M, Bosi P, Trevisi P, Colombo M, Priori D, Manconi P, Giunchedi P, Gavini E, Boatto G. Encapsulation and modified-release of thymol from oral microparticles as adjuvant or substitute to current medications. *Phytomedicine.* 2014; 21:1627–32.

[36] Ranjha NM, Qureshi UF. Preparation and characterization of crosslinked acrylic acid/hydroxypropyl methyl cellulose hydrogels for drug delivery. *Int J Pharmacy Pharm Sci*. 2014; 6:400–10.

[37] Zang S, Dong G, Peng B, Xu J, Ma Z, Wang X, Liu L, Wang Q. A comparison of physicochemical properties of sterilized chitosan hydrogel and its applicability in a canine model of periodontal regeneration. *Carbohyd Polym*. 2014; 113:240–8.

[38] Arora G, Malik K, Singh I, Arora S, Rana V. Formulation and evaluation of controlled release matrix mucoadhesive tablets of domperidone using Salvia plebeian gum. *J Adv Pharm Technol Res*. 2011; 2:163–9

[39] Sosnik A, Seremeta KP. Advantages and challenges of the spray-drying technology for the production of pure drug particles and drug-loaded polymeric carriers. *Adv Colloid Interfac. Science*, 2015; 223:40–54.

[40] Sollohub K. Spray Drying Technique. I: Hardware and Process Parameters. *J Pharm Sci.* 2009; 99:575–87.

[41] Freiberg S, Zhu XX. Polymer microspheres for controlled drug release. *Int J Pharm*. 2004; 282:1–18.

[42] Drury JL, Mooney DJ. Hydrogels for tissue engineering: scaffold design variables and applications. *Biomaterials*. 2003;24:4337–51.

## GENERAL CONCLUSIONS

In my PhD thesis, the great potential of different drug delivery systems has been confirmed.

The novel platforms proposed for transarterial embolization would be promising for embolization therapies. The results obtained suggest that *in situ gelling* solutions, preformed microparticles and *in situ forming* microspheres could be a valid alternative to conventional embolic agents.

Chitosan/glycerophosphate hydrogels have shown potential not only as embolic system, but also as imaging tool during hepatic resection. Indeed, thermosensitive solutions form compact gels suitable for occlusion of tumour feeding vessel. In addition, strong interaction between chitosan and fluorescent indocyanine green can be exploited for intraoperative visualization of tumour nodules.

Cellulose acetate butyrate microspheres, obtained through multi-step process, have shown appropriate features for embolic application. In fact, these microsystems have a suitable particle size for the injection through a catheter. Moreover, indocyanine release profile and fluorescence studies demonstrate the capability of the platforms to retain the dye, releasing very low ICG amount over 4 weeks. Also in this case, the prolonged visualization of microspheres could be useful during the surgical resection of the liver tumour previously embolized with the same particles.

*In situ forming* microspheres represent an innovative formulation for HCC treatment. Due to their physical properties, these formulations can injected through a microcatheter close to the tumour nodule. Thereafter, the contact of this emulsion with the aqueous blood component leads to microsphere formation resulting in occlusion of tumour vessels. Furthermore, *in vitro* controlled release of anti-inflammatory drug for the treatment of post embolization syndrome has been demonstrated.

In addition to drug delivery systems for embolization of liver tumours, other research lines involving different therapeutic applications have been developed.

Microparticulate controlled delivery systems have been realize for the treatment of ocular infections from Gram-positive and Gram-negative bacteria. The ionic interactions between ciprofloxacin and chondroitin sulphate/lambda carrageenan led to coprecipitates formation. The results confirm that these microparticles can be employed as vehicles for

the sustained release of ciprofloxacin after being displaced by the mediums ions in the precorneal region.

Finally, composite chitosan/alginate hydrogel with poly(lactic-co-glycolic acid) microspheres loaded with deferoxamine mesilate has been proposed as a novel strategy for the treatment of iron dysregulation diseases, which require different approaches, methods and time of treatment. The drug has been encapsulated in biodegradable microspheres of poly(lactic-co-glycolic acid) but the co-formulation with chitosan/alginate hydrogel was necessary in order to obtain sustained drug release: hydrogel is better capable to control the deferoxamine release compared to polymeric microspheres. The final system have shown versatility and usefulness with regard to the disease and/or administration route.

In conclusion, the promising results of all systems prepared confirm their potential utility in diagnostic and therapeutic applications.

## LICENCE AGREEMENTS

# ELSEVIER LICENSE
# TERMS AND CONDITIONS

Oct 19, 2016

This Agreement between Elena Piera Porcu ("You") and Elsevier ("Elsevier") consists of your license details and the terms and conditions provided by Elsevier and Copyright Clearance Center.

| | |
|---|---|
| License Number | 3966390979594 |
| License date | Oct 12, 2016 |
| Licensed Content Publisher | Elsevier |
| Licensed Content Publication | Biotechnology Advances |
| Licensed Content Title | Indocyanine green delivery systems for tumour detection and treatments |
| Licensed Content Author | Elena P. Porcu,Andrea Salis,Elisabetta Gavini,Giovanna Rassu,Marcello Maestri,Paolo Giunchedi |
| Licensed Content Date | September–October 2016 |
| Licensed Content Volume Number | 34 |
| Licensed Content Issue Number | 5 |
| Licensed Content Pages | 22 |
| Start Page | 768 |
| End Page | 789 |
| Type of Use | reuse in a thesis/dissertation |
| Portion | full article |
| Format | both print and electronic |
| Are you the author of this Elsevier article? | Yes |
| Will you be translating? | No |
| Order reference number | |
| Title of your thesis/dissertation | Development of novel platforms for diagnosis and therapy in experimental medicine |
| Expected completion date | Apr 2017 |
| Estimated size (number of pages) | 200 |
| Elsevier VAT number | GB 494 6272 12 |

| | |
|---|---|
| Requestor Location | Elena Piera Porcu<br>via Muroni 23 A<br><br>Sassari, 07100<br>Italy<br>Attn: Elena Piera Porcu |
| Total | **0.00 EUR** |

Terms and Conditions

**INTRODUCTION**

1. The publisher for this copyrighted material is Elsevier. By clicking "accept" in connection with completing this licensing transaction, you agree that the following terms and conditions apply to this transaction (along with the Billing and Payment terms and conditions established by Copyright Clearance Center, Inc. ("CCC"), at the time that you opened your Rightslink account and that are available at any time at http://myaccount.copyright.com).

**GENERAL TERMS**

2. Elsevier hereby grants you permission to reproduce the aforementioned material subject to the terms and conditions indicated.

3. Acknowledgement: If any part of the material to be used (for example, figures) has appeared in our publication with credit or acknowledgement to another source, permission must also be sought from that source. If such permission is not obtained then that material may not be included in your publication/copies. Suitable acknowledgement to the source must be made, either as a footnote or in a reference list at the end of your publication, as follows:

"Reprinted from Publication title, Vol /edition number, Author(s), Title of article / title of chapter, Pages No., Copyright (Year), with permission from Elsevier [OR APPLICABLE SOCIETY COPYRIGHT OWNER]." Also Lancet special credit - "Reprinted from The Lancet, Vol. number, Author(s), Title of article, Pages No., Copyright (Year), with permission from Elsevier."

4. Reproduction of this material is confined to the purpose and/or media for which permission is hereby given.

5. Altering/Modifying Material: Not Permitted. However figures and illustrations may be altered/adapted minimally to serve your work. Any other abbreviations, additions, deletions and/or any other alterations shall be made only with prior written authorization of Elsevier Ltd. (Please contact Elsevier at permissions@elsevier.com)

6. If the permission fee for the requested use of our material is waived in this instance, please be advised that your future requests for Elsevier materials may attract a fee.

7. Reservation of Rights: Publisher reserves all rights not specifically granted in the combination of (i) the license details provided by you and accepted in the course of this licensing transaction, (ii) these terms and conditions and (iii) CCC's Billing and Payment terms and conditions.

8. License Contingent Upon Payment: While you may exercise the rights licensed immediately upon issuance of the license at the end of the licensing process for the transaction, provided that you have disclosed complete and accurate details of your proposed use, no license is finally effective unless and until full payment is received from you (either by publisher or by CCC) as provided in CCC's Billing and Payment terms and conditions. If full payment is not received on a timely basis, then any license preliminarily granted shall be deemed automatically revoked and shall be void as if never granted. Further, in the event that you breach any of these terms and conditions or any of CCC's Billing and Payment terms and conditions, the license is automatically revoked and shall be void as if never granted. Use of materials as described in a revoked license, as well as any use of the materials

beyond the scope of an unrevoked license, may constitute copyright infringement and publisher reserves the right to take any and all action to protect its copyright in the materials.

9. Warranties: Publisher makes no representations or warranties with respect to the licensed material.

10. Indemnity: You hereby indemnify and agree to hold harmless publisher and CCC, and their respective officers, directors, employees and agents, from and against any and all claims arising out of your use of the licensed material other than as specifically authorized pursuant to this license.

11. No Transfer of License: This license is personal to you and may not be sublicensed, assigned, or transferred by you to any other person without publisher's written permission.

12. No Amendment Except in Writing: This license may not be amended except in a writing signed by both parties (or, in the case of publisher, by CCC on publisher's behalf).

13. Objection to Contrary Terms: Publisher hereby objects to any terms contained in any purchase order, acknowledgment, check endorsement or other writing prepared by you, which terms are inconsistent with these terms and conditions or CCC's Billing and Payment terms and conditions. These terms and conditions, together with CCC's Billing and Payment terms and conditions (which are incorporated herein), comprise the entire agreement between you and publisher (and CCC) concerning this licensing transaction. In the event of any conflict between your obligations established by these terms and conditions and those established by CCC's Billing and Payment terms and conditions, these terms and conditions shall control.

14. Revocation: Elsevier or Copyright Clearance Center may deny the permissions described in this License at their sole discretion, for any reason or no reason, with a full refund payable to you. Notice of such denial will be made using the contact information provided by you. Failure to receive such notice will not alter or invalidate the denial. In no event will Elsevier or Copyright Clearance Center be responsible or liable for any costs, expenses or damage incurred by you as a result of a denial of your permission request, other than a refund of the amount(s) paid by you to Elsevier and/or Copyright Clearance Center for denied permissions.

**LIMITED LICENSE**

The following terms and conditions apply only to specific license types:

15. **Translation**: This permission is granted for non-exclusive world **English** rights only unless your license was granted for translation rights. If you licensed translation rights you may only translate this content into the languages you requested. A professional translator must perform all translations and reproduce the content word for word preserving the integrity of the article.

16. **Posting licensed content on any Website**: The following terms and conditions apply as follows: Licensing material from an Elsevier journal: All content posted to the web site must maintain the copyright information line on the bottom of each image; A hyper-text must be included to the Homepage of the journal from which you are licensing at http://www.sciencedirect.com/science/journal/xxxxx or the Elsevier homepage for books at http://www.elsevier.com; Central Storage: This license does not include permission for a scanned version of the material to be stored in a central repository such as that provided by Heron/XanEdu.

Licensing material from an Elsevier book: A hyper-text link must be included to the Elsevier homepage athttp://www.elsevier.com . All content posted to the web site must maintain the copyright information line on the bottom of each image.

**Posting licensed content on Electronic reserve**: In addition to the above the following clauses are applicable: The web site must be password-protected and made available only to bona fide students registered on a relevant course. This permission is granted for 1 year only. You may obtain a new license for future website posting.

17. **For journal authors:** the following clauses are applicable in addition to the above:

**Preprints:**

A preprint is an author's own write-up of research results and analysis, it has not been peer-reviewed, nor has it had any other value added to it by a publisher (such as formatting, copyright, technical enhancement etc.).

Authors can share their preprints anywhere at any time. Preprints should not be added to or enhanced in any way in order to appear more like, or to substitute for, the final versions of articles however authors can update their preprints on arXiv or RePEc with their Accepted Author Manuscript (see below).

If accepted for publication, we encourage authors to link from the preprint to their formal publication via its DOI. Millions of researchers have access to the formal publications on ScienceDirect, and so links will help users to find, access, cite and use the best available version. Please note that Cell Press, The Lancet and some society-owned have different preprint policies. Information on these policies is available on the journal homepage.

**Accepted Author Manuscripts:** An accepted author manuscript is the manuscript of an article that has been accepted for publication and which typically includes author-incorporated changes suggested during submission, peer review and editor-author communications.

Authors can share their accepted author manuscript:

- – immediately
    - via their non-commercial person homepage or blog
    - by updating a preprint in arXiv or RePEc with the accepted manuscript
    - via their research institute or institutional repository for internal institutional uses or as part of an invitation-only research collaboration work-group
    - directly by providing copies to their students or to research collaborators for their personal use
    - for private scholarly sharing as part of an invitation-only work group on commercial sites with which Elsevier has an agreement
- – after the embargo period
    - via non-commercial hosting platforms such as their institutional repository
    - via commercial sites with which Elsevier has an agreement

In all cases accepted manuscripts should:

- – link to the formal publication via its DOI
- – bear a CC-BY-NC-ND license - this is easy to do
- – if aggregated with other manuscripts, for example in a repository or other site, be shared in alignment with our hosting policy not be added to or enhanced in any way to appear more like, or to substitute for, the published journal article.

**Published journal article (JPA):** A published journal article (PJA) is the definitive final record of published research that appears or will appear in the journal and embodies all value-adding publishing activities including peer review co-ordination, copy-editing, formatting, (if relevant) pagination and online enrichment.

Policies for sharing publishing journal articles differ for subscription and gold open access articles:

**Subscription Articles:** If you are an author, please share a link to your article rather than the full-text. Millions of researchers have access to the formal publications on ScienceDirect, and so links will help your users to find, access, cite, and use the best available version.

Theses and dissertations which contain embedded PJAs as part of the formal submission can be posted publicly by the awarding institution with DOI links back to the formal publications on ScienceDirect.

If you are affiliated with a library that subscribes to ScienceDirect you have additional private sharing rights for others' research accessed under that agreement. This includes use for classroom teaching and internal training at the institution (including use in course packs and courseware programs), and inclusion of the article for grant funding purposes.

**Gold Open Access Articles:** May be shared according to the author-selected end-user license and should contain a CrossMark logo, the end user license, and a DOI link to the formal publication on ScienceDirect.

Please refer to Elsevier's posting policy for further information.

18. **For book authors the following clauses are applicable in addition to the above:** Authors are permitted to place a brief summary of their work online only. You are not allowed to download and post the published electronic version of your chapter, nor may you scan the printed edition to create an electronic version.**Posting to a repository:** Authors are permitted to post a summary of their chapter only in their institution's repository.

19. **Thesis/Dissertation**: If your license is for use in a thesis/dissertation your thesis may be submitted to your institution in either print or electronic form. Should your thesis be published commercially, please reapply for permission. These requirements include permission for the Library and Archives of Canada to supply single copies, on demand, of the complete thesis and include permission for Proquest/UMI to supply single copies, on demand, of the complete thesis. Should your thesis be published commercially, please reapply for permission. Theses and dissertations which contain embedded PJAs as part of the formal submission can be posted publicly by the awarding institution with DOI links back to the formal publications on ScienceDirect.

**Elsevier Open Access Terms and Conditions**

You can publish open access with Elsevier in hundreds of open access journals or in nearly 2000 established subscription journals that support open access publishing. Permitted third party re-use of these open access articles is defined by the author's choice of Creative Commons user license. See our open access license policy for more information.

**Terms & Conditions applicable to all Open Access articles published with Elsevier:**

Any reuse of the article must not represent the author as endorsing the adaptation of the article nor should the article be modified in such a way as to damage the author's honour or reputation. If any changes have been made, such changes must be clearly indicated.

The author(s) must be appropriately credited and we ask that you include the end user license and a DOI link to the formal publication on ScienceDirect.

If any part of the material to be used (for example, figures) has appeared in our publication with credit or acknowledgement to another source it is the responsibility of the user to ensure their reuse complies with the terms and conditions determined by the rights holder.

**Additional Terms & Conditions applicable to each Creative Commons user license:**

**CC BY:** The CC-BY license allows users to copy, to create extracts, abstracts and new works from the Article, to alter and revise the Article and to make commercial use of the Article (including reuse and/or resale of the Article by commercial entities), provided the user gives appropriate credit (with a link to the formal publication through the relevant DOI), provides a link to the license, indicates if changes

**Our Ref: LA/IEDD/P9147**

18 November 2016

Dear Elena Piera Porcu,

**Material requested:** Andrea Salis, Giovanna Rassu, Maria Budai-Szűcs, Ilaria Benzoni, Erzsébet Csányi, Szilvia Berkó, Marcello Maestri, Paolo Dionigi, Elena P Porcu , Elisabetta Gavini & Paolo Giunchedi (2015) Development of thermosensitive chitosan/glicerophospate injectable in situ gelling solutions for potential application in intraoperative fluorescence imaging and local therapy of hepatocellular carcinoma: a preliminary study, Expert Opinion on Drug Delivery, 12:10, 1583-1596

Thank you for your correspondence requesting permission to reproduce the above mentioned material from our Journal in your printed thesis entitled 'Development of novel platforms for diagnosis and therapy in experimental medicine' and to be posted in the university's repository - University of Pavia (Italy).

We will be pleased to grant permission on the sole condition that you acknowledge the original source of publication and insert a reference to the article on the Journals website: http://www.tandfonline.com

This is the authors accepted manuscript of an article published as the version of record in Expert Opinion on Drug Delivery © 20 Sep 2016 http://dx.doi.org/10.1080/17425247.2016.1238456

This permission does not cover any third party copyrighted work which may appear in the material requested.

Please note that this license does not allow you to post our content on any third party websites or repositories.

Thank you for your interest in our Journal.

Yours sincerely

Lee-Ann

**Lee-Ann Anderson** – Senior Permissions Executive, Journals
Routledge, Taylor & Francis Group
3 Park Square, Milton Park, Abingdon, Oxon, OX14 4RN, UK.
Tel: +44 (0)20 7017 7932
Fax:+44 (0)20 7017 6336
Web: www.tandfonline.com
e-mail: lee-ann.anderson@tandf.co.uk

**Our Ref: LA/IDDI/P9148**

18 November 2016

Dear Elena Piera Porcu,

**Material requested:** Elisabetta Gavini, Maria Cristina Bonferoni, Giovanna Rassu, Giuseppina Sandri, Silvia Rossi, Andrea Salis, Elena Piera Porcu & Paolo Giunchedi (2016) Engineered microparticles based on drug–polymer coprecipitates for ocular-controlled delivery of Ciprofloxacin: influence of technological parameters, Drug Development and Industrial Pharmacy, 42:4, 554-562

Thank you for your correspondence requesting permission to reproduce the above mentioned material from our Journal in your printed thesis entitled 'Development of novel platforms for diagnosis and therapy in experimental medicine' and to be posted in the university's repository - University of Pavia (Italy).

We will be pleased to grant permission on the sole condition that you acknowledge the original source of publication and insert a reference to the article on the Journals website: http://www.tandfonline.com

This is the authors accepted manuscript of an article published as the version of record in Drug Development and Industrial Pharmacy© 20 Sep 2016 http://dx.doi.org/10.3109/03639045.2015.1100201

This permission does not cover any third party copyrighted work which may appear in the material requested.

Please note that this license does not allow you to post our content on any third party websites or repositories.

Thank you for your interest in our Journal.

Yours sincerely

Lee-Ann

**Lee-Ann Anderson** – Senior Permissions Executive, Journals
Routledge, Taylor & Francis Group
3 Park Square, Milton Park, Abingdon, Oxon, OX14 4RN, UK.
Tel: +44 (0)20 7017 7932
Fax:+44 (0)20 7017 6336
Web: www.tandfonline.com
e-mail: lee-ann.anderson@tandf.co.uk

# ELSEVIER LICENSE
# TERMS AND CONDITIONS

Oct 19, 2016

This Agreement between Elena Piera Porcu ("You") and Elsevier ("Elsevier") consists of your license details and the terms and conditions provided by Elsevier and Copyright Clearance Center.

| | |
|---|---|
| License Number | 3967570187803 |
| License date | Oct 14, 2016 |
| Licensed Content Publisher | Elsevier |
| Licensed Content Publication | Carbohydrate Polymers |
| Licensed Content Title | Composite chitosan/alginate hydrogel for controlled release of deferoxamine: A system to potentially treat iron dysregulation diseases |
| Licensed Content Author | Giovanna Rassu,Andrea Salis,Elena Piera Porcu,Paolo Giunchedi,Marta Roldo,Elisabetta Gavini |
| Licensed Content Date | 20 January 2016 |
| Licensed Content Volume Number | 136 |
| Licensed Content Issue Number | n/a |
| Licensed Content Pages | 10 |
| Start Page | 1338 |
| End Page | 1347 |
| Type of Use | reuse in a thesis/dissertation |
| Portion | full article |
| Format | both print and electronic |
| Are you the author of this Elsevier article? | Yes |
| Will you be translating? | No |
| Order reference number | |
| Title of your thesis/dissertation | Development of novel platforms for diagnosis and therapy in experimental medicine |
| Expected completion date | Apr 2017 |
| Estimated size (number of pages) | 200 |
| Elsevier VAT number | GB 494 6272 12 |
| Requestor Location | Elena Piera Porcu<br>via Muroni 23 A<br><br>Sassari, 07100<br>Italy<br>Attn: Elena Piera Porcu |
| Total | **0.00 EUR** |
| Terms and Conditions | |

**INTRODUCTION**

1. The publisher for this copyrighted material is Elsevier. By clicking "accept" in connection with completing this licensing transaction, you agree that the following terms and conditions apply to this transaction (along with the Billing and Payment terms and conditions established by Copyright Clearance Center, Inc. ("CCC"), at the time that you opened your Rightslink account and that are available at any time at http://myaccount.copyright.com).

**GENERAL TERMS**

2. Elsevier hereby grants you permission to reproduce the aforementioned material subject to the terms and conditions indicated.

3. Acknowledgement: If any part of the material to be used (for example, figures) has appeared in our publication with credit or acknowledgement to another source, permission must also be sought from that source. If such permission is not obtained then that material may not be included in your publication/copies. Suitable acknowledgement to the source must be made, either as a footnote or in a reference list at the end of your publication, as follows:

"Reprinted from Publication title, Vol /edition number, Author(s), Title of article / title of chapter, Pages No., Copyright (Year), with permission from Elsevier [OR APPLICABLE SOCIETY COPYRIGHT OWNER]." Also Lancet special credit - "Reprinted from The Lancet, Vol. number, Author(s), Title of article, Pages No., Copyright (Year), with permission from Elsevier."

4. Reproduction of this material is confined to the purpose and/or media for which permission is hereby given.

5. Altering/Modifying Material: Not Permitted. However figures and illustrations may be altered/adapted minimally to serve your work. Any other abbreviations, additions, deletions and/or any other alterations shall be made only with prior written authorization of Elsevier Ltd. (Please contact Elsevier at permissions@elsevier.com)

6. If the permission fee for the requested use of our material is waived in this instance, please be advised that your future requests for Elsevier materials may attract a fee.

7. Reservation of Rights: Publisher reserves all rights not specifically granted in the combination of (i) the license details provided by you and accepted in the course of this licensing transaction, (ii) these terms and conditions and (iii) CCC's Billing and Payment terms and conditions.

8. License Contingent Upon Payment: While you may exercise the rights licensed immediately upon issuance of the license at the end of the licensing process for the transaction, provided that you have disclosed complete and accurate details of your proposed use, no license is finally effective unless and until full payment is received from you (either by publisher or by CCC) as provided in CCC's Billing and Payment terms and conditions. If full payment is not received on a timely basis, then any license preliminarily granted shall be deemed automatically revoked and shall be void as if never granted. Further, in the event that you breach any of these terms and conditions or any of CCC's Billing and Payment terms and conditions, the license is automatically revoked and shall be void as if never granted. Use of materials as described in a revoked license, as well as any use of the materials beyond the scope of an unrevoked license, may constitute copyright infringement and publisher reserves the right to take any and all action to protect its copyright in the materials.

9. Warranties: Publisher makes no representations or warranties with respect to the licensed material.

10. Indemnity: You hereby indemnify and agree to hold harmless publisher and CCC, and their respective officers, directors, employees and agents, from and against any and all claims arising out of your use of the licensed material other than as specifically authorized pursuant to this license.

11. No Transfer of License: This license is personal to you and may not be sublicensed, assigned, or transferred by you to any other person without publisher's written permission.

12. No Amendment Except in Writing: This license may not be amended except in a writing signed by both parties (or, in the case of publisher, by CCC on publisher's behalf).

13. Objection to Contrary Terms: Publisher hereby objects to any terms contained in any purchase order, acknowledgment, check endorsement or other writing prepared by you, which terms are inconsistent with these terms and conditions or CCC's Billing and Payment terms and conditions. These terms and conditions, together with CCC's Billing and Payment terms and conditions (which are incorporated herein), comprise the entire agreement between you and publisher (and CCC) concerning this licensing transaction. In the event of any conflict between your obligations established by these terms and conditions and those established by CCC's Billing and Payment terms and conditions, these terms and conditions shall control.

14. Revocation: Elsevier or Copyright Clearance Center may deny the permissions described in this License at their sole discretion, for any reason or no reason, with a full refund payable to you. Notice of such denial will be made using the contact information provided by you. Failure to receive such notice will not alter or invalidate the denial. In no event will Elsevier or Copyright Clearance Center be responsible or liable for any costs, expenses or damage incurred by you as a result of a denial of your permission request, other than a refund of the amount(s) paid by you to Elsevier and/or Copyright Clearance Center for denied permissions.

**LIMITED LICENSE**

The following terms and conditions apply only to specific license types:

15. **Translation**: This permission is granted for non-exclusive world **English** rights only unless your license was granted for translation rights. If you licensed translation rights you may only translate this content into the languages you requested. A professional translator must perform all translations and reproduce the content word for word preserving the integrity of the article.

16. **Posting licensed content on any Website**: The following terms and conditions apply as follows: Licensing material from an Elsevier journal: All content posted to the web site must maintain the copyright information line on the bottom of each image; A hyper-text must be included to the Homepage of the journal from which you are licensing at http://www.sciencedirect.com/science/journal/xxxxx or the Elsevier homepage for books at http://www.elsevier.com; Central Storage: This license does not include permission for a scanned version of the material to be stored in a central repository such as that provided by Heron/XanEdu.

Licensing material from an Elsevier book: A hyper-text link must be included to the Elsevier homepage athttp://www.elsevier.com . All content posted to the web site must maintain the copyright information line on the bottom of each image.

**Posting licensed content on Electronic reserve**: In addition to the above the following clauses are applicable: The web site must be password-protected and made available only to bona fide students registered on a relevant course. This permission is granted for 1 year only. You may obtain a new license for future website posting.

17. **For journal authors:** the following clauses are applicable in addition to the above:

**Preprints:**

A preprint is an author's own write-up of research results and analysis, it has not been peer-reviewed, nor has it had any other value added to it by a publisher (such as formatting, copyright, technical enhancement etc.).

Authors can share their preprints anywhere at any time. Preprints should not be added to or enhanced in any way in order to appear more like, or to substitute for, the final versions of articles however authors can update their preprints on arXiv or RePEc with their Accepted Author Manuscript (see below).

If accepted for publication, we encourage authors to link from the preprint to their formal publication via its DOI. Millions of researchers have access to the formal publications on ScienceDirect, and so links will help users to find, access, cite and use the best available version. Please note that Cell Press, The Lancet and some society-owned have different preprint policies. Information on these policies is available on the journal homepage.

**Accepted Author Manuscripts:** An accepted author manuscript is the manuscript of an article that has been accepted for publication and which typically includes author-incorporated changes suggested during submission, peer review and editor-author communications.

Authors can share their accepted author manuscript:

- – immediately
    - via their non-commercial person homepage or blog
    - by updating a preprint in arXiv or RePEc with the accepted manuscript
    - via their research institute or institutional repository for internal institutional uses or as part of an invitation-only research collaboration work-group
    - directly by providing copies to their students or to research collaborators for their personal use
    - for private scholarly sharing as part of an invitation-only work group on commercial sites with which Elsevier has an agreement
- – after the embargo period
    - via non-commercial hosting platforms such as their institutional repository
    - via commercial sites with which Elsevier has an agreement

In all cases accepted manuscripts should:

- – link to the formal publication via its DOI
- – bear a CC-BY-NC-ND license - this is easy to do
- – if aggregated with other manuscripts, for example in a repository or other site, be shared in alignment with our hosting policy not be added to or enhanced in any way to appear more like, or to substitute for, the published journal article.

**Published journal article (JPA):** A published journal article (PJA) is the definitive final record of published research that appears or will appear in the journal and embodies all value-adding publishing activities including peer review co-ordination, copy-editing, formatting, (if relevant) pagination and online enrichment.

Policies for sharing publishing journal articles differ for subscription and gold open access articles:

**Subscription Articles:** If you are an author, please share a link to your article rather than the full-text. Millions of researchers have access to the formal publications on ScienceDirect, and so links will help your users to find, access, cite, and use the best available version.

Theses and dissertations which contain embedded PJAs as part of the formal submission can be posted publicly by the awarding institution with DOI links back to the formal publications on ScienceDirect.

If you are affiliated with a library that subscribes to ScienceDirect you have additional private sharing rights for others' research accessed under that agreement. This includes use for classroom teaching and internal training at the institution (including use in course packs and courseware programs), and inclusion of the article for grant funding purposes.

**Gold Open Access Articles:** May be shared according to the author-selected end-user license and should contain a CrossMark logo, the end user license, and a DOI link to the formal publication on ScienceDirect.

Please refer to Elsevier's posting policy for further information.

18. **For book authors** the following clauses are applicable in addition to the above: Authors are permitted to place a brief summary of their work online only. You are not allowed to download and post the published electronic version of your chapter, nor may you scan the printed edition to create an electronic version.**Posting to a repository:** Authors are permitted to post a summary of their chapter only in their institution's repository.

19. **Thesis/Dissertation**: If your license is for use in a thesis/dissertation your thesis may be submitted to your institution in either print or electronic form. Should your thesis be published commercially, please reapply for permission. These requirements include permission for the Library and Archives of Canada to supply single copies, on demand, of the complete thesis and include permission for Proquest/UMI to supply single copies, on demand, of the complete thesis. Should your thesis be published commercially, please reapply for permission. Theses and dissertations which contain embedded PJAs as part of the formal submission can be posted publicly by the awarding institution with DOI links back to the formal publications on ScienceDirect.

**Elsevier Open Access Terms and Conditions**

You can publish open access with Elsevier in hundreds of open access journals or in nearly 2000 established subscription journals that support open access publishing. Permitted third party re-use of these open access articles is defined by the author's choice of Creative Commons user license. See our open access license policy for more information.

**Terms & Conditions applicable to all Open Access articles published with Elsevier:**

Any reuse of the article must not represent the author as endorsing the adaptation of the article nor should the article be modified in such a way as to damage the author's honour or reputation. If any changes have been made, such changes must be clearly indicated.

The author(s) must be appropriately credited and we ask that you include the end user license and a DOI link to the formal publication on ScienceDirect.

If any part of the material to be used (for example, figures) has appeared in our publication with credit or acknowledgement to another source it is the responsibility of the user to ensure their reuse complies with the terms and conditions determined by the rights holder.

**Additional Terms & Conditions applicable to each Creative Commons user license:**

**CC BY:** The CC-BY license allows users to copy, to create extracts, abstracts and new works from the Article, to alter and revise the Article and to make commercial use of the Article (including reuse and/or resale of the Article by commercial entities), provided the user gives appropriate credit (with a link to the formal publication through the relevant DOI), provides a link to the license, indicates if changes were made and the licensor is not represented as endorsing the use made of the work. The full details of the license are available athttp://creativecommons.org/licenses/by/4.0.

**CC BY NC SA:** The CC BY-NC-SA license allows users to copy, to create extracts, abstracts and new works from the Article, to alter and revise the Article, provided this is not done for commercial purposes, and that the user gives appropriate credit (with a link to the formal publication through the relevant DOI), provides a link to the license, indicates if changes were made and the licensor is not represented as endorsing the use made of the work. Further, any new works must be made available on the same conditions. The full details of the license are available at http://creativecommons.org/licenses/by-nc-sa/4.0.

**CC BY NC ND:** The CC BY-NC-ND license allows users to copy and distribute the Article, provided this is not done for commercial purposes and further does not permit distribution of the Article if it is changed or edited in any way, and provided the user gives appropriate credit (with a link to the formal publication through the relevant DOI), provides a link to the license, and that the licensor is not represented as endorsing the use made of the work. The full details of the license are available

**ACKNOWLEDGMENTS**

*I would like to express my deep gratitude to Prof. Paolo Giunchedi and Prof. Paolo Dionigi, my research supervisors, for giving me this great opportunity. Thanks to Dr Marcello Maestri for the collaboration in his research field.*

*Many thanks to Prof. Gavini and to Dr Giovanna Rassu, for teaching and helping me during these years of work together. Without their support, this PhD would not have been achievable.*

*I especially would also thank my "lab-colleagues" for their scientific suggestions and the good moments spent with them in last three years.*